



The
University
Of
Sheffield.

A novel solid-state processing route to generate cost-effective titanium alloy components

Nicholas Samuel Weston

The University of Sheffield
Department of Materials Science and Engineering

A thesis submitted in partial fulfilment of the requirements for the degree
of
Doctor of Philosophy

April 2017

Abstract

This thesis demonstrates progress towards a step-change in the economics of titanium. Titanium's properties make it desirable to designers, but it is frequently overlooked due to high costs; making research into reducing costs of considerable interest. Examining the literature shows cost reduction possibilities in two main areas; extraction, and downstream processing. Lower-cost extraction has previously received much attention, but in isolation will not produce the required reductions. Powder metallurgy techniques allow near net shape (NNS) production with limited material wastage and processing steps; also allowing utilisation of powders/particulates produced by many developing extraction methods. Combining products from alternative extraction with novel solid-state downstream processing has potential to produce truly cost-effective titanium alloy components.

Chapter 4 establishes field assisted sintering technology (FAST) as a rapid and effective method to fully consolidate commercial and developing titanium alloy powders, with a wide variety of chemistries, morphologies, and sizes, including material from the Metalysis FFC process. FAST scalability was successfully tested by producing a 5.5 kg, 250 mm diameter, specimen. Chapter 5 shows that titanium alloy preforms produced via FAST behave equivalently to conventionally processed melt, multi-step forged, products. The shapes and microstructures produced were not those typically required for components. Consequently, chapter 6 investigates the proposed cost-effective processing route of producing wrought microstructures in two steps from powder, which has been termed *FAST-forge*. A fully dense, microstructurally homogeneous, shaped preform billet formed via FAST was finished with a precision one-step forging operation that refined the microstructure, verifying the *FAST-forge* concept at laboratory-scale.

It is anticipated with further development, and by utilising finite element modelling, that it will be possible to produce semi-complex NNS components with competitive mechanical properties in just two steps. Therefore, *FAST-forge* has potential to be disruptive technology that could enable the desired step-change in the economics of titanium.

Dedication

To my parents, Ken and Elaine, and my sister Katie. You provided me with the environment to thrive. You taught me to be inquisitive and to love puzzles. By always believing in me and allowing me to find my own way, I learnt to believe in myself. Everything that I achieve began with you, and for that I am and always will be grateful.

To Sally, you're the best thing that ever happened to me and I love you to the moon and back. Thank you for the endless patience, for making me laugh, and for making me (and this thesis) better.

“You’re not obligated to win. You’re obligated to keep trying to do the best
you can every day.”

~Marian Wright Edelman

“One of the advantages of being disorganised
is that one is always having surprising discoveries.”

~Winnie the Pooh
A.A. Milne

Acknowledgements

First and foremost I would like to thank my supervisors, Dr Martin Jackson and Dr Fatos Derguti, for all their help and guidance throughout my project, both academically and personally. Without them I may never have taken this road, and would certainly not have reached my destination. Thanks must also go to my industrial supervisor, Dr Matthew Lunt of the Defence Science and Technology Laboratory (DSTL), for always being interested and supportive but having the faith to let me find my own way.

I would also like to thank Metalysis Ltd for supplying material to parts of this investigation, and especially Dr Ian Mellor, Dr Kartik Rao, and Lucy Grainger for their valuable inputs.

I am appreciative to the Advanced Metallic Systems Centre for Doctoral Training for providing the opportunity and the skills for me to undertake this project. Particular thanks go to Dr Brad Wynne for his enthusiasm and enlightening discussions, and to Dr Claire Hinchliffe for keeping things running smoothly.

I am indebted to a number of fellow researchers and technicians for assisting with experimental work: Dr Akemi Nogiwa-Valdez, Dr Amit Rana, Dr Luke Marshall, Mrs Sarah Hinton, Mr Dean Haylock, Mr Ian Watts, Mr Kyle Arnold, and Mr Michael Bell. Without their help, support, and patience I would still be in the lab.

Thank you to my family and all the friends I've made during my time in Sheffield. Especially all my colleagues, past and present, in D1 for making it such a pleasurable place to work; the endless tea, coffee, cake and humour probably kept me sane.

Finally I'd like to recognise the financial support of the Engineering and Physical Sciences Research Council and DSTL for providing the funding which made all of this possible.

Contents

Abstract	iii
Dedication	iv
Acknowledgements	vi
1 Introduction	1
1.1 Motivation for Lower-Cost Titanium	1
1.2 Current Cost of Titanium Components	1
1.3 Cost Reduction Strategy	2
1.4 Project Aim	4
1.5 Project Objectives	4
1.6 Thesis Outline	4
2 Literature Review	7
2.1 Overview	7
2.2 Historical Background	7
2.3 Fundamentals of Titanium	9
2.3.1 Basic Properties	9
2.3.2 Crystal Structure	10
2.3.3 Diffusion	12
2.3.4 Mechanisms of Deformation	12

2.3.4.1	Slip	13
2.3.4.2	Twinning	14
2.3.5	Titanium Alloy Classification	14
2.3.5.1	α Alloys	16
2.3.5.2	Near α Alloys	17
2.3.5.3	$\alpha + \beta$ Alloys	17
2.3.5.4	β Alloys	17
2.3.6	Phase Transformations	18
2.3.6.1	Nucleation and Diffusional Growth	19
2.3.6.2	Martensitic	19
2.3.7	Microstructure Property Relationship	20
2.4	Conventional Route for Forged Titanium Alloy Component Production	23
2.4.1	Ores and Refining	24
2.4.2	Kroll Process Extraction	25
2.4.3	Ingot Production	25
2.4.4	Thermomechanical Processing	26
2.4.4.1	Primary Processing to Mill Products	27
2.5	Secondary Processing to Produce Components	28
2.5.1	Forging	28
2.5.2	Microstructural Evolution During Forging	30
2.5.2.1	Dynamic Deformation Mechanisms	31
2.5.2.2	Dynamic Globularisation	32

2.5.2.3	Flow Curves	33
2.5.3	Heat Treatment	34
2.5.4	Thermomechanical Testing	35
2.6	Producing Cost-Effective Titanium	37
2.6.1	Overview of Alternative Extraction Methods	37
2.6.1.1	The Metalysis FFC Process	38
2.6.2	Cost-Effective Downstream Processing	39
2.6.2.1	Powder Metallurgy	40
2.6.2.2	Field Assisted Sintering Technology	41
3	Methods and Materials	47
3.1	Experimental Techniques	47
3.1.1	Field Assisted Sintering Technology	47
3.1.2	Hot Axisymmetric Compression Testing	50
3.1.2.1	Machine Overview	50
3.1.2.2	Testing Procedure	51
3.1.3	Heat Treatment	52
3.1.4	Particle Size Analysis	52
3.1.5	Microhardness	53
3.1.6	Metallography	54
3.1.7	Density	54
3.1.8	Finite Element Modelling	55
3.1.9	Carbon-Oxygen-Nitrogen Levels	56

3.2	Titanium Alloy Powders	56
3.2.1	Alloy Composition	57
3.2.2	Powder Morphologies and Microstructures	58
3.2.3	Particle Size Distribution	60
4	Consolidation of Titanium Alloy Powders via Field Assisted Sintering Technology	63
4.1	Introduction	63
4.2	Experimental Approach	64
4.2.1	Materials	65
4.2.2	Dwell Temperature and Dwell Pressure Parametric Study	66
4.2.3	Dwell Time and Heating Rate Parametric Study	67
4.3	Results and Discussions	68
4.3.1	Dwell Temperature and Dwell Pressure Parametric Study	68
4.3.1.1	Effect of Dwell Temperature and Dwell Pressure on Density	68
4.3.1.2	Effect of Dwell Temperature and Dwell Pressure on Microstructural Evolution	76
4.3.1.3	Effect of Dwell Temperature and Dwell Pressure on Rheology	84
4.3.2	Dwell Time and Heating Rate Parametric Study	87
4.3.2.1	Effect of Dwell Time and Heating Rate on Density	87
4.3.2.2	Effect of Dwell Time and Heating Rate on Microstructure	87
4.3.2.3	Effect of Dwell Time and Heating Rate on Rheology	93

4.3.3	Effect of Alloy Chemistry and Powder Morphology on Rheology	95
4.3.4	Effect of Mould Size on FAST Processing	97
4.3.5	Interstitial Pick-Up and Microhardness Values After FAST	98
4.4	Conclusions	100
5	Thermomechanical Processing of Titanium Alloys Consolidated Via Field Assisted Sintering Technology	103
5.1	Introduction	103
5.2	Experimental Approach	104
5.2.1	Materials	104
5.2.2	FAST	105
5.2.3	Axisymmetric Compression Testing	105
5.2.3.1	Correction of Recorded Load-Displacement Data	107
5.2.3.2	Conversion to Stress-Strain Data	110
5.2.3.3	Correction for Friction Effects	110
5.2.3.4	Isothermal Correction	111
5.2.3.5	Initial Constitutive Equation Development . . .	115
5.2.3.6	Strain Rate Correction	118
5.2.4	Finite Element Simulation of the Axisymmetric Compression	119
5.3	Results and Discussions	120
5.3.1	Microstructure and Density After FAST Processing . . .	120
5.3.2	Flow Curves and Microstructures after Hot Axisymmetric Compression	121

5.3.2.1	Ti-6Al-4V	125
5.3.2.2	Rutile	130
5.3.2.3	CP-Ti	134
5.3.2.4	Ti-5553	138
5.3.3	Integrating the Generated Material Data into FE Modelling	142
5.3.4	Vickers Microhardness Testing	144
5.4	Conclusions	145
6	FAST-<i>forg</i>e – a new cost-effective hybrid processing route for consolidating titanium powder into near net shape forged components	147
6.1	Introduction	147
6.2	Experimental Approach	150
6.2.1	Materials	152
6.2.2	FAST	153
6.2.2.1	FAST Processing for Initial Shaped Mould and Mould Material Study	153
6.2.2.2	FAST Processing for FAST- <i>forg</i> e Study	155
6.2.3	Hot Upset Forging	155
6.2.4	Heat Treatment	155
6.2.5	Finite Element Simulation of the Forging	156
6.3	Results and Discussions	156
6.3.1	Simple Shaped FAST Study	157
6.3.1.1	Micrographs of Underfilled Moulds	157

6.3.1.2	Micrographs of Overfilled Moulds	159
6.3.1.3	Power and Temperature Profiles of Steel and Graphite Mould Assemblies	162
6.3.2	FAST- <i>forg</i> e Study	164
6.3.2.1	Power and Current Requirements	164
6.3.2.2	Microstructures after FAST	164
6.3.2.3	Experimental Load-Displacement Curves	167
6.3.2.4	Microstructure Evolution Post One-Step Forging	169
6.3.2.5	Microstructure Post Heat Treatment	173
6.3.2.6	Finite Element Simulation	177
6.4	Conclusions	179
7	Summary, Conclusions, and Future Work	181
7.1	Summary	181
7.2	Conclusions	182
7.2.1	Consolidation of Titanium Alloy Powders via FAST	183
7.2.2	Thermomechanical Processing of Titanium Alloys Consolidated via FAST	184
7.2.3	FAST- <i>forg</i> e	185
7.2.4	Concluding Remarks	186
7.3	Future Work	187
A	Technical Drawings of FAST Mould Assemblies and Components	204
B	Published Work Reuse Permissions	208

List of Figures

1.1	Chart demonstrating the two main areas of manufacturing cost for 25 mm titanium alloy plate when conventionally processed; with relative cost factors for each sub area also shown. Produced from data reported by Kraft [5].	2
1.2	Schematic diagram outlining the two-step FAST-forge process – the proposed cost-effective solid-state processing route for producing titanium alloy components from powder.	3
2.1	Schematic diagram showing the atomic unit cell of the (a) hexagonal close packed α titanium crystal structure and (b) body centred cubic β titanium crystal structure. The most densely packed planes and directions are also indicated. Redrawn from [1, 3].	10
2.2	Plot of titanium rate of self-diffusion and diffusion rate of a selection of alloying elements in the α and β phases (dashed line is the β transus temperature). Reported by Lutjering [1].	12
2.3	Schematic diagram showing the planes and directions most favourable for slip in hcp α phase titanium. Redrawn from [1, 3].	14
2.4	Schematic pseudo-binary phase diagrams showing effects of alloying element additions on the crystal structure of titanium. Redrawn from [1, 3].	15
2.5	Pseudo-binary section of an isomorphous β phase diagram showing the position of the different alloy classifications. Redrawn from [28].	17

2.6	Schematic diagram outlining the Burgers relationship that is followed when the bcc β titanium crystal structure transforms to the hcp α titanium crystal structure upon cooling from above the β transus temperature, and the slight atomic distortion that also occurs. Redrawn from [3].	19
2.7	Light micrographs illustrating how cooling rate and start temperature can influence the microstructure when cooling titanium alloys from elevated temperatures. Parts (a), (b), and (c) were cooled from above the β transus, and parts (d), (e), and (f) were cooled from the two-phase $\alpha + \beta$ region. Parts (a) and (d) had a slow cooling rate, parts (b) and (e) had an intermediate cooling rate, and parts (c) and (f) had the quickest cooling rate. Reproduced and adapted from [1] and [29].	22
2.8	Schematic diagram giving an overview of the conventional processing route to produce wrought titanium components from titanium ore. Adapted from diagrams in [30, 31].	23
2.9	Schematic diagram illustrating an example of a typical primary processing route used to convert VAR/CHM ingots into mill products. Redrawn from [1, 2].	27
2.10	Schematic diagram illustrating examples of two types of typical secondary processing route. (a) $\alpha + \beta$ secondary working and heat treatment used to produce bi-modal microstructures. (b) β secondary working and heat treatment used to produce fully lamellar microstructures. Redrawn from [1, 3, 2].	29
2.11	Schematic diagram showing a proposed mechanism for the globularisation of α laths in $\alpha + \beta$ titanium alloys. (a) unrecrystallised, (b) the beginning of recrystallisation, (c) recrystallised α moving into adjacent α laths, (d) recrystallised α consuming adjacent α laths. Redrawn from [43].	32
2.12	Schematic diagram showing example flow curve shapes for material that undergoes dynamic recovery or dynamic recrystallisation (as labelled).	33

3.1	Photograph of the FCT Systeme GmbH Type HP D 25 FAST Furnace at The University of Sheffield; showing detail of the graphite mould assembly between the conducting hydraulic rams (right). Schematic cross-section of the FAST system's main components and mould assembly (bottom left). Graph outlining the variation in processing parameters during a FAST cycle (top left).	47
3.2	Schematic showing the geometrical features of the double truncated cone specimen used in this work.	48
3.3	Photographs and schematic outlining the major components of The University of Sheffield's thermomechanical compression machine (a), close-up view of the tool posts and furnace (b) (note the furnace has been moved to the rear to enable viewing of the tool posts), close-up of a double truncated cone specimen held in the robot gripper arms (c). The dimensions of the standard test specimens used are shown.	50
3.4	Schematic showing the effect of particle size on laser diffraction. .	53
3.5	Light micrographs showing particle size and morphology for the studied titanium alloy powders: (a) GA CP-Ti, (b) HDH CP-Ti, (c) GA Ti-6-4, (d) HDH Ti-6-4, (e) Metalysis spherical-spongy pigment-derived, (f) Metalysis angular-spongy rutile-derived, (g) Metalysis Spheroidised rutile-derived 150-250 μm , (h) GA Ti-5553. .	59
3.6	Graph showing the cumulative volume particle size distribution for the studied titanium alloy powders.	60
3.7	Cross-polarised light micrographs showing microstructure for the studied titanium alloy powders: (a) GA CP-Ti, (b) HDH CP-Ti, (c) GA Ti-6-4, (d) HDH Ti-6-4, (e) Metalysis spherical-spongy pigment-derived, (f) Metalysis angular-spongy rutile-derived, (g) Metalysis Spheroidised rutile-derived 150-250 μm , (h) GA Ti-5553. .	61

4.1	Schematic showing the experimental points in the design of experiments type approach used for the parametric study into the effect of dwell temperature and dwell pressure.	66
4.2	Bright-field micrographs showing increased density with increased dwell temperature and/or dwell pressure during constant heating rate and dwell time FAST processing of GA CP-Ti, HDH CP-Ti, spherical-spongy pigment-derived and angular-spongy rutile-derived Metalysis powders.	71
4.3	Bright-field micrographs of GA CP-Ti powder showing the increase in density with increased dwell temperature and/or dwell pressure during constant heating rate and dwell time FAST processing.	72
4.4	Bright-field micrographs of HDH CP-Ti powder showing the increase in density with increased dwell temperature and/or dwell pressure during constant heating rate and dwell time FAST processing.	73
4.5	Bright-field micrographs of spherical-spongy pigment-derived Metalysis powder showing the increase in density with increased dwell temperature and/or dwell pressure during constant heating rate and dwell time FAST processing.	74
4.6	Bright-field micrographs of angular-spongy rutile-derived Metalysis powder showing the increase in density with increased dwell temperature and/or dwell pressure during constant heating rate and dwell time FAST processing.	75
4.7	Cross-polarised light micrographs showing microstructural development during constant heating rate and dwell time FAST processing with varying dwell temperatures and dwell pressures for GA CP-Ti, HDH CP-Ti, spherical-spongy pigment-derived, and angular-spongy rutile-derived Metalysis powders.	77

4.8	Cross-polarised light micrographs of GA CP-Ti powder showing the change in microstructure with increased dwell temperature and/or dwell pressure during constant heating rate and dwell time FAST processing.	78
4.9	Cross-polarised light micrographs of HDH CP-Ti powder showing the change in microstructure with increased dwell temperature and/or dwell pressure during constant heating rate and dwell time FAST processing.	79
4.10	Cross-polarised light micrographs of spherical-spongy pigment-derived Metalysis powder showing the change in microstructure with increased dwell temperature and/or dwell pressure during constant heating rate and dwell time FAST processing.	80
4.11	Cross-polarised light micrographs of angular-spongy rutile-derived Metalysis powder showing the change in microstructure with increased dwell temperature and/or dwell pressure during constant heating rate and dwell time FAST processing.	81
4.12	Cross-polarised light micrograph of GA CP-Ti processed via FAST at 1200°C-35 MPa, with a heating rate of 25°Cmin ⁻¹ and dwell time of 10 min. The efficacy of FAST as a powder consolidation technique is demonstrated when comparing the diameter of the largest starting GA powder particles to the approximate outlines of a selection of prior β grain boundaries.	82

4.13	Effect of dwell temperature and dwell pressure on rheology curves calculated from FAST machine output data for GA CP-Ti, HDH CP-Ti, spherical-spongy pigment-derived, and angular-spongy rutile-derived alloy powders. A heating rate of $25^{\circ}\text{Cmin}^{-1}$ and a 10 min dwell time were used for all curves. (a) Change in relative density with dwell temperature increase from 709°C to 1200°C and 35 MPa dwell pressure. (b) Consolidation rates corresponding to the 1200°C curves in part (a). (c) Change in density with dwell pressure increase from 25 MPa to 45 MPa at 750°C dwell temperature. (d) Consolidation rates for HDH CP-Ti corresponding to the curves in part (c).	84
4.14	Light micrographs showing microstructural development of CP-Ti HDH powder during FAST processing at 1200°C -22 MPa, with varying heating rate and dwell time: (a) $25^{\circ}\text{Cmin}^{-1}$ and 10 min, (b) $25^{\circ}\text{Cmin}^{-1}$ and 30 min, (c) $100^{\circ}\text{Cmin}^{-1}$ and 10 min, (d) $100^{\circ}\text{Cmin}^{-1}$ and 30 min	89
4.15	Light micrographs showing microstructural development of Ti-6Al-4V HDH powder during FAST processing at 1200°C -22 MPa, with varying heating rate and dwell time: (a) $25^{\circ}\text{Cmin}^{-1}$ and 10 min, (b) $25^{\circ}\text{Cmin}^{-1}$ and 30 min, (c) $100^{\circ}\text{Cmin}^{-1}$ and 10 min, (d) $100^{\circ}\text{Cmin}^{-1}$ and 30 min	90
4.16	Light micrographs showing microstructural development of PS rutile-derived powder during FAST processing at 1200°C -22 MPa, with varying heating rate and dwell time: (a) $50^{\circ}\text{Cmin}^{-1}$ and 10 min, (b) $50^{\circ}\text{Cmin}^{-1}$ and 60 min, (c) $200^{\circ}\text{Cmin}^{-1}$ and 10 min, (d) $200^{\circ}\text{Cmin}^{-1}$ and 60 min	91
4.17	Light micrographs showing microstructural development of Ti-5553 GA powder during FAST processing at 1200°C -22 MPa, with varying heating rate and dwell time: (a) $25^{\circ}\text{Cmin}^{-1}$ and 10 min, (b) $25^{\circ}\text{Cmin}^{-1}$ and 30 min, (c) $100^{\circ}\text{Cmin}^{-1}$ and 10 min, (d) $100^{\circ}\text{Cmin}^{-1}$ and 30 min	92

4.18	Effect of heating rate on rheology curves calculated from FAST machine output data. Dwell temperature and pressure were kept constant at 1200°C and 22 MPa for all curves. Change in density versus temperature when increasing heating rate (as labelled) for HDH Ti-6Al-4V (a), HDH CP-Ti (d), GA Ti-5553 (g), PS rutile-derived (j). Change in density versus time for increasing heating rate (as labelled) for HDH Ti-6Al-4V (b), HDH CP-Ti (e), GA Ti-5553 (h), PS rutile-derived (k). Variation in consolidation rate for increasing heating rate (as labelled) for HDH Ti-6Al-4V (c), HDH CP-Ti (f), GA Ti-5553 (i), PS rutile-derived (l).	94
4.19	Effect of alloy chemistry and powder morphology on rheology curves when dwell temperature and dwell pressure were kept constant at 1200°C and 22 MPa. (a) Change in density versus temperature for 20 mm specimens of the labelled powders with a heating rate of 100°Cmin ⁻¹ . (b) Change in density versus temperature for 80 mm specimens of the labelled powders with a heating rate of 200°Cmin ⁻¹	95
4.20	Bright-field light micrographs showing microstructures etched with Kroll's reagent from the centre (a) to the edge (e) of a 5.5 kg 250 mm diameter GA Ti-6-4 FAST disc produced at Kennametal Manufacturing (UK) Ltd. Photograph of the 250 mm diameter FAST disc with tennis ball for scale (f).	96
4.21	Effect of mould size on rheology curves. A dwell temperature of 1200°C, dwell pressure of 22 MPa, and heating rate of 100°Cmin ⁻¹ were used unless otherwise labelled. (a) Change in relative density versus temperature for 20 mm and 80 mm specimens of HDH Ti-6-4 and HDH CP-Ti. (b) Change in relative density versus temperature for an 80 mm specimen compared to a 250 mm specimen of GA Ti-6-4.	97
4.22	Light micrographs showing a defined region of increased α phase at the surface in contact with the graphite mould due to carbon diffusion into Ti-5553 FAST specimens processed at 1200°C and etched with Kroll's reagent, after a 10 min dwell (a), after a 20 min dwell (b), and after a 30 min dwell (c).	100

5.1	Schematic showing the location that the axisymmetric compression testing cylinders were extracted from in the 80 mm diameter FAST discs.	106
5.2	Graphs showing the five types of data recorded during axisymmetric TMC compression testing; upper tool displacement from specified zero position vs. time (a), upper tool velocity vs. time (b), load on the upper tool vs. time (c), specimen temperature vs. time (d). Parts (a), (b), and (c) are magnified on the deformation and part (d) shows the whole test. (Example data is from a Ti-6Al-4V HDH test at 850°C and 1 s ⁻¹)	107
5.3	Graph illustrating the required corrections to the load-displacement data produced during axisymmetric TMC compression testing. (Example data is from a Ti-6Al-4V HDH test at 850°C and 1 s ⁻¹)	109
5.4	Graph showing the measured true stress P_i vs. true strain curve calculated from the corrected load and displacement data recorded during axisymmetric TMC compression testing, and also illustrating the outcome of an increasing value of friction factor when correcting the measured true stress for frictional effects. (Example data is from a Ti-6Al-4V HDH test at 850°C and 1 s ⁻¹)	111
5.5	Graph of an example temperature profile during a TMC axisymmetric compression test for induction heating, deformation (zoomed area), and quenching. (Example data is from a Ti-6Al-4V HDH test at 850°C and 1 s ⁻¹)	112

- 5.6 Figure showing the graphs used to calculate a value for Q_{def} for Ti-6Al-4V HDH tested at 850°C, 950°C, and 1050°C, at strain rates of 0.01 s⁻¹, 0.1 s⁻¹, and 1 s⁻¹. These graphs are at the strain increment of 0.6; the same methodology was performed at additional strain increments but is not presented. (a) Graph showing the relationship between instantaneous values of $\ln(\dot{\epsilon})$ and σ_i allowing the calculation of $\ln(\dot{\epsilon})$ at fixed σ_i and temperature; where the vertical lines intersect the linear trendlines. (b) Graph showing the relationship between measured temperature rise and $\ln(\dot{\epsilon})$ allowing the prediction of temperature as $\dot{\epsilon}$ varies using the linear trendlines. (c) Graph of interpolated values of $\ln(\dot{\epsilon})$ vs. $\frac{1}{T}$ for fixed true stress, where the average gradient of the linear trendlines is $-\frac{Q_{def}}{R}$; constructed using the values obtained from parts (a)+(b). 113
- 5.7 Graph for Ti-6Al-4V HDH tested at 850°C and 1 s⁻¹ showing the measured true stress P_i vs. true strain, which has first been corrected for frictional effects σ_i , and then isothermally corrected for deformational heating effects σ_{iso} 114
- 5.8 Figure showing the graphs used to calculate the coefficients for constitutive equations. (a) $\ln(Z)$ vs. $\ln(\sigma)$ to obtain A_1 and n for Eq. 5.17, (b) $\ln(Z)$ vs. σ to obtain A_2 and β for Eq. 5.18, (c) $\ln(Z)$ vs. $\ln(\sinh(\alpha\sigma))$ to obtain A_3 and n' for Eq. 5.19 116
- 5.9 Plots of constitutive equation coefficients as functions of strain with fitted polynomial trendlines allowing calculation for continuous values of strain. (a) β vs. ϵ . (b) n vs. ϵ . (c) C_3 vs. ϵ . (d) n' vs. ϵ 117
- 5.10 Plots showing typical behaviour of strain rate vs. time for the three testing conditions used in this investigation (a) 0.01 s⁻¹, (b) 0.1 s⁻¹, and (c) 1 s⁻¹. 119

5.11	Low and high magnification cross-polarised light micrographs (a)-(f) and bright field after etching with Kroll's reagent (g)-(h) showing the post-FAST microstructures of Ti-6Al-4V HDH (a)+(b), rutile-derived PS alloy (c)+(d), CP-Ti HDH(e)+(f), and Ti-5553 GA (g)+(h).	122
5.12	Flow curves showing true stress vs. true strain behaviour at the labelled axisymmetric compression conditions for Ti-6Al-4V HDH powder processed via FAST.	126
5.13	Light micrographs of the higher strain central regions of the deformed Ti-6Al-4V HDH FAST specimens.	128
5.14	Light micrographs of the lower strain edge regions of the deformed Ti-6Al-4V HDH FAST specimens.	129
5.15	Flow curves showing true stress vs. true strain behaviour at the labelled axisymmetric compression conditions for rutile-derived PS powder processed via FAST.	130
5.16	Light micrographs of the higher strain central regions of the deformed rutile-derived PS FAST specimens.	132
5.17	Light micrographs of the lower strain edge regions of the deformed rutile-derived PS FAST specimens.	133
5.18	Flow curves showing true stress vs. true strain behaviour at the labelled axisymmetric compression conditions for CP-Ti HDH powder processed via FAST.	135
5.19	Light micrographs of the higher strain central regions of the deformed CP-Ti HDH FAST specimens.	136
5.20	Light micrographs of the lower strain edge regions of the deformed CP-Ti HDH FAST specimens. Post-Forge edge region	137
5.21	Flow curves showing true stress vs. true strain behaviour at the labelled axisymmetric compression conditions for Ti-5553 GA powder processed via FAST.	138

5.22	Light micrographs of the higher strain central regions of the deformed Ti-5553 GA FAST specimens.	140
5.23	Light micrographs of the lower strain edge regions of the deformed Ti-5553 GA FAST specimens.	141
5.24	Graph showing the disparity in values between the experimentally measured true stress values and those calculated through the developed constitutive equation for Ti-6Al-4V HDH.	142
5.25	Ti-6Al-4V HDH Experiment vs. Simulation Load-displacement curves	143
6.1	Schematic diagram outlining the two-step hybrid “FAST- <i>forg</i> e” process – a proposed cost-effective solid-state processing route for producing titanium alloy components from powder.	149
6.2	Photograph demonstrating the outcome at each stage of the two-step FAST- <i>forg</i> e process; the starting Ti-6Al-4V HDH powder (left) to the intermediate shaped preform billet, a double truncated cone FAST specimen with a light surface machine (centre), and the final forged specimen (right).	150
6.3	Schematic showing the shaped graphite inserts used to assess the capabilities of FAST to produce shaped preforms; from l-r the upper and lower diameters decrease from 20 mm to 0 mm in 5 mm increments.	151
6.4	Schematic showing the two methods used to make the double truncated cone specimens. Method 1 produced a 100 mm diameter × 15 mm thick FAST disc, which smaller cylinders were extracted from via electro-discharge machining (EDM), and then machined to the final dimensions shown (known as “bulk” double cone specimens). Method 2 used shaped graphite inserts in a 20 mm diameter FAST mould assembly to produce shaped preforms, which then had a surface machine to give the final dimensions shown (known as “shaped” double cone specimens).	152

6.5	Photographs of the underfilled and overfilled 0-15 mm double cone FAST specimens.	156
6.6	Montage of light micrographs showing a central cross section of an underfilled 0 mm double cone demonstrating homogeneous porosity distribution.	157
6.7	Montage of light micrographs showing a central cross section of an underfilled 5 mm double cone demonstrating homogeneous porosity distribution.	157
6.8	Montage of light micrographs showing a central cross section of an underfilled 10 mm double cone demonstrating homogeneous porosity distribution.	158
6.9	Montage of light micrographs showing a central cross section of an underfilled 15 mm double cone demonstrating homogeneous porosity distribution.	158
6.10	Cross-polarised light micrographs showing the microstructure of the 0 mm double cone specimen at the locations indicated on the schematic cross-section.	160
6.11	Cross-polarised light micrographs showing the microstructure of the 5 mm double cone specimen at the locations indicated on the schematic cross-section.	161
6.12	Cross-polarised light micrographs showing the microstructure of the 10 mm double cone specimen at the locations indicated on the schematic cross-section.	161
6.13	Graphs showing various machine recorded data during FAST processing of Ti-6Al-4V HDH FAST specimens when using all-steel mould assemblies, all-graphite mould assemblies, and combinations of the two materials; (a) current, (b) power, (c) top pyrometer temperature, (d) temperature measured by thermocouple in the ring mould, and the upper support.	163

6.14	Graph showing the current (a) and power (b) requirements during FAST processing for a 100 mm bulk disc and 20 mm mould with shaped inserts.	164
6.15	Graph showing the temperature profiles during FAST processing of three types of Ti-6Al-4V specimen (a). A 100 mm diameter disc used for bulk double cone specimens; allowed to “free” cool after current switch-off (solid line). A 20 mm shaped mould when allowed to “free” cool after current switch-off (dotted line) with associated microstructure (b). A 20 mm shaped mould with “controlled” cool (dashed line) and associated microstructure (c).	165
6.16	Cross-polarised light micrographs of Ti-6Al-4V double truncated cone specimens produced via FAST at a dwell temperature of 1200°C. Showing microstructures from a shaped specimen (Shaped 1-4) at the locations outlined in the top left diagram; and a characteristic microstructure of the homogeneous bulk specimen (bottom right).	167
6.17	Graphs of load displacement curves during hot upset forging of Ti-6Al-4V double truncated cone specimens at 950°C and strain rates of 0.01 s ⁻¹ , 0.1 s ⁻¹ , and 1 s ⁻¹ . Bulk (solid lines) and shaped (dashed lines).	168
6.18	Bright-field light micrographs after etching with Kroll’s reagent of the microstructural evolution with increasing strain from edge to centre of the double truncated cone specimens after forging at 950°C and 0.01 s ⁻¹ ; produced from bulk (left) and via shaped FAST (right).	170
6.19	Bright-field light micrographs after etching with Kroll’s reagent of the microstructural evolution with increasing strain from edge to centre of the double truncated cone specimens after forging at 950°C and 0.1 s ⁻¹ ; produced from bulk (left) and via shaped FAST (right).	171

6.20	Bright-field light micrographs after etching with Kroll's reagent of the microstructural evolution with increasing strain from edge to centre of the double truncated cone specimens after forging at 950°C and 1 s ⁻¹ ; produced from bulk (left) and via shaped FAST (right).	172
6.21	Light micrographs showing microstructures of the bulk double cone specimen produced with FAST conditions of 1200°C, 50 MPa, 100°Cmin ⁻¹ , and 30 min dwell time. Forged at 950°C and a strain rate of 0.01 s ⁻¹ after etching with Kroll's reagent — low strain area (a) and high strain area (b). Under cross-polarised light after a subsequent heat treatment at 950°C for 120 min with either a furnace cool (low strain area (c) and high strain area (d)) or a water quench (low strain area (e) and high strain area (f)). .	174
6.22	Light micrographs showing microstructures of the bulk double cone specimen produced with FAST conditions of 1200°C, 50 MPa, 100°Cmin ⁻¹ , and 30 min dwell time. Forged at 950°C and a strain rate of 0.1 s ⁻¹ after etching with Kroll's reagent — low strain area (a) and high strain area (b). Under cross-polarised light after a subsequent heat treatment at 950°C for 120 min with either a furnace cool (low strain area (c) and high strain area (d)) or a water quench (low strain area (e) and high strain area (f)). .	175
6.23	Light micrographs showing microstructures of the bulk double cone specimen produced with FAST conditions of 1200°C, 50 MPa, 100°Cmin ⁻¹ , and 30 min dwell time. Forged at 950°C and a strain rate of 1 s ⁻¹ after etching with Kroll's reagent — low strain area (a) and high strain area (b). Under cross-polarised light after a subsequent heat treatment at 950°C for 120 min with either a furnace cool (low strain area (c) and high strain area (d)) or a water quench (low strain area (e) and high strain area (f)). .	176
6.24	Graphs comparing the load displacement curves during the upset forging of double truncated cone specimens at 850°C (a), 950°C (b) and 1050°C (c) at strain rates of 0.01 s ⁻¹ , 0.1 s ⁻¹ and 1 s ⁻¹ (as labelled); from bulk FAST material (solid lines) against those obtained from DEFORM TM FE simulation (dotted lines).	178

A.1	Technical drawing showing the dimensions of the components of the 20 mm diameter all-graphite FAST mould assembly.	204
A.2	Technical drawing showing the dimensions of the components of the 80 mm diameter all-graphite FAST mould assembly.	205
A.3	Technical drawing showing the dimensions of the 20 mm diameter shaped graphite inserts for the 20 mm FAST mould assemblies. .	206
A.4	Technical drawing showing the dimensions of the components of the 20 mm diameter all-steel FAST mould assembly used in chapter 6.	207
B.1	License giving permission to reproduce the paper published in the Journal of Materials Science by Weston et al. [65].	208
B.2	License giving permission to reproduce the paper published in the Proceedings of the 13th World Conference on Titanium by Weston et al. [66].	209
B.3	License giving permission to reproduce the paper published in the Journal of Materials Processing Technology by Weston et al. [67].	210

List of Tables

2.1	Approximate basic properties of titanium based alloys compared to the other main metallic structural materials based on iron, nickel, aluminium. (Reproduced from data by Lutjering [1], Leyens [3], and Froes [24].)	9
2.2	Approximate relationship between selected mechanical properties and microstructure type and size in titanium alloys; + indicates an improvement in that property for that type of microstructure and vice-versa for -, negligible effect is shown by o. (Reproduced from Leyens [3].)	21
3.1	The composition of the titanium alloy powders used in this study.	57
3.2	Summary of the particle size distributions of the titanium alloy powders used in this study.	62
4.1	Density achieved by the four Ti alloy powders after FAST processing at the specified conditions during the parametric study of dwell temperature and dwell pressure; organised by increasing dwell temperature.	68
4.2	Interstitial element content pre- and post-FAST processing and Vickers Hardness values post-FAST.	99
5.1	Alloy chemistries, powder morphologies, FAST processing conditions, and powder masses used to produce the 80 mm diameter discs for the axisymmetric compression testing specimens.	105
5.2	Calculated values of activation energy for deformation Q_{def} for the four alloys used in this study and additional example values from the literature.	123

5.3	Values of the constants need to fit a 6 th -order polynomial equation to the variation of constitutive equation coefficients with strain for the data produced by axisymmetric compression of Ti-6Al-4V HDH consolidated via FAST.	124
5.4	Values of the constants need to fit a 6 th -order polynomial equation to the variation of constitutive equation coefficients with strain for the data produced by axisymmetric compression of rutile-derived PS consolidated via FAST.	124
5.5	Values of the constants need to fit a 6 th -order polynomial equation to the variation of constitutive equation coefficients with strain for the data produced by axisymmetric compression of CP-Ti HDH consolidated via FAST.	125
5.6	Values of the constants need to fit a 6 th -order polynomial equation to the variation of constitutive equation coefficients with strain for the data produced by axisymmetric compression of Ti-5553 GA consolidated via FAST.	125
5.7	Vickers microhardness values for the Ti-6Al-4V HDH powder after FAST processing and subsequent hot axisymmetric compression at the listed conditions.	144
6.1	FAST processing conditions, type of double cone inserts, mass of powder, and mould material used for the initial study on producing shaped FAST preforms.	154

1. Introduction

1.1 Motivation for Lower-Cost Titanium

The excellent properties of titanium alloys, such as a higher specific strength than steels, exceptional corrosion resistance, high melting point, low thermal expansion and biocompatibility, make them highly desirable materials for applications in many industries [1, 2]. Titanium is a plentiful resource being the ninth most abundant element in the Earth's crust; however, a high affinity for oxygen and nitrogen, which can cause severe embrittlement, requires the use of vacuum or inert atmospheres during extraction from the ore, and the ensuing downstream processing and fabrication [3]. The increased time and additional complexity of such processing requirements are reflected in the relatively high cost of titanium mill products, which largely limits their usage to the aerospace and chemical sectors where material properties and performance take precedence over price [4]. Thus research into lowering the cost of titanium, to the point where it can compete with steel and aluminium, has considerable significance to a substantial number of industries who currently cannot justify its use.

1.2 Current Cost of Titanium Components

The production costs for titanium alloy components can be approximately broken down into two main areas, as illustrated in the example of 25 mm thick plate in Fig.1.1 [5]. The first area of ingot production accounts for around half of the total cost in this instance, which encompasses the ore handling and extraction via the Kroll process followed by alloying and homogenisation, which is most commonly achieved via vacuum arc remelting (VAR) and sometimes in combination with electron beam or plasma arc cold hearth remelting. The second area of downstream processing yields the remaining cost, which in this example is the thermomechanical processing of the VAR ingot; normally via multi-stage forging and reheats to generate the required shape and properties. The proportion of the cost associated with downstream processing will rise as the complexity of the final component increases due to additional expensive steps, such as secondary forging, heat treatment, and machining. For example the

buy-to-fly ratio of titanium for the F-22 fighter jet is 12.2:1 (i.e., over 45.8 of the 50 tonnes purchased for each aircraft ends up as scrap metal, mostly as machining swarf) [6]. Therefore, in order for titanium to compete with the price of commodity metals in non-aerospace sectors, cost reductions in both areas are required.

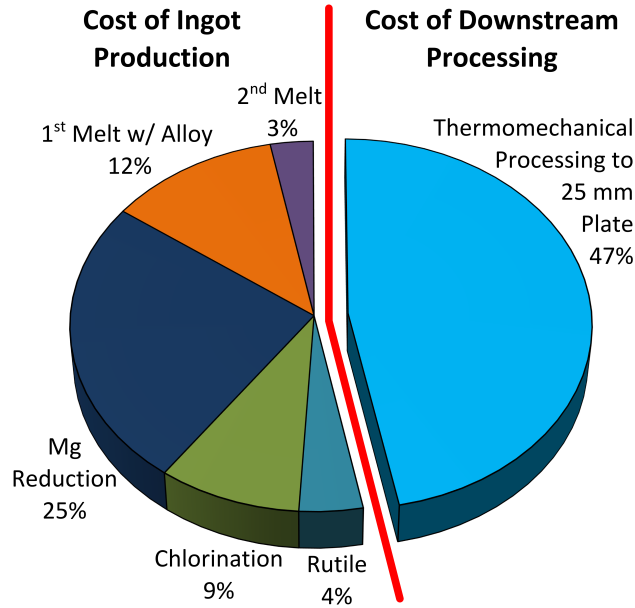


Figure 1.1 – Chart demonstrating the two main areas of manufacturing cost for 25 mm titanium alloy plate when conventionally processed; with relative cost factors for each sub area also shown. Produced from data reported by Kraft [5].

1.3 Cost Reduction Strategy

Attempting to reduce the cost in both areas produces the need for a dual approach that utilises a novel extraction method combined with subsequent cost-effective downstream processing. A lower-cost alternative to the sixty-year-old Kroll process is required to make savings in the first area. An extensive quantity of research has occurred over the past two decades to pursue a viable substitute, and several different approaches are being developed around the globe [5, 7]. There has been significant progress made, although none of these methods are currently operating at a commercial level due to difficulties such as scale-up. However, owing to the cost structure already outlined, lower-cost extraction alone will not be enough to realise the desired cost reductions. It is in the second area of downstream processing that the most dominant effect can be achieved; consequently it is interesting to note that many of the developing extraction approaches produce powder or particulate titanium. Cost savings can

be made by removing as many of the traditional time consuming and expensive multi-stage steps as possible, and replacing them with a novel cost-effective processing route, where the consolidation of lower-cost powders into mill product and near net shape components will occur [8, 9, 10, 11, 12]. Powder metallurgy (PM) techniques offer the potential to achieve this due to their ability to produce fully dense near net shape parts with competitive properties in minimal steps; with the added benefit of being in the solid state to limit oxygen and nitrogen pick-up.

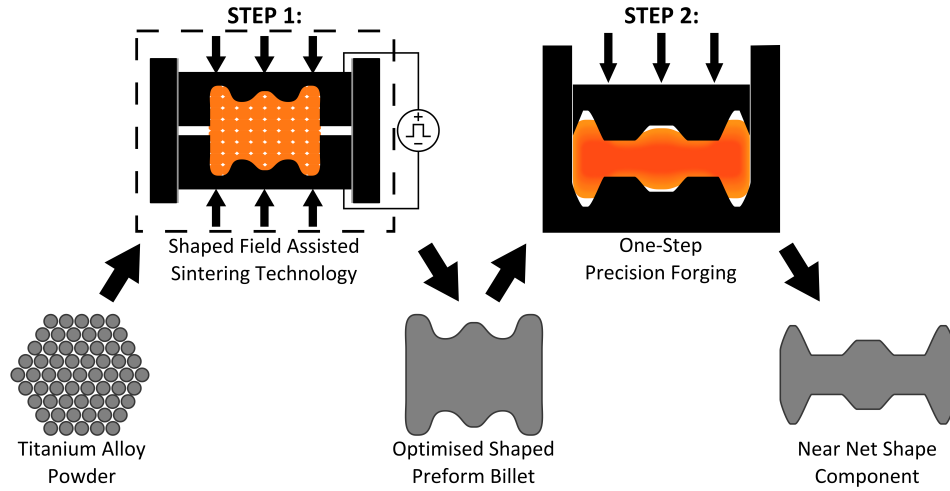


Figure 1.2 – Schematic diagram outlining the two-step FAST-forge process – the proposed cost-effective solid-state processing route for producing titanium alloy components from powder.

Field Assisted Sintering Technology (FAST) is a PM technique that has seen an exponential increase in attention over the last few decades due to the increased availability of commercially built facilities [13, 14]. FAST has demonstrated the potential for cost savings due to reduced processing times at lower temperatures, whilst achieving equivalent or improved material properties [15, 16]. Therefore FAST offers the opportunity to consolidate titanium alloy powders as part of a cost-effective processing route. However, the geometries and microstructures, and therefore mechanical properties, required by titanium alloy components in demanding applications will not generally be producible by solely using FAST. More complex shapes and microstructural refinement can be achieved by a subsequent precision one-step hot forging operation on FAST preforms. For this forging operation to be the most cost-effective it is likely that the FAST preform will need shape and definition beyond that of the discs typically produced. A correctly shaped FAST preform would allow near net shape flashless forging;

further reducing costs by removing the need for large machining operations. This novel cost-effective processing route has been termed FAST-*forge*, and will allow manufacturing of shaped parts with forged properties for dynamically loaded applications in two steps from titanium alloy powders, as shown schematically in Fig. 1.2. FAST-*forge* has the potential to develop into a disruptive technology, and its combination with lower-cost powder from an alternative extraction method could trigger the desired step-change in the economics of titanium; allowing usage in industries where cost is currently seen as prohibitive.

1.4 Project Aim

The aim of this project is to demonstrate the feasibility of producing cost-effective titanium components with wrought properties by consolidating titanium alloy powder, potentially from a lower-cost extraction route, in the fewest steps possible via FAST-*forge*; a novel solid-state downstream processing route.

1.5 Project Objectives

- Investigate the suitability and effectiveness of FAST to consolidate a range of commercial and emerging lower-cost titanium alloy powders
- Understand how FAST processing parameters and feedstock characteristics effect density and microstructure of FAST preforms
- Examine the response of titanium alloy powder preforms consolidated via FAST to deformation under thermomechanical processing conditions
- Combine the knowledge gained from the previous three objectives to establish a laboratory-scale cost-effective processing route — including exploring the capabilities of FAST to produce simple shaped preforms that could be finished with a precision forging operation

1.6 Thesis Outline

The thesis presented here will demonstrate the achievement of the stated aim through completing the above objectives. The thesis will be presented as follows:

Chapter 2 will give a more detailed background of what makes titanium such an attractive material by discussing the fundamentals of titanium alloy metallurgy;

structure and properties, alloy classification, deformation mechanisms and response to thermomechanical processing, in particular forging. An overview of the current conventional production methods will also be given, followed by a summary of the main emerging lower-cost extraction methods and their current status. Next, the most common PM techniques, with specific focus on FAST, will be discussed.

Many of the titanium alloy powders utilised in this work are common across all experimental work and information on their chemistry, morphology, and size will therefore be presented in Chapter 3. Details about the general experimental methods used will also be shown, with specifics added in the relevant chapters where necessary.

Chapter 4 will present how feedstock size, morphology, and chemistry affect the processing conditions required when consolidation of titanium alloy powders (both conventional and lower-cost) is undertaken via FAST; including maximum sintering temperature and pressure, and the hold time at these conditions, as well as the heating rate and mould dimensions. The evolution of porosity and microstructure was studied to assess the material response to varying processing conditions. In addition different materials densified under the same sintering cycle were also compared to understand the effect of feedstock properties on consolidation.

Chapter 5 focuses on the response of titanium alloys consolidated via FAST to thermomechanical processing. Forging conditions were replicated by undertaking hot axisymmetric compression testing on several commercial and lower-cost alloys. Compressions were completed at a range of temperatures and strain rates to allow an assessment of the material's forgeability. The resulting stress-strain data was used as input for finite element (FE) modelling, using the software DEFORMTM [17]. Comparing load-displacement data produced via modelling with experimental values demonstrated an ability to accurately simulate forging loads and strain profiles, which were then linked to microstructural evolution.

Chapter 6 brings together the knowledge gained from the experiments conducted in Chapters 4 and 5 to demonstrate that it is possible to produce near net shape components with excellent properties from powder in two steps, as shown schematically in Fig. 1.2. This was done at the laboratory scale by using FAST to produce a small simple shaped preform billet, which was hot upset forged in one

step. The choice of a double truncated cone geometry for this specimen allowed assessment of the capabilities of FAST to produce shaped preforms. The hot deformation allowed information to be gained linking microstructural evolution to thermomechanical processing parameters, which in future will allow process optimisation via FE modelling linked to a microstructural model.

Finally, Chapter 7 summarises the work undertaken, presents the main conclusions of the project, and makes recommendations for further work to be undertaken.

2. Literature Review

2.1 Overview

This chapter aims to give a thorough overview of titanium and its alloys. A brief historical background to give context is followed by an introduction to titanium metallurgy; including its properties, crystal structure, deformation mechanisms, and phase transformations. The next section discusses alloying element additions and the alloy classification system, as well as typical properties and behaviours of the different types of alloy. In the following sections the current conventional methods of producing and processing titanium alloys are detailed, and then potential methods of producing lower-cost titanium alloy components via alternative extraction techniques and subsequent cost-effective downstream processing.

2.2 Historical Background

In 1791 the Reverend William Gregor, a British mineralogist, discovered titanium in his analysis of the mineral manaccanite (a variety of ilmenite) found in river sand near Tregonwell Mill in Manaccan, Cornwall, UK. He declared manaccanite to contain magnetic iron united with the oxide of an unknown metallic element, which he proposed to name manaccanite [18]. Four years later a German chemist, Martin Klaproth, independently isolated the oxide of an unknown metal from the mineral rutile and, due to difficulty in its isolation, took inspiration for its name from Greek mythology. The Titans, children of Uranos and Gaia, were so hated by their father they were imprisoned in the deepest part of the underworld; it would be over 100 years before “titanium” metal was subsequently extracted from its oxide [2]. Upon examination of manaccanite Klaproth conceded Gregor’s prior discovery, but the name titanium became favoured.

Despite difficulty in its isolation titanium is not a rare substance, accounting for approximately 0.6% of the Earth’s crust, making it the ninth most abundant element and fourth most abundant structural metal [1]. It is mainly located in two key ores; rutile (TiO_2) and ilmenite (FeTiO_3). In 1887 the Swedes

Nilson and Petterson produced ~ 95 % pure titanium by reducing TiCl_4 with sodium in a steel vessel [19], and with further improvements (vacuum vessel) the first extraction of high purity titanium was achieved by Hunter in 1910 for the General Electric Company, USA [20]. Concern over the volatility and thus commercial scalability of the Hunter process led Wilhelm Justin Kroll to develop a more efficient method in 1940 whilst working at the Bureau of Mines in Albany, Oregon, USA (initial work was undertaken in his home country of Luxembourg before fleeing the Nazi occupation of Germany during WWII). Kroll's method used magnesium to reduce TiCl_4 in a molybdenum-lined crucible at $\sim 1000^\circ\text{C}$ in the presence of argon [21]. The product was known as "titanium sponge" due to its porous nature and spongy appearance. The sponge was separated from the magnesium salts by leaching and acid treatments before being crushed and compressed into bars and melted in specialised vacuum equipment. The Bureau of Mines deemed Kroll's process to show the most promise for industrialisation and work continued to develop it under Wartman; initially by increasing the batch size, utilising an unlined reaction vessel, and tapping off the molten MgCl_2 at intermediate stages [22]. Further work developed the more efficient technique of vacuum distillation for removing unused magnesium and MgCl_2 to replace the leaching process [23].

Kroll's initial trip to the USA in 1938 to sell his process generated no interest from the major non-ferrous metal companies, despite his assurances this new metal had a plentiful ore supply, excellent corrosion resistance, and mechanical strength comparable with stainless steel [19]. However, after the conclusion of WWII there began to be much more interest in the properties of titanium. By 1948 in the USA the DuPont Company (with strong government support), followed by TIMET in 1951 and RMI in 1958, had successfully commercialised the Kroll process and were producing titanium sponge at a large capacity [24]. In Europe, the UK and France developed sponge production capabilities from 1951. Japan started sponge production in 1952 and had large-capacity facilities by 1954. The Soviet Union initiated sponge production in 1954 and by 1979 were the world's largest titanium sponge producers [1]. The Kroll process remains the dominant titanium sponge production method to this day. Global sponge production in 2016 stands at an estimated 200 000 t per year, with China the largest producer, followed by Japan, Russia, USA, Kazakhstan, and Ukraine [25]. This annual level of global titanium sponge production approximately equates to the quantity of stainless steel produced globally in a single day. The addition

of alloying elements to improve mechanical properties began to be investigated from around 1950, with the major breakthrough coming from the USA in 1954 with Ti-6Al-4V, which combined excellent properties with good producibility and still remains the “workhorse” of the titanium industry.

2.3 Fundamentals of Titanium

2.3.1 Basic Properties

Values for a range of titanium’s basic properties are shown in Table 2.1 [1, 3, 24]. Values for iron, nickel, and aluminium based alloys are also given for comparison.

Table 2.1 – *Approximate basic properties of titanium based alloys compared to the other main metallic structural materials based on iron, nickel, aluminium.
(Reproduced from data by Lutjering [1], Leyens [3], and Froes [24].)*

	α Ti	Fe	Ni	Al
Melting Temperature ($^{\circ}\text{C}$)	1670	1538	1455	660
Allotropic Transformation ($^{\circ}\text{C}$)	$\beta \xrightarrow{882} \alpha$	$\gamma \xrightarrow{912} \alpha$	–	–
Crystal Structure	bcc \rightarrow hcp	fcc \rightarrow bcc	fcc	fcc
Young’s Modulus @ RT (GPa)	115	215	200	72
Yield Stress Level (MPa)	1000	1000	1000	500
Density (gcm^3)	4.5	7.9	8.9	2.7
Comparative Corrosion Resistance	V. High	Low	Medium	High
Comparative Reactivity w/ Oxygen	V. High	Low	Low	High
Comparative Price of Metal	V. High	Low	High	Medium
Thermal Expansion Coefficient (10^{-6}K^{-1})	8.4	11.8	13.4	23.1
Thermal conductivity ($\text{Wm}^{-1}\text{K}^{-1}$)	20	80	90	237
Specific Heat Capacity ($\text{Jkg}^{-1}\text{K}^{-1}$)	523	450	440	900
Electrical Resistivity ($\mu\Omega\text{m}$)	0.42	0.09	0.07	0.03

It is immediately obvious that titanium offers clear advantages in terms of specific strength, corrosion resistance, and thermal expansion. However, those benefits come with a significant increase in cost, which means titanium only finds use in applications where the property-cost trade-off can be justified. These applications were traditionally the aerospace industry, which drove the development of titanium post WWII and was the major consumer. Nowadays

the aerospace industry (civil and military) is still the dominant consumer, but its share of the total market has now fallen below 50 % due to the chemical, power generation, and biomedical industries using increasing amounts of titanium alloys [26].

The increased cost can mainly be attributed to titanium's high affinity for oxygen, which frequently makes the use of vacuum and inert atmospheres necessary. Conversely, the high affinity for oxygen is also responsible for the superior corrosion performance, as a stable and adhered oxide film forms when titanium is exposed to air. Due to its higher melting point it also offers advantages over the lighter aluminium when operating above temperatures of 150°C. The maximum service temperature is around 600°C due to excessive growth of the oxide surface layer causing embrittlement.

2.3.2 Crystal Structure

Titanium can crystallise in various crystal structures, similarly to a number of other common metals (e.g. iron), although each one is only stable within a particular temperature range. The complete transformation from one crystal structure into another is called an allotropic phase transformation and the temperature at which this occurs is known as the transus temperature.

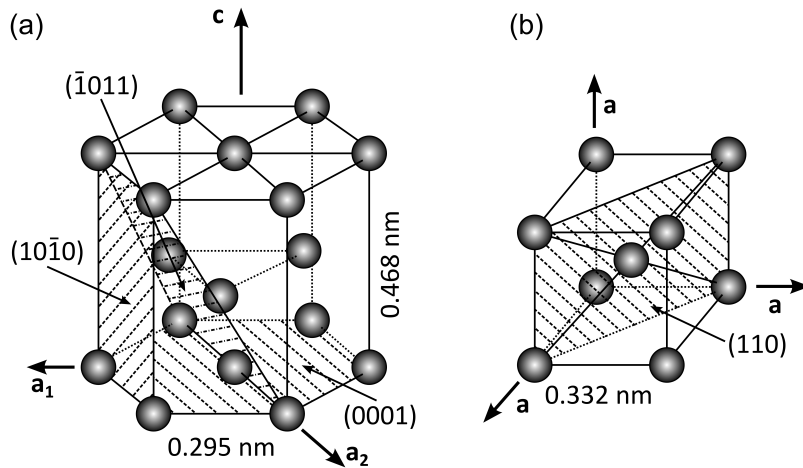


Figure 2.1 – Schematic diagram showing the atomic unit cell of the (a) hexagonal close packed α titanium crystal structure and (b) body centred cubic β titanium crystal structure. The most densely packed planes and directions are also indicated. Redrawn from [1, 3].

At low temperatures pure titanium and the majority of its alloys crystallise to an hexagonal close-packed (hcp) structure called α titanium. However, at higher

temperatures a body-centred cubic (bcc) structure is stable, which is referred to as β titanium. The temperature at which this change in stable crystal structure occurs is known as the β transus temperature and for pure titanium it is $\sim 882^\circ\text{C}$. The precise transformation temperature is dependant on purity and is therefore greatly influenced by interstitial and substitutional element content. A schematic outlining the atomic unit cells of titanium's hcp α phase and bcc β phase is shown in Fig. 2.1.

In Fig. 2.1a the lattice parameters and the most densely packed planes for the hcp structure are shown. At room temperature the lattice parameter a has a value of 0.295 nm and c has a value of 0.468 nm; this gives c/a value of 1.587 for pure α titanium, which is less than the ratio of 1.633 for an ideal hcp structure. The three most densely packed planes are indicated; the (0001), one of the three $\{10\bar{1}0\}$, and one of the six $\{10\bar{1}1\}$, known as the basal, prismatic, and pyramidal planes respectively. The three axes, labelled a_1 , a_2 , and a_3 , indicate the close-packed directions with indices $\langle 11\bar{2}0 \rangle$. In Fig. 2.1b the lattice parameter and the most densely packed planes for the bcc structure are shown. The lattice parameter has a value of 0.332 nm for pure β titanium at 900°C . One of the six most densely packed $\{110\}$ plane variants is shown and the close-packed directions are the four $\langle 111 \rangle$ directions.

$$(hkl) = (hkil) \quad (2.1)$$

$$\text{where, } i = -(h + k) \quad (2.2)$$

$$[u'v'w'] = [uvw] \quad (2.3)$$

$$\text{where, } u = \frac{1}{3}(2u' - v') \quad (2.4)$$

$$v = \frac{1}{3}(2v' - u') \quad (2.5)$$

$$t = -(u + v) \quad (2.6)$$

$$w = w' \quad (2.7)$$

The symmetry of the bcc unit cell allows the use of a three-axis system to describe equivalent planes and directions. However, the reduced symmetry of the hcp unit cell means that a four-axis system is needed, which is known as Miller-Bravais notation. A system to convert between the two notations is necessary as titanium

contains both crystal structures. This can be achieved for planes through using Eq. 2.1 and Eq. 2.2, and for directions using Eq. 2.3-2.7 [27].

The nature of these two different crystal structures and the corresponding allotropic transformation temperature is of key importance to titanium's usefulness as a material. Manipulation of the crystal structure, and thus microstructure, through alloying additions and processing allows a varied range of properties to be achieved.

2.3.3 Diffusion

Diffusion rates are closely linked to the crystal structure; the rate of diffusion is several orders of magnitude slower in the hcp α phase due to its more densely packed atoms [3]. Self diffusion of titanium in the α phase is three orders of magnitude slower than in the β phase, see Fig. 2.2 [1]. The reduced rate of diffusion in the α phase leads to improved creep performance of α and near- α alloys over alloys containing larger quantities of β phase.

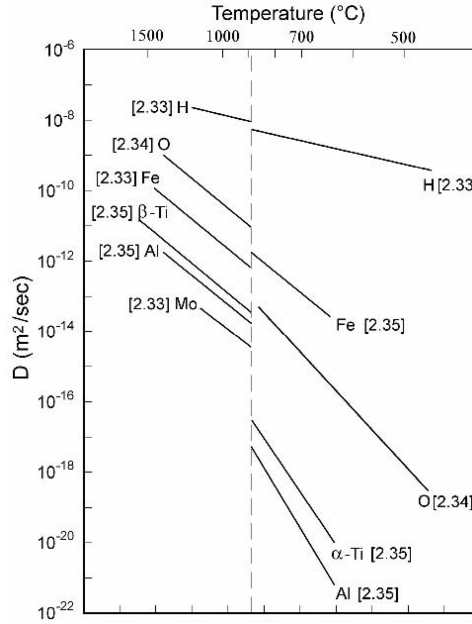


Figure 2.2 – Plot of titanium rate of self-diffusion and diffusion rate of a selection of alloying elements in the α and β phases (dashed line is the β transus temperature). Reported by Lutjering [1].

2.3.4 Mechanisms of Deformation

Plastic deformation is closely linked to the crystal structure. The ease of plastic deformation increases with the available number of slip systems, which are

equivalent to opportunities for dislocation glide to occur in crystal lattices. The number of slip systems is defined by the number of slip planes multiplied by the number of slip directions. The planes and directions with the most densely packed atoms are the most energetically favourable for deformation. The ease of deformation of the bcc β phase is much easier than hcp α phase due to having 12 slip systems compared to 3. Therefore the ductile behaviour observed in α phase titanium at lower temperatures is reliant on the activation of an alternative mode of deformation in addition to conventional dislocation slip systems, which is known as twinning. However, twinning is almost entirely suppressed for alloys containing both α and β phases or single β phase.

The non-symmetrical nature of the hcp crystal structure intrinsically causes highly anisotropic mechanical behaviour for α phase titanium, particularly in the elastic regime. The Young's modulus in a single crystal varies from 145 GPa perpendicular to the basal plane to 100 GPa parallel to it. The results are less pronounced in polycrystalline material although it is still possible to produce a crystallographic "texture" when processing titanium alloys. Texture leads to anisotropic properties and therefore care should be taken to minimise it where possible.

2.3.4.1 Slip

The more densely packed the atoms in a plane are, the easier it is for dislocations to move through a glide mechanism. Therefore the hcp structure should deform more easily than the bcc. However, the length of the minimal slip path is also important and is less in the bcc structure, making deformation more favourable in β phase titanium. Exceeding a critical resolved shear stress (CRSS) for each slip system is also necessary to initiate slip. The lattice distortion resulting from dislocation motion in slip systems can be referred to by a Burgers vector, which represents the magnitude and direction of the distortion.

The possible planes and directions for slip in α phase titanium are indicated in Fig. 2.3. The most densely packed directions are of the type $\langle 11\bar{2}0 \rangle$, which are most favourable for slip. The planes containing this \vec{a} type Burgers vector are the (0001) basal plane, the three $\{10\bar{1}0\}$ prismatic planes, and the six $\{10\bar{1}1\}$ pyramidal planes. The total number of combinations for these slip planes and directions gives 12 slip systems, although only four of these systems are independent. This means the von Mises criterion of five independent slip systems

for homogeneous plastic deformation cannot be met without activation of a slip system containing a non-basal type Burgers vector. This can either be of the \vec{c} type in $[0001]$ direction, or the $\vec{c} + \vec{a}$ type in $\langle 11\bar{2}3 \rangle$ direction. Experimental observation has shown that $\vec{c} + \vec{a}$ slip of the type $\langle 11\bar{2}3 \rangle \{11\bar{2}2\}$ is most favourable, although its occurrence will be much lower than the \vec{a} type slip discussed.

The slip systems in β phase titanium are the $\{110\}$, $\{112\}$, and $\{123\}$ planes, all in the $\langle 111 \rangle$ direction, which agrees with the generally observed modes for bcc metals.

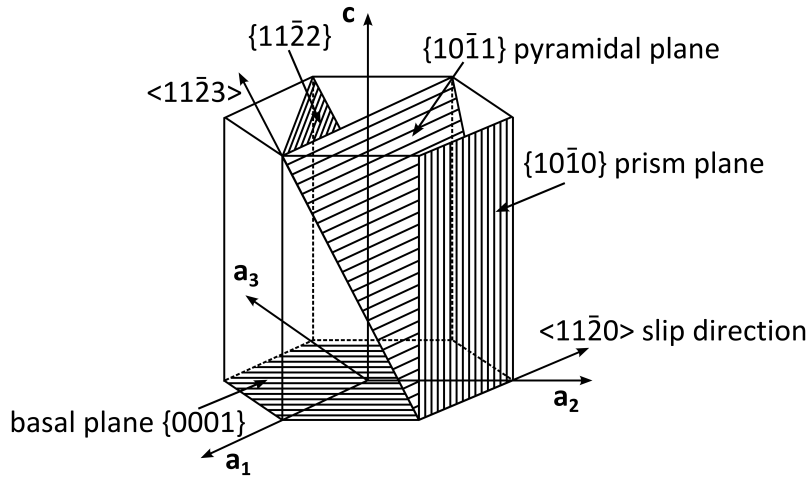


Figure 2.3 – Schematic diagram showing the planes and directions most favourable for slip in hcp α phase titanium. Redrawn from [1, 3].

2.3.4.2 Twinning

Twinning is especially important to accommodate plastic deformation at low temperatures in hcp α phase titanium when the applied stress is parallel to the c-axis so that dislocations with \vec{a} type Burgers vectors have zero CRSS and cannot move. As this work focuses on the hot deformation of titanium alloys, where twinning is not prevalent, further details on the mechanisms of twinning will not be given here.

2.3.5 Titanium Alloy Classification

The addition of alloying elements to titanium tend to either increase or decrease the β transus temperature from the 882°C of pure titanium. Elements are said to be α stabilising if they increase the transus temperature or β stabilising if they decrease it.

Aluminium as a substitutional element, and oxygen, nitrogen, and carbon

as interstitial elements, are all strong α stabilisers that increase the transus temperature with increasing content, as is shown schematically in the pseudo-binary phase diagram in Fig. 2.4a. They also introduce an $\alpha + \beta$ phase region. Aluminium is one of the most commonly used alloying additions due to raising the transus temperature and having large solubility in both the α and β phases. Oxygen can also be considered as an alloying addition when its primary purpose is to increase strength levels, as is the case in the four commercially pure (CP) grades.

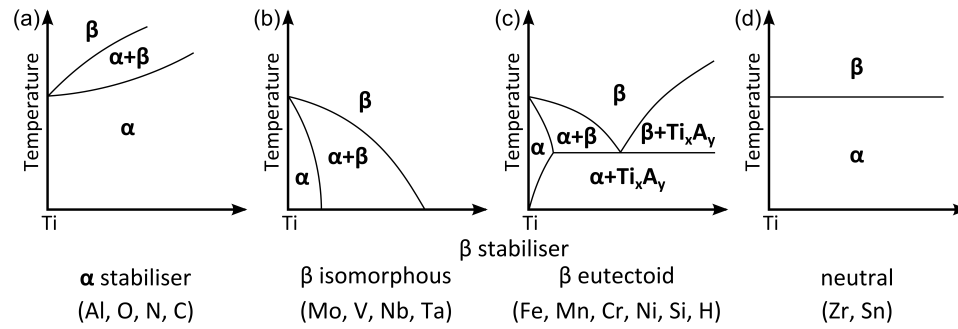


Figure 2.4 – Schematic pseudo-binary phase diagrams showing effects of alloying element additions on the crystal structure of titanium. Redrawn from [1, 3].

The elements causing β stabilisation are split into isomorphous or eutectoid forming elements depending upon their effect on the pseudo-binary phase diagram, as seen in Fig. 2.4b and Fig. 2.4c respectively. The isomorphous elements are far more important due to their increased solid solubility, whereas even low volume fractions of the eutectoid elements can form brittle intermetallic compounds. In sufficient concentrations the isomorphous elements can stabilise the β phase down to room temperature; the most commonly used are vanadium, molybdenum, and niobium, with tantalum and rhenium not usually considered due to their high densities. The commonly used eutectoid forming elements are iron, chromium, and silicon, with others having very limited usage in specialised alloys. The interstitial element hydrogen is a eutectoid former with a low eutectoid temperature that, in combination with its high diffusivity in titanium, allows a special process of microstructural refinement (or powder production) known as the hydrogenation-dehydrogenation (HDH) process. HDH uses hydrogen as a temporary alloying addition before it is removed with temperature and vacuum. For in-service use the maximum level of hydrogen is kept below ~ 150 ppm to prevent embrittlement.

A third class of alloying elements can be considered as being neutral i.e. they

have little effect upon the transus temperature. Zirconium and hafnium exhibit the same β to α allotropic phase transformation as titanium and have complete solubility in both phases. Tin is a β eutectoid former but has negligible effect on the transus temperature. Zirconium and tin are common additions but are considered as α stabilisers due to the chemical similarity of zirconium to titanium and the interchangeability of tin with aluminium when both are present. This demonstrates the interactions that occur between alloying elements and the difficulty in understanding complicated alloys in terms of binary systems. However, in an effort to allow comparison, the effect of different α stabilising elements in a multicomponent alloy can be expressed by an aluminium equivalent via Eq. 2.8 [26]. Equally, the effect of different β stabilising elements can be expressed by a molybdenum equivalent via Eq. 2.9 [1]. Care should be taken if trying to use these equations quantitatively but they can give useful qualitative information on the expected behaviour of an alloy with a known chemistry.

$$Al_{eq} = [Al] + 0.17[Zr] + 0.33[Sn] + 10[O + C + 2N] \quad (2.8)$$

$$Mo_{eq} = [Mo] + 0.20[Ta] + 0.28[Nb] + 0.40[W] + 0.67[V] + 1.25[Cr] \\ + 1.25[Ni] + 1.7[Mn] + 1.7[Co] + 2.5[Fe] \quad (2.9)$$

Subsequently, titanium alloys are conventionally classified into five categories. These are designated according to the position on a pseudo-binary β isomorphous phase diagram due to the alloying elements present, see Fig. 2.5.

2.3.5.1 α Alloys

Alloys containing exclusively α and/or neutral stabilising elements are referred to as α alloys. Commercially pure titanium grades 1-4 are the most well known α alloys, which only differ by oxygen content from 0.18-0.40 %. Typical applications for α alloys are those where corrosion resistance is paramount and strength is a secondary consideration, such as the chemical and process engineering industry.

2.3.5.2 Near α Alloys

Alloys that contain minimal amounts of β stabilising elements, and thus β phase when heat treating well below the β transus temperature, are referred to as near- α alloys. The amount of β phase is typically $<5\%$. The small amount of β phase helps to control the α grain size and increases tolerance to hydrogen. Near- α alloys are classically used at high temperatures due combining the excellent creep behaviour of α alloys with the high strength of $\alpha + \beta$ alloys; Ti-6Al-2Sn-4Zr-2Mo is a typical example.

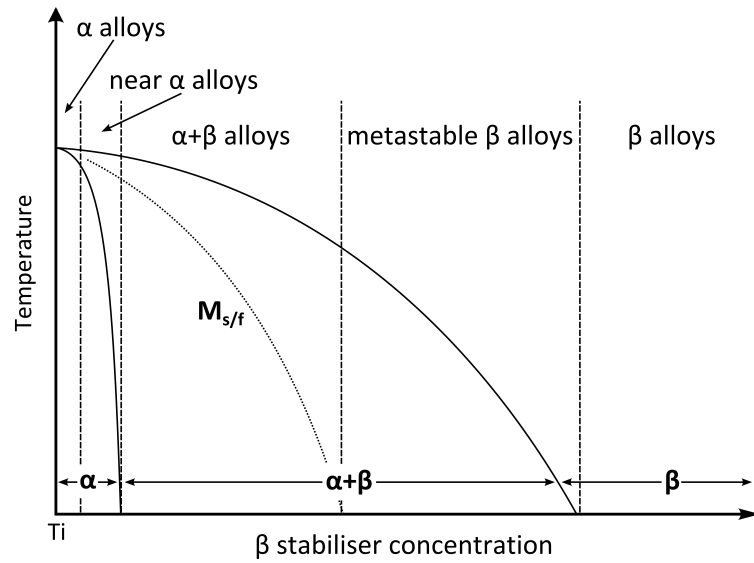


Figure 2.5 – Pseudo-binary section of an isomorphous β phase diagram showing the position of the different alloy classifications. Redrawn from [28].

2.3.5.3 $\alpha + \beta$ Alloys

The $\alpha + \beta$ alloys fall between the $\alpha/\alpha + \beta$ line and the intersection of the martensitic start/finish ($M_{s/f}$) line with room temperature. This indicates that upon rapid cooling from the β phase to room temperature they will transform martensitically. The most common $\alpha + \beta$ alloy is Ti-6Al-4V, which accounts for 50 % of alloys currently in use, due to its excellent balance of strength, ductility, fracture, and fatigue properties.

2.3.5.4 β Alloys

The term β alloy indicates these alloys should sit to the right of the $\alpha + \beta/\beta$ line in Fig. 2.4. This would be the case for alloys with sufficiently high concentrations of β stabilising elements, although they rarely exist as commercial alloys. Therefore, the majority of compositions available commercially as β alloys

are in fact metastable β alloys. This means they are actually located in the $\alpha + \beta$ region but, with high cooling rates from above the β transus to room temperature, they do not transform martensitically; if the cooling rate is high enough the β phase can be retained at room temperature. These alloys can be age hardened to the highest strength levels of any alloy (~ 1400 MPa), but at a reduced ductility. Complex tailoring of microstructure can achieve high strength and high toughness. The alloys Ti-10V-2Fe-3Al and Ti-5Al-5V-5Mo-3Cr have found applications in landing gears for the aerospace industry.

2.3.6 Phase Transformations

Upon cooling from above the β transus temperature the transformation from bcc β titanium into hcp α titanium can occur in two ways depending upon the cooling rate and alloy composition; the transformation is suppressed in β and metastable β alloys. The transformation is either martensitic or diffusion controlled by nucleation and growth. There is a relationship between the crystallographic orientation of the α phase and the β phase, first discovered in zirconium by Burgers (and later also confirmed for titanium), and thus known as the Burgers relationship:

$$\begin{aligned} \{110\}_{\beta} || \{0001\}_{\alpha} \\ \langle 111 \rangle_{\beta} || \langle 1120 \rangle_{\alpha} \end{aligned}$$

The relationship shows that the most densely packed bcc β phase crystal planes transform into the basal planes of the hcp α phase. There are 6 slip planes and 2 slip directions in a bcc crystal, which means the hcp crystal can transform into one of 12 variants of orientation. This variety of possible orientations is reflected in the transformed microstructure and will be discussed further below.

The spacing between the $\{110\}$ bcc planes is slightly less than the $\{0001\}$ hcp basal planes. Therefore, there is a slight atomic distortion during the β to α phase transformation as the c -axis contracts relative to the a -axis, which manifests as the lower than ideal c/a ratio previously mentioned, see Fig. 2.6. There is also a corresponding macroscopic increase in volume observed upon cooling through the β transus temperature.

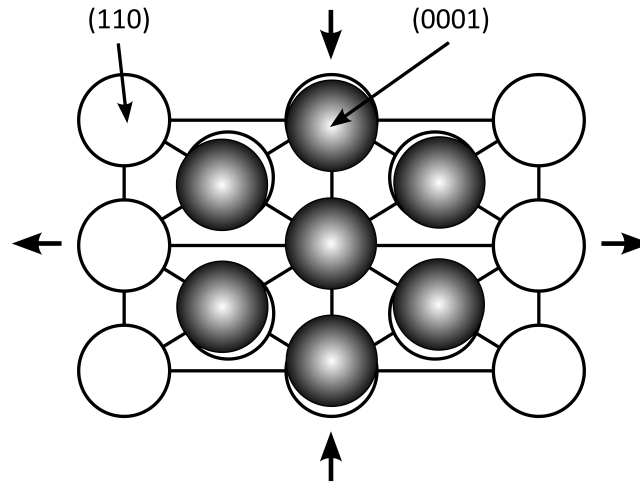


Figure 2.6 – Schematic diagram outlining the Burgers relationship that is followed when the bcc β titanium crystal structure transforms to the hcp α titanium crystal structure upon cooling from above the β transus temperature, and the slight atomic distortion that also occurs. Redrawn from [3].

2.3.6.1 Nucleation and Diffusional Growth

If a sufficiently slow cooling rate from the β phase region into the $\alpha + \beta$ region is used to suppress martensitic transformation, then the α phase first nucleates preferentially at the prior β grain boundaries. A near continuous layer of α on the β grain boundaries is formed in this way. As cooling continues then further α plates nucleate, either at the interface of the continuous α layer or at the prior β grain boundary, and grow as parallel plates with the same variant of the Burgers relationship into the β grain. If a new α plate nucleates at the $\alpha - \beta$ boundary on an old α plate then the most energetically favourable direction for its growth is perpendicular to the old plate. These regions of parallel plates are called α colonies. The α colonies continue to grow inwards until they meet other colonies, usually with a different variant of the Burgers relationship. Within a single prior β grain the number of orientations for the α colonies is limited to 12. This results in repetitions of the orientation variant in different α colonies within the prior β grain. Consequently, a very characteristic transformed β microstructure ensues, which at specific cooling rates can appear similar to a woven basket; thus giving the terminology basket-weave (Widmanstätten) structures. The individual α plates in the colonies are separated by retained β matrix.

2.3.6.2 Martensitic

The martensitic type of transformation is a microstructurally homogeneous transformation of a bcc lattice into a hcp lattice over a specific volume, which

occurs due to the cooperative movement of atoms in a shear type process. The transformed volume is typically disc shaped in most titanium alloys. Activation of the shear systems $[111]_{\beta}(11\bar{2})_{\beta}$ and $[111]_{\beta}(\bar{1}01)_{\beta}$ (or $[2\bar{1}\bar{1}3]_{\alpha}(\bar{2}112)_{\alpha}$ and $[2\bar{1}\bar{1}3]_{\alpha}(\bar{1}011)_{\alpha}$ in hcp notation) allows the shear transformation to occur. Martensite is designated as α' and is found in two morphologies: massive martensite (also called lath or packet martensite) and acicular martensite. Massive martensite is only observed in pure titanium or highly dilute alloys and alloys with high martensitic transformation temperature. It appears as large irregular regions showing no clear features under light microscopy, but the regions contain packets of very fine parallel α laths of the same Burgers variant. Alloys with higher solute content and lower martensitic transformation temperatures transform to the acicular morphology. This appears as a mixture of individual α laths that are each a different variant of the Burgers relationship. The α' hexagonal martensite is supersaturated in β stabilising elements and decomposes to $\alpha + \beta$ by precipitation of β particles at dislocations or plate boundaries if annealed in the $\alpha + \beta$ phase region. It is possible in alloys with higher amounts of alloying elements for the crystal structure of martensite to become so distorted it loses its hexagonal symmetry and must be referred to as α'' martensite, which has an orthorhombic structure.

2.3.7 Microstructure Property Relationship

As already indicated the microstructure has a considerable effect on the properties of titanium alloys. The microstructure of conventional titanium alloys is usually primarily described by the quantity, size, and arrangement of the α and β phases. The extreme cases are the lamellar microstructure generated by cooling from above the β transus temperature and the equiaxed microstructure produced during recrystallisation (see section 2.5.2.1), see Fig. 2.7. In either case the microstructural arrangement can be coarse or fine. Table 2.2 qualitatively shows the general trends that have been observed between microstructure type and a selection of mechanical properties; a + symbol indicates an improvement in that property for that type of microstructure and vice-versa for a – symbol, and a negligible effect is shown by the o symbol. It can be seen that to achieve an improvement in some properties it is beneficial to be able to produce a specific microstructure. This is usually achieved through extensive thermomechanical processing, which will be discussed in detail later in this chapter (see section 2.4.4).

Table 2.2 – Approximate relationship between selected mechanical properties and microstructure type and size in titanium alloys; + indicates an improvement in that property for that type of microstructure and vice-versa for -, negligible effect is shown by \circ . (Reproduced from Leyens [3].)

Fine	Coarse	Property	Lamellar	Equiaxed
\circ	\circ	Young's Modulus	\circ	+/- (texture)
+	-	Strength	-	+
+	-	Ductility	-	+
-	+	Fracture Toughness	+	-
+	-	Fatigue Crack Initiation	-	+
-	+	Fatigue Crack Propagation	+	-
-	+	Creep Strength	+	-
+	-	Superplasticity	-	+
+	-	Oxidation Behaviour	+	-

A simple example is now given of how mechanical properties can be altered through microstructural manipulation of Ti-6Al-4V by performing cooling at different rates from different starting temperatures, see Fig. 2.7. In very slow cooling conditions from above the β transus temperature a thick continuous layer of grain boundary α can form and the α colonies can be as large as half the β grain size, see Fig. 2.7a. Due to this type of microstructure being reliant upon diffusional processes the rate of cooling significantly impacts upon it. As cooling rate is increased there is less time for diffusion, so there is a thinning of the grain boundary α , the individual α laths, and the size of the α colonies decreases, see Fig. 2.7b. If the cooling rate is high enough then the β phase transforms martensitically. This is seen as a mixture of individual α laths, each with a different variant of the Burgers relationship, see Fig. 2.7c.

If the cooling occurs from within the two-phase $\alpha + \beta$ region then there will be a certain amount of α phase present when cooling commences and the remaining β phase matrix will transform as described for cooling from the β phase field. The β grain size will be significantly smaller than when cooling from above the β transus temperature due to the presence of the second phase particles preventing

growth [29]. The α phase present is often referred to as primary α and its quantity is related to alloy chemistry and temperature before cooling [2]; the primary α morphology is usually equiaxed if the cooling is occurring after a heat treatment. The quantity of primary α present after cooling is related to cooling rate, as is the morphology of the transformed β phase. A slow cooling rate will allow the primary α to continue to grow during cooling and the transformed β will have thick α laths, see Fig. 2.7d. An intermediate cooling rate will reduce the growth of the primary α and produce finer α laths, see Fig. 2.7e. Finally, a very quick cooling rate will allow negligible growth of the primary α phase and martensitically transform the β phase, see Fig. 2.7f. These types of two-phase microstructures are usually referred to as duplex or bi-modal [3, 29].

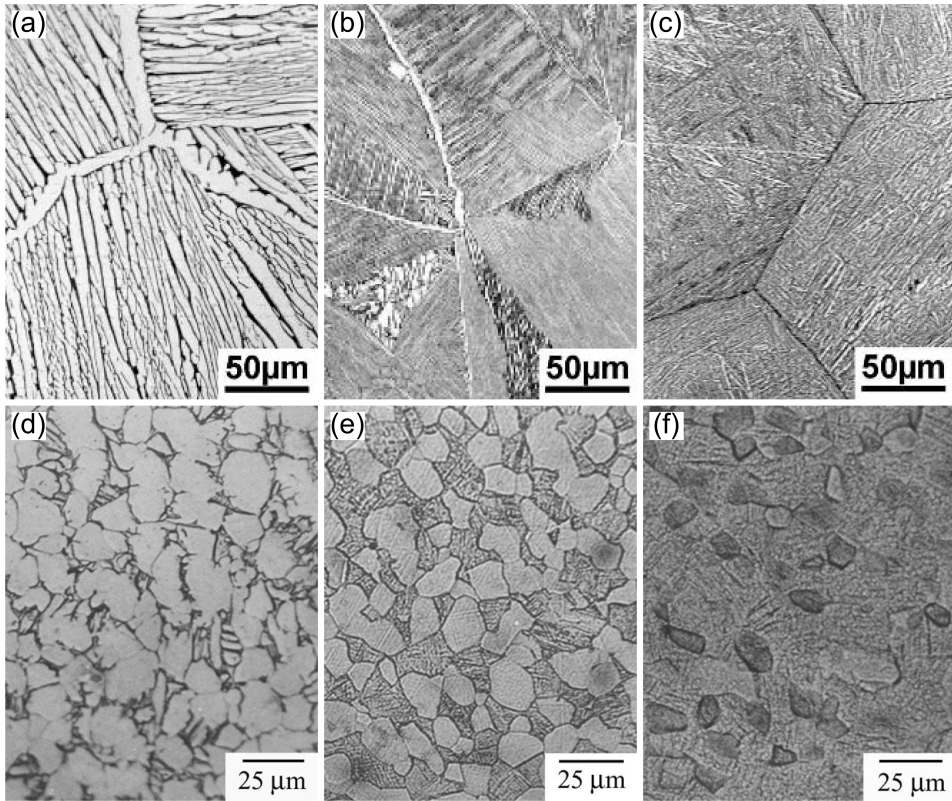


Figure 2.7 – Light micrographs illustrating how cooling rate and start temperature can influence the microstructure when cooling titanium alloys from elevated temperatures. Parts (a), (b), and (c) were cooled from above the β transus, and parts (d), (e), and (f) were cooled from the two-phase $\alpha + \beta$ region. Parts (a) and (d) had a slow cooling rate, parts (b) and (e) had an intermediate cooling rate, and parts (c) and (f) had the quickest cooling rate. Reproduced and adapted from [1] and [29].

2.4 Conventional Route for Forged Titanium Alloy Component Production

This section will outline the steps in the processing route that is approximately followed for the conventional production of forged titanium alloy components. This route, and slight variations of it, are the methods currently being used by industry to manufacture components, see Fig 2.8. The schematic overview of the processing route in Fig 2.8 shows the sequential steps in the route, but what is not made clear is that it is not followed from start to finish in one complete operation; multiple companies specialise in the different areas. The main steps will be discussed individually below.

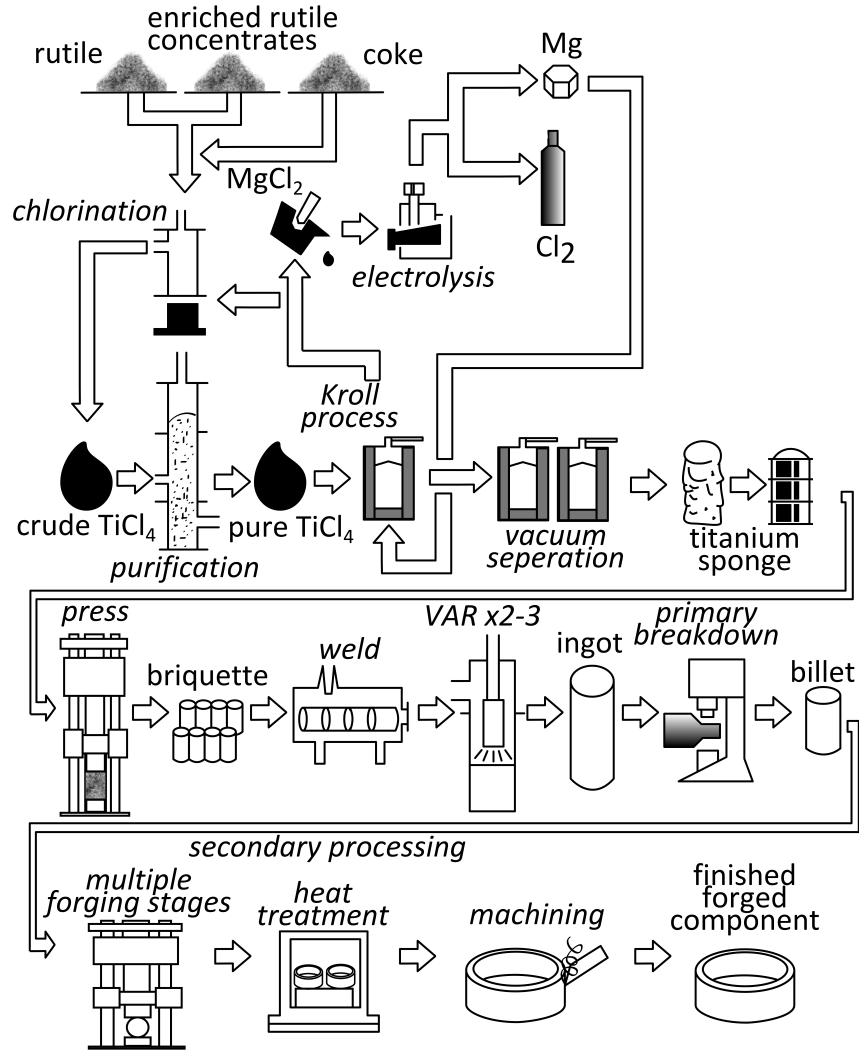


Figure 2.8 – Schematic diagram giving an overview of the conventional processing route to produce wrought titanium components from titanium ore. Adapted from diagrams in [30, 31].

2.4.1 Ores and Refining

The phrase “titanium ore” covers a large variety of naturally or industrially occurring resources that are available to the titanium dioxide pigment or titanium metal industries. As previously mentioned, the two key ores are rutile (TiO_2) and ilmenite (FeTiO_3). Rutile contains approximately 93-96 % TiO_2 and ilmenite has approximately 40-65 % [32]. The main deposits are found in Australia, South Africa, USA, India, Sri Lanka, Canada, Norway, and Finland. Rutile, whilst higher in TiO_2 content, is less frequently found in commercially viable deposits. In 2016 world deposits of rutile were estimated at 59 Mt and ilmenite at 770 Mt [33]. This means ilmenite is the most important resource for titanium production [34]; ilmenite accounted for 89 % of the 6.6 Mt total global titanium containing mineral consumption in 2016 [33].

Processing and refining of the various ores is undertaken to allow production of TiO_2 . TiO_2 finds extensive use as a pigment in paints and cosmetics, as a filler in paper, plastics, and rubber, and in glass making as a flux. Only a small fraction of globally produced TiO_2 is subsequently used to produce titanium metal [25]. The conversion of the ores into pigment grade TiO_2 is achieved either by the sulphate process or the chloride process.

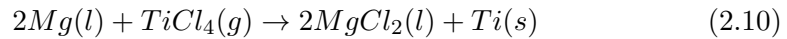
The sulphate process can directly use ilmenite as a feedstock. The process initially uses warm concentrated sulphuric acid to dissolve the iron as iron sulphate, which crystallises upon cooling and can be filtered out. Reheating the remaining solution causes hydrolysis of the titanium oxygen sulphate, which produces a gel of hydrated TiO_2 and sulphuric acid waste. Heating the hydrated TiO_2 in a rotary furnace drives off the water and produces crystallised TiO_2 [32]. The use of large quantities of sulphuric acid and the subsequent waste products has potential environmental implications if not handled correctly.

The chloride process tends to dominate the industry due to advantages in cost and waste management, with the trade off being it needs a higher purity feedstock. Natural rutile can be used directly as a feedstock after a series of magnetic, gravitational, and electrostatic separation techniques are applied. It is possible to produce synthetic rutile through upgrading ilmenite by removing the iron using one of several available methods [34] (e.g. the Becher process [35]); the typical content of TiO_2 rises to ~ 92 %. A product called high titanium slag (~ 85 -90 % TiO_2 content) can be produced by smelting ilmenite in an

electric arc furnace, which also produces pig iron. The chloride process uses chlorination of the feedstock TiO_2 at high temperature with coke as a reducing agent to produce titanium tetrachloride (TiCl_4). The TiCl_4 is further purified by fractional distillation. High purity TiO_2 is then produced through conversion of TiCl_4 at high temperature in the presence of pure O_2 .

2.4.2 Kroll Process Extraction

As discussed in section 2.2, Wilhelm Justin Kroll invented a method to extract titanium metal from its oxide in 1940, which used liquid magnesium to reduce gaseous TiCl_4 in a molybdenum-lined crucible at $\sim 1000^\circ\text{C}$ in the presence of argon [21], see Eq. 2.10 and the initial steps in Fig. 2.8.



The TiCl_4 can be created by the chloride process as described in section 2.4.1. The porous and spongy nature of the extraction product led to it being called titanium sponge. Separation of the sponge from the magnesium salt was originally achieved by leaching and acid treatments, but is now mostly accomplished continually during the reaction by vacuum distillation; the magnesium and chlorine can also then be recovered for reuse [24]. After cooling the titanium sponge can then be removed from the process vessel and is crushed/sheared and sized; too fine and too coarse particles are undesirable.

2.4.3 Ingot Production

Titanium sponge is converted into solid ingots of CP titanium, and titanium alloys, through melting and re-solidification via vacuum arc remelting (VAR) or more recently cold hearth melting (CHM). These specialised techniques are required to prevent the reactive titanium from contacting furnace refractories or the atmosphere [1]. It is possible to introduce performance hindering defects during melting. It is therefore essential that the processes used to melt titanium minimise the potential for defects and allow it to perform at a level that justifies its cost.

VAR begins with mechanically compressing the titanium sponge (and any alloying additions) into briquettes, which are then welded together in an inert

gas welding chamber to form the first electrode. It is possible (and there is a strong monetary incentive) to incorporate titanium scrap that has been carefully controlled and cleaned into the electrode at this stage. The electrode is attached to a stub and inserted into a vacuum vessel that consists of a water cooled copper crucible. A high current is passed through the electrode causing an arc to form and thus local melting and consumption of the electrode. A melt pool forms and solidifies in the copper crucible. The ingot is removed from the vacuum vessel, inverted, and melted again; alloys for rotating aerospace parts are usually melted for a third time.

CHM is a newer technique that uses a water cooled copper vessel, known as the hearth, and either a plasma arc or electron beam as the heat source. Careful control of the heat source allows a thin layer of titanium to form against the copper vessel, which prevents contamination of the molten titanium by contacting it. The exact layout of a CHM furnace is not fixed. A typical example would be an initial melting hearth, before the molten metal flows over a weir into a first refining hearth, and then a second weir into a second refining hearth, before finally flowing over an exit lip into an ingot mould; non-circular ingot cross-sections are possible with CHM.

2.4.4 Thermomechanical Processing

The term thermomechanical processing refers to combining mechanical plastic deformation processes with thermal treatment processes to achieve a change in a material's microstructure. The ingot microstructure produced after melting during VAR or CHM is not a useful one in the context of mechanical properties for titanium alloy components. Achieving the highest quality components can only be achieved by using thermomechanical processing to refine and homogenise the microstructure. Selecting the appropriate thermomechanical processing route makes it possible to tailor the product's microstructure and shape to precisely meet the desired property requirements and geometry [3].

The thermomechanical treatment of ingots produced via VAR or CHM can be divided into two components. Primary processing breaks down an ingot to improve microstructural and chemical homogeneity, and also produces more usable product forms such as bar, plate, and billet. Secondary processing produces the desired final microstructural condition and a final shape that minimises the need for further shaping through material removal process such as

machining. An overview of primary processing will now be given followed by a more detailed discussion of some secondary processing methods.

2.4.4.1 Primary Processing to Mill Products

Due to titanium's properties being so strongly linked to microstructure it is important that great care is taken in controlling the thermomechanical processing operations; issues in the early stages of primary processing may never be removed and can impact upon finished component performance [2]. It is common for there to be coordination between supplier, forger, and customer as the influence of early processing on final properties can be so pronounced [3].

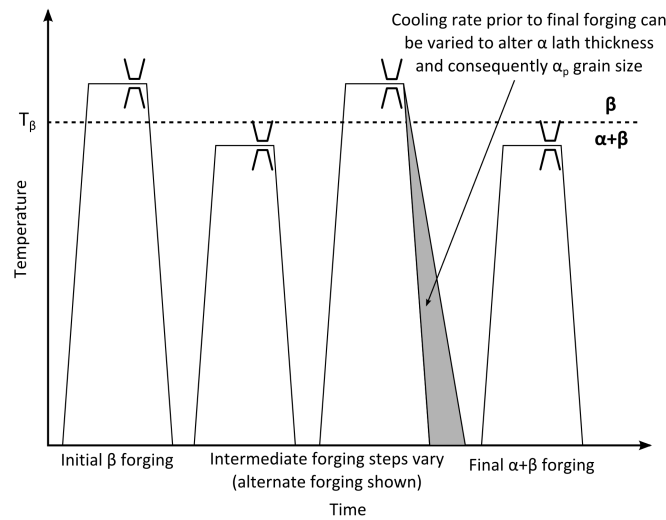


Figure 2.9 – Schematic diagram illustrating an example of a typical primary processing route used to convert VAR/CHM ingots into mill products. Redrawn from [1, 2].

The majority of primary processing is a selection of forging operations, see Fig. 2.9; although direct rolling of rectangular ingots produced via CHM is also now possible. Before primary processing can begin it is necessary to perform some surface conditioning via grinding/turning to produce a smoother surface free from any contaminants and stress concentrators [26]. It may be necessary to perform surface conditioning to remove oxide scale several times throughout primary and secondary processing; this impacts upon the final metal yield and thus adds another factor to the high cost. The exact nature of any thermomechanical processing route is heavily dependant upon the exact titanium alloy that is being used. Therefore the following process overview is representative rather than exact. An open forging press is typically used for the first primary processing step of cogging the billet. Cogging involves rotating

the ingot 90° around its major axis and moving it forward between each bite, thus creating a billet that is smaller in diameter and elongated compared to the starting ingot. The initial deformation usually occurs above the β transus temperature, imparts $\sim 30\%$ strain, and is cooled rapidly to minimise grain boundary α , see step 1 in Fig. 2.9. Depending upon the alloy and the grain size requirements the cogging process can be repeated several further times with the deformation temperature either above or below the β transus temperature (or alternating between the two) and the cooling rate varied accordingly, see steps 2 and 3 in Fig. 2.9. The fundamental concept of this procedure is to increase the compositional and structural homogeneity to improve response to subsequent processing steps [1]. The final step is usually performed in the $\alpha + \beta$ region and produces an ingot with a size that can be ultrasonically inspected and a structure that is amenable to further processing into mill products; typically a fine equiaxed α for an alloy like Ti-6Al-4V, see step 4 in Fig. 2.9. There are primarily three types of mill products; billet, bar, and flat rolled sheet if < 25 mm thick or flat rolled plate if > 25 mm thick. Billet and thicker bar are usually made using a rotary forging machine. Sheet/plate and thinner bar are made using a rolling mill.

2.5 Secondary Processing to Produce Components

Further thermomechanical processing of mill products is used to produce geometries closer to that of the final component, before being finished by a metal removal step such as machining. Additional heat treatment stages may also be undertaken at various points in the secondary processing. There are a significant variety of processes that can be used for secondary processing; forging (of several varieties), rolling (hot and cold), extrusion, wire drawing, ring rolling, and a variety of alloy specific heat treatments. The focus of this project is the forging and heat treatment response of titanium alloys consolidated from powder, so the following sections will focus on forging and heat treatment discussions.

2.5.1 Forging

Secondary forging can either be open die or closed die. In open die forging the material is not laterally constrained. Closed die forging usually utilises shaped dies to achieve a geometry as close to near net shape as the process and its tolerances allow. A combination of open and closed die forging where the workpiece geometry gradually increase in complexity may be used to ensure that

the correct amount of deformation is achieved and that a defect free product is achieved [1]. The number of forging steps required will depend upon the size of the forging, the complexity of the component, and the workability of the alloy used [1]. It will be necessary to reheat the workpiece after each deformation. This complex sequence of forging and reheat steps further adds to the cost of wrought titanium alloy components. The first major parameter to consider is whether the forging will occur above or below the β transus temperature, or a combination of the two during different operations. The component's application will define its mechanical property requirements and therefore the forging route will be designed to produce a microstructure to meet these requirements.

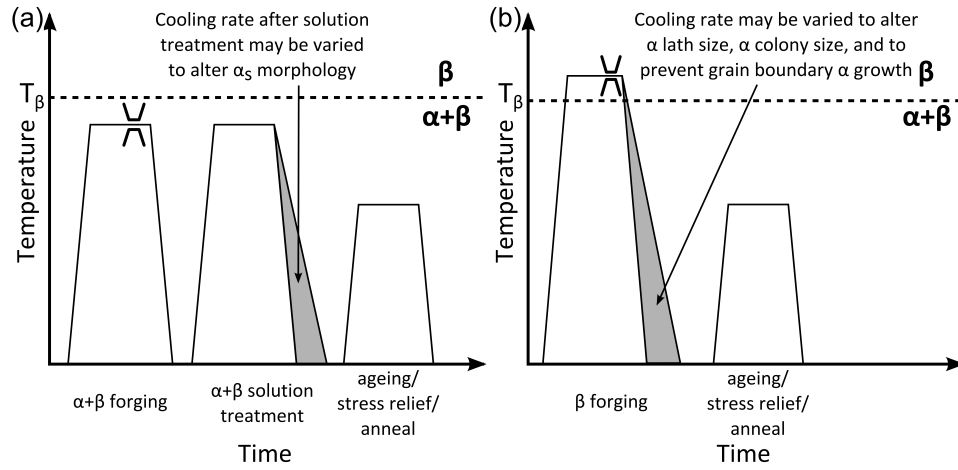


Figure 2.10 – Schematic diagram illustrating examples of two types of typical secondary processing route. (a) $\alpha + \beta$ secondary working and heat treatment used to produce bi-modal microstructures. (b) β secondary working and heat treatment used to produce fully lamellar microstructures. Redrawn from [1, 3, 2].

Forging in the $\alpha + \beta$ phase region, typically 30-100°C below the β transus temperature, is used to produce either a fully equiaxed or a bimodal microstructure, see step 1 in Fig. 2.10a. The forging temperature needs to be sufficiently high to keep the forging load low and to reduce the propensity for cracking at high levels of deformation, but low enough to prevent adiabatic heating taking the workpiece over the β transus temperature, which would compromise the microstructural development [3]. The temperature, level of strain, and strain rate need to be carefully selected to ensure the desired microstructural refinement/features are achieved; typically in $\alpha + \beta$ forging this is a fine equiaxed primary α morphology through recrystallisation processes. Sometimes the properties offered by a fully lamellar microstructure are called for. This requires forging above the β transus temperature and then careful

control of the cooling rate is required to prevent the formation of continuous grain boundary α , which is deleterious to performance, see step 1 in Fig. 2.10b. Care needs to be taken that the initial dwell period before forging is not too long else excessive β grain coarsening may occur.

The development of computer modelling capabilities, in particular finite element (FE) modelling, has allowed components to be forged to nearer net shape. The linking of thermomechanical processing parameters to microstructural features and integrating this into the simulation capability also means it is possible to confidently predict the microstructure that will be produced in all areas of the forging [1]. However, it is still standard practice that a significant amount of machining will occur after the final forging stage. In aerospace forgings this machining can remove over 90 % of the forged weight, with the practice so common that the terminology “buy-to-fly” ratio has been adopted. The example previously given in the introduction highlights this heavy machining practice; the buy-to-fly ratio of titanium alloys for the F-22 fighter jet is 12.2:1, which means over 45 of the 50 tonnes purchased for each aircraft is machined away [6]. This extensive machining is still required as it may not be possible to produce the desired microstructures in very complex shapes, if they could even be produced. For safety critical applications there is also the need for a forged component with a shape and cross section that can be ultrasonically inspected to check for defects. These forging/inspection limitations have a twofold impact on cost (1) a greater initial mass of material has to be purchased (2) the cost of material removal through machining is increased.

Despite the complexity and cost of producing and machining forgings they are still the primary source for titanium alloy products because they can achieve the best properties; or properties tailored to a specific application.

2.5.2 Microstructural Evolution During Forging

When designing a forging process it is necessary to compromise between conditions that give optimum workability (or forgeability) and conditions that create the desired microstructure [36]. The term workability is generally applied with regard to preventing cracking or defects during forging, and the measurement of flow stresses and total working loads. These factors can impact upon the plastic flow conditions (temperature, strain, and strain rate) applied, die material and wear, and the capacity of the forging press required. Of

equal importance is the selection of processing parameters to produce desirable microstructures. The ability to predict and model microstructural evolution during hot deformation processes has increased drastically over the previous two decades. Thus, the design of a thermomechanical process to produce a specific microstructure is becoming ever more prevalent [36]. A brief overview of some of the mechanisms involved, and observed phenomena, in hot forging of titanium alloys will now be discussed.

2.5.2.1 Dynamic Deformation Mechanisms

A major advantage of thermomechanical processing is the ability to produce microstructures that are not achievable through conventional thermal and mechanical processes. Dislocations are rapidly generated and are readily able to glide in active slip planes during hot working. As the level of imparted work increases the dislocation density rises, which leads to a higher strain energy in the workpiece due to dislocation interaction and entanglement. This higher strain energy at elevated temperature provides a sufficient driving force to make dynamic restoration processes, such as dynamic recovery and dynamic recrystallisation, occur; where the dynamic term implies the process occurs during deformation.

Dynamic recovery processes reduce the total system energy by decreasing the dislocation density and are typically prevalent in materials with high stacking fault energy, such as β phase titanium. During dynamic recovery pairs of dislocations with opposite signs are annihilated because of the ease of climb and pairs of dislocations with the same signs combine to form subgrain structures [36]. Because this process creates and destroys subgrains continuously the observed microstructure typically contains equiaxed subgrains within elongated primary grains. A steady-state is reached when the rate of dislocation creation due to the ongoing deformation process is equalled by the rate of dislocation annihilation through dynamic recovery processes.

In low stacking fault energy materials, such as α titanium, mobile dislocations are dissociated, which makes annihilation by climb processes difficult; this leads to higher dislocation densities. The mobility of grain boundaries increases rapidly as the temperature is increased and this, combined with differences in dislocation density across the boundary, leads to the nucleation and growth of new strain free grains. This process is known as discontinuous dynamic recrystallisation

(DDRX). At high strains a fully recrystallised structure can be created. The newly created strain free grains are subjected to additional deformation during processing and therefore begin to accumulate dislocations, which drives further recrystallisation. A steady-state can be achieved where the rate of dislocation creation due to deformation is balanced by the annihilation of dislocations through the nucleation and growth of new grains; dynamic recovery will also play a part as these mechanisms do not act in isolation. The presence of a second phase further complicates the mechanisms occurring. The residual dislocations play an important role in microstructural evolution during subsequent heat treatment, see section 2.5.3.

2.5.2.2 Dynamic Globularisation

Dynamic globularisation is a specific mechanism found in titanium alloys. The term globularisation refers to the propensity for acicular α laths, formed by slow cooling from above the β transus temperature, to become a more equiaxed α morphology. The dynamic term again refers to the process occurring during deformation. The starting microstructure and deformation conditions both significantly effect the globularisation process. The production of an equiaxed primary α phase in a transformed β matrix gives a very good balance of properties to $\alpha + \beta$ alloys and is therefore a highly desirable microstructure [37]. Therefore, the mechanisms for initiation and progression of globularisation of the primary α phase have been studied extensively [38, 39, 40, 41, 42].

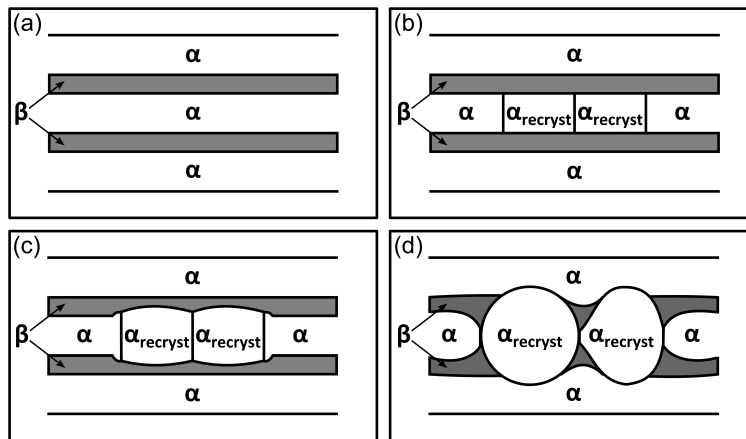


Figure 2.11 – Schematic diagram showing a proposed mechanism for the globularisation of α laths in $\alpha + \beta$ titanium alloys. (a) unrecrystallised, (b) the beginning of recrystallisation, (c) recrystallised α moving into adjacent α laths, (d) recrystallised α consuming adjacent α laths. Redrawn from [43].

The mechanisms of dynamic globularisation are hypothesised to be caused by the development of localised shear bands within primary α crystals during hot deformation, which creates a subgrain structure. At a critical strain it is possible for the β phase to penetrate the α/α interfaces created, which splits the α lath in a process known as “pinch off”, see Fig. 2.11. The initiation of dynamic globularisation has been attributed to the break up of α phase at grain boundaries and within α plates that are preferentially orientated for localised shear to occur. Globularisation is thought to preceded in two stages (1) the break up of the α structure through deformation and (2) diffusion based coalescence. It has also been noted that at the onset of globularisation that a large proportion of the α plates have orientated themselves perpendicular to the compression direction, which may promote increased local shearing due to the loss of active slip systems.

2.5.2.3 Flow Curves

The stress vs. strain curves (or flow curves) measured under hot working conditions are a function of the dominant dynamic deformation mechanism occurring. Thus, for high stacking fault energy materials the flow curve exhibits an initial period of working hardening that then reaches a steady-state value, see Fig. 2.12.

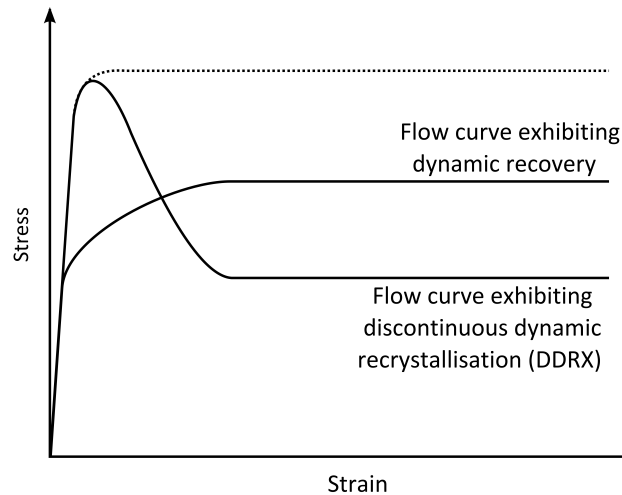


Figure 2.12 – Schematic diagram showing example flow curve shapes for material that undergoes dynamic recovery or dynamic recrystallisation (as labelled).

The value of steady-state stress is a function of the deformation temperature and strain rate; it increases with decreasing temperature and increasing strain rate. In materials where DDRX dominates the shape of the flow curve is significantly

altered from those where dynamic recovery dominates. Flow curves for DDRX also exhibit an initial period of work hardening to a peak stress that is followed by a period of flow softening until a steady-state value is reached, which follows the same dependence on temperature and strain rate as for dynamic recovery. The peak stress for materials where DDRX is dominant is lower than if dynamic recovery were the dominant mechanism, see the dotted line in Fig. 2.12.

2.5.3 Heat Treatment

As discussed, the forging conditions can be used to manipulate the microstructure. Subsequent heat treatments can be used to further tailor the microstructure for a variety of reasons. The primary purposes of heat treatment are (1) to reduce residual stresses developed during processing/fabrication, (2) to produce an acceptable combination of strength and ductility through annealing, (3) to increase strength through solution treating and ageing, (4) to optimize other mechanical properties such as fracture toughness or fatigue strength [2].

The response of titanium alloys to heat treatment is dependant upon their chemistry and not all heat treatment cycles are useful for all alloys [2]. Stress relieving and annealing can be used on α and near- α alloys, but high strength cannot be achieved in α alloys through solution treatment due to the lack of β phase. Solution treating and ageing produces the highest strength in $\alpha+\beta$ alloys. Heat treating metastable β alloys can be quite complex due to the particular characteristics of precipitating α phase from retained β ; stress relieving and ageing may be combined, and solution treating and annealing may be the same operation [2].

Stress relieving is performed to reduce potentially harmful residual stresses introduced through processing and fabrication operations. A major outcome is the prevention of component distortion. Stress relieving does not adversely alter the strength and ductility levels. Stress relieving may not be necessary when other heat treatments in the processing achieve similar effects. A typical stress relief heat treatment for Ti-6Al-4V would be 480-650°C for 1-4 h [2]. Slower cooling (furnace or air) is typically used to prevent the reintroduction of residual stresses through uneven cooling.

Annealing is a fairly broad term, but broadly speaking it includes heat treatments that are designed to increase room temperature ductility, toughness, and dimensional stability. The annealing heat treatment should be selected to achieve

a specific outcome, as the improvements of one type of property generally reduces levels of another property. Some typical annealing processes are mill annealing, recrystallisation annealing, and beta annealing. Mill annealing is a general purpose heat treatment usually applied to mill products; it is not a full anneal and can leave traces of deformation in the microstructure. Recrystallisation annealing improves toughness and takes place in the upper $\alpha + \beta$ phase region followed by slow cooling. Beta annealing slow cools from above the β transus temperature. A typical annealing heat treatment for Ti-6Al-4V would be 705-790°C for 1-4 h followed by air or furnace cooling [2].

Different combinations of solution treating and ageing can produce a wide range of strength and ductility in $\alpha + \beta$ and β alloys. Solution treating occurs high in the $\alpha + \beta$ phase region to produce an increase in the β phase volume fraction, which is retained by rapid cooling (quenching). Upon ageing the retained β phase decomposes. The solution treating temperature dictates the quantity of retained β phase and thus the response to ageing. A typical solution treatment and ageing operation for Ti-6Al-4V would be 955-970°C for 1 h followed by water quenching and then ageing at 480-595°C for 4-8 h (or 705-760°C for 2-4 h) [2].

2.5.4 Thermomechanical Testing

Laboratory testing can be used to simulate thermomechanical processing in order to gain an understanding of the deformation characteristics of materials. To provide useful information it is necessary to know the state of stress and strain in a test specimen under a known load. To replicate hot forging it is possible to deform a cylindrical axisymmetric compression test specimen between two flat anvils; the principal stress and principal strain act on a plane perpendicular to the compression direction [44]. It is also important to remember the constant volume relationship, which allows calculation of the instantaneous stress and strain when the starting dimensions are known and the level of deformation and load is recorded [45]. Where the specimen ends touch the anvils frictional effects act to oppose the flow of material, whereas at mid-height the material is free to flow, thus the specimen tends to take on a barrelled geometry. Excessive barrelling leads to large errors in calculated stress and strain values and friction should therefore be minimised as much as is practical [45]. Elevated temperature testing means that good strain rate control is necessary because metals become much more sensitive to strain rate at higher temperatures.

When considering the friction forces it is useful to consider the material in contact with the tools to have a constant shear strength. We can then assume this interface shear strength is a fraction (known as \bar{m}) of the material's shear yield stress, where \bar{m} is known as the interface friction factor [45]. For perfect sliding \bar{m} equals zero, and for sticking friction \bar{m} equals one. The interface friction factor is more commonly used than Coulomb friction in hot metal forming processes with large deformations because it is independent of the normal stress at the interface, and is more easily measured experimentally.

The experimentally measured true stress (P_i) from the axisymmetric compression testing needs to be corrected to account for the effects of friction, which can cause the load needed for deformation to be significantly increased. A value for the friction corrected instantaneous true stress (σ_i) can be calculated using Eq. 2.11 [46, 45].

$$\sigma_i = \frac{P_i}{1 + \left(\frac{2\bar{m}r}{3\sqrt{3}h} \right)} \quad (2.11)$$

A value for the interface friction factor \bar{m} needs to be determined in order to utilise Eq. 2.11. This can be done experimentally using the ring compression test [47] or alternatively by deforming specimens of varying initial height under the same test conditions and finding the friction factor that converges the resulting flow curves together [48, 49].

As stated, FE modelling has become a common tool to provide load and microstructural predictions during complex forging operations. However, a comprehensive data set is required for this modelling to be accurate. The effect of thermomechanical processing parameters on loads and microstructural evolution needs to be understood, due to their inevitable variation even when nominally isothermal forging, to allow successful process modelling. Levels of strain, strain rate, and temperature can significantly affect the microstructure of titanium alloys and the load required to deform them. Cylindrical axisymmetric compression specimens can be used to obtain data on deformation loads, but a large test matrix would be needed to characterise microstructural evolution using this method. The novel double truncated cone testing approach developed by Jackson et al. [50] allows this microstructural characterisation in far fewer tests

due to the predictable and controlled strain distribution in the forged specimen. A double cone specimen can be tested at a set temperature and strain rate to give information relating to a larger range of strains compared to a cylinder, from almost zero at the edge to high strains in the centre. Small specimen dimensions limit temperature variations so that a good approximation of isothermal forging can be realised, as well as allowing metallographic preparation and inspection of the entire specimen.

2.6 Producing Cost-Effective Titanium

The previous sections have indicated the difficulties associated with extracting titanium from its ore and subsequent processing, which directly leads to the high relative cost of titanium alloy components. This has led to under utilisation of titanium, despite its excellent combination of properties. The current processing route, outlined in section 2.4, has been improved and optimised over the preceding six decades but it is unlikely that the conventional route will ever achieve the cost reductions necessary to allow competition with commodity metals. Therefore, significant energy has been directed towards developing a new cost-effective processing route.

As outlined in sections 1.2 and 1.3, and shown in Fig. 1.1, the current cost breakdown of titanium alloy components can be split into two main areas; the cost of ingot production and the cost of downstream processing (the example ignores the cost of machining, which can be equally as high in some instances). For a truly cost-effective processing route it is necessary to target cost reductions in both areas. Reducing the cost of extraction/melting and then processing in a conventional manner will not achieve high enough savings; neither will using a new processing route with conventional ingot material.

2.6.1 Overview of Alternative Extraction Methods

The energy and time intensive Kroll process is at best a semi-continuous batch process, which in part contributes to high cost of titanium sponge. In 1959 Kroll predicted that a competitive electrolytic extraction process would be developed within 10 years [51], with the expectation it would achieve similar savings as the Hall-Héroult process for aluminium [52]. However, the technological barriers to an alternative extraction method proved more difficult to overcome than Kroll had expected and no such process is yet operating commercially.

The business opportunity presented by a viable lower-cost alternative to the sixty year old Kroll process has led to the development of multiple different approaches around the globe. Fray [7] gives an overview and discussion of the majority of these, and a selection of the more developed/promising techniques will be discussed here. Specific attention will be given to the Metalysis FFC process as it is this powder that is available for testing during this project. In the UK, electro-deoxidation is being developed by Metalysis Ltd [53], including the production of novel titanium alloys directly from synthetic rutile feedstock [54], see section 2.6.1.1 below. Several methods are being investigated in the USA: ADMA Products, Inc. are using hydrogen during the Kroll process' chlorination stage to produce TiH_2 powder, which can then be densified and simultaneously dehydrided by a variety of methods, which is reportedly occurring at the pilot-plant scale [55]; Cristal Metals (through acquisition of ITP) are performing nearly continuous sodium reduction of TiCl_4 in the Armstrong process [56]; and MER Corporation are electrowinning from carbothermally reduced titanium oxide [57]. In South Africa, CSIR are trialling continuous metallothermic reduction of TiCl_4 in molten salt [58]. In Australia, CSIRO use continuous magnesium reduction of TiCl_4 in a fluidised bed reactor in the TiRO^{TM} process [59].

2.6.1.1 The Metalysis FFC Process

Metalysis Ltd. was spun out of the University of Cambridge in 2000 to commercialise the FFC process developed there by Fray, Farthing, and Chen [60]. It moved its headquarters to a location just outside Sheffield, South Yorkshire, UK in 2004 and has developed links with The University of Sheffield, which has allowed testing small quantities of their titanium powder in this work.

The FFC process can directly reduce TiO_2 to pure titanium metal in a molten salt electrolyte. A typical reaction cell consists of a graphite anode and a cathode consisting of the metal oxide/s, which are both submerged in a bath of molten CaCl_2 . The application of a current at elevated temperature under a protective atmosphere leads to the ionisation of oxygen, which diffuses to the anode and produced carbon oxides. This leaves the pure metal remaining at the cathode, where it is subsequently harvested. A key benefit of the process, due to being completely in the solid state, is being able to produce a range of alloys directly, including compositions that are considered impossible/difficult via conventional processing (e.g. Ti-Ta [61] and Ti-W [62]).

Traditionally the process used high purity TiO_2 to produce preforms that were then used at the cathode. However it has recently been shown that it is possible to produce powder directly from natural or synthetic rutile, which has the potential for large cost reductions as they are the lowest cost feedstock possible [53]. Synthetic rutile has a propensity to contain what would classically be considered impurities such as iron and aluminium, but these elements are also commonly used as alloying additions. Therefore, the manipulation of the ore source and production process used to make the synthetic rutile can allow control over these impurities and allow direct production of alloy powders. This reduces the need to add additional metal oxides to the process and again has the potential to be a very cost-effective source for titanium alloy powders [54].

The exact electrochemical reaction mechanisms are beyond the scope of this review but have been reported elsewhere [54].

2.6.2 Cost-Effective Downstream Processing

Using alternative downstream processing methods for titanium alloys that are more cost-effective has the potential to achieve less expensive titanium components. The conventional processing route for titanium alloys is a labour-intensive, multi-step, batch process, as shown in section 2.4. Removing, or replacing with superior alternatives, as many of these traditional multi-stage thermomechanical processing steps as possible will allow cost savings to be made in the downstream processing. A key factor in addition to the removal of steps is the greater utilisation of metal so that there is less wastage of material. A reduction in processing steps and material waste can potentially be achieved through using near net shape technologies.

Casting is a near net shape technology that can offer benefits in certain applications. However, it will not be discussed here as it involves melting, which is not a sensible use of a powder feedstock; it also accounts for less than 2 % of titanium metal usage [26].

Almost all of the alternative extraction processes discussed in section 2.6.1 produce a powder or particulate titanium product. The form of these feedstocks indicates that powder metallurgy (PM) techniques may offer opportunities for cost reductions and this will be examined in the following section.

2.6.2.1 Powder Metallurgy

Most PM routes, with the notable exception of additive layer manufacturing, utilise sintering, which is the process of consolidating powders to make solid objects without melting the particles. Thermal activation of mass transport processes, which are driven by the reduction of surface and grain boundary energies, makes this possible [63]. High temperatures, relative to the material's melting point, are used to allow full consolidation to be achieved. Titanium alloy powder cost remains the largest barrier to PM techniques being more cost-effective [1].

Additive layer manufacturing (ALM) uses the principle of slicing a solid geometry into multiple layers, which are then built up layer by layer through selectively melting a feedstock powder [64]. ALM has received significant attention over the past decade and is frequently touted as being very cost-effective, but issues surrounding microstructure/properties, processing times, and surface finish remain. The powder feedstock also needs to be quite fine and spherical, which is not typical of the powders produced via alternative extraction. ALM will therefore not be investigated further.

Metal injection moulding (MIM) was developed in the 1970s and 1980s as a process to produce small and complex net shape parts [64]. Metallic powder in the sub-45 μm size range is combined with an organic binder into a granule form, which is then forced into a mould by an injection moulding machine. The following step is to remove the binder (thermally or with a solvent) and then sinter the part to 95-99 % density. MIM can have cost-benefits if producing large numbers of small parts. However the required small powder size, complex use of binders, and residual porosity mean it is discarded as part of this study.

Hot isostatic pressing (HIP) places metal powder in a mild steel can, where vacuum desorption and out-gassing are performed, before the can is placed in a pressure chamber and subjected to a thermal and pressure cycle [64]. HIP can achieve full density in titanium parts and produce significantly larger components than other PM techniques. Recent developments mean it is possible to design cans to produce near net shape sintered parts that require minimal machining. The steel can needs to be removed after sintering, which is achieved through machining or pickling. HIP is a mature technology and offers clear cost savings for certain applications, but the processing times can still be slow and the initial

design of the steel can is very complicated. It is doubtful that HIP will be able to offer the true step change in economics that this study is attempting.

2.6.2.2 Field Assisted Sintering Technology

This section is adapted from the papers published by Weston et al. in the Journal of Materials Science [65], the Proceedings of the 13th World Conference on Titanium [66], and the Journal of Materials Processing Technology [67].

As with all processes there is much interest in reducing associated costs and therefore a method to achieve higher densities at lower temperatures, and in less time, is desirable. The use of electric current to activate a rapid sintering process is such a method; referred to variously as spark plasma sintering (SPS), field assisted sintering technique (FAST), and pulsed electric current sintering (PECS).

FAST allows the solid state consolidation of powders by combining the effects of high temperature with the application of uniaxial pressure. The heat is generated through Joule heating as DC current is applied through a mould assembly containing the powder, either continuously or pulsed in a chosen pattern, which allows very high heating rates to be attained compared to more traditional sintering methods. Hydraulically actuated rams allow the application of axial mechanical load to produce the required pressure. FAST is considered an effective method for rapid sintering due to the high heating rates and the blend of heat and pressure; with broad agreement that it can produce equivalent or improved properties, compared with conventional techniques like hot isostatic pressing (HIP), whilst operating with reduced processing times and/or lower temperatures [16]. The relatively recent increased availability of commercially built FAST devices has led to a rapid expansion in the use of this approach and research into its fundamental principles. This has led to a large increase in both patent applications and published work, the latter of which has shown an exponential growth since the early 1990s with the majority of the work being undertaken in China and Japan [16]. FAST is reported to be a useful tool in the consolidation of numerous materials, many of which were traditionally considered difficult to consolidate; tungsten-carbide processed with a smaller grain size and improved properties in less than half the time by Eriksson et al. [68].

Whilst beyond the scope of this work a thorough review of the wide variety of materials successfully processed via FAST is presented by Orrù et al. [13]. The

review papers by Munir et al. [16, 15] further show the overriding view is that FAST provides benefits over traditional methods of sintering. These benefits are well reported within the literature and include the intrinsic advantages of lower sintering temperature and shorter processing times, as well as the reported improvement in comparative properties. The electric current appears to play a role in enhancing the sintering beyond simple Joule heating, and it is routinely proposed that high localised currents create the eponymous “spark plasma”, which increases sintering via a mechanism of particle surface cleaning or localised melting/evaporation. However, there is currently insufficient experimental evidence of spark plasma, suggesting that the term is misleading at best; Hulbert et al. were unable to detect it in a variety of powders across a wide spectrum of conditions using a range of techniques [69]. It should also be noted that the reporting of lower temperature reduced time benefits combined with improved properties cannot necessarily be treated as independent factors; it is likely that in some cases the improved properties come from the lower temperature and shorter processing time leading to different compositions and microstructures. Not all property enhancements can be assigned to the lower temperature. The application of pressure and current in the FAST process can be shown to have beneficial effects when compared to methods such as pressureless sintering and hot pressing.

The current in FAST is frequently attributed with only causing Joule heating and thus allowing control of the process temperature, but it has been shown to have further, non-thermal, enhancing effects. Several works report experiments that have a method of applying current within a furnace environment to allow the independent assessment of current and temperature parameters; the temperature used would usually be significantly higher than the utilised currents would achieve through Joule heating alone. The use of a tri-layer arrangement with a distinct material sandwiched between two wafers of a different material has been used, Ti-Ni by Garay et al. [70], Ag-Zn by Friedman et al. [71], Al-Au by Bertolino et al. [72], and Mo-Si by Chen et al. [73]. This arrangement allowed the assessment of current upon reaction layer growth and also whether current direction was important by comparison of the two interfaces. There was unanimous agreement that the presence of a current greatly increased the rate of growth of the reaction layers and that no directional effects were noticeable. There was general agreement that electromigration was not the dominant mechanism of growth due to the lack of directional effects and that

an increase in defect concentration or atomic mobility was a more likely cause of the current's enhancing effects. Similar work with tungsten wires sandwiched between tungsten plates by Toyofuku et al. [74], and copper spheres between copper plates by Frei et al. [75], showed the enhancement of neck growth between wire/sphere and plate under the presence of a current, which the authors attributed to an increase in electromigration. The work on Mo-Si by Chen also showed that the pulse pattern and frequency was inconsequential with product layer thickness depending solely upon temperature and time. Xie et al. also showed for aluminium powder that for frequencies of 0 and 300 Hz, and 10 and 40 kHz, in a variety of pulse patterns that density, resistivity, and tensile strength were not significantly effected [76].

Increasing process efficiency and saving energy is crucial in a low-cost processing route for titanium alloys and FAST clearly shows the potential to assist with this. The energy efficiency of FAST compared to conventional hot pressing is demonstrated by Musa et al. using Ti-Al₂O₃-TiC composites; the lower temperature and reduced time to produce a material with slightly improved properties via FAST led to a 90-95 % energy saving [77]. Whilst the precise saving will vary with conditions and materials Musa et al. have demonstrated the significant cost reductions possible. Present commercial FAST systems most commonly use all graphite mould assemblies, which conduct with a higher resistivity than most metals, meaning it dissipates electrical energy to heat at reasonable current densities. Drawbacks of these assemblies include (1) current flows through the entire mould dissipating electrical energy over a large volume compared to the specimen volume (2) current leaks through the die reducing specimen current density and its positive effects (3) graphite conducts heat well resulting in high heat loss to surroundings requiring higher power input. However, Chennoufi et al. used a mould assembly with a thermal/electrical insulation layer between stainless steel plungers and the ring, and heat-generating graphite foils between sample and plungers [78]. This insulation prevents leakage currents so that current density through the specimen is maximised (up to three times higher than conventional all-graphite assemblies) also reducing heat loss to surroundings. A 900°C steady-state target temperature was achieved with 15 times less power input and over 4 times less current, coupled with an increase in maximum allowable load, but an upper temperature limit of 1000°C.

Whilst titanium alloys are suitable for processing by FAST there is relatively

little published work. The economics of a low-cost processing route are less beneficial unless a low-cost feedstock is available and therefore titanium alloy PM routes have historically received less attention than more exotic materials. Published work falls mainly into two categories; (1) the production of titanium alloys for biomedical applications and (2) production of ultrafine-grained (UFG) titanium alloys usually with a high energy ball milling stage preceding the sintering to produce the nano-crystalline microstructure to be preserved within the FAST machine. Handtrack et al. aimed to improve the biocompatibility of CP-Ti through increasing strength and wear resistance by producing UFG titanium containing Ti_3Si_5 dispersoids [79]. High energy ball milling was used to create nano-crystalline Ti-Si particles which were processed via FAST at a variety of temperatures and pressures. A nano-scale α grain size with finely dispersed Ti_3Si_5 was produced after FAST at 700°C for 6 minutes at 80 MPa; lower temperatures and hold times failed to completely diffuse the silicon particles and higher temperatures and hold times led to a ballooning grain size. Strength comparable to, and hardness exceeding, Ti-6Al-4V were reported. Sumida et al. similarly claimed to be able to produce Ti_3Si_5 dispersoids within a titanium matrix, but starting with SiO_2 powder and using conditions between 800-1200°C and 19 MPa for 5 minutes [80]. The increased temperature required is likely due to the reduced pressure and the use of SiO_2 rather than pure silicon, additionally the powders used were 20-40 μm in size, thus having larger distances for diffusion. Nicula et al. and Sakamoto et al. both used the FAST process to produce titanium compacts with tailored porosity to improve biocompatibility [81, 82]. The porosity aimed to allow increased cell adhesion and osseointegration as well as more closely matching the Young's modulus and strength of human bone. Both research teams reported successes with more closely matching bone properties and increased cell growth on porous substrates. FAST as a titanium joining technique has been investigated; He et al. showed it possible to join Ti-6Al-4V at 700°C and 5 MPa in 5 minutes, achieving a joint strength 91 % of the bulk alloy, greatly exceeding hot pressing results, and showed that grains and phases grew across the interface [83]. Miriyev et al. demonstrated a 250 MPa joint strength between Ti-6Al-4V and low-alloy AISI 4330 steel by FAST at 900°C and 35 MPa for 60 minutes, with the advantage that the highly brittle intermetallic products found in conventional welding did not form due to a layer of TiC forming [84]. Other researchers have also demonstrated that fully dense titanium can be produced via FAST: Chaudhari

et al. (1300°C, 50 MPa, 10 minute hold), Menapce et al. (950/1050°C, 60 MPa, 5 minute hold), and Eriksson et al. suggest that particle deformation is the most significant contribution to densification, rather than spark discharge or heating anisotropy at neck regions, due to the temperature of maximum densification rate during FAST coinciding with the maximum strain rate during compression testing [85, 86, 87]. They additionally state that increasing pressure led to more rapid compaction as well as current pulsing having little effect. Zadra et al. processed CP-Ti at 60 MPa for 5 minutes between 700-1150°C and showed that the material was almost fully dense at 800°C, with small increases in density at higher temperatures and a rapid grain growth above the β transus temperature [88]. They also showed that interstitial content of carbon, oxygen, and nitrogen remains constant from the starting material independent of processing temperature and optimum mechanical properties achieved at 900°C.

The FAST process appears to offer clear advantages with regards to powder consolidation, but there may also be disadvantages. Temperature and stress gradients across samples may lead to microstructural/compositional heterogeneity, especially in larger samples or near net shape parts. Work by Munoz et al. [89] simulating the FAST process has shown that the temperature distribution inside samples is mainly controlled by their thermal conductivity; low conductivity leads to significant temperature gradients and high conductivity leads to homogeneous temperature distributions. Anselmi-Tamburini et al. support this and additionally claim current density is also a large factor in temperature profiles; a higher local current density giving higher local heating [90]. They also reported simulations of copper where uniform stress was seen across most of the sample, both radially and axially. There is an exception at the edge where top and bottom saw significantly different stresses; this would possibly lead to differences in microstructure/density. They surmise that stress gradients play a more important role in sample microstructure during FAST due to their larger size.

In summary, it is clear that complex mechanisms are operating in the FAST process to produce the enhanced sintering that is seen, and they are not yet fully understood. There has been relatively little attention given to the processing of titanium alloy powder via the FAST route. Most studies are concerned with using the unique capabilities of FAST to retain UFG structures or retain porosity and not attain full density. Producing UFG titanium alloys entails starting with very

small powder sizes and usually involves heavy pre-processing via high energy ball milling. This is not applicable in the case of a low-cost processing route due to the added cost, complexity, and particle size differing greatly from those produced via alternative extraction routes. The production of porous titanium also has little to offer when exceeding the properties of conventional wrought product is desired. No published work on the FAST of titanium alloy feedstock produced via alternative extraction methods has been discovered.

There is an absence of published work on producing anything other than simple disc shaped specimens via FAST and therefore the limitations of this technology to produce complex geometries is currently unknown.

3. Methods and Materials

3.1 Experimental Techniques

This section discusses the experimental equipment and techniques that were used throughout the work. A general overview and standard operating procedure is given where equipment was used repeatedly for a variety of testing; exact parameters and conditions will be detailed at the appropriate point in specific chapters.

3.1.1 Field Assisted Sintering Technology

The titanium alloy powders were consolidated using either an FCT Systeme GmbH SPS Furnace Type HP D 25 located at The University of Sheffield, see Fig. 3.1, or an FCT Systeme GmbH SPS Furnace Type H-HP D 250 located at Kennametal Manufacturing (UK) Ltd in Newport, Wales; the same methodology was used in both cases.

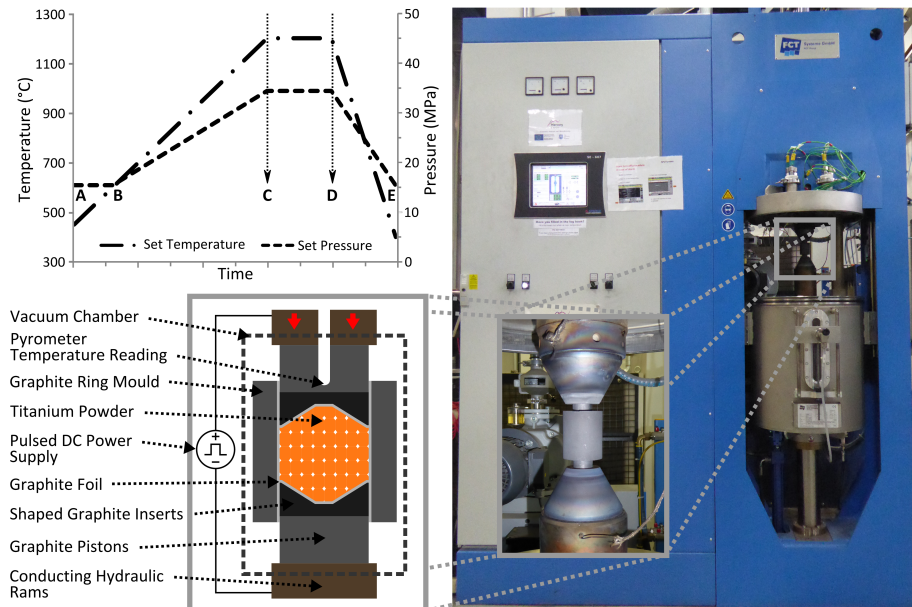


Figure 3.1 – Photograph of the FCT Systeme GmbH Type HP D 25 FAST Furnace at The University of Sheffield; showing detail of the graphite mould assembly between the conducting hydraulic rams (right). Schematic cross-section of the FAST system's main components and mould assembly (bottom left). Graph outlining the variation in processing parameters during a FAST cycle (top left).

Firstly, the mass of titanium alloy powder, m , needed to achieve selected specimen dimensions at full density can be calculated using Eq. 3.1 below, where ρ is the density of the selected alloy and V is the volume of the specimen. When producing uniform thickness disc shaped specimens the volume is simply the radius of the selected mould, r , multiplied by π and the desired specimen thickness t , see Eq. 3.2. For more complex shapes the calculation of V becomes a question of geometry; for the double truncated cone specimens used in part of this work the volume can be calculated using Eq. 3.3, where h is the height of a single truncated cone, R_1 is the radius of the base of the truncated cone, R_2 is the radius of the upper part of the truncated cone, and t is the thickness of the central cylinder between the two truncated cones, see Fig. 3.2.

$$m = \rho V \quad (3.1)$$

$$V = t\pi r^2 \quad (3.2)$$

$$V = \left(\frac{2\pi h}{3} (R_1^2 + R_1 R_2 + R_2^2) \right) + t\pi R_1^2 \quad (3.3)$$

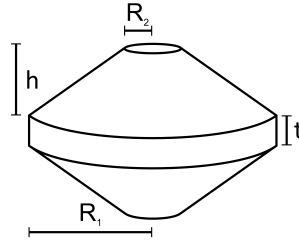


Figure 3.2 – Schematic showing the geometrical features of the double truncated cone specimen used in this work.

The appropriate mould assembly to produce the desired specimen was then selected. This study used all-graphite mould assemblies to produce uniform thickness discs with diameter dependent upon the specific mould used; these were either 20 mm or 80 mm in diameter. Each mould assembly consists of a graphite ring, two graphite pistons, two graphite supports (which taper from the diameter of the conducting hydraulic rams to the diameter of the graphite pistons), and a small graphite pin to align the mould assembly with the lower ram. Technical drawings of these two mould assemblies are provided in appendix A, see Fig. A.1 for the 20 mm assembly and Fig. A.2 for the 80 mm assembly. Chapter 6 also experiments with using a 20 mm diameter all-steel mould assembly with shaped graphite inserts to produce shaped specimens. The all-steel mould assembly

consisted of the same components (ring, pistons, supports, and pin), but with dimensions altered slightly to allow for the additional graphite inserts; a technical drawing is provided in appendix A, see Fig. A.4.

Next, the selected ring mould was lined with graphite foil to help with specimen removal and prolong mould life by preventing excessive wear. The powder was placed into this ring mould between two close-fitting graphite pistons, which were also separated from the powder by graphite foil discs. The graphite pistons had flat ends to produce a simple disc shaped specimen, or additional shaped graphite inserts could be added to produce the desired shaped specimens, as seen in Fig. 3.1. A carbon felt jacket was added around the exterior of the graphite ring to help prevent radiative heat loss. This mould assembly was then sealed in the machine's vacuum chamber between the two conducting hydraulic rams and appropriately tapered supports, and held with a put-on load of 5 kN to ensure good electrical contact was made.

A pre-programmed sintering cycle was then started. The same basic cycle was used for all processing runs, seen in Fig. 3.1, with the main processing variables (heating rate, dwell temperature, dwell pressure, and dwell time) altered as required. First the vacuum chamber was evacuated, backfilled with argon, then evacuated again. Pulsed DC current was then applied to the mould assembly through the conducting rams, with the repeating pattern of 15 ms on and 5 ms off. Initially the heating is uncontrolled up to 450°C due to the operating limits of the pyrometer used (point A on the graph in Fig. 3.1). Above 450°C a selected constant heating rate was applied, controlled by a pyrometer viewing axially downwards onto the upper graphite piston's inner face, up to a chosen dwell temperature (points A-C in Fig. 3.1). Once 600°C was reached (point B) the applied load is set to increase at a rate so that the desired dwell pressure would occur simultaneously with the dwell temperature (point C). These maximum conditions were then maintained for a set dwell time (points C-D). Two options are then possible for cooling (points D-E); free or controlled. For free cooling the current is turned off and the assembly is allowed to cool at the maximum possible rate, which varies depending upon the size of the mould assembly. For controlled cooling a reduced current is used to slow down the cooling to any selected rate. The load was also gradually decreased back to 5 kN during the cool and then maintained to aid with heat removal through the water cooled rams. Once the mould assembly reached room temperature the vacuum was released from the

chamber to allow its removal. The specimen was then pressed out of the ring mould and the graphite foil removed by grit blasting.

3.1.2 Hot Axisymmetric Compression Testing

3.1.2.1 Machine Overview

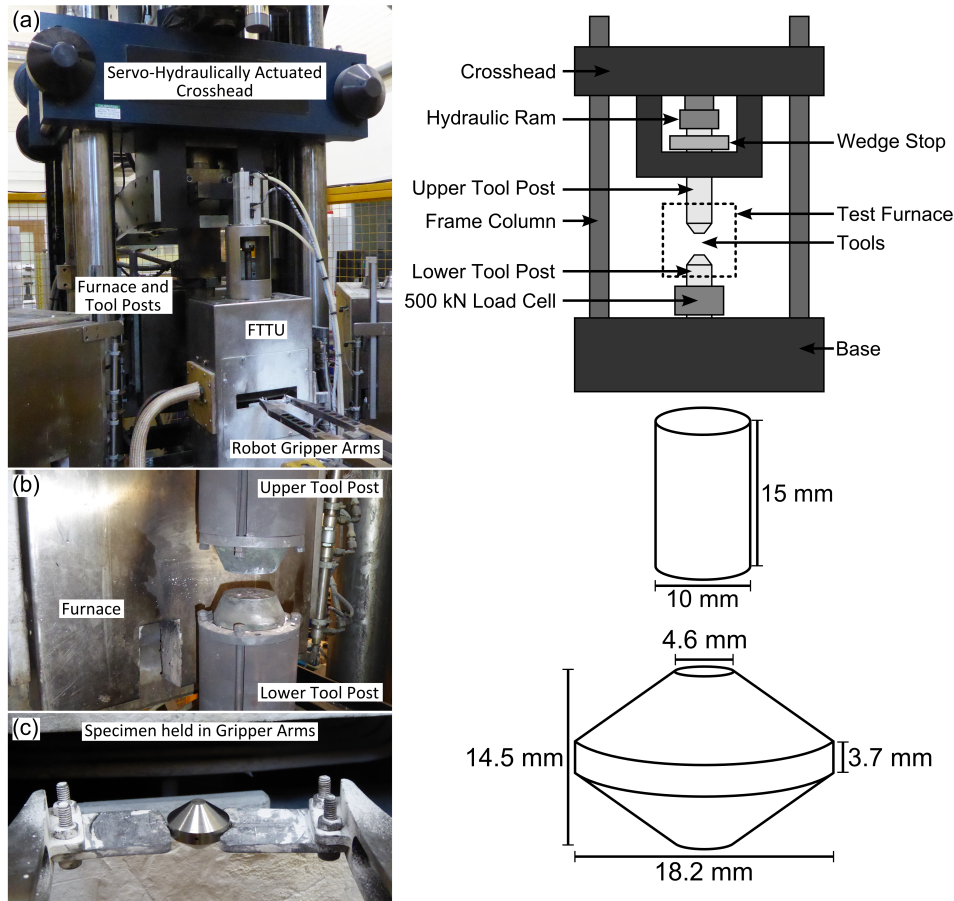


Figure 3.3 – Photographs and schematic outlining the major components of The University of Sheffield’s thermomechanical compression machine (a), close-up view of the tool posts and furnace (b) (note the furnace has been moved to the rear to enable viewing of the tool posts), close-up of a double truncated cone specimen held in the robot gripper arms (c). The dimensions of the standard test specimens used are shown.

The replication of the one-step forging operation was undertaken using The University of Sheffield’s thermomechanical compression machine (TMC), which was purpose designed and built to simulate metal forming processes, see Fig. 3.3. The TMC consists of two main components, the test furnace and the fast thermal treatment unit, and is controlled via custom software running on a PC; this allowed pre-programming of complete test cycles that could be conducted in

a fully automated fashion. The test furnace contained two M22 steel tool posts, where the lower one remained stationary and the upper one was servo hydraulically actuated via a closed-loop control system to allow deformations. Induction heating of specimens up to test temperature was possible in the fast thermal treatment unit (FTTU) located immediately in front of the test furnace. Hydraulically controlled robot gripper arms were used to manipulate the specimen during testing; allowing positioning at the correct height before automatically moving forward into the FTTU and then into the test furnace for deformation where they remain gripping the sample, followed by specimen retrieval.

A 1.1 mm diameter hole was drilled so as to be located at the centre of the specimen, allowing an N-type thermocouple to be inserted, giving control during induction heating and temperature data during deformation. The TMC machine has a maximum load capacity of 500 kN, deformation velocity control from 0.01 mms^{-1} to $2.9 \times 10^3 \text{ mms}^{-1}$, and stopping point accuracy less than $\pm 0.1 \text{ mm}$ to give good control over applied strain. The typical geometry of the cylindrical test specimens used to gather flow stress data was 10 mm diameter by 15 mm tall and the double truncated cone specimens were 18.2 mm diameter by 14.5 mm tall, see Fig. 3.3. The testing guidance provided in the UK National Physical Laboratory Good Practice Guide (GPG) for Hot Axisymmetric Testing was utilised with the aim of achieving reliable results through following best practice [44].

3.1.2.2 Testing Procedure

Before testing could begin it was necessary to turn on the test furnace approximately two hours before the commencement of testing. This allowed the furnace, tool posts, and tools to reach thermal equilibrium at the programmed temperature. Initial specimen dimensions were recorded according to the guidance provided in the GPG [44]. Once the test furnace temperature was stable, and immediately before testing, the displacement transducer was zeroed. This was achieved by bringing the test tools into contact with each other under self-weight and then marking this position as the zero location, which allows accurate recording of the sample height during deformation. Next, the specimen was placed in the robot arms, a thermocouple was attached, and a boron nitride coating applied to limit interstitial pick up and reduce friction. An automated test cycle was then started: the specimen was heated in the

FTTU at 4°Cs^{-1} to the test temperature and held for 30 seconds to allow homogenisation and minimise any temperature oscillations. The robot arms quickly moved the specimen into the test furnace, where a constant strain rate deformation to a set strain occurred, before rapidly withdrawing for a water quench to room temperature. A data logger recorded time, temperature, load, velocity, and displacement information throughout the test, to be utilised in further analysis and calculation of flow curves. The frequency of the data logged was adjusted depending upon the strain rate being used; lower strain rates allowed for a reduced frequency and vice-versa. The deformed samples were sectioned centrally, parallel to the compression axis, to allow microstructural observation.

3.1.3 Heat Treatment

A programmable tube furnace was used to perform heat treatments on specimens. To reduce excessive interstitial contamination the specimens were coated in glass lubricant and flowing argon gas was fed into the furnace. The furnace temperature was set using the electronic control unit and a stopwatch used to measure the appropriate length of time before specimen removal. The specimens were then either allowed to air cool or were quenched in water, before having the glass lubricant or any oxide scale removed by grit blasting.

3.1.4 Particle Size Analysis

A Malvern Mastersizer 3000 was used to give a particle size distribution (PSD) for the selected titanium alloy powders. This technique utilises laser diffraction to calculate particle sizes by measuring the angular variation in the intensity of light scattered as a laser beam passes through a dispersed sample (wet or dry dispersion) of the desired particulate. The larger particles scatter the incident light relatively less at a higher intensity, whilst smaller particles produce a weaker intensity higher angle scattering, see Fig. 3.4.

The Mie theory of light scattering can then be used to interpret the scattering patterns produced, allowing calculation of the size of the particles responsible [91]. Information on the refractive index of both dispersant and sample are required; the values used for these measurements were 1.33 for water and 2.47 for titanium. The particle sizes are then reported as volume-equivalent sphere diameters, which can be plotted against cumulative volume % to give the PSD. Single number reporting of a size distribution is sometimes useful and some form

of mean is the most common; the volumetric mean (known as the $D[4,3]$) is useful for samples where the interest is the size of particle making up the bulk of the sample volume. Percentiles are another way of quantifying PSD and allowing easier comparison between powders. Percentiles are defined as DvX , where D refers to particle diameter, v refers to volume, and X is the percentage of the sample below the quoted particle size; so a $Dv50$ of $75\text{ }\mu\text{m}$ would mean that 50% of the sample volume is made up of particles with diameters less than $75\text{ }\mu\text{m}$. The three most commonly used are $Dv10$, $Dv50$, $Dv90$, which give a good indication of the spread of particle sizes. Unfortunately very irregularly shaped particles can produce errors when using this kind of analysis but there is little viable alternative.

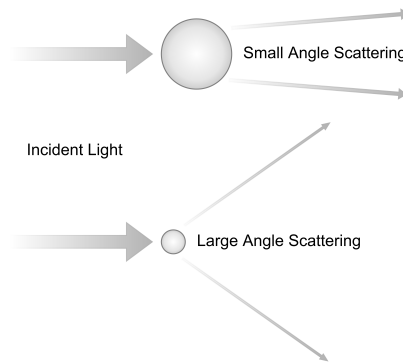


Figure 3.4 – Schematic showing the effect of particle size on laser diffraction.

This work used wet dispersion with deionised water as the dispersant, which was agitated by a propeller rotating at 2500 rpm to ensure the particles were effectively dispersed. Small amounts of the alloy powder were added to the wet dispersion unit until the laser obscuration was between 5-10 % (a value recommended by the manufacturer to give accurate results). The water containing the powder was continuously circulated through the system and a series of 20 measurements were taken to check for consistency, then an average taken. The system was thoroughly flushed and calibrated, including the removal of background noise, before each run to prevent cross-contamination and improve accuracy.

3.1.5 Microhardness

Microhardness testing was performed using a Struers Durascan-70. Metallographically prepared samples were indented using a Vickers hardness tip with a mass of 1 kg applied for 15 s. The two diagonals of the indent were

then measured and averaged to give a value for the indent diameter, which was then converted to a Vickers hardness value. Each indent was placed at least three diameters from the previous indent to prevent interference, as prescribed by the ASTM standard [92]. Each sample was indented with at least 10 points, well away from the sample edges, to allow an average value of hardness to be obtained.

3.1.6 Metallography

Standard metallographic preparation for titanium alloys was used for all specimens where microstructural observation was required. If necessary the specimens were sectioned to reveal a face of interest using an abrasive cut-off wheel. Specimens were then either hot-mounted using Bakelite if near to full density or cold-mounted in an epoxy-based resin if porous or a powder. The mounted specimens could then be ground using progressively finer silicon carbide papers lubricated with flowing water and then 9 μm diamond suspension on a Struers MD Largo pad, before a final chemical/mechanical polish using colloidal silica of 0.05 μm diluted by 20% with hydrogen peroxide. Kroll's reagent was applied as an etchant, if needed, until increased microstructural detail was visible. A Nikon Eclipse LV150 light microscope was used under reflected light conditions in bright field mode to perform microstructural observations and assessment of porosity; additional microstructural detail could be seen by applying a cross-polarised light filter when needed. The microscope was equipped with a CCD digital camera attached to a neighbouring PC with Buehler Omnimet image capture software, which allowed the capture of micrographs.

3.1.7 Density

The density of specimens was checked by two methods; using Archimedes' principle or image analysis of bright field micrographs.

Archimedes' principle allows the calculation of bulk density, i.e. the total mass of material divided by the total volume it occupies, which includes material volume, inter-material void volume, and any internal porosity within particles. The measurement was carried out using the methodology described in the ASTM Standard C194-09 [93]. It was necessary to coat the samples to be measured in a wax layer to prevent water intrusion into any porosity open to the surface that would have given erroneously high measurements of the bulk density. The measured bulk density can then be compared to the known volumetric mass

density for each alloy to calculate the density as a percentage. The method used is outlined below:

1. Weigh specimen in air = m_1
2. Coat specimen in thin layer of paraffin wax to prevent water ingress into pores, ensuring no trapped air bubbles, and weigh wax coated specimen in air = m_2
3. Weigh wax coated specimen in water = m_3
4. Calculate volume of wax:

$$V_{wax} = \frac{m_2 - m_1}{\rho_{wax}}$$

where ρ_{wax} = density of used paraffin wax = 0.91 g/cm³

5. Calculate volume of wax coated specimen:

$$V_{specimen} = \frac{m_2 - m_3}{\rho_{water}}$$

where ρ_{water} = density of water at temperature recorded at time of test

6. Calculate density of specimen:

$$\rho_{specimen} = \frac{m_1}{V_{specimen} - V_{wax}}$$

This method was complemented by image analysis of bright field light micrographs, using the software ImageJ [94]. The micrographs were converted to 8-bit greyscale images and then into black and white images using a threshold algorithm; the threshold is set so that everything lighter than the pores is made white whilst they are made black. The porosity can then be calculated by dividing the number of black pixels by the total number of pixels in the image. An average value for five-to-ten images from random locations across a specimen was measured.

3.1.8 Finite Element Modelling

The finite element software DEFORMTM [17] was used to simulate the hot compression tests of both the cylinder and the double cone specimens. Due to the axisymmetric nature of the specimens it was possible to use a 2-D model of

half the geometry, which simplified the simulation and reduced processing time. An appropriate number of elements were selected, detailed in specific chapters, to produce the required resolution of output values. The hot compression testing of each alloy provided rheology data in the form of stress values at a range of strains for each combination of strain rate and temperature tested; this was input to the software as tabulated data and used as the relevant material model. Due to the high temperature and large strains involved in hot forging the material response was assumed to be fully plastic. For each test condition the initial temperature was set to that recorded by the thermocouple at the start of the experimental compression, and the measured temperature profile during the tests was used as a boundary condition for the specimen ensuring the simulation matched the experimental conditions as closely as possible. Two non-meshed rigid platens were used to represent the tool posts as their experimental deformation can be treated as negligible. The upper platen was set to move vertically downwards with a velocity to produce a constant strain rate to match the experiment. Contact boundary conditions between the specimen and platens were established and a shear friction factor (\bar{m}) specified.

3.1.9 Carbon-Oxygen-Nitrogen Levels

The interstitial contents were measured by an external laboratory located at Metalysis Ltd. The content of oxygen and nitrogen was measured using the inert gas fusion method with an ELTRA O/N 900; additionally, carbon content was found using the combustion method with an ELTRA C/S 800. Testing was performed on small pieces (typically ~ 0.1 g) of the desired material and 3 repeats were conducted; if there was greater than 10 % variation between repeats then further tests were performed.

3.2 Titanium Alloy Powders

The ultimate goal is to combine the novel solid-state downstream processing route developed during this work with powder/particulate from a lower-cost alternative extraction method. However, due to the low availability of such powder much of the work presented will involve the use of commercially available conventionally produced powder. These commercial powders were chosen to allow demonstration of the processing route as proof of concept and also to give a baseline for any future work with lower-cost powders. The use of commercial alloy chemistries also allowed direct comparison of properties and microstructures

produced in this work with conventionally produced wrought material. Small amounts of powder from the Metalysis FFC process were also utilised in some parts of the study to demonstrate the robustness of the proposed consolidation route in accepting a variety of feedstocks. The composition of the utilised alloys is given in the next section, followed by a section showing the morphology and microstructure of each feedstock powder, and finally their particle size distributions.

3.2.1 Alloy Composition

Nominally five alloy chemistries were used, although slight variations were found in the different morphologies, shown in Table 3.1: Grade 2 commercially pure titanium (CP-Ti), Ti-6Al-4V (Ti-6-4), Ti-5Al-5V-5Mo-3Cr (Ti-5553), and two novel alloys produced by Metalysis - one derived directly from natural rutile and one from pigment grade titanium dioxide.

Table 3.1 – *The composition of the titanium alloy powders used in this study.*

Alloy	Morphology	Composition (wt.%)									
		Ti	Al	V	Mo	Cr	Fe	C	H	N	O
CP-Ti	GA spherical	Bal.	–	–	–	–	0.05	0.005	0.001	0.004	0.19
CP-Ti	HDH angular	Bal.	–	–	–	–	0.01	0.004	0.010	0.001	0.13
Ti-6-4	GA spherical	Bal.	6.00	4.00	–	–	0.10	0.030	0.003	0.010	0.15
Ti-6-4	HDH angular	Bal.	6.34	4.02	–	–	0.21	0.026	0.016	0.013	0.16
Ti-5553	GA spherical	Bal.	5.90	5.24	5.12	2.71	0.40	0.57			
rutile-derived	PS spherical	Bal.	Commercially Sensitive					0.143	–	0.010	0.24
rutile-derived	angular-spongy	Bal.	Commercially Sensitive					0.170	–	0.005	0.73
pigment-derived	spherical-spongy	Bal.	Commercially Sensitive					0.092	–	0.002	0.14

The spherical CP-Ti and Ti-6-4 were purchased from Arcam, Mölndal, Sweden. The angular CP-Ti and HDH Ti-6-4 were purchased from Reading Alloys Inc., (an Ametek Company), Robeson, PA, USA. All four materials were certified within ASTM specifications for the respective grade. The spherical Ti-5553 was produced by TLS Technik, Bitterfeld, Germany from a billet remaining from another project. The exact chemistries for the Metalysis powders cannot be given as they are commercially sensitive at this stage of development, but approximate amounts of α and β stabilising elements are summarised through an Al_{eq} wt.% and a Mo_{eq} wt.%. The plasma spheroidised (PS) rutile-derived

alloy has an Al_{eq} of ~ 4.6 wt.% and a Mo_{eq} of ~ 2.7 wt.%. The angular-spongy rutile-derived alloy has an Al_{eq} of ~ 9.2 wt.% and a Mo_{eq} of ~ 3.9 wt.%. The spherical-spongy pigment-derived alloy has an Al_{eq} of ~ 2.5 wt.% and a Mo_{eq} of ~ 0.8 wt.%. Reasonably low levels of interstitial elements have been achieved although the powders provided for this study are from research and development work so have not yet been optimised; the oxygen content of the angular-spongy rutile-derived alloy is higher than desirable, which has skewed the reported Al_{eq} .

3.2.2 Powder Morphologies and Microstructures

The morphologies of the powders used in this work can be seen in Fig. 3.5, which also gives an overview of their approximate sizes. The commercial powders were either spherical, see Fig. 3.5a, 3.5c, and 3.5h, due to production via gas atomisation (GA) or angular, see Fig. 3.5b and 3.5d, due to production via the hydride-dehydride (HDH) method. A small percentage of the spherical particles have an internal pore, which is an artefact of the production process. The angular and largely irregular HDH morphology is due to being produced by crushing of scrap, swarf, and billet off-cuts.

All the as-reduced powders produced by the Metalysis process are spongy in nature with internal porosity in the particles. The rutile-derived powder in its raw form is quite angular due to the shape of the rutile ore feedstock, but with smoother corners than the HDH powders, and contains the internal porosity giving it a spongy appearance, see Fig. 3.5f. An additional plasma spheroidisation (PS) step can be used to produce a spherical powder similar to those formed via GA, which also removes the internal porosity, see Fig. 3.5g. The morphology of the pigment-derived powder is dependent upon the TiO_2 preform shape created before the reduction step; approximately spherical beads 1-2 mm in diameter, see Fig. 3.5e were used in this work.

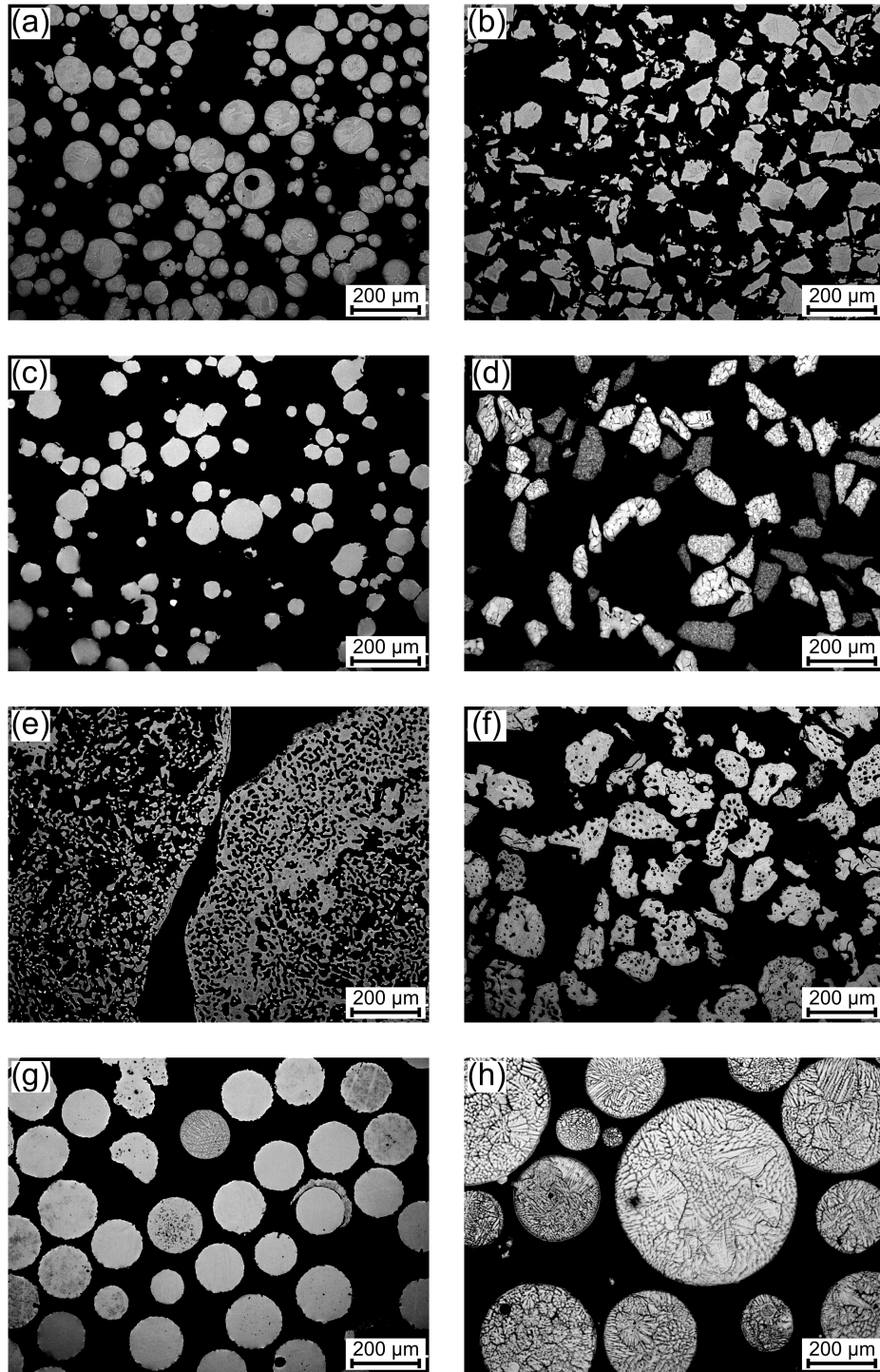


Figure 3.5 – Light micrographs showing particle size and morphology for the studied titanium alloy powders: (a) GA CP-Ti, (b) HDH CP-Ti, (c) GA Ti-6-4, (d) HDH Ti-6-4, (e) Metalysis spherical-spongy pigment-derived, (f) Metalysis angular-spongy rutile-derived, (g) Metalysis Spheroidised rutile-derived 150-250 μm , (h) GA Ti-5553.

Figure 3.7 also shows the starting microstructures of the powders before sintering. The spherical particles show microstructures expected when rapidly cooling from the liquid phase; the Ti-6-4 and rutile-derived alloy show very fine acicular laths of martensite, the CP-Ti shows a range of α grain sizes smaller than the particles with possible twinning visible in some particles, the Ti-5553 shows what appears to be a prior β grains with a complex sub-grain structure present. The CP-Ti HDH powder also shows a range of α grain size and morphology within the particles and has twinning within the grains as well. The Ti-6-4 HDH powder appears to exhibit two different length-scales of microstructure; some particles have approximately equiaxed 5-10 μm diameter α grains, whilst others have α grains in the 20-30 μm range. The angular-spongy rutile-derived powder shows a similar microstructure to Ti-6-4 HDH although the α grains are less regular in size and shape. The pigment-derived powder contains sub 50 μm equiaxed α grains with twinning present, although the high levels of porosity makes it difficult to fully assess.

3.2.3 Particle Size Distribution

Figure 3.6 shows details of the PSD of the alloy powders, with further analysis shown in Table 3.2; Dv10, Dv50 and Dv90 are the diameters that 10, 50 and 90 % of particles are smaller than, respectively.

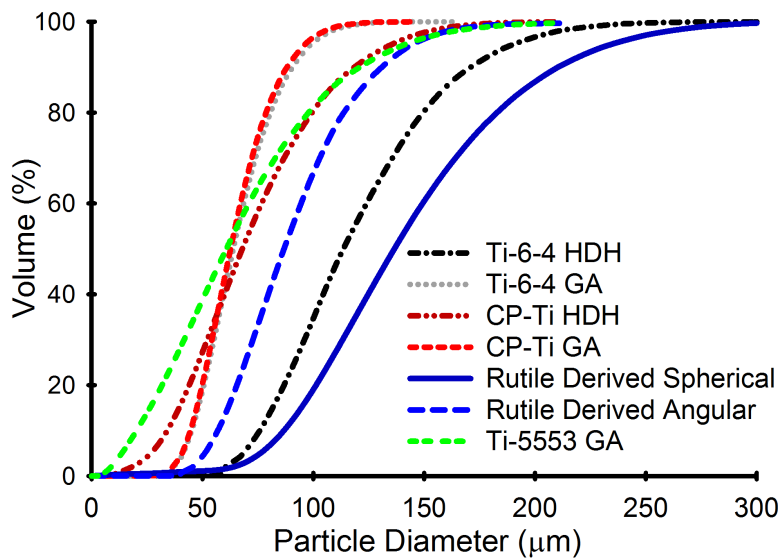


Figure 3.6 – Graph showing the cumulative volume particle size distribution for the studied titanium alloy powders.

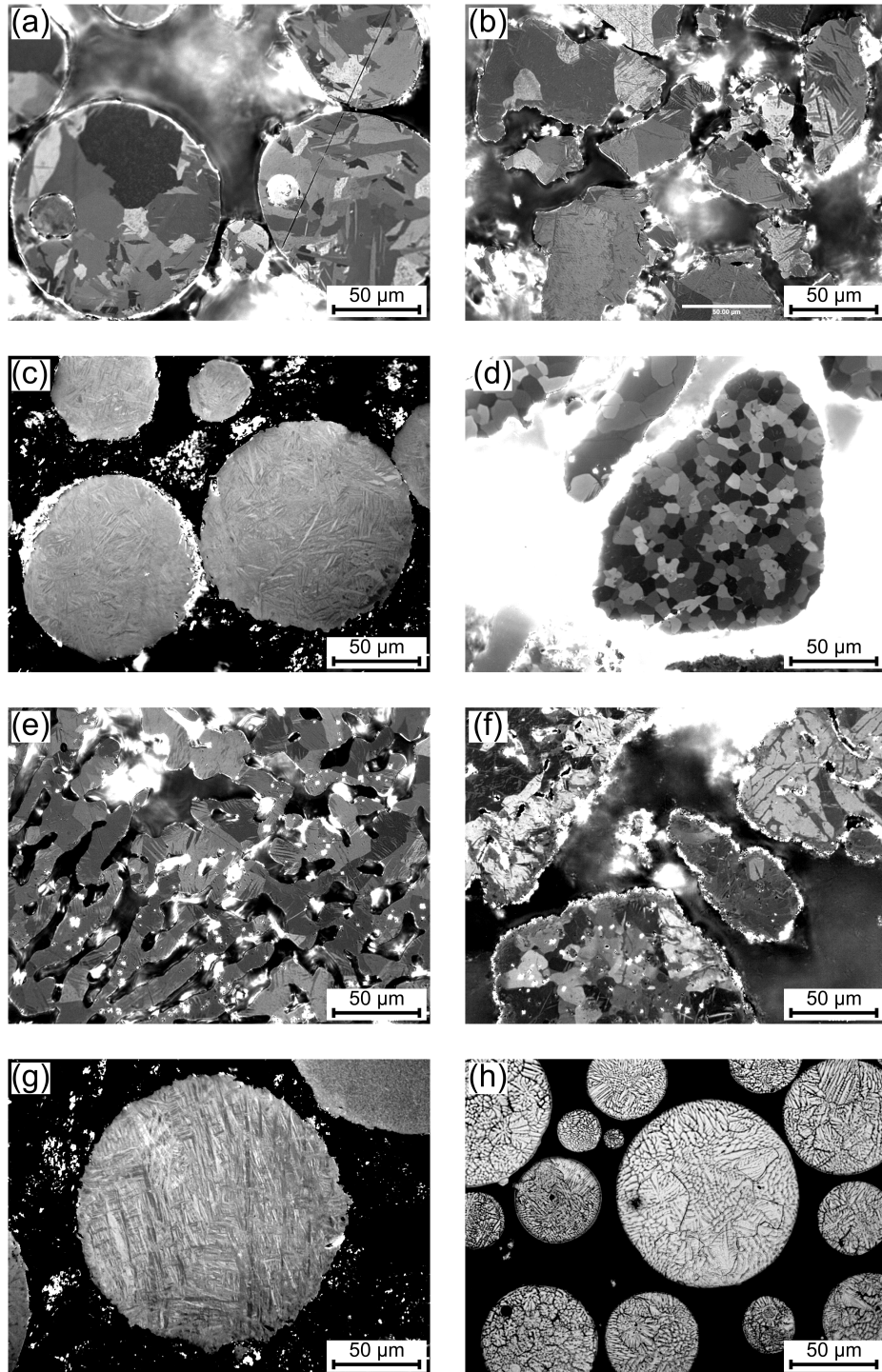


Figure 3.7 – Cross-polarised light micrographs showing microstructure for the studied titanium alloy powders: (a) GA CP-Ti, (b) HDH CP-Ti, (c) GA Ti-6-4, (d) HDH Ti-6-4, (e) Metalysis spherical-spongy pigment-derived, (f) Metalysis angular-spongy rutile-derived, (g) Metalysis Spheroidised rutile-derived 150-250 μm , (h) GA Ti-5553.

The spherical CP-Ti and Ti-6-4 have almost identical PSD with $\sim 80\%$ of the particle diameters being between $50\text{--}100\ \mu\text{m}$ with a $\sim 70\ \mu\text{m}$ median. The HDH CP-Ti and Ti-6-4 are quite different in size but have a similarly shaped distribution, the diameters of the middle 80% of particles fall within $\sim 100\ \mu\text{m}$ of each other, but the CP-Ti is approximately $50\ \mu\text{m}$ smaller across the entire distribution. The Ti-5553 was sieved to have particle diameters less than $150\ \mu\text{m}$, but was not sieved to have a minimum size, which is shown by a much lower Dv10. The Metalysis alloys were all provided sieved in particular size ranges; PS rutile-derived alloy between $150\text{--}250\ \mu\text{m}$ and angular-spongy rutile-derived alloy between $75\text{--}250\ \mu\text{m}$. These size fractions are carried through into the PSD with both alloys having the middle 80% within this range. The $1\text{--}2\ \text{mm}$ diameter spherical-spongy pigment-derived alloy was too large to put through particle size analyser to get a PSD.

Table 3.2 – Summary of the particle size distributions of the titanium alloy powders used in this study.

Alloy	Morphology	Composition (%)		
		Dv10 (μm)	Dv50 (μm)	Dv90 (μm)
CP-Ti	HDH angular	50.3	71.1	100
CP-Ti	GA spherical	38.6	77.2	135
Ti-6-4	HDH angular	51.1	72.5	104
Ti-6-4	GA spherical	86.1	129	196
Ti-5553	GA spherical	22.9	69.0	142
rutile-derived	spherical $150\text{--}250\ \mu\text{m}$	152	197	235
rutile-derived	angular-spongy	94.7	150	231
pigment-derived	spherical-spongy	N/A	N/A	N/A

4. Consolidation of Titanium Alloy Powders via Field Assisted Sintering Technology

The majority of the results presented in this chapter are drawn from the paper published in the Journal of Materials Science by Weston et al. [65]. The final publication is available at Springer via <http://dx.doi.org/10.1007/s10853-015-9029-6>. Permission for reuse has been obtained and the agreement can be seen in Fig. B.1 in appendix B.

4.1 Introduction

As discussed in the review of the literature, there has been relatively little attention paid to the consolidation of metallic powders via FAST when compared to ceramics. Titanium powders in particular do not feature heavily, probably due to their high cost limiting the potential of FAST for cost-effective processing. Some focus has been directed towards using the low-temperature and reduced-time processing benefits of FAST to produce ultrafine-grained microstructures that have improved properties beyond conventionally processed material. However, this approach necessitates using very small powder sizes and usually involves heavy pre-processing via high-energy ball milling, which is not applicable as part of a cost-effective processing route due to the additional time, cost, and utilising finer particle sizes than typically produced from alternative extraction methods. Another area of focus has been for biomedical research, where retaining porosity within titanium samples has been studied with the aim of improving osseointegration and more closely matching the mechanical properties of bone. This approach has little to offer when the goal is to match or exceed wrought material properties. There has been no published work on the FAST consolidation of titanium alloy feedstock produced via alternative extraction methods.

Consequently, this chapter will present work showing the effect of FAST processing conditions and mould size on density, microstructure, and rheology when consolidating titanium alloy powders. A variety of feedstock alloys are

used, with different size distributions, morphologies, and chemistries, to assess whether these have an impact on the required processing conditions. Rheology behaviour derived from FAST machine data, specimen density, microhardness, grain size, $\alpha + \beta$ phase size and morphology, and interstitial pick-up will be analysed to allow assessment of FAST as a cost-effective processing step.

It was possible to produce 99.9 % density and homogeneous microstructures with all the commercially available conventional powders. The Metalysis powders that contained internal particle porosity (described as spongy) were more difficult to fully consolidate and the maximum density achieved was ~ 98 %; although the PS rutile-derived powder behaved very similarly to the gas atomised commercial powder and achieved 99.9 % density. Unlike commercial powders, the Metalysis powders did not produce completely homogeneous microstructures at low dwell times, but this improved as dwell time increased.

This chapter demonstrates that FAST is capable of fully consolidating a range of titanium alloy feedstocks and producing homogeneous microstructures in one solid-state processing step. FAST offers clear benefits over some more traditional PM techniques; it's more rapid, lower-cost, and negates the need for mild-steel canning and decanning of samples. Therefore, it is deemed a viable tool as part of a cost-effective processing route for titanium alloy components; especially if combined with a potentially lower-cost feedstock from an alternative extraction method.

4.2 Experimental Approach

The experimental approach taken in this chapter was to undertake parametric studies to assess the effect of the FAST furnace's processing parameters (maximum sintering temperature and pressure, dwell time at these conditions, and heating rate) had on specimen density and microstructure. Initially a design-of-experiments type approach was utilised to assess the response of the titanium alloy powders to the dwell temperature and dwell pressure; a further parametric study then assessed the effect of heating rate and dwell time. The use of a wide variety of alloy chemistries and powder morphologies in the parametric studies also allows their effect upon FAST processing to be studied.

Additionally, rheology data in the form of consolidation curves are presented. The linear displacement of the FAST furnace's hydraulic rams was recorded

continually throughout the sintering cycles. The starting density of each powder specimen can be found by first calculating what the final height of the specimen should be at the measured achieved density (see Table 4.1). The recorded total ram travel is added to this to give the starting height of the unconsolidated powder; the starting density can then be calculated, as the mass of powder and mould dimensions are known. The ram displacement data can then be normalised against the displacement that would be required to achieve full density to give a relative density throughout the cycle, which allows comparison of all specimens regardless of powder mass or mould size. The compliance of the machine and thermal expansion of the mould sets is constant throughout the study, thus has not been corrected for.

The effect of mould size was also investigated by producing a single 250 mm diameter, 5.5 kg, FAST specimen in the large-scale FAST furnace at Kennametal Manufacturing (UK) Ltd. The processing methodology was identical to that used on the small-scale FAST furnace. The rheology data for the 80 mm diameter disc specimens produced for chapter 5 is also presented to give an intermediate point between the two extremes of mould size used.

Carbon, oxygen, and nitrogen content were measured before and after FAST processing for a selection of specimens using the method described in section 3.1.9. Vickers microhardness was also measured on a selection of specimens after FAST using the method described in section 3.1.5.

All specimens were allowed to free cool and then grit blasted to remove residual graphite foil. The 20 mm diameter specimens were sectioned parallel to the compression axis into two semi-circular halves. Standard metallographic preparation was undertaken on one half to allow microstructural examination as described in sections 3.1.6. Density was calculated through image analysis of bright-field micrographs and the use of Archimedes' principle on the remaining half, as detailed in section 3.1.7. Electrical discharge machining (EDM) was used to remove cylinders from the 250 mm diameter specimen to allow the same microstructural examination and density measurement to occur.

4.2.1 Materials

The alloy chemistries and particle morphologies of the four powders used in the dwell temperature and dwell pressure study were GA CP-Ti, HDH CP-Ti, angular-spongy rutile-derived Metalysis powder, and spherical-spongy

pigment-derived Metalysis powder. The alloy chemistries and particle morphologies of the four powders used in the dwell time and heating rate study were an α alloy (HDH CP-Ti), an $\alpha + \beta$ alloy (HDH Ti-6-4), and a β alloy (GA Ti-5553), as well as the Metalysis rutile-derived alloy that had been plasma spheroidised (PS). Full details on each type of powder were presented in section 3.2.

4.2.2 Dwell Temperature and Dwell Pressure Parametric Study

A parametric study was undertaken, using a design-of-experiments type approach, to initially assess how GA CP-Ti powder, HDH CP-Ti powder, angular-spongy rutile-derived and spherical-spongy pigment-derived Metalysis powders behaved in the FAST furnace. Dwell temperature and dwell pressure were used as the variable factors, with density as the measured output. A two-factor central composite design study was used that gave 9 experimental points; consisting of an embedded two-level full factorial design, augmented by star points to expand the design space and a centre point to check for response curvature, see Fig. 4.1. An additional outlying point to check material response at higher temperature was also used giving a total of 10 experimental runs for each alloy.

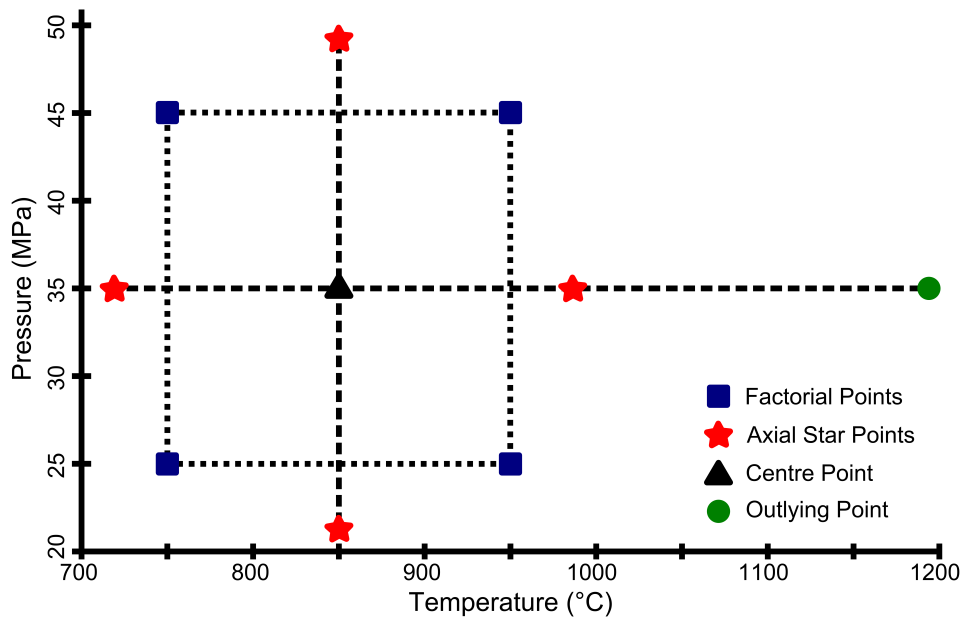


Figure 4.1 – Schematic showing the experimental points in the design of experiments type approach used for the parametric study into the effect of dwell temperature and dwell pressure.

The mass of powder used for this part of the study was 14.17 g to give a final full density thickness of ~ 10 mm. Simple disc specimens were prepared as described in section 3.1.1 with a constant heating rate of $25^{\circ}\text{Cmin}^{-1}$ and dwell time of 10 min. The dwell temperature and dwell pressure were varied from run to run as described in Table 4.1. The experimental order of the runs was randomised from that presented in Table 4.1 to help negate systematic errors, but they are listed in order of increasing dwell temperature for clarity.

4.2.3 Dwell Time and Heating Rate Parametric Study

To assess the effect of changing the heating rate and varying the dwell time on microstructure, density, and consolidation a further parametric study was undertaken. During this study the dwell temperature and pressure were kept constant at 1200°C and 22 MPa, which were selected using the knowledge gained from the dwell temperature and dwell pressure study as capable of producing $>99\%$ density. The 22 MPa dwell pressure was selected as previous work had shown that this was the maximum pressure that could be safely used without mould breakage when scaling up to 80 mm diameter specimens. Using 22 MPa with 20 mm diameter moulds during this study meant that the porosity levels and microstructures could be assessed prior to using 80 mm mould assemblies to produce specimens for use in further forging studies, which are discussed in the chapter 5. The heating rates used for the commercial alloys were $25^{\circ}\text{Cmin}^{-1}$, $50^{\circ}\text{Cmin}^{-1}$, and $100^{\circ}\text{Cmin}^{-1}$. The dwell times used were 10 min, 20 min, and 30 min. The heating rates used for the rutile-derived alloy were $50^{\circ}\text{Cmin}^{-1}$, $100^{\circ}\text{Cmin}^{-1}$, and $200^{\circ}\text{Cmin}^{-1}$. The dwell times used were 10 min, 30 min, and 60 min. The extended dwell time was selected for the rutile-derived alloy as it seemed to be more difficult to fully consolidate in the previous section.

4.3 Results and Discussions

The results of the parametric studies will be reported in terms of processing parameter effect on density, microstructure, and rheology. The dwell temperature and dwell pressure parametric study will be presented and discussed first, followed by results and discussions for the dwell time and heating rate study. Three smaller sections with results on (1) the effect of alloy chemistry and powder morphology on rheology, (2) the effect of FAST mould size, and (3) interstitial pick-up and microhardness values will also be shown and discussed.

4.3.1 Dwell Temperature and Dwell Pressure Parametric Study

4.3.1.1 Effect of Dwell Temperature and Dwell Pressure on Density

The parametric study showed that density is proportional to the dwell temperature and dwell pressure with all four materials; an increase in temperature and/or pressure caused an increase in final density, see Table 4.1.

Table 4.1 – Density achieved by the four Ti alloy powders after FAST processing at the specified conditions during the parametric study of dwell temperature and dwell pressure; organised by increasing dwell temperature.

Run No.	Dwell Temp. (°C)	Pressure (MPa)	Density (%)			
			GA CP-Ti	HDH CP-Ti	spherical-spongy pigment-derived	angular-spongy rutile-derived
1	709	35	93.6	90.8	82.2	82.0
2	750	25	90.5	89.7	82.1	85.9
3	750	45	97.5	97.1	92.9	92.7
4	850	21	96.9	95.6	89.6	95.0
5	850	35	98.3	98.3	96.5	96.6
6	850	49	99.1	98.7	97.9	97.6
7	950	25	99.4	99.1	95.7	97.3
8	950	45	99.4	99.4	97.5	97.1
9	991	35	99.8	99.9	97.8	97.8
10	1200	35	99.9	99.9	98.2	97.9

Increasing the pressure yields larger improvements in consolidation at lower temperatures, where decreased densities occur. It can be seen that for Run

#3 at 750°C-45 MPa that the density increases by ~7-10 % for all materials when compared to Run #2 at 750°C-25 MPa. For the commercial non-spongy materials it is possible to achieve >99 % density with lower pressure at higher temperatures so increasing the pressure from 25 MPa to 45 MPa at 950°C has little effect; a 0.3 % increase for HDH CP-Ti and no observed increase for GA CP-Ti. The same increase in pressure at 950°C for the Metalysis powders allows for a 1.8 % increase in density for the pigment-derived powder. However, anomalously the rutile-derived powder shows a 0.2 % decrease in density with increased pressure at 950°C. This opposes expectations and is likely the result of experimental error in the density measurement via Archimedes' principle, or heterogeneous distribution of porosity within the specimen introducing error into the image analysis. Interestingly, it can be seen from Run #10 at the highest temperature that the spongy materials appear to reach a maximum achievable density of ~98 %; Runs #6-9 at slightly decreased temperatures and/or pressures come close to this value. It is thought that beyond 98 % density that no further increase can be achieved by removal of inter-particle porosity and the remaining 2 % is comprised of trapped internal (intra-particle) porosity due to the spongy morphology. Increased pressure is not effective at removing this type of porosity as the bulk material supports the majority of the load and the rigid mould completely encapsulates the material, which prevents further plastic deformation aiding in pore removal. Increased dwell times at higher temperatures may aid with removing this remaining porosity through traditional sintering mechanisms. The effect of temperature is also greater at temperature levels which do not achieve full consolidation; there is a greater increase in density from 750-850°C than from 850-950°C for all the materials, and an increase from 991-1200°C makes little difference. There appears to be a minimum temperature for full consolidation, or removal of all inter-particle porosity in the case of a spongy morphology, and beyond this there can be no further density increase during the relatively short dwell times used in this study, regardless of further increases in temperature.

The bright-field micrographs for six selected conditions are shown in Fig. 4.2, allowing a direct comparison of the behaviour of all four materials, which correlates well with the results discussed above. The images are also separated out into individual materials, which can be seen in Fig. 4.3 for GA CP-Ti, Fig. 4.4 for HDH CP-Ti, Fig. 4.5 for spherical-spongy pigment-derived powder, and Fig. 4.6 for angular-spongy rutile-derived powder. The porosity is visible as the

darkest areas of the bright-field micrographs, with some microstructural features visible in greyscale. There is a clear reduction in porosity for all materials as the temperature and pressure increase from 750°C-25 MPa, to 850°C-35 MPa, and then to 950°C-45 MPa, see parts (b), (c), and (d) in Figs. 4.3-4.6. The GA CP-Ti increases from 90.5 - 98.3 - 99.4 %, the HDH CP-Ti from 89.7 - 98.3 - 99.4 %, the pigment-derived from 82.1 - 96.5 - 97.5 %, and the rutile-derived from 85.9 - 96.6 - 97.1 %. Similarly, the increase in density due to solely increasing the dwell temperature from 709°C, to 850°C, then to 991°C, and finally to 1200°C can be seen in parts (a), (c), (e), and (f) in Fig. 4.3-4.6.

After processing at 750°C-25 MPa the outline of the starting powders can still be seen with all materials, as the inter-particle voids have not been completely filled, and the internal porosity of the spongy powders has not been removed. There is visual evidence of initial plastic deformation of some particles and neck growth between adjacent particles.

Due to the amplifying nature of the point contacts between particles the magnitude of the applied load initially causes particle deformation to be the dominant consolidation mechanism. As the particles deform it allows the contact areas to grow, which decreases the effective load seen by the particles; this continues until equilibrium is reached and sintering mechanisms become dominant. After processing at 850°C-35 MPa there is a significant reduction in porosity. The networks of joined voids have become isolated pores and fewer prior particles can be seen. After processing at 950°C-45 MPa there is close to complete removal of porosity from the GA CP-Ti and HDH CP-Ti; the remaining porosity consists of fine, spherical, and isolated pores. The inter-particle voids are also removed in both the pigment-derived and rutile-derived alloys. There are heterogeneously distributed small spherical pores remaining in the pigment alloy, with areas of almost complete consolidation next to areas with significant porosity. In the rutile-derived material the small spherical pores are more homogeneously distributed. Increasing the temperature beyond 950°C, to 991°C and 1200°C, allows a small increase in density for all materials, even with a corresponding reduction in pressure. This is likely due to the increased levels of diffusion seen in titanium's β phase, which is further enhanced as temperature increases.

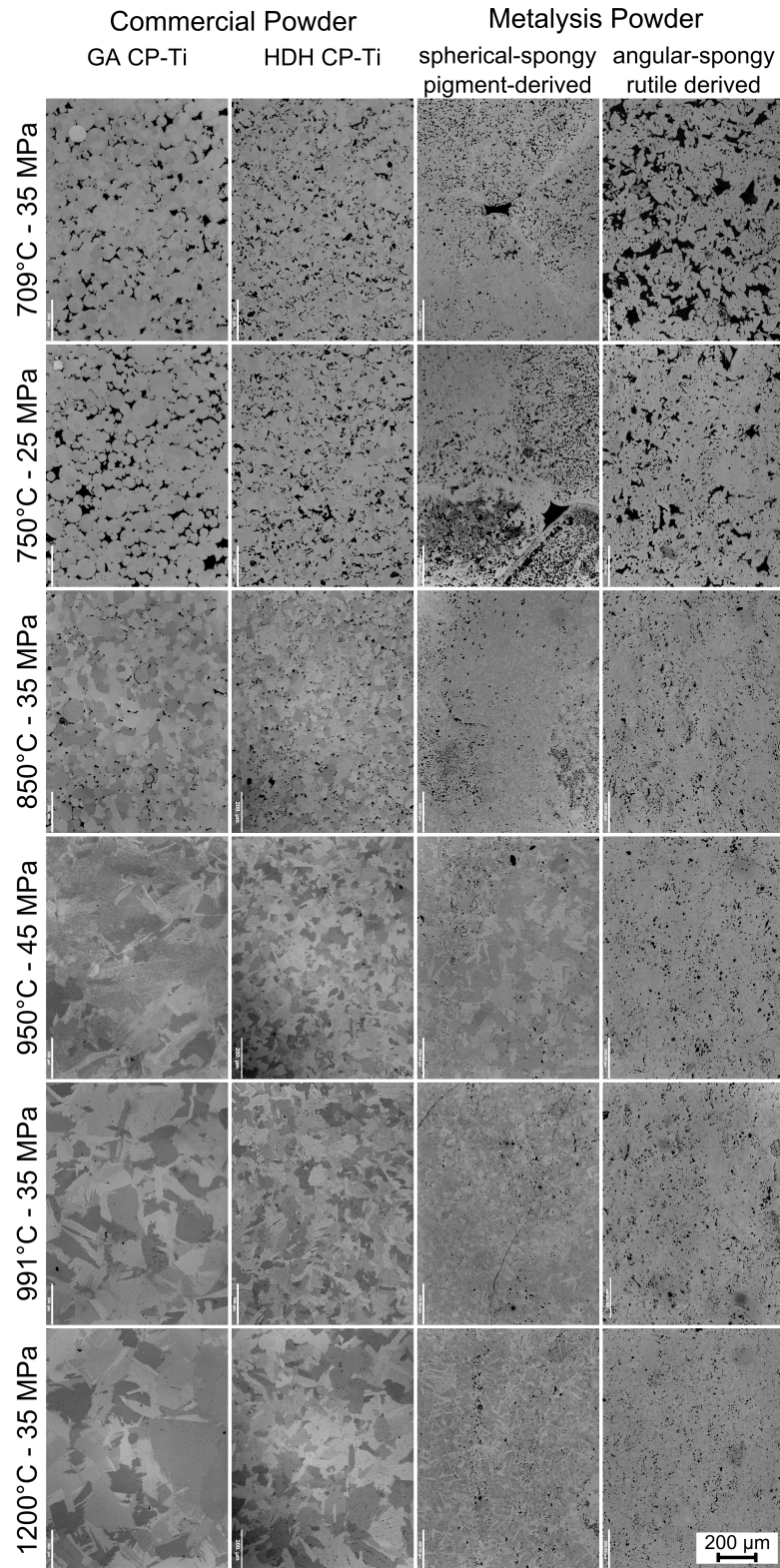


Figure 4.2 – Bright-field micrographs showing increased density with increased dwell temperature and/or dwell pressure during constant heating rate and dwell time FAST processing of GA CP-Ti, HDH CP-Ti, spherical-spongy pigment-derived and angular-spongy rutile-derived Metalysis powders.

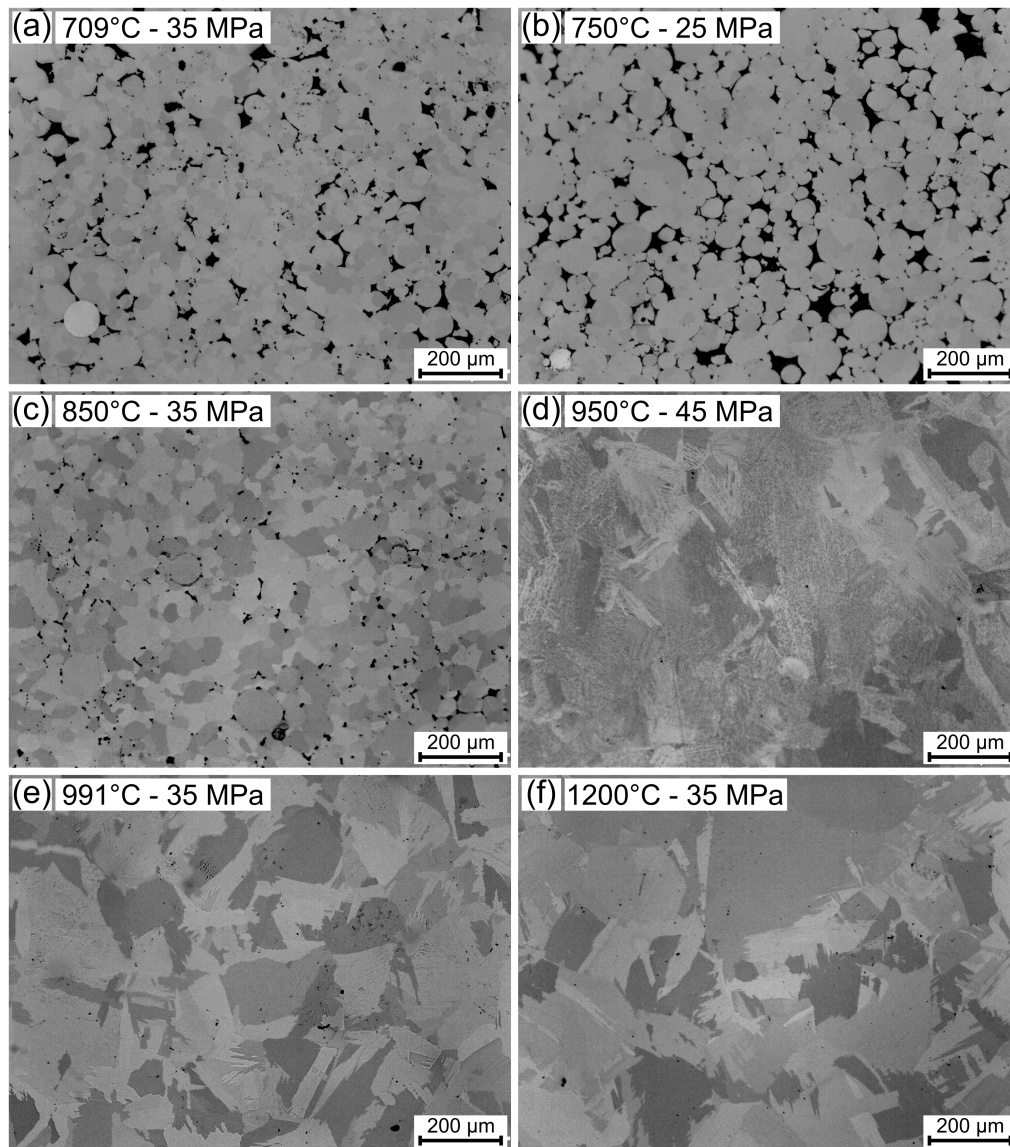


Figure 4.3 – Bright-field micrographs of GA CP-Ti powder showing the increase in density with increased dwell temperature and/or dwell pressure during constant heating rate and dwell time FAST processing.

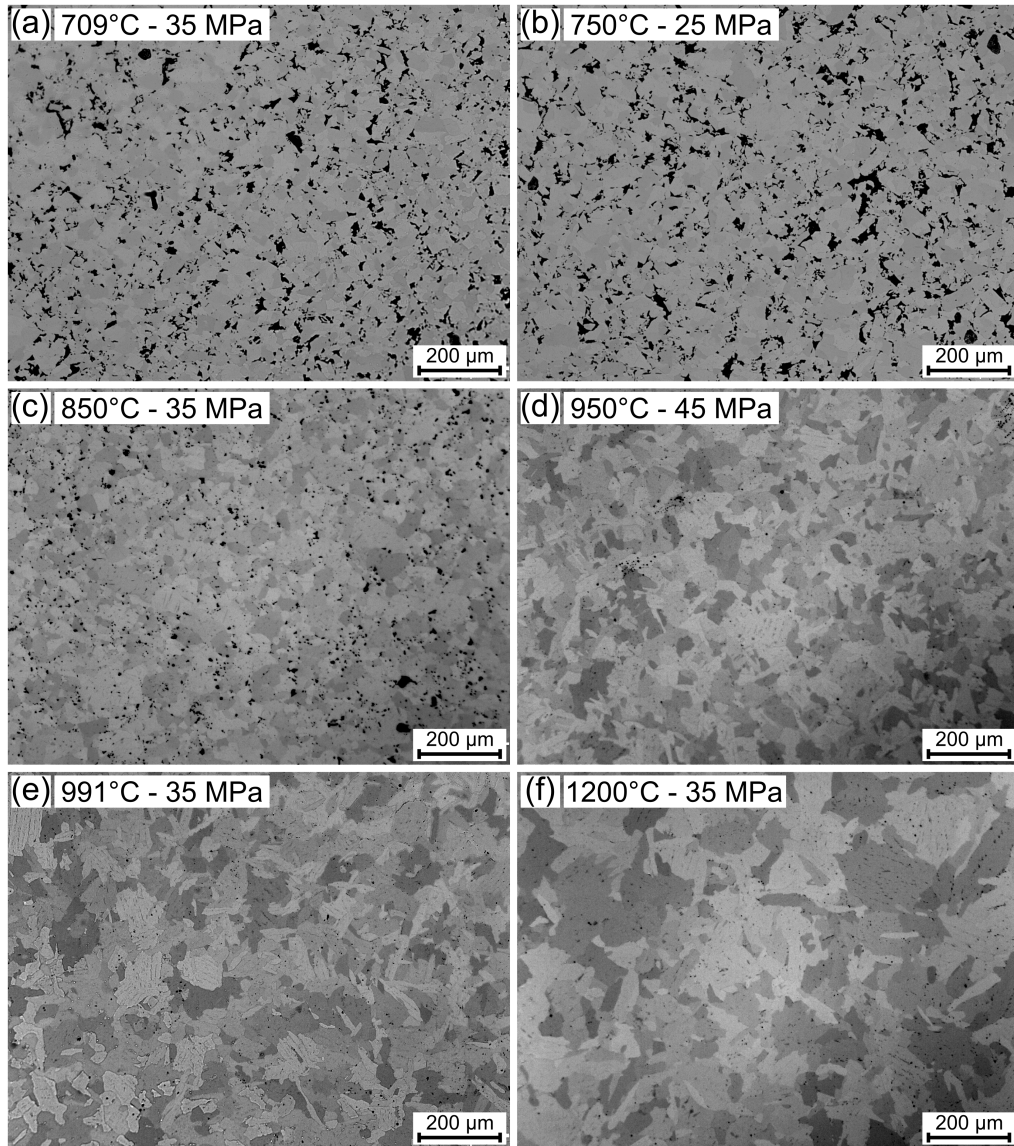


Figure 4.4 – Bright-field micrographs of HDH CP-Ti powder showing the increase in density with increased dwell temperature and/or dwell pressure during constant heating rate and dwell time FAST processing.

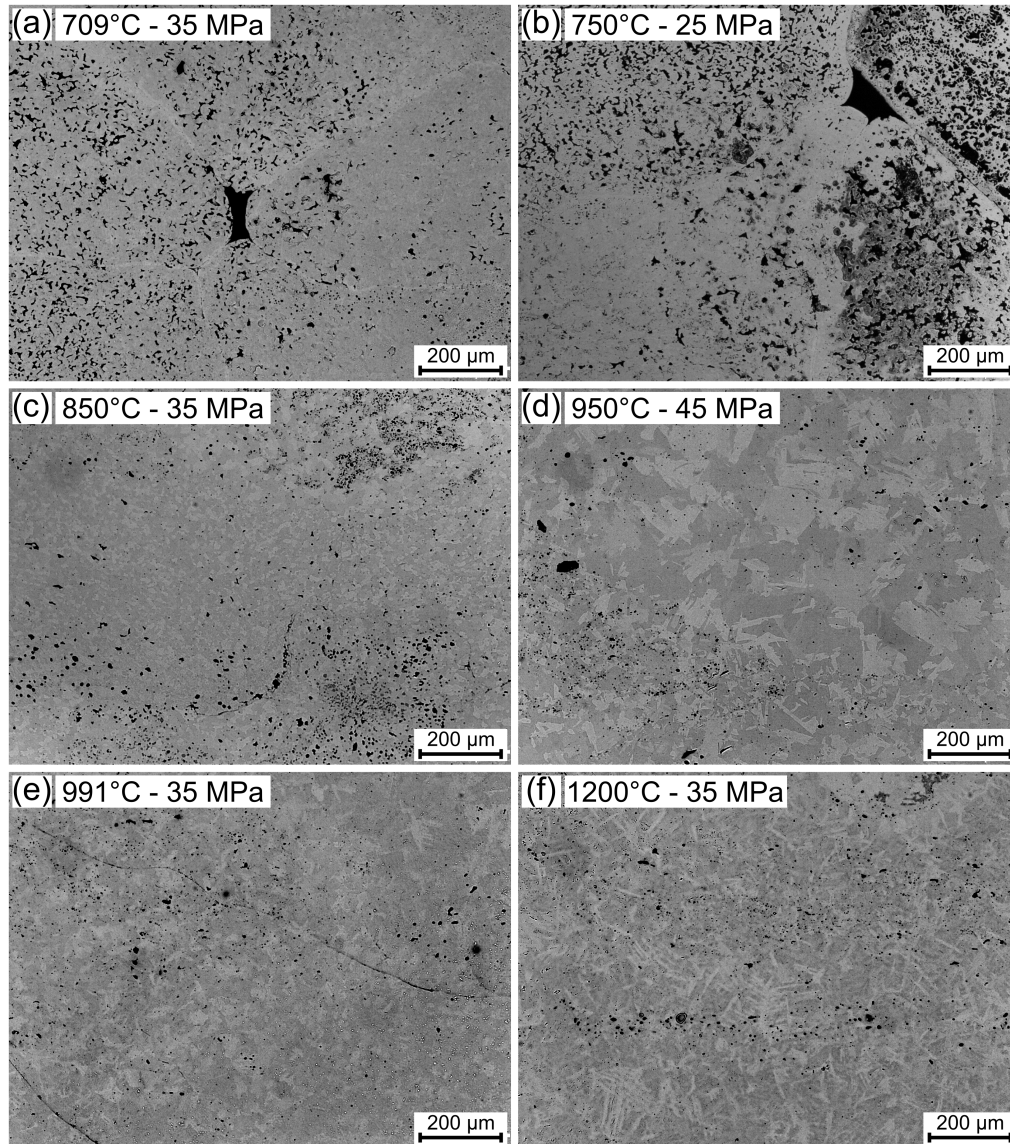


Figure 4.5 – Bright-field micrographs of spherical-spongy pigment-derived Metalysis powder showing the increase in density with increased dwell temperature and/or dwell pressure during constant heating rate and dwell time FAST processing.

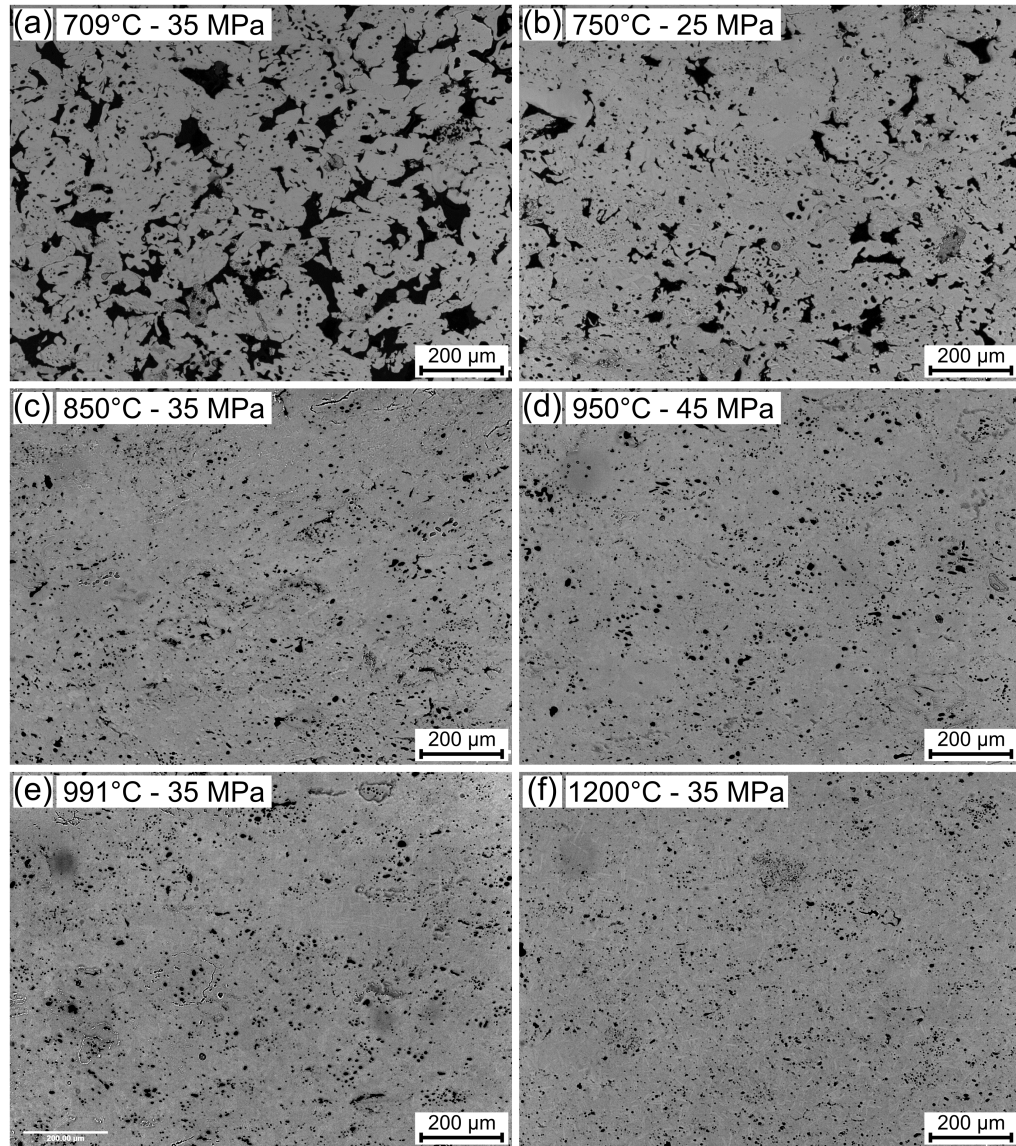


Figure 4.6 – Bright-field micrographs of angular-spongy rutile-derived Metalysis powder showing the increase in density with increased dwell temperature and/or dwell pressure during constant heating rate and dwell time FAST processing.

4.3.1.2 Effect of Dwell Temperature and Dwell Pressure on Microstructural Evolution

High magnification cross-polarised light micrographs for all four materials are presented side-by-side in Fig. 4.7 to allow comparison of microstructural evolution. However, it is difficult to directly compare the microstructure of the Metalysis alloys to the CP-Ti due to their significantly different chemistries and spongy nature giving retained porosity that interacts with grain growth. Fig. 4.8 for GA CP-Ti, Fig. 4.9 for HDH CP-Ti, Fig. 4.10 for spherical-spongy pigment-derived powder, and Fig. 4.11 for angular-spongy rutile-derived powder present lower magnification microstructures of each individual material after processing at 709°C-35 MPa in parts (a), 750°C-25 MPa in parts (b), 850°C-35 MPa in parts (c), 950°C-45 MPa in parts (d), 991°C-35 MPa in parts (e), and 1200°C-35 MPa in parts (f). Parts (a) and (b) represent the lowest densities achieved and parts (e) and (f) show the highest.

There has clearly been a change in microstructure from the starting powders, see Fig. 3.7, even when the density achieved is low at processing conditions of 709°C-35 MPa (part (a)) and 750°C-25 MPa (part (b)). Recovery and potentially recrystallisation have allowed α grain growth within the powder particles; the large amounts of porosity prevent further growth beyond particle boundaries at this point. The GA CP-Ti demonstrates the most equiaxed structure with more variation shown in the HDH, mirroring their respective PSDs, see Fig. 3.6. The Metalysis alloys have areas where α grain growth has begun and other areas where it is limited. Increased α grain growth can be seen after processing at 850°C-35 MPa, which is expected at the increased temperature, see part (c) of Figs. 4.8-4.11. The growth is still limited by prior particle size and porosity; the largest grain sizes in the commercial materials roughly correspond to prior particle sizes. The heterogeneous nature of grain growth has continued in the spongy Metalysis powders. This could be due to two factors: the heterogeneous internal porosity prevents grain growth in some places but not in areas with higher density, or there are variations in chemical composition from particle to particle.

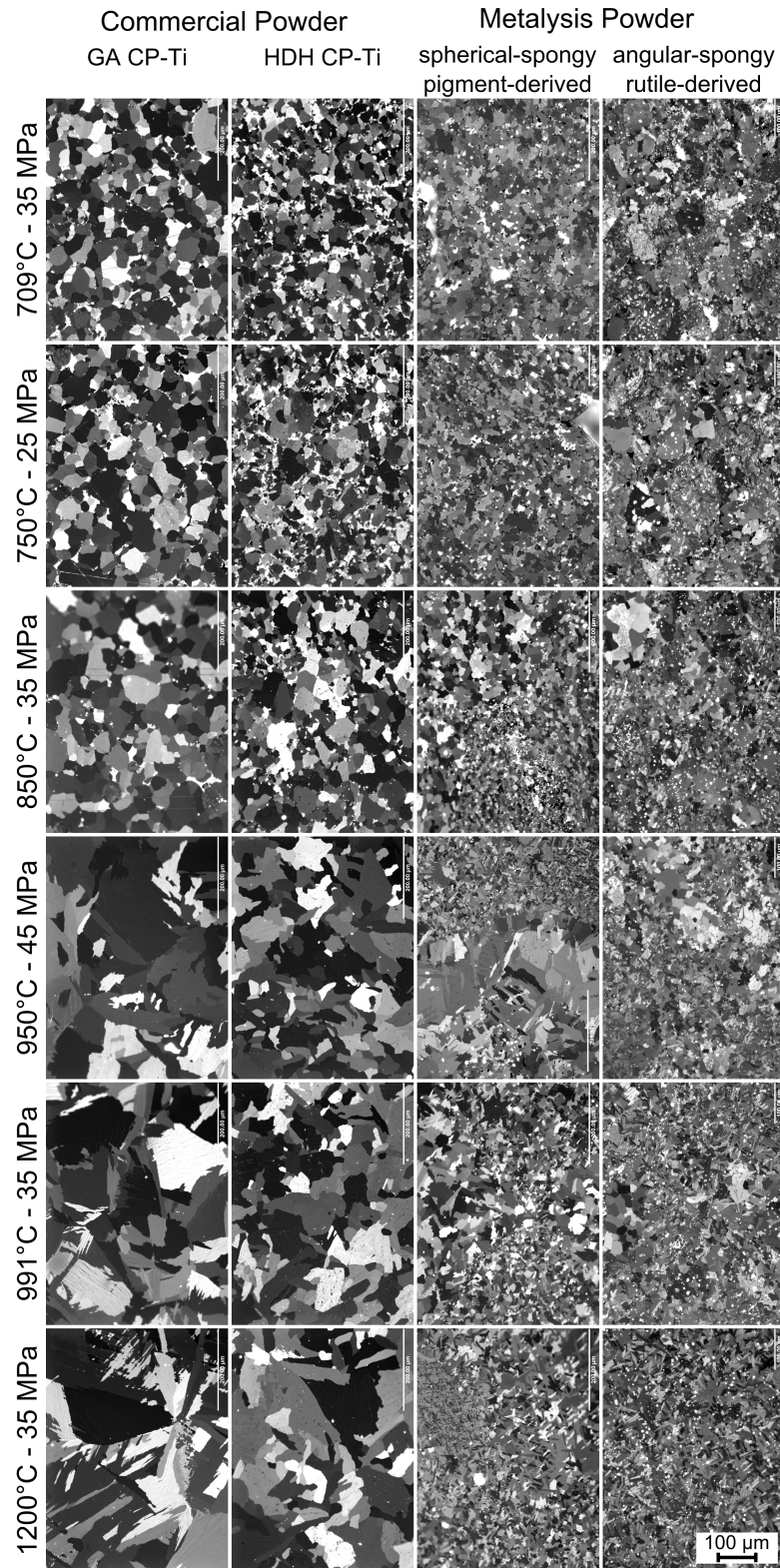


Figure 4.7 – Cross-polarised light micrographs showing microstructural development during constant heating rate and dwell time FAST processing with varying dwell temperatures and dwell pressures for GA CP-Ti, HDH CP-Ti, spherical-spongy pigment-derived, and angular-spongy rutile-derived Metalysis powders.

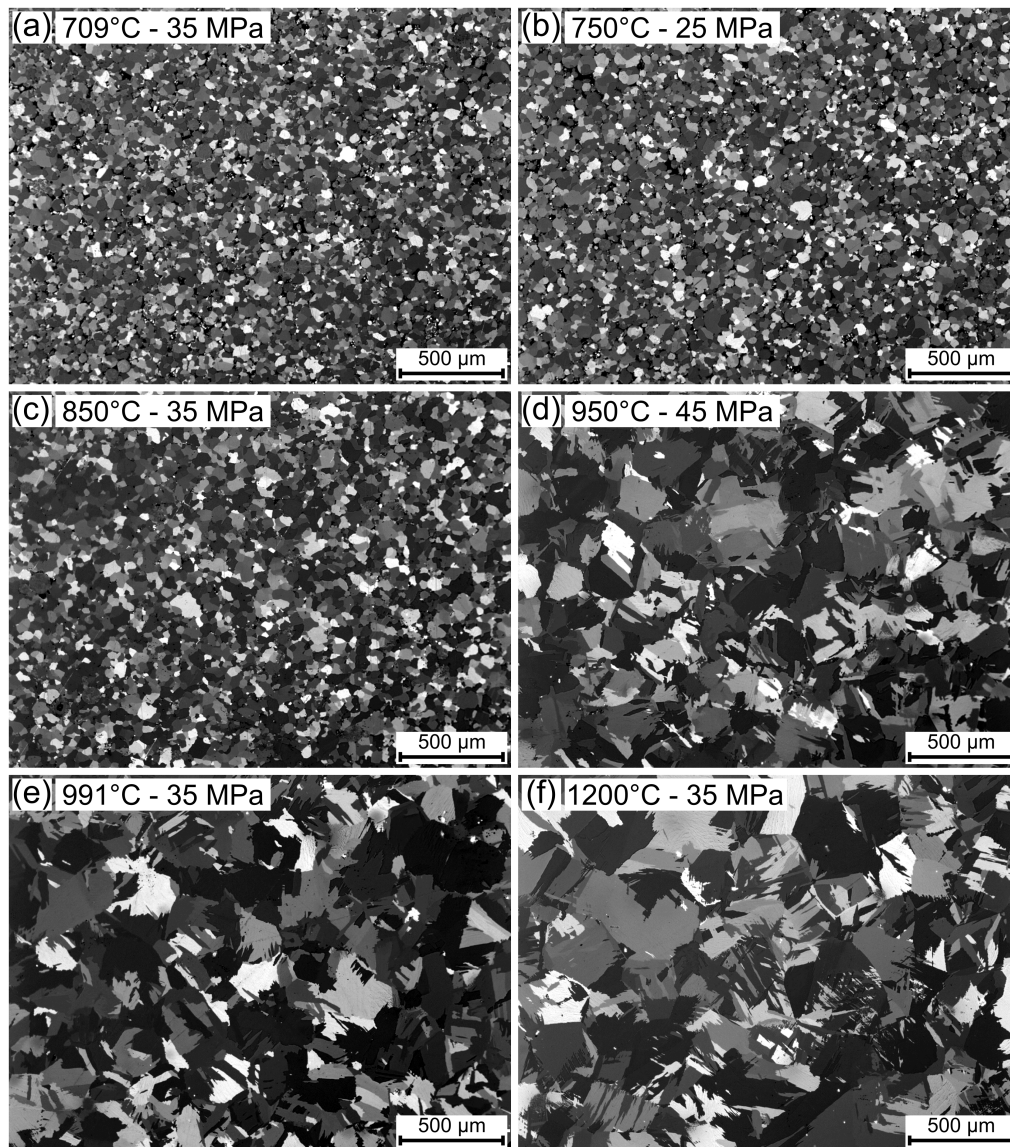


Figure 4.8 – Cross-polarised light micrographs of GA CP-Ti powder showing the change in microstructure with increased dwell temperature and/or dwell pressure during constant heating rate and dwell time FAST processing.

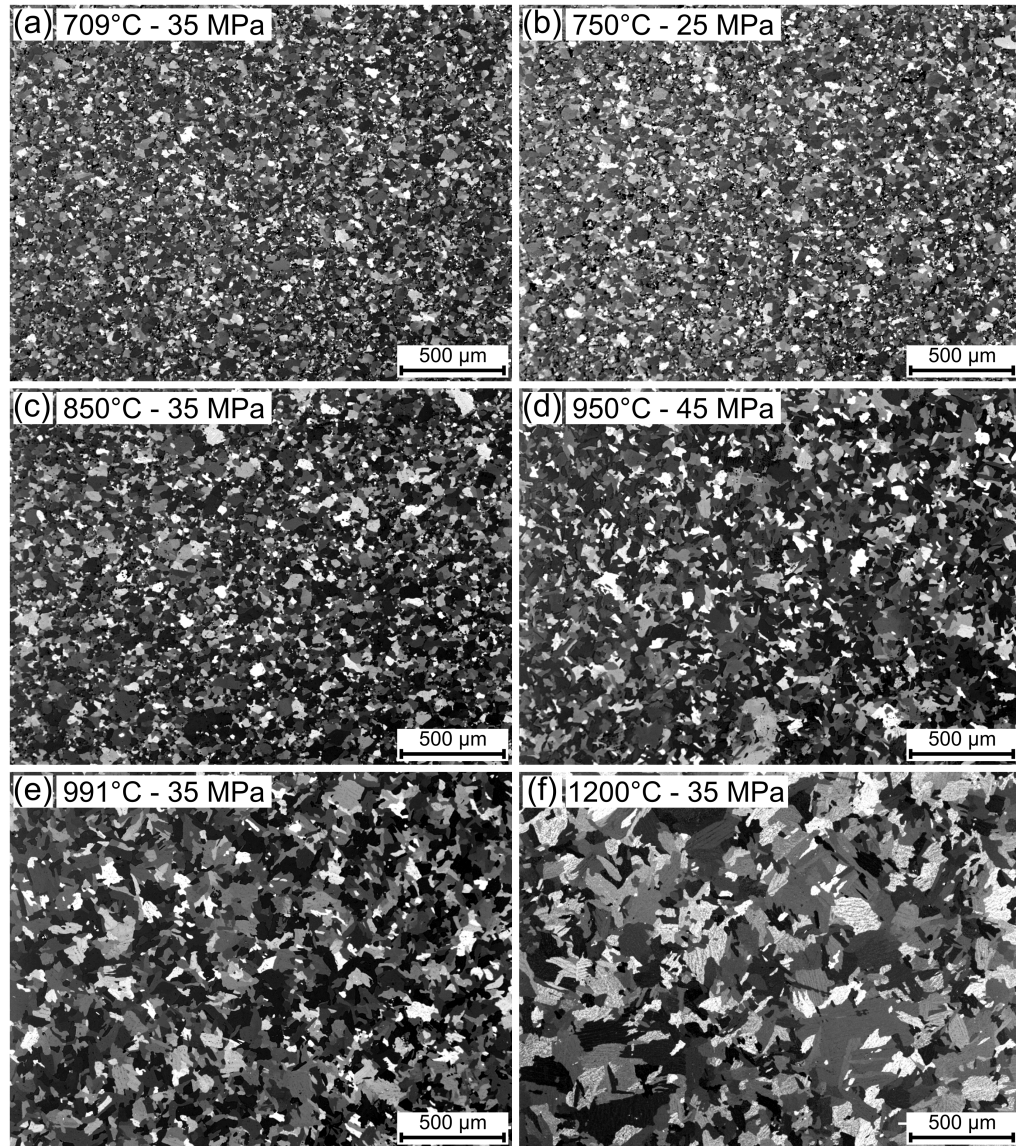


Figure 4.9 – Cross-polarised light micrographs of HDH CP-Ti powder showing the change in microstructure with increased dwell temperature and/or dwell pressure during constant heating rate and dwell time FAST processing.

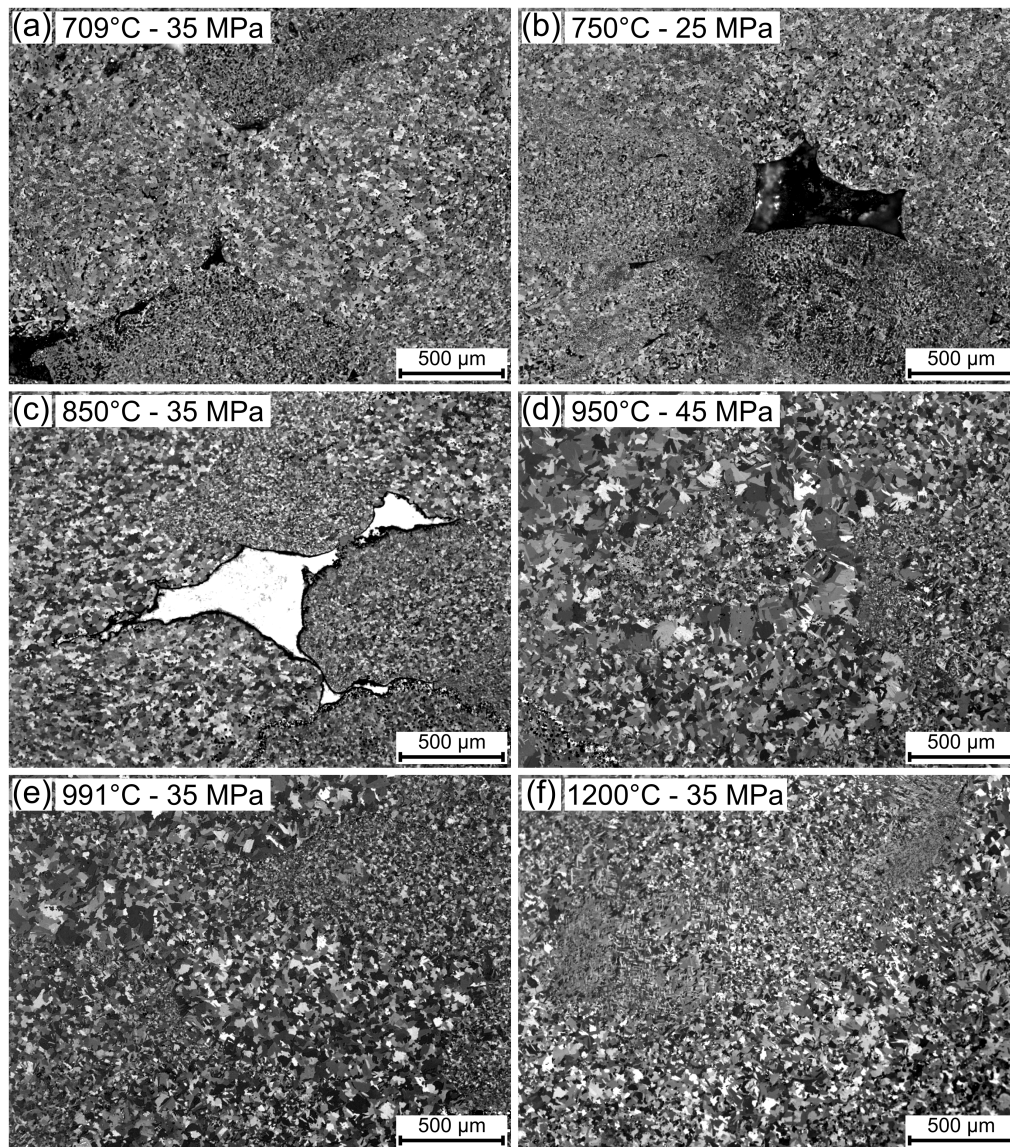


Figure 4.10 – Cross-polarised light micrographs of spherical-spongy pigment-derived Metalysis powder showing the change in microstructure with increased dwell temperature and/or dwell pressure during constant heating rate and dwell time FAST processing.

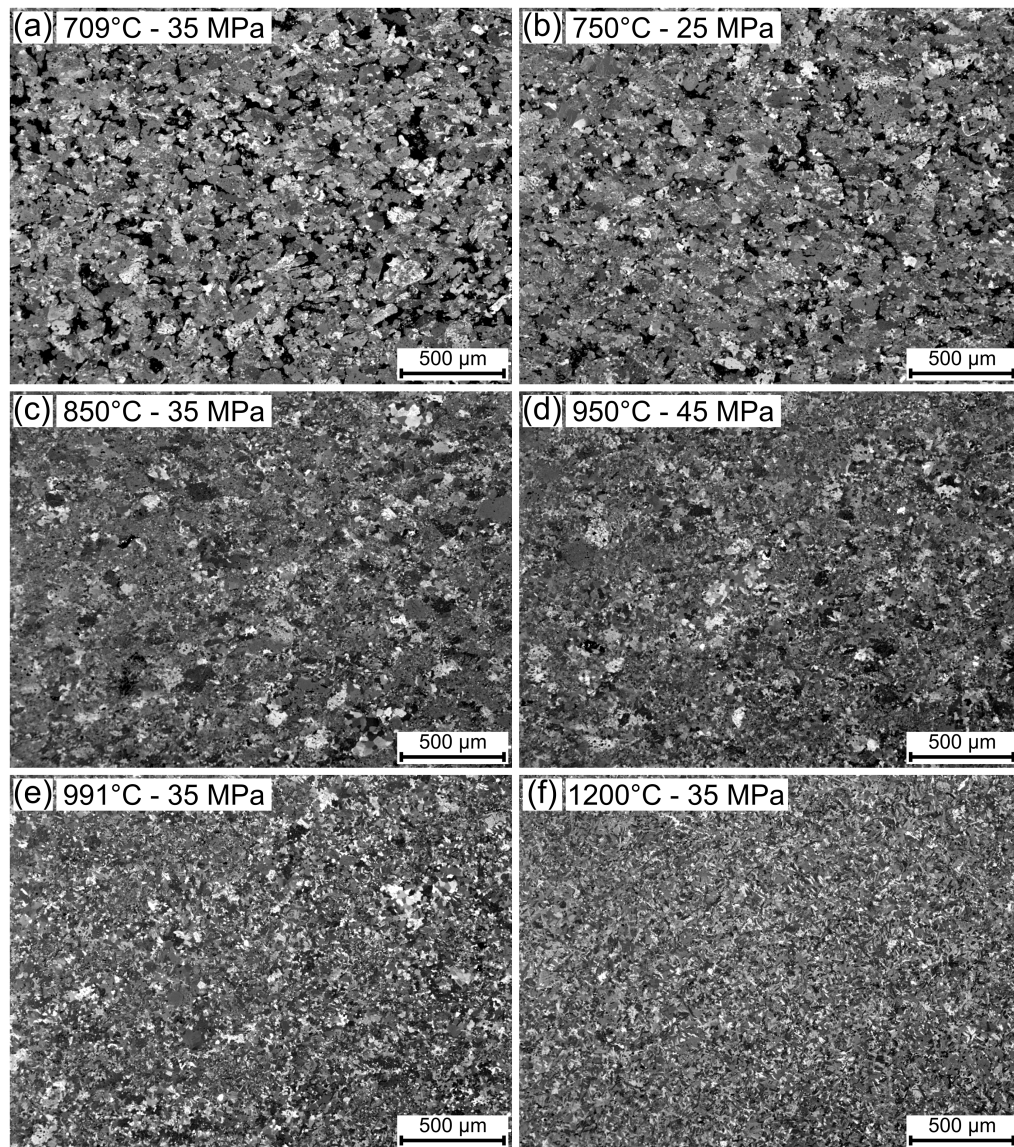


Figure 4.11 – Cross-polarised light micrographs of angular-spongy rutile-derived Metalysis powder showing the change in microstructure with increased dwell temperature and/or dwell pressure during constant heating rate and dwell time FAST processing.

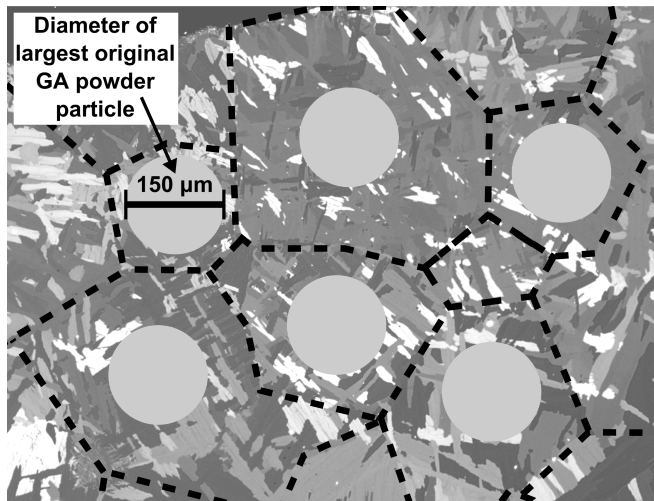


Figure 4.12 – Cross-polarised light micrograph of GA CP-Ti processed via FAST at 1200°C-35 MPa, with a heating rate of 25°Cmin⁻¹ and dwell time of 10 min. The efficacy of FAST as a powder consolidation technique is demonstrated when comparing the diameter of the largest starting GA powder particles to the approximate outlines of a selection of prior β grain boundaries.

At 950°C-45 MPa (part (d)) for the GA and HDH CP-Ti there is a clear change in behaviour, which is then continued at 991°C-35 MPa (part (e)) and 1200°C-35 MPa (part (f)). It appears the density reaches a point where the remaining porosity is no longer pinning grain boundary migration so there can be a rapid increase in prior β grain size. Additionally, as the β transus temperature for CP-Ti of 912°C [1] has been exceeded, the material has fully transformed to β phase, which allows increased atomic diffusion and therefore grain growth. This is most clearly demonstrated by the GA CP-Ti with a sudden change in observed prior β grain size, whereas there is a smoother transition shown by the HDH CP-Ti, which also retains a slightly smaller grain size throughout. This behaviour is clearly shown in Fig. 4.12, where it can be seen that the prior β grain size has increased beyond the largest starting GA powder particle diameter; this demonstrates the potential efficacy of FAST as a powder consolidation technique. The microstructure suggests the material should not behave like a traditional sintered powder component as there has been full diffusion bonding between particles and even grain growth beyond their original dimensions. In essence the billet will now behave like a wrought product with no evidence of original powder characteristics.

The spongy-spherical pigment-derived alloy still shows a very heterogeneous microstructure after processing at 1200°C. This continues to suggest that the

combination of the heterogeneous distribution of porosity and chemistry is responsible. At 1200°C there are areas that have a transformed β structure, whilst some areas continue to exhibit growth of primary α . The natural impurities that are found in the pigment-derived alloy, see Table 3.1, mean it behaves more like an $\alpha + \beta$ alloy as opposed to a pure CP-Ti α alloy. The larger length-scales involved in this morphology also prevent complete homogenisation by diffusional processes. This can be seen in the micrographs where the areas of dissimilar microstructure correlate well with the starting particle dimensions.

The angular-spongy rutile-derived powder exhibits a similar behaviour, in that pockets of grain growth give a heterogeneous microstructure at temperatures up to 991°C. However, at 1200°C there appears to have been full homogenisation and refinement of the grain structure. Again this implies that chemistry as well as porosity is responsible for the microstructural changes observed. The chemical composition of the rutile-derived alloy, which contains small amounts of elements naturally found in the rutile ore, suggests it may behave more like an $\alpha + \beta$ alloy (such as Ti-6Al-4V). Additionally, there will be some natural variation from particle to particle. At 991°C the alloy will contain areas that are primary α , which will undergo grain growth, and areas with higher quantities of β stabilising elements that will locally be above the β transus and thus form a transformed β structure upon cooling. The micrographs imply that between 991°C and 1200°C the rutile-derived material has fully undergone the α to β phase transformation allowing β grain growth and some chemical homogenisation through diffusion processes, meaning the micrograph in part (f) of Fig. 4.11 shows a fully transformed β structure.

The larger variation in grain size experienced by the HDH powder at lower temperatures could be explained by the greater random packing of the angular particles. There will be areas with higher initial particle-to-particle contacts and less porosity that will initially undergo more rapid densification than areas with less particle interactions and larger pores. This initial densification will be by plastic flow and, due to the lower packing density and angular point contacts amplifying the applied load, the HDH will have areas of higher deformation. These highly deformed areas have the potential to recrystallize finer grains, which can be seen around the coarser grains in the micrographs of Fig. 4.9. This initial grain refinement due to higher levels of plastic deformation may explain why the HDH appears to retain a smaller prior β grain size compared to the GA CP-Ti.

4.3.1.3 Effect of Dwell Temperature and Dwell Pressure on Rheology

A selection of the data recorded by the FAST machine and converted into level and speed of consolidation during the processing runs is presented in Fig. 4.13.

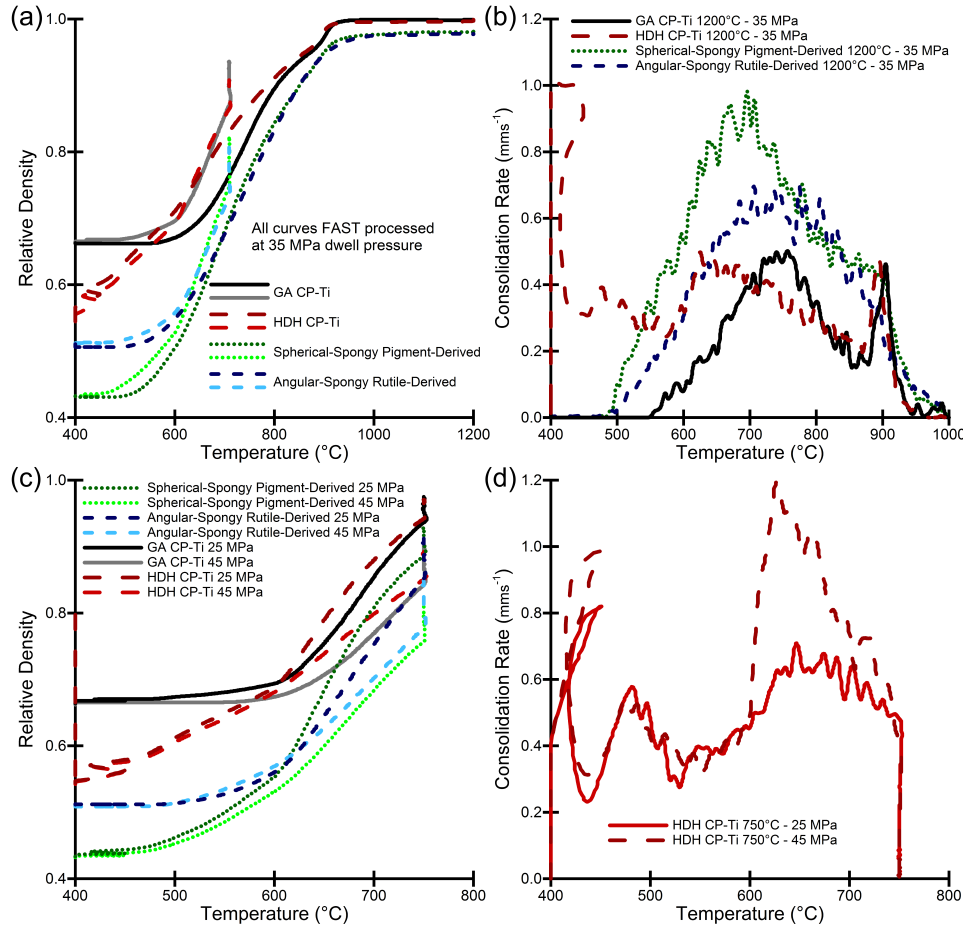


Figure 4.13 – Effect of dwell temperature and dwell pressure on rheology curves calculated from FAST machine output data for GA CP-Ti, HDH CP-Ti, spherical-spongy pigment-derived, and angular-spongy rutile-derived alloy powders. A heating rate of $25^{\circ}\text{Cmin}^{-1}$ and a 10 min dwell time were used for all curves. (a) Change in relative density with dwell temperature increase from 709°C to 1200°C and 35 MPa dwell pressure. (b) Consolidation rates corresponding to the 1200°C curves in part (a). (c) Change in density with dwell pressure increase from 25 MPa to 45 MPa at 750°C dwell temperature. (d) Consolidation rates for HDH CP-Ti corresponding to the curves in part (c).

Fig. 4.13a shows the difference in consolidation behaviour when processing at a dwell temperature of 709°C or 1200°C for all four materials, whilst all other parameters are kept constant. At a dwell temperature of 709°C none of the alloys have reached full density and continue to compact during the dwell period. At a dwell temperature of 1200°C the GA and HDH CP-Ti reach full density by

1000°C and no further compaction occurs during the dwell period. The Metalysis alloys behave similarly except that they only reach ~98 % density and this increases very slightly during the dwell period. The differences in consolidation behaviour are also clearly visible in Fig. 4.13b where the speed of consolidation is plotted against temperature when processing at 1200°C. The HDH CP-Ti begins compacting first in the processing cycle with an initial spike followed by an approximately constant rate of consolidation, which then increases rapidly when additional load is applied at 600°C. The rate then gradually decreases before spiking again at 890°C and then rapidly decreasing to zero at 1000°C. The GA CP-Ti does not begin to consolidate until a temperature of 550°C is reached. Its consolidation rate then linearly increases until reaching a short period of constant consolidation between 700 and 750°C and then gradually decreases until a similar spike to the HDH is seen at 890°C. The Metalysis powders begin to consolidate at ~500°C. The pigment-derived alloy shows a linearly increasing consolidation rate up to 700°C followed by a linearly decreasing rate until 890°C where the rate stabilises for approximately 20°C, before decreasing to zero at 1000°C. The rutile-derived alloy also shows a linearly increasing consolidation rate up to 700°C and then stabilises until 800°C before linearly decreasing to zero at 1000°C; there is no noticeable change in rate around 900°C like the other three alloys.

Fig. 4.13c shows that using an increased dwell pressure (increased from 25 to 45 MPa in this example) at a dwell temperature of 750°C, where full consolidation is not reached, allows each alloy to consolidate more when other parameters are kept constant. The curves clearly diverge after 600°C. This is due to the specific sintering cycle used in this study where the initial 5 kN load is held constant until a temperature of 600°C is attained; this attempts to reduce stress on the dies as graphite's mechanical properties generally increase with temperature. After 600°C the load, and therefore pressure, is increased at a rate to simultaneously achieve maximum coincidentally with the temperature. Thus, when increased dwell pressure is used at a fixed dwell temperature the rate of load increase is necessarily greater. This is further illustrated in Fig. 4.13d for the HDH CP-Ti where the consolidation rate increases more rapidly post-600°C when a higher dwell pressure is used. The more rapid increase in pressure after 600°C when using higher dwell pressures increases the rate of plastic deformation of particles which manifests as a faster consolidation rate. Lower dwell pressures can still achieve full consolidation so long as the corresponding dwell temperature

is high enough such that the flow stress of the material is below the applied pressure.

The consolidation behaviour of the HDH and GA CP-Ti, which have almost identical chemistries and differ only in their particle size and morphology, is interesting. The more irregularly shaped HDH powder has a slightly wider size distribution. As previously discussed it processes to a smaller grain size at all tested conditions, and a slight reduction in density at conditions that do not produce full consolidation. It was thought the reason for this could be the reduced packing density of the angular HDH powder; 54 % compared to 65 % for the spherical GA powder. However, this difference is quickly eradicated in the initial stages of the process, see Fig. 4.13a and Fig. 4.13c. The HDH powder undergoes a significant amount of compaction before 600°C when the load is constant at 5 kN, increasing to ~65-70 % density, whereas during this initial part of the cycle the GA powder is stable at its 65 % starting density. It is thought this is due to the effective stress being increased due to the point nature of the HDH particle contacts acting to concentrate the applied stress more than the circular GA particle contacts; the reduced number of contacts due to the initially lower packing density also aids this. This amplification of applied load allows earlier consolidation by plastic flow as the yield stress is exceeded. The GA morphology seems to consolidate more during the dwell period than the HDH for conditions that do not achieve >99 % density. Plastic flow is clearly more effective for consolidating HDH powder earlier in the cycle, but after the particle contacts become large enough that the effective stress falls below the flow stress, diffusion mechanisms are more effective in the final removal of porosity with the GA morphology. The exact mechanisms acting are unclear. Different chemistries make it difficult to directly compare the Metalysis alloys to CP-Ti, although their behaviour fits between that described for the HDH and GA powders. They both densify less when using equivalent processing conditions, possibly due to the spongy nature of the particles meaning internal porosity is retained. They begin initial densification at 500°C, which is later than the HDH but earlier than the GA. The intermediate morphology (more angular than GA but less than HDH) is likely responsible for this through a similar mechanism as discussed for the HDH; the porous and/or angular particles amplifying applied load.

Another interesting feature to note in Fig. 4.13a and Fig. 4.13b is the obvious increase in consolidation rate for the GA and HDH CP-Ti, and to a lesser

extent the pigment-derived alloy, beginning at $\sim 890^{\circ}\text{C}$ and peaking at $\sim 910^{\circ}\text{C}$. A possible explanation for this is that when titanium alloys undergo the α to β phase transformation there is a large increase in diffusivity; self-diffusion of titanium in the β phase is approximately three orders of magnitude higher than in the α phase [1]. The start temperature is approximately 20°C lower than the expected β transus of 912°C , although the transformation is not instantaneous and uncertainties in the temperature measurement could also explain this discrepancy. The powders are $\sim 95\%$ dense at this point, where diffusional sintering mechanisms become dominant. The increased consolidation rate seen is therefore very likely to be caused by the material going above the β transus temperature, which allows increased rates of diffusion and thus sintering. There is no obvious change in densification rate for the rutile-derived alloy, which indicates a β transus temperature that occurs after a high density has already been achieved. As discussed in the microstructure section 4.3.1.2 the alloying elements, or higher than desirable interstitial levels, could cause this.

4.3.2 Dwell Time and Heating Rate Parametric Study

4.3.2.1 Effect of Dwell Time and Heating Rate on Density

The effect of dwell time or heating rate on porosity was expected to be minimal for the sintering conditions selected in this study as almost full density should be achieved, which can be seen in Figs. 4.14-4.17. The dwell temperature and dwell pressure used produced $>99\%$ density at all heating rates even at the shortest dwell time. However, if it had not been possible to utilise temperatures and pressures to achieve full density it should be noted that increasing the dwell period would allow further densification to occur, as was seen in the consolidation curves in Fig. 4.13a.

4.3.2.2 Effect of Dwell Time and Heating Rate on Microstructure

The microstructures produced in the specimens during the heating rate and dwell study are shown in Fig. 4.14 for HDH CP-Ti, Fig. 4.15 for HDH Ti-6-4, Fig. 4.16 for PS rutile-derived alloy, and Fig. 4.17 for GA Ti-5553. The HDH CP-Ti shows an increase in prior β grain size and α lath colony size when the heating rate was increased from 25 to $100^{\circ}\text{Cmin}^{-1}$. There is minimal qualitative difference in prior β grain size between a dwell time of 10 and 30 min at either heating rate. The HDH Ti-6-4 also shows little discernible difference in grain size or morphology when the dwell time is increased from 10 to 30 min, but does again show increased prior β grain size when the heating rate is increased

from 25 to 100°Cmin⁻¹. Conversely, the PS rutile-derived alloy shows little qualitative difference in microstructure when the heating rate is varied from 50 to 200°Cmin⁻¹, but there is a small increase in prior β grain size when the dwell time is further increased from 10 to 60 min. The GA Ti-5553 matches the behaviour of the PS rutile-derived alloy; virtually no increase in β grain size when heating rate is increased from 25 to 100°Cmin⁻¹, and a small amount of β grain growth with an increase in dwell time from 10 to 30 min. The microstructural changes apparent with a constant dwell temperature and dwell pressure but different heating rates and dwell times correlate more to particle morphology than alloy chemistry. The angular HDH powders saw an increase in prior β grain size with higher heating rates, but the spherical powders saw no discernible difference. The two morphologies again showed opposite effects when an increased dwell time caused grain growth for the spherical powders but not for the angular powders.

It initially appears counter-intuitive that increased heating rate could cause an increased grain size when using angular powder, as the specimen will actually spend a decreased time above room temperature; ~ 25 min compared to ~ 60 min. However, it is thought the higher heating rates allow traditional sintering mechanisms to be bypassed. The higher the heating rate the more quickly the particles reach the point where the applied load exceeds the materials' flow strength and allows consolidation through plastic deformation. Rapid rearrangement and plastic deformation allows for removal of the inter-particle voids early in the cycle and thus allows grain growth as there is less porosity pinning grain boundary migration. At lower-heating rates there is more time for the particles to undergo diffusional bonding processes and produce necks between particles that can support some of the load and reduce plastic deformation. The removal of porosity is therefore slower and its presence retards grain growth. As discussed the angular point nature of the HDH particle contacts amplifies the applied load more than for spherical particles, meaning the heating rate effect is more dominant for that morphology. It is unclear why the spherical particles appear to undergo more grain growth during the dwell period. It was shown that HDH CP-Ti retained a slightly smaller prior β grain size compared to GA CP-Ti at equivalent conditions, possibly due to higher deformation initiating recrystallisation, which may also be playing a role in impeding further growth. It should also be noted that with the increased dwell times used it was expected more grain growth would be seen than was actually seen for any of the materials.

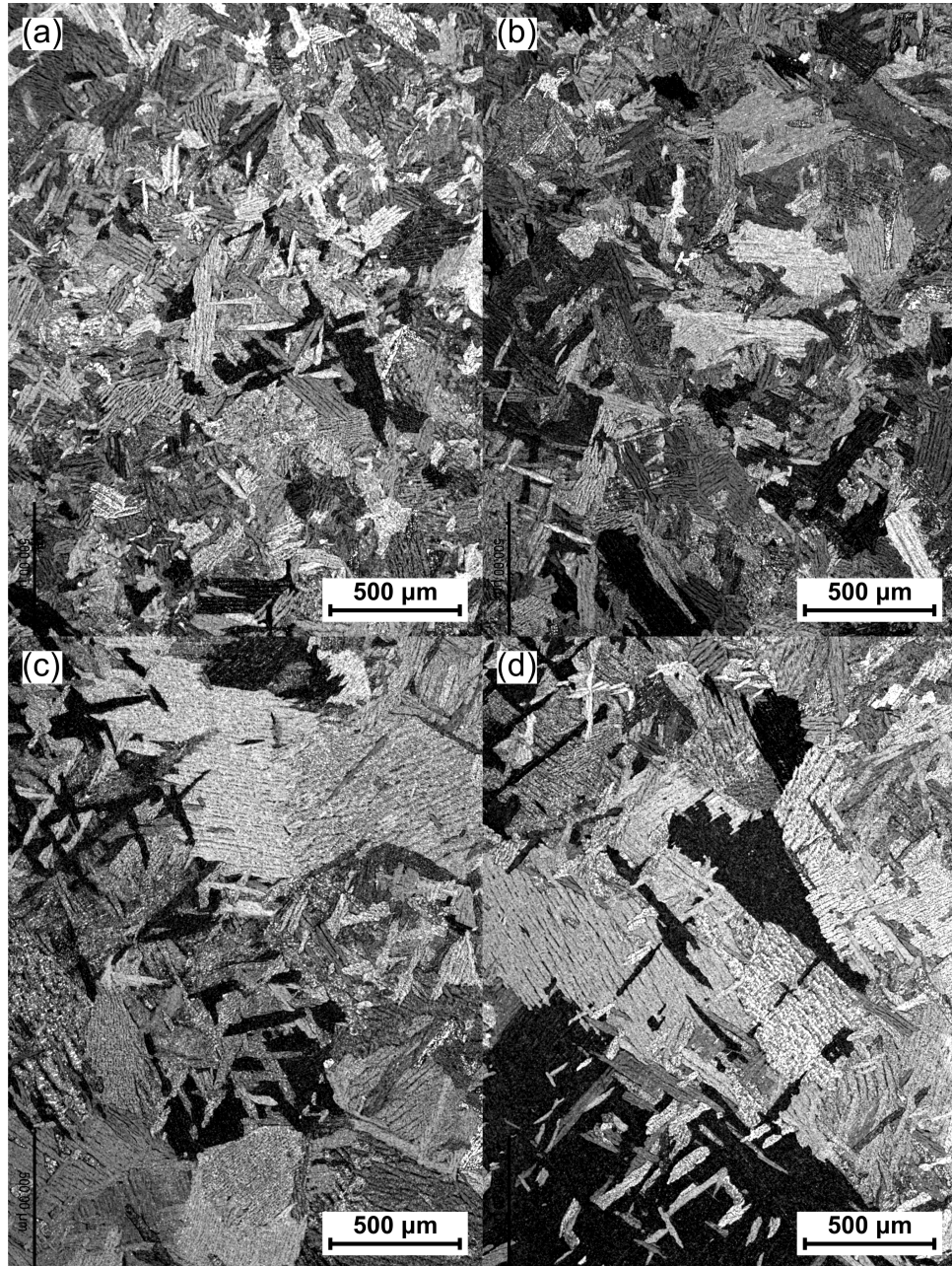


Figure 4.14 – Light micrographs showing microstructural development of CP-Ti HDH powder during FAST processing at 1200 °C-22 MPa, with varying heating rate and dwell time: (a) 25 °Cmin⁻¹ and 10 min, (b) 25 °Cmin⁻¹ and 30 min, (c) 100 °Cmin⁻¹ and 10 min, (d) 100 °Cmin⁻¹ and 30 min

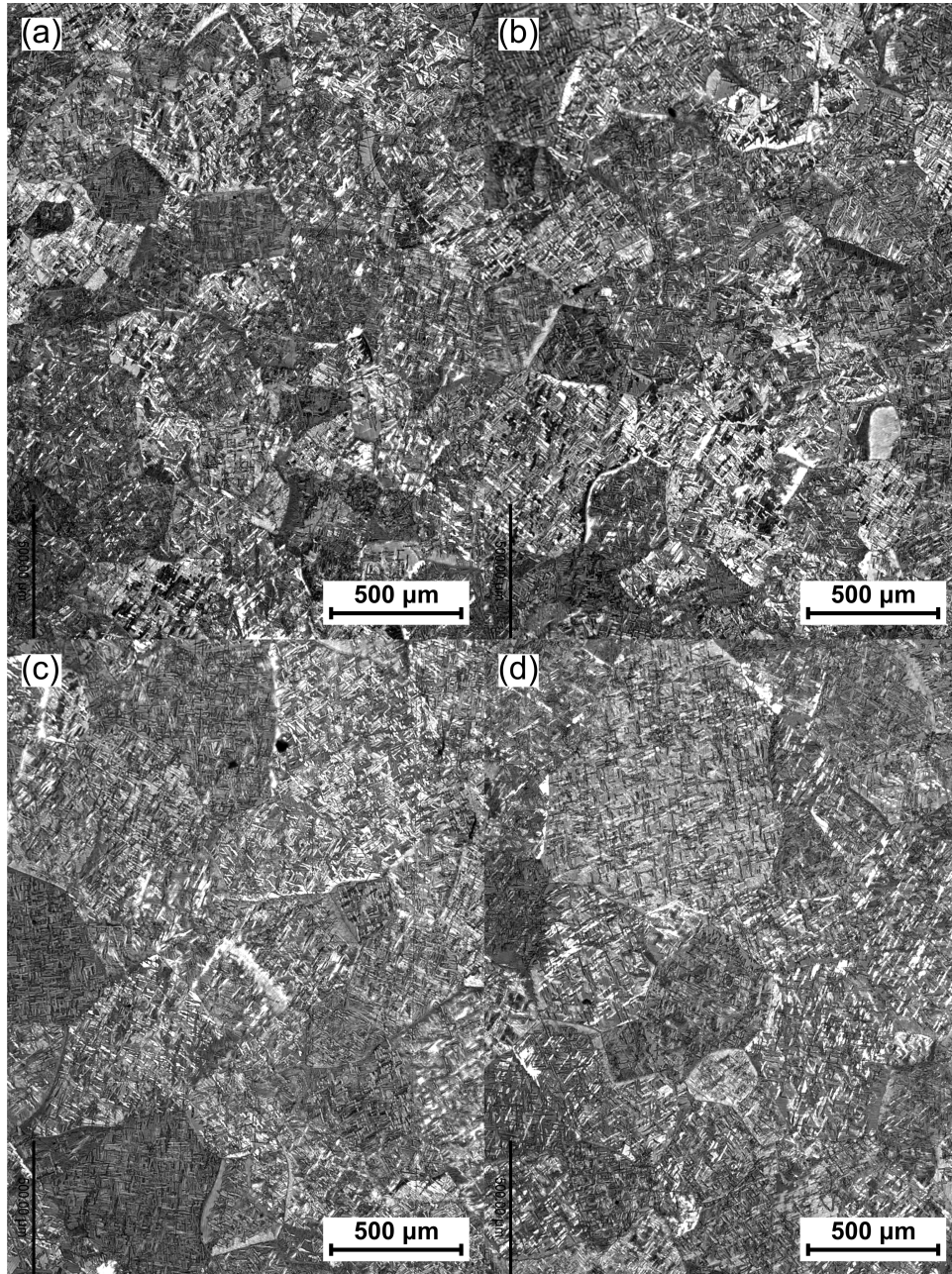


Figure 4.15 – Light micrographs showing microstructural development of Ti-6Al-4V HDH powder during FAST processing at 1200 °C-22 MPa, with varying heating rate and dwell time: (a) 25 °Cmin⁻¹ and 10 min, (b) 25 °Cmin⁻¹ and 30 min, (c) 100 °Cmin⁻¹ and 10 min, (d) 100 °Cmin⁻¹ and 30 min

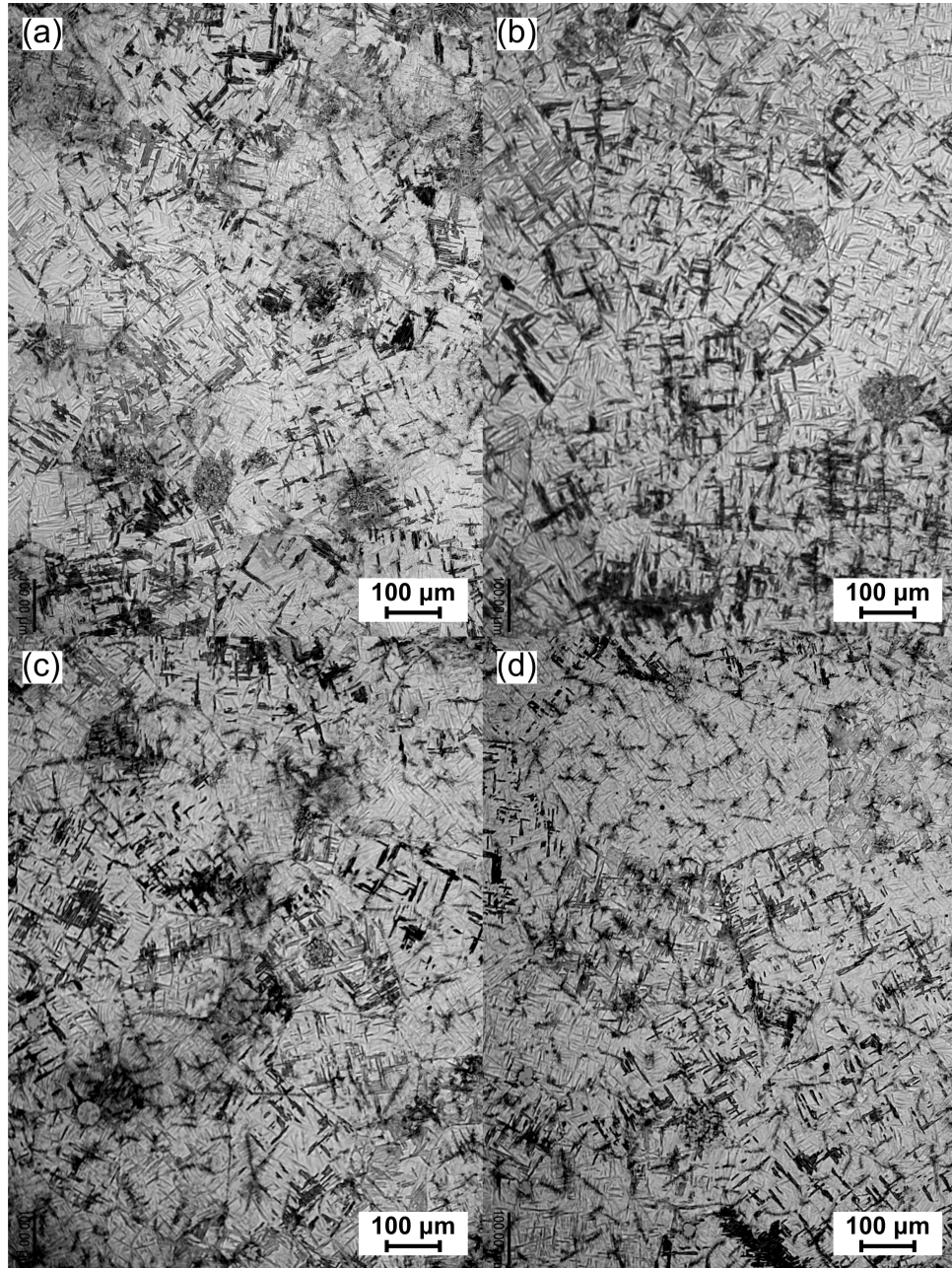


Figure 4.16 – Light micrographs showing microstructural development of PS rutile-derived powder during FAST processing at 1200 °C-22 MPa, with varying heating rate and dwell time: (a) 50 °Cmin⁻¹ and 10 min, (b) 50 °Cmin⁻¹ and 60 min, (c) 200 °Cmin⁻¹ and 10 min, (d) 200 °Cmin⁻¹ and 60 min

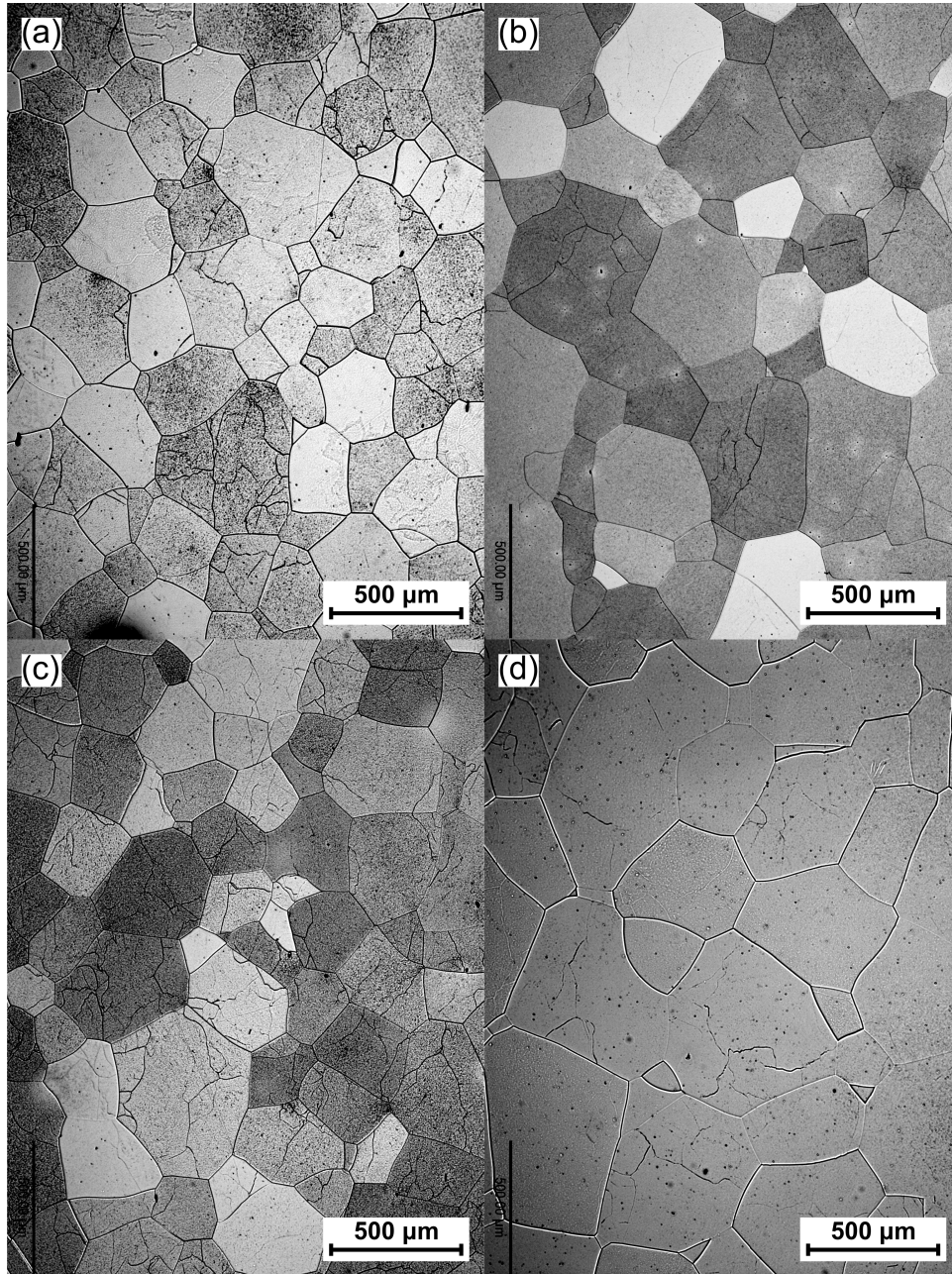


Figure 4.17 – Light micrographs showing microstructural development of Ti-5553 GA powder during FAST processing at 1200 °C-22 MPa, with varying heating rate and dwell time: (a) 25 °Cmin⁻¹ and 10 min, (b) 25 °Cmin⁻¹ and 30 min, (c) 100 °Cmin⁻¹ and 10 min, (d) 100 °Cmin⁻¹ and 30 min

4.3.2.3 Effect of Dwell Time and Heating Rate on Rheology

When the heating rate is increased the relative density of the HDH Ti-6-4, HDH CP-Ti, GA Ti-5553, and PS rutile-derived alloy powders appears to be less at a given temperature during the cycle, see part (a), (d), (g), and (j) of Fig. 4.18. This increased density may be explained by the location of the temperature measurement. The majority of the Joule heating occurs in the graphite as its resistivity is higher than titanium's resistivity. Temperature is measured from the inside of the top graphite piston and at higher heating rates it is possible the temperature of the graphite may be significantly different to the powder compact. These thermal gradients would mean actual powder temperature is lower than the recorded temperature and would cause a shift in the consolidation curve to the right of the graphs. However, if the relative density caused by different heating rates is instead plotted against time, see part (b), (e), (h), and (k) of Fig. 4.18, then there are clearly much higher rates of consolidation at higher heating rates. This may add the factor of viscoplastic effects into the behaviour seen in part (a), (d), (g), and (j) of Fig. 4.18. The applied load is increased more rapidly when a higher heating rate is used, as dwell temperature and pressure achieve maximum values simultaneously, so the strain rate seen by the particles is higher. It is more difficult to deform material at higher strain rates and therefore the flow stress that needs to be exceeded at equivalent temperatures will be greater with a higher heating rate, which could result in a reduced density. The lag in relative density at equivalent temperature is mirrored when studying the consolidation rate versus temperature. There is a small shift to higher temperatures for the maximum rate of consolidation, see the peaks in part (c), (f), (i), and (l) of Fig. 4.18, which is again likely a result of temperature gradients and/or viscoplastic effects. Apart from this small lag the increased heating rate does not seem to affect the consolidation behaviour for any of the alloys; the shapes of the curves are similar and full density is reached at a slightly higher recorded temperature (but in a significantly quicker time). The spherical morphologies show similar consolidation behaviour with the rate exponentially increasing to a peak before exponentially decreasing back to zero. The HDH Ti-6-4 increases linearly before exponentially decreasing to zero. The HDH CP-Ti shows different behaviour with an initial spike followed by an increase to a first peak value then gradually decreasing consolidation; as discussed previously there is then a spike due to exceeding the β transus temperature but this is a feature of chemistry not morphology.

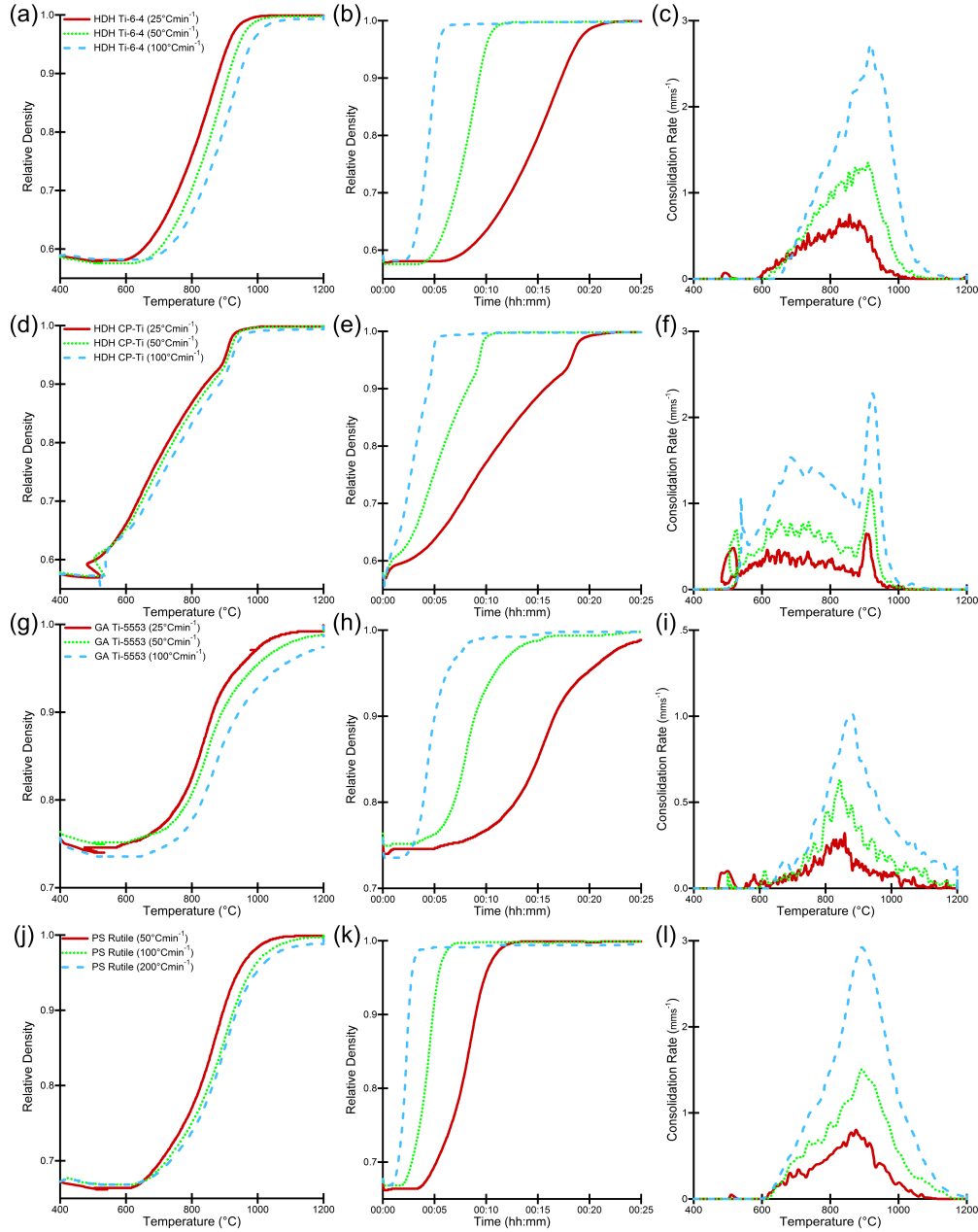


Figure 4.18 – Effect of heating rate on rheology curves calculated from FAST machine output data. Dwell temperature and pressure were kept constant at 1200°C and 22 MPa for all curves. Change in density versus temperature when increasing heating rate (as labelled) for HDH Ti-6Al-4V (a), HDH CP-Ti (d), GA Ti-5553 (g), PS rutile-derived (j). Change in density versus time for increasing heating rate (as labelled) for HDH Ti-6Al-4V (b), HDH CP-Ti (e), GA Ti-5553 (h), PS rutile-derived (k). Variation in consolidation rate for increasing heating rate (as labelled) for HDH Ti-6Al-4V (c), HDH CP-Ti (f), GA Ti-5553 (i), PS rutile-derived (l).

4.3.3 Effect of Alloy Chemistry and Powder Morphology on Rheology

The effect of powder chemistry and morphology on consolidation is further compared in Fig. 4.19. Similar patterns are seen as were discussed in section 4.3.1.3 with regards to angular compared to spherical morphology. Alloy chemistry also plays an important role in changing consolidation behaviour as can be seen in Fig. 4.19a when a 20 mm HDH Ti-6-4 specimen is less dense than a 20 mm HDH CP-Ti specimen at a given temperature when all other conditions are equal. This is also true when the specimen diameter is increased to 80 mm and additionally for the spherical GA morphology, shown in Fig. 4.19b. Similarly the GA Ti-5553 chemistry has the highest starting density but is then the last to reach full density during sintering. The rutile-derived alloy chemistry behaves intermediately between the CP-Ti and Ti-6-4.

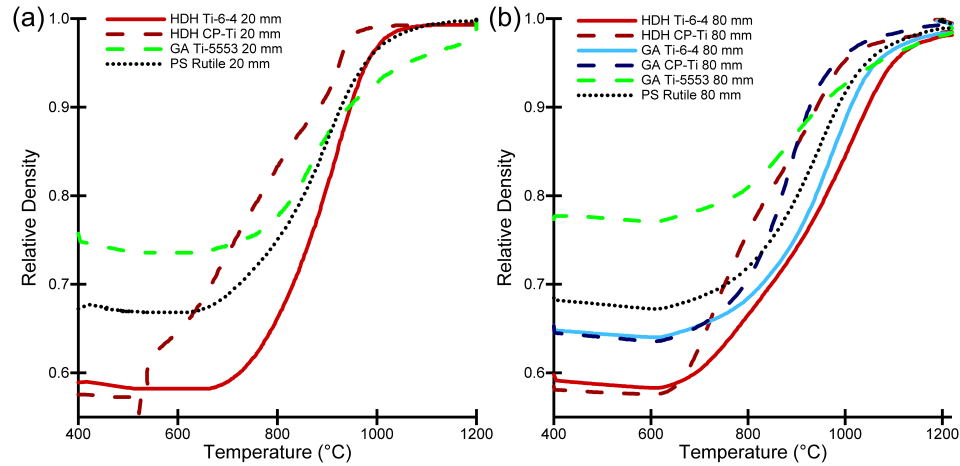


Figure 4.19 – Effect of alloy chemistry and powder morphology on rheology curves when dwell temperature and dwell pressure were kept constant at 1200°C and 22 MPa . (a) Change in density versus temperature for 20 mm specimens of the labelled powders with a heating rate of $100^{\circ}\text{Cmin}^{-1}$. (b) Change in density versus temperature for 80 mm specimens of the labelled powders with a heating rate of $200^{\circ}\text{Cmin}^{-1}$.

The increased flow strength of the Ti-6-4 and Ti-5553 at elevated temperature, compared to CP-Ti, is thought to prevent the same level of particle deformation by plastic flow occurring when equivalent loads are applied and therefore retards consolidation until higher temperatures are attained. The increase in consolidation rate when the β transus temperature was reached with the CP-Ti in the dwell temperature and pressure study is not seen with Ti-6-4 chemistry in this study. The increased β transus temperature of Ti-6-4 means that very

high consolidation has already been achieved by the time this temperature has been reached. The β transus temperature effect on consolidation rate is also not seen for the Ti-5553 alloy even though it has the lowest transus temperature of the three. This could be due to the rapid densification by plastic flow already occurring making any potential increase in diffusion negligible in comparison.

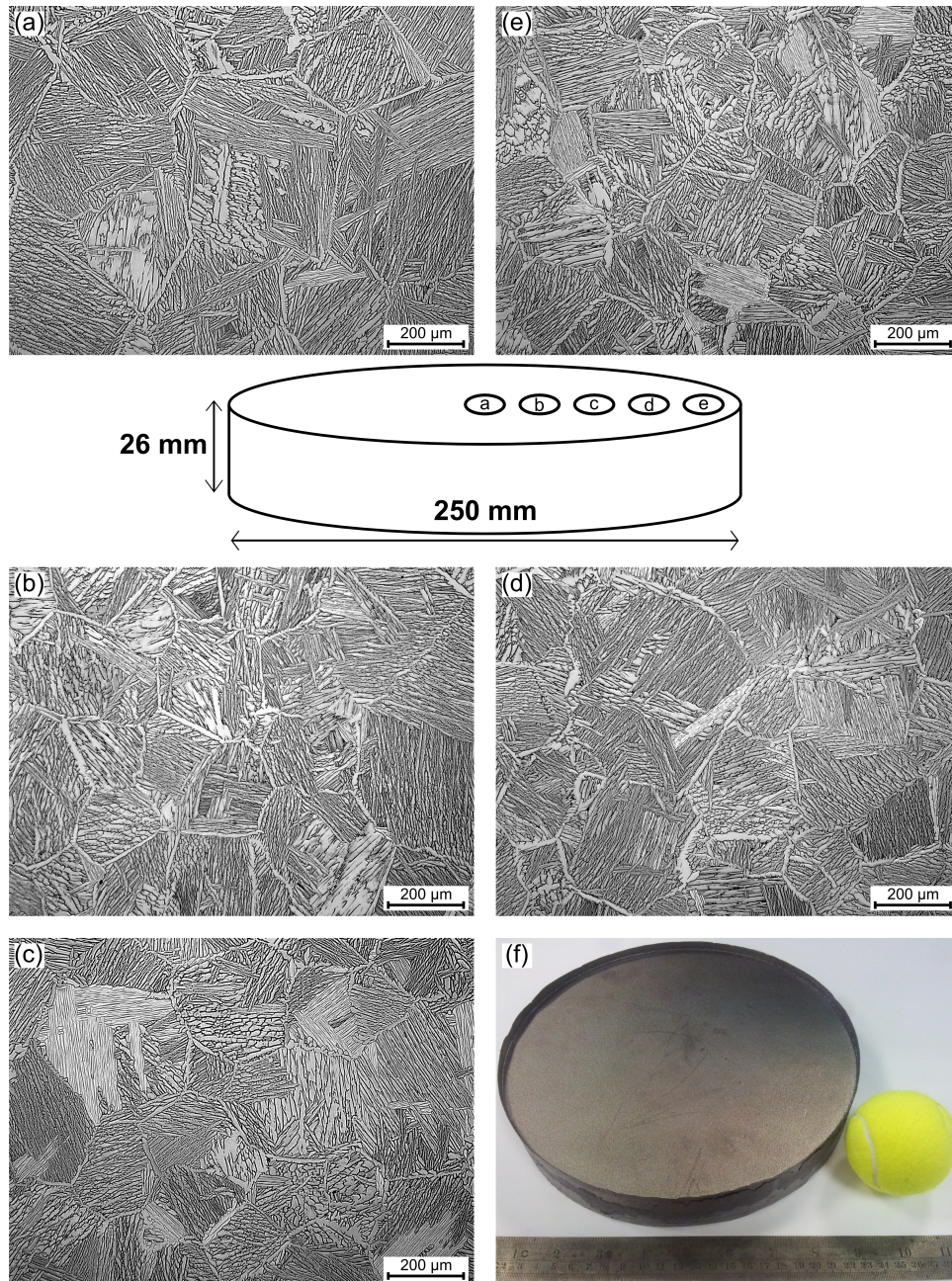


Figure 4.20 – Bright-field light micrographs showing microstructures etched with Kroll's reagent from the centre (a) to the edge (e) of a 5.5 kg 250 mm diameter GA Ti-6-4 FAST disc produced at Kennametal Manufacturing (UK) Ltd. Photograph of the 250 mm diameter FAST disc with tennis ball for scale (f).

4.3.4 Effect of Mould Size on FAST Processing

The microstructures produced across the radius of a 250 mm diameter FAST disc produced in the large-scale FAST furnace at Kennametal Manufacturing (UK) Ltd can be seen in Fig. 4.20. The microstructure is comparable in terms of prior β grain size, α lath colony size, α lath thickness, and grain boundary α from the centre (Fig. 4.20a) to the edge (Fig. 4.20e). The microstructure is also very similar to that produced in 20 mm moulds under equivalent processing conditions. The calculated density from image analysis of bright-field micrographs was also constant at 99.99 % across the disc. This suggests that if any thermal and/or pressure gradients, or current flow inhomogeneity, do exist within larger samples that they do not impact upon density or microstructure at this scale, or that sufficiently high temperature was used to allow homogenisation during the dwell period.

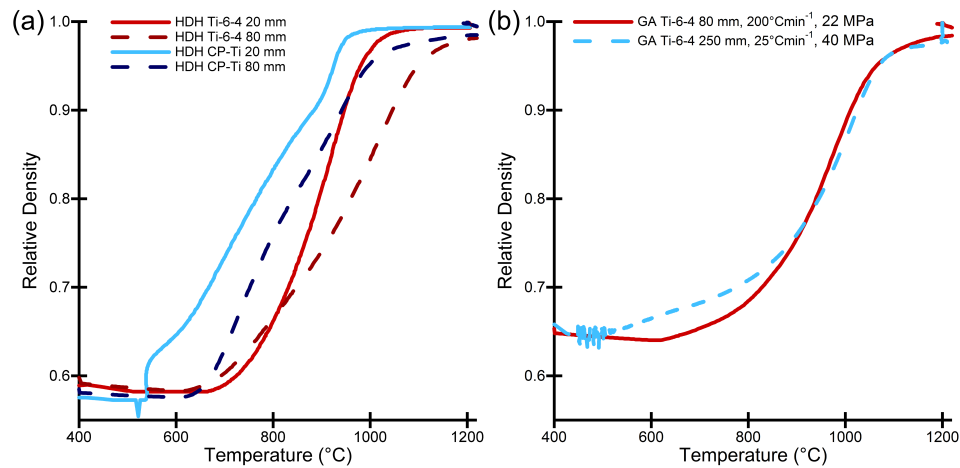


Figure 4.21 – Effect of mould size on rheology curves. A dwell temperature of 1200°C, dwell pressure of 22 MPa, and heating rate of 100°Cmin⁻¹ were used unless otherwise labelled. (a) Change in relative density versus temperature for 20 mm and 80 mm specimens of HDH Ti-6-4 and HDH CP-Ti. (b) Change in relative density versus temperature for an 80 mm specimen compared to a 250 mm specimen of GA Ti-6-4.

The consolidation curves produced from the FAST machine data show that there is a significant lag in consolidation at a given temperature when the mould size is increased from 20 mm to 80 mm for both HDH CP-Ti and HDH Ti-6-4, see Fig. 4.21a. This may be explained through the additional mass of powder required; as the mould diameter doubles the mass of powder needed to achieve the same thickness quadruples. In this case there was an increase from 10 g to 300 g. This extra quantity of powder could exacerbate the potential problems

already discussed with regard to measured temperature values compared to actual powder values. This lag in consolidation is overcome, or almost so, by the time the dwell temperature is reached. The increased thermal mass of the 80 mm samples means there is usually an overshoot of dwell temperature before control is regained, and by this time the same density is achieved as for the 20 mm moulds. For the largest 250 mm diameter mould used in this work with GA Ti-6-4 powder this was not the case and densification continued during the dwell period, which is seen as a vertical line in Fig. 4.21b. A slower heating rate of $25^{\circ}\text{Cmin}^{-1}$ and increased dwell pressure of 40 MPa were used for the 250 mm diameter mould and this allowed the consolidation curve to closely track the curve for the 80 mm mould when using $200^{\circ}\text{Cmin}^{-1}$ heating rate and dwell pressure of 22 MPa. This further demonstrates the previously observed and discussed competing effects of heating rate, dwell pressure, and mould size on the consolidation behaviour of titanium alloy powders during FAST processing.

4.3.5 Interstitial Pick-Up and Microhardness Values After FAST

The carbon, oxygen, and nitrogen content of the GA CP-Ti, GA Ti-6-4, and PS rutile-derived Metalysis powders were measured before and after 80 mm FAST processing with the levels shown in Table 4.2. The material was processed at 1200°C under 22 MPa pressure with a heating rate of $200^{\circ}\text{Cmin}^{-1}$ and a dwell time of 60 min. The interstitial levels reported for the PS rutile-derived alloy in this table differ from those in chapter 3. This is due to a small preliminary batch being provided for this initial study, with a larger batch provided for the work in chapter 5.

The unprocessed GA CP-Ti powder was within ASTM specification for interstitial content (800 ppm C, 2500 ppm O, 300 ppm N) as was the GA Ti-6-4 powder (800 ppm C, 2000 ppm O, 500 ppm N), but the Metalysis powder was outside of these limits. The average amount of carbon pick-up was 159 ppm, excluding the anomalous result of carbon level reducing for the rutile-derived alloy. The average oxygen pick-up was 132 ppm and the average nitrogen pick-up was 180 ppm. This allowed the commercial materials to stay within specification after FAST processing for carbon and oxygen content, but to raise the nitrogen level 12 % above specification for the CP-Ti. The Metalysis powder provided for this work was from developmental work and therefore has slightly elevated interstitial content, but still experienced minimal additional

pick-up during FAST processing. The oxygen and nitrogen pick-up are likely due to atmospheric contamination and could potentially be reduced further if a higher vacuum was used during processing. The carbon pick-up comes from the specimen contact with the graphite mould assembly.

Table 4.2 – *Interstitial element content pre- and post-FAST processing and Vickers Hardness values post-FAST.*

Material	Processing Step	Interstitial Level (ppm)			Vickers Hardness	ASTM Vickers
		Carbon	Oxygen	Nitrogen		
GA CP-Ti	Powder	34	1204	121	-	-
	Post-FAST	238	1440	336	168	~ 150
GA Ti-6-4	Powder	153	1487	252	-	-
	Post-FAST	266	1585	394	340	~ 350
PS rutile-derived	Powder	3830	3232	175	-	-
	Post-FAST	3463	3295	358	281	N/A

A defined region of increased α phase, stabilised due to carbon diffusion, was visible at the edges of the Ti-5553 specimens after etching with Kroll's reagent, see Fig. 4.22. This region was not observed in the other processed materials. The thickness of the layer was seen to increase with dwell time and its more noticeable presence in these specimens is probably due to the increased diffusion rate in the single phase β in this alloy. At a temperature of 1200°C with 22 MPa pressure and a heating rate of 25°Cmin⁻¹ the layer was ~550 μ m thick after a 10 min dwell, ~700 μ m thick after a 20 min dwell, and ~900 μ m thick after a 30 min dwell. The interstitial levels reported were measured in material taken from the centre of the specimens away from this diffusion zone, as it is likely this layer would be removed in subsequent processing steps as part of the cost-effective route; such as a finish machining step. Diffusion layers are common in sintering technologies for titanium powder, with an iron rich layer of contamination typically found when processing via HIP with mild-steel cans, which also has to be subsequently removed. Reducing carbon contamination may be possible by insulating the material from the mould but care would need to be taken that this barrier did not prevent the beneficial electric current from flowing through the specimen.

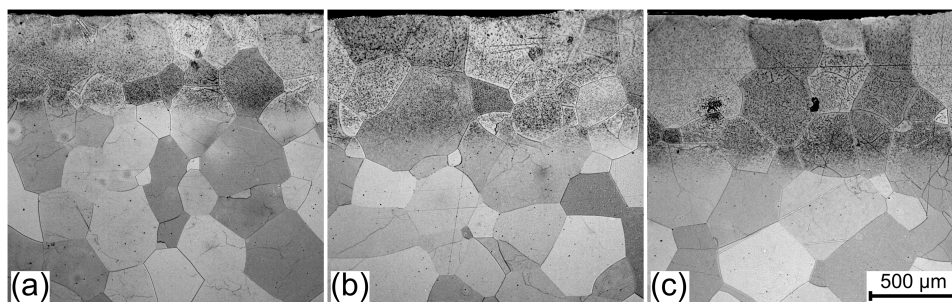


Figure 4.22 – Light micrographs showing a defined region of increased α phase at the surface in contact with the graphite mould due to carbon diffusion into Ti-5553 FAST specimens processed at 1200°C and etched with Kroll’s reagent, after a 10 min dwell (a), after a 20 min dwell (b), and after a 30 min dwell (c).

Table 4.2 also gives values of Vickers hardness for the materials after FAST consolidation. The commercial materials are very close to hardness values reported for conventionally processed titanium. The hardness of the Metalysis alloy lies between the CP-Ti and Ti-6-4 values, which would be expected due to the small amounts of additional elements found in its chemistry.

4.4 Conclusions

This chapter has demonstrated that the processing of titanium alloy feedstocks via FAST is a viable method for their consolidation. Furthermore, combining FAST with potentially lower-cost powders from alternative extraction methods could provide drastic cost reductions and contribute towards developing a disruptive technology. The FAST process is largely tolerant of input material and, with some tailoring of processing conditions, it is possible to achieve high levels of density and homogeneous microstructures for a variety of starting chemistries and morphologies.

The dwell temperature and dwell pressure are the most influential processing parameters when attempting to achieve full consolidation. The highest pressure that is practical should be used and the limiting factor found in this work was the strength of the graphite ring mould and graphite pistons. Higher dwell temperatures produced higher densities when other parameters were kept constant. This is due to increased plastic deformation of particles and enhanced sintering mechanisms when the temperature is increased, although this needs to be balanced against possible contamination of interstitial elements at extreme temperatures. Using dwell temperatures above the β transus temperature offers

an advantage due to the higher diffusion rates found in the β phase, but the disadvantage of high grain growth when full density is approached.

At the processing conditions used in this study increasing the heating rate did not alter the levels of consolidation achieved as all rates achieved full density. The main benefit of high heating rates is in reducing the total process cycle time. The slight downside to this is the apparent small increase in grain size, although this is probably acceptable from a cost-saving standpoint and could additionally be countered by reducing the dwell time; a further thermomechanical step would also allow refinement. The dwell period allows further densification to occur if the processing conditions have not achieved full consolidation previously; it appears this becomes more necessary for larger moulds and higher masses of powder. If high density has been achieved then the dwell period allows diffusional processes to continue and this manifests as grain growth. At the small-scale 20 mm diameter size used here increasing the dwell time from 10 to 60 min produced a small increase to the grain size.

Decreasing the feedstock size, or having a size distribution containing smaller particles, allows easier consolidation due to potential for increased packing density and smaller length-scales involved for diffusional processes. It is still possible to achieve full density with larger and irregular shaped particles. The particle morphology has little effect on the achievable final density, although it appears angular particles allow retention of a slightly smaller grain size. The largest barrier to full consolidation via FAST is particles with internal porosity (spongy) with the densities of only $\sim 98\%$ achieved with the conditions studied here. It is postulated that an increase in dwell pressure or alternatively an additional preprocessing step may improve this; the plasma spheroidisation of the rutile-derived alloy allowed $>99\%$ density to be achieved. Alloy chemistry also affected the response to processing conditions. The variations in material flow stress at high temperatures gives different levels of plastic deformation in the particles and the different β transus temperatures alters diffusion rates; materials with lower flow stress and β transus are more easily fully consolidated.

Successfully producing a fully dense and microstructurally homogeneous 250 mm diameter 5.5 kg disc via FAST demonstrates the next step in scalability for the process and technology; showing that it is already possible to produce preforms at the size of real world components. For example, FAST could be used as

part of a processing route to produce components for the valve train in internal combustion engines (e.g. rocker arms or connecting rods) or parts for aircraft landing gear assemblies; giving the well-known benefits of high-strength titanium alloys to these applications but at a significant cost reduction.

The low level of interstitial pick-up further shows the suitability of FAST for processing titanium powders. The ability to use vacuum and/or argon keeps contamination low. The thin layer of stabilised α due to carbon ingress is not foreseen as being overly problematic and would easily be removed via a light finish machining operation; currently when titanium powder is HIP'ed an iron rich diffusion layer is formed from the mild steel can, which also has to be removed post-HIP. The microhardness values give a good indication that the mechanical properties should be competitive when compared to conventional wrought material.

The microstructures and simple disc shaped specimens produced in this chapter are not what would typically be required for titanium alloy components. When conventionally processing titanium alloys the microstructure would typically be refined by additional thermomechanical working in the single β phase and/or high in the $\alpha + \beta$ phase region to produce the desired mechanical properties. Therefore, an assessment of FAST material under forging conditions is now needed to investigate forgability and microstructural refinement. If FAST material performs sufficiently well during subsequent thermomechanical processing it will be a strong indicator that FAST is capable of being a key part in a cost-effective processing route. This investigation will be performed in the following chapter with the aim of establishing a processing window that will allow a one-step forging operation to be utilised on FAST preforms to produce near net shape components with wrought properties.

5. Thermomechanical Processing of Titanium Alloys Consolidated Via Field Assisted Sintering Technology

The results for the FAST consolidation and subsequent hot axisymmetric compression of Ti-6Al-4V HDH powder presented in this chapter were published in the Proceedings of the 13th World Conference on Titanium by Weston et al. [66]. The final publication is available at Wiley via: <http://dx.doi.org/10.1002/9781119296126.ch18>. Permission for reuse has been obtained and the agreement can be seen in Fig. B.2 in appendix B.

5.1 Introduction

The previous chapter demonstrated the ability of FAST to produce 98-99.9 % density for a range of starting titanium alloy powder sizes, morphologies, and chemistries. As discussed in chapter 2 it is believed that some amount of subsequent thermomechanical deformation will be required to improve upon the limitations of shape, microstructure, and mechanical properties produced via FAST.

The literature review showed that during conventional processing titanium alloys typically undergo many hot deformations and heat treatments to transform them from the large sized and microstructurally coarse ingots produced via VAR or CHM routes to useful mill products/semi-finished components, which then undergo extensive machining to produce the required final dimensions. The last deformation usually occurs high in the $\alpha + \beta$ phase region to reduce the forming loads required yet still produce the bi-modal microstructure that is typically desired. For a processing route to be cost-effective it is essential to remove and/or reduce as many of these traditional steps as possible. Therefore, this chapter studies the response to thermomechanical processing of a range of titanium alloys that were consolidated via FAST. The main goal was the production of rheology data linked to thermomechanical processing parameters

(temperature, strain rate, and strain). Additionally, investigations of associated microstructural evolution were undertaken. The ability to successfully model the flow behaviour of a metal during thermomechanical processing is key to improving the efficiency of any such industrial operations, and additionally can allow greater understanding of the associated dynamic microstructural responses. Rheology data generated in this study was utilised as an input to FE simulations of the axisymmetric compression tests in the form of a tabulated data material model. Efforts were also made to develop constitutive equations to use as material models following the methodology outlined by Davenport et al. [95], which assumes that the flow stress is solely a product of strain, strain rate, and temperature.

5.2 Experimental Approach

The experimental approach used in this chapter was to replicate, in a controlled manner, the variation in thermomechanical parameters typically seen when processing titanium alloys. This was done through hot axisymmetric compression testing on the TMC machine to allow rheology data as a function of the varied processing parameters to be obtained. Initially, 80 mm diameter disc specimens were prepared via FAST from four alloys that were then used to produce test specimens for the subsequent studies. For the compression testing each alloy was studied at three temperatures and three strain rates in order to gather information on the extended processing window around the expected industrial deformation conditions; additionally this is the minimum number required to attempt to develop constitutive equations for modelling the material's flow behaviour. The deformed specimens were water quenched immediately after testing to preserve the microstructural features. The sectioning and metallographic preparation of all the deformed samples also allowed examination of the microstructural features produced by the varying processing conditions.

5.2.1 Materials

The alloy chemistries and particle morphologies of the four powders used in this chapter were CP-Ti HDH, Ti-6Al-4V HDH, Ti-5553 GA, and Metalysis rutile-derived PS. Full details on each type of powder were presented in section 3.2.

5.2.2 FAST

One uniform thickness 80 mm diameter FAST disc was produced from each powder following the standard processing procedure described in section 3.1.1. The FAST processing conditions and mass of powder used for each disc are shown in Table. 5.1. The processing conditions used for the rutile-derived alloy disc for the forging study were different as they were made primarily for a different project, with the unused material then utilised in this work. The previous chapter demonstrated that dwell time and heating rate are less significant to specimen microstructure and density. Therefore it was not envisaged that a significant effect on deformational behaviour would occur. The mass of powder aimed to give a final thickness of ~ 14 mm apart from the rutile-derived alloy aimed for ~ 10 mm thickness due to limitations on the quantity of powder available.

Table 5.1 – *Alloy chemistries, powder morphologies, FAST processing conditions, and powder masses used to produce the 80 mm diameter discs for the axisymmetric compression testing specimens.*

Material	Mass (g)	FAST Processing Conditions			
		Dwell Temp. (°C)	Dwell Press. (MPa)	Heat Rate (°Cmin ⁻¹)	Dwell Time (min)
Ti-6Al-4V HDH	312	1200	22	200	30
CP-Ti HDH	317	1200	22	200	30
Ti-5553 GA	327	1200	22	200	30
Rutile-derived PS	227	1200	22	25	10

5.2.3 Axisymmetric Compression Testing

An overview of the TMC machine and an outline of the general testing procedure used can be found in sections 3.1.2.1 and 3.1.2.2. The commercial alloy compression specimen cylinders were extracted from the 80 mm FAST discs as shown in Fig. 5.1a. 10 mm diameter bars were removed perpendicular to the compression direction using electrical discharge machining and then sectioned into 15 mm lengths to give 10×15 mm test cylinders. The rutile-derived alloy specimens were taken parallel to the compression direction with 7.5 mm diameter cylinders removed from the 10 mm thick FAST disc to give 7.5×10 mm test pieces. The machine's minimum strain rate of 0.01 s^{-1} was utilised, which was increased by a factor of ten to 0.1 s^{-1} and again to 1 s^{-1} to give a range of test conditions. The Ti-6Al-4V HDH and rutile-derived PS were tested at 850°C ,

950°C, and 1050°C. The CP-Ti HDH was tested at 700°C, 800°C, and 900°C. The Ti-5553 GA was tested at 785°C, 810°C, and 835°C.

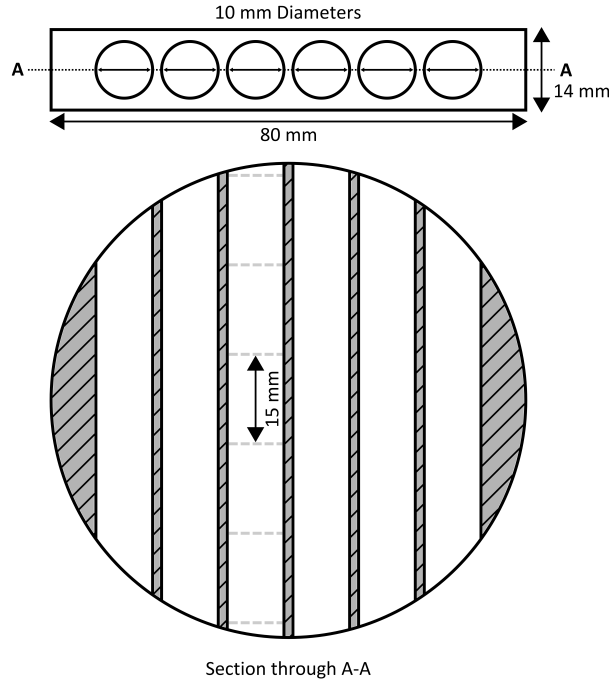


Figure 5.1 – Schematic showing the location that the axisymmetric compression testing cylinders were extracted from in the 80 mm diameter FAST discs.

An example of the raw data recorded during testing by the TMC machine is shown in Fig. 5.2. The data consists of time from the beginning of the test t (s), upper tool displacement from the user specified zero position $d_{recorded}$ (mm) in part (a), upper tool velocity v (mms^{-1}) in part (b), load F (kN) in part (c), and specimen temperature from the embedded thermocouple T ($^{\circ}\text{C}$) in part (d). This data needs to be “post-processed” to allow the production of fully corrected flow curves, which can then be used as an input for FE modelling either in a tabulated data form or with further manipulation as constitutive equations. The procedure adopted to correct the raw data in this work is based on the methodology developed by Roebuck et al. [44], Loveday et al. [96], Davenport et al. [95], and Evans et al. [97]. A semi-automated MS Excel spreadsheet was developed to increase the speed and precision of this data correction and analysis. The calculations performed by the spreadsheet will be outlined below using example data from one of the experimental tests.

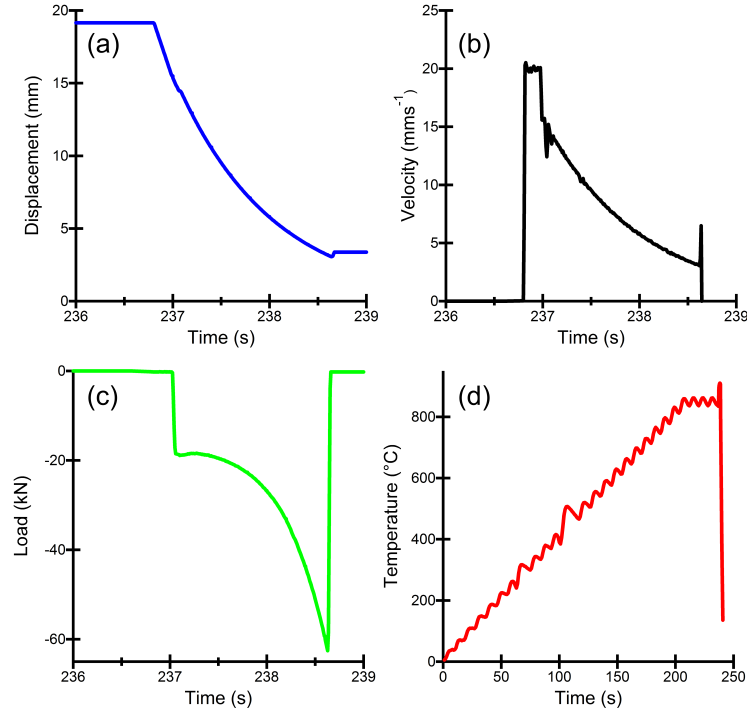


Figure 5.2 – Graphs showing the five types of data recorded during axisymmetric TMC compression testing; upper tool displacement from specified zero position vs. time (a), upper tool velocity vs. time (b), load on the upper tool vs. time (c), specimen temperature vs. time (d). Parts (a), (b), and (c) are magnified on the deformation and part (d) shows the whole test. (Example data is from a Ti-6Al-4V HDH test at 850°C and 1 s⁻¹)

5.2.3.1 Correction of Recorded Load-Displacement Data

The initial steps are concerned with correcting the displacement data to account for the compliance of the machine, the thermal expansion of the test specimen, any drift in the displacement measurement from the user specified zero position, and any discrepancy between machine recorded and user measured final specimen height. The TMC machine compliance was calculated to be $\sim 475 \text{ kNmm}^{-1}$ in previous work by Davies [48], meaning that at maximum load the machine frame and tooling could be deformed by more than 1 mm. By measuring the displacement produced when loading the machine with the tools in direct contact and fitting a curve to the results it was possible to give a value of compliance as a function of load. This correction factor is now automatically applied to the raw displacement, as a function of measured raw load, when test data is exported from the TMC. This correction is demonstrated in Fig. 5.3 when the final unloading portion of the load-displacement curve becomes vertical, showing that the relaxation of the machine is no longer included in the data.

The first post-processing step is to calculate the initial height and radius of the specimen corrected for thermal expansion, h_{0h} and r_{0h} , using Eq. 5.1 and Eq. 5.2, where h_{0c} is the average measured height at room temperature and r_{0c} is half the average diameter measured at room temperature, α_t is the coefficient of thermal expansion, T and T_c are the temperature of the test and the temperature at which the specimen was measured. It is convenient to relocate the zero displacement position to the initial height of the test specimen at the designated test temperature in order to give an increasing displacement as the test progresses rather than decreasing, which allows clearer visualisation when plotting the data. This initial uncorrected displacement of the tool, d_{uncorr} , can be calculated using Eq. 5.3. The recorded load (F) is negative due to the convention of compressive actions being represented as negative. However, it is again convenient when visualising the data to multiply F by -1 to give a positive and increasing number for load as the test progresses.

$$h_{0h} = h_{0c} + \alpha_t h_{0c} (T - T_c) \quad (5.1)$$

$$r_{0h} = r_{0c} + \alpha_t r_{0c} (T - T_c) \quad (5.2)$$

$$d_{uncorr} = h_{0h} - d_{recorded} \quad (5.3)$$

The uncorrected tool displacement is plotted against the load to give an initial load vs. displacement curve as seen in Fig. 5.3. It is necessary to correct this curve to ensure that the initial linear elastic portion of the curve intercepts the origin - i.e. there is zero load at zero displacement. This should be achieved during the machine zeroing process before testing commences, although there is usually still a small discrepancy present due to the thickness of any lubricant applied and slight misalignments in the tool platens. The value required to offset the curve so that it travels through the origin, the zero-offset value d_{offset} , can be calculated by fitting a linear trend line to the initial elastic part of the curve, with equation $y = mx + c$, where m is the gradient and c is the y-intercept; the zero-offset value is the displacement at zero load and can be found by rearrangement, see Eq. 5.4. The displacement values corrected for zero-offset, d_{zero} , are found by subtracting the zero-offset value from every uncorrected displacement value, see Eq. 5.5.

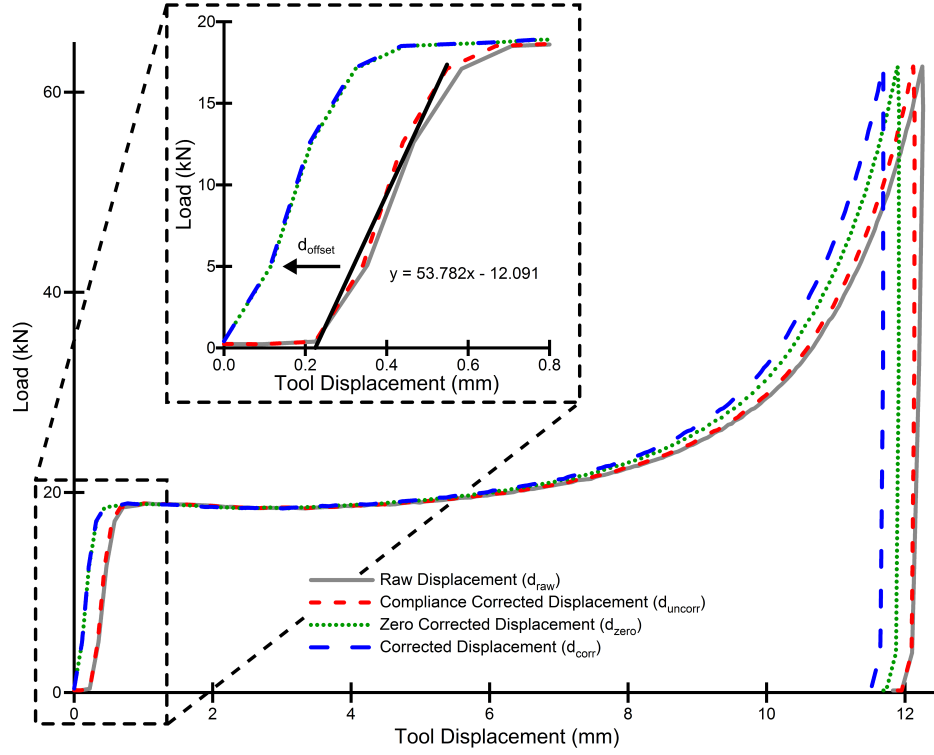


Figure 5.3 – Graph illustrating the required corrections to the load-displacement data produced during axisymmetric TMC compression testing. (Example data is from a Ti-6Al-4V HDH test at 850° C and 1 s⁻¹)

$$d_{offset} = \frac{-c}{m} \quad (5.4)$$

$$d_{zero} = d_{uncorr} - d_{offset} \quad (5.5)$$

$$d_{corr} = d_{zero} \left(\frac{h_{0h} - h_{fh}}{d_{zero,max}} \right) \quad (5.6)$$

There usually still exists a small discrepancy between the maximum machine recorded displacement ($d_{zero,max}$) and the maximum user measured height change ($h_{0h} - h_{fh}$) of the specimen. The final hot height h_{fh} is found by manually measuring the specimen post test at room temperature h_{fc} and then correcting for thermal expansion in the same way as Eq. 5.1. This discrepancy may arise due to the breakdown and thinning out of lubrication as the test progresses or due to very slight misalignments between the tool platens and specimens; i.e. the tool faces and/or the specimen ends are not perfectly parallel leading to a deviation between the recorded displacement and average measured final height. A scaling correction can be applied to ensure the maximum recorded

displacement is equivalent to the maximum measured height change, which gives a fully corrected displacement (d_{corr}), see Eq. 5.6. This fully corrected displacement is also plotted against load in Fig. 5.3.

5.2.3.2 Conversion to Stress-Strain Data

The recorded load and corrected displacement can now be used to calculate instantaneous values of measured true stress (P_i) and true strain (ε_i) throughout the test. First instantaneous values of hot height (h) and radius (r) can be calculated from the fully corrected displacement values via Eq. 5.7 and Eq. 5.8, where the constancy of specimen volume is utilised and it is assumed at this point there is no barrelling due to friction.

$$h = h_{0h} - d_{corr} \quad (5.7)$$

$$r = \sqrt{\frac{h_{0h} r_{0h}^2}{h}} \quad (5.8)$$

$$P_i = \frac{F}{\pi r^2} \quad (5.9)$$

$$\varepsilon_i = \ln\left(\frac{h_0}{h}\right) \times -1 \quad (5.10)$$

The instantaneous value of measured true stress is then given by Eq. 5.9, which is the instantaneous recorded load F divided by the instantaneous area (assuming no barrelling). The instantaneous value of true strain is given by Eq. 5.10; this value is again multiplied by -1 to allow for easier graphical representation as compressive strain is conventionally portrayed as a negative value. The resulting curve can be seen in Fig. 5.4.

5.2.3.3 Correction for Friction Effects

To give a value for the instantaneous true stress (σ_i) the measured true stress needs to be corrected to account for the effects of friction, which can cause the load needed for deformation to be significantly increased, see Eq. 5.11 [46, 45].

$$\sigma_i = \frac{P_i}{1 + \left(\frac{2\bar{m}r}{3\sqrt{3}h}\right)} \quad (5.11)$$

A value for the interface friction factor \bar{m} needs to be determined in order to utilise Eq. 5.11. This can be done experimentally using the ring compression test [47] or alternatively by deforming specimens of varying initial height under the same test conditions and finding the friction factor that converges the resulting flow curves together [48, 49]. A value of 0.3 is typically recommended for the hot forging of titanium alloys [98] and was used as a first approximation in this study. The effect of varying the interface friction factor can be seen in Fig. 5.4.

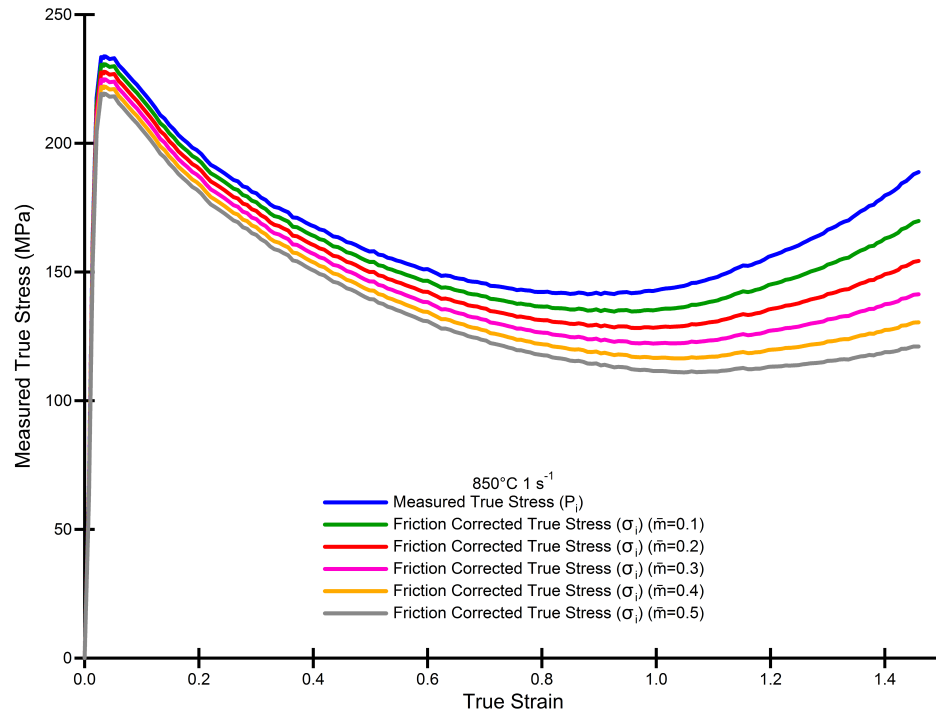


Figure 5.4 – Graph showing the measured true stress P_i vs. true strain curve calculated from the corrected load and displacement data recorded during axisymmetric TMC compression testing, and also illustrating the outcome of an increasing value of friction factor when correcting the measured true stress for frictional effects. (Example data is from a Ti-6Al-4V HDH test at 850°C and 1 s⁻¹)

5.2.3.4 Isothermal Correction

An example of the level of temperature rise possible is shown in Fig. 5.5 for Ti-6Al-4V HDH in a test at 850°C and 1 s⁻¹. Deviation away from the nominal testing temperature will produce an over- or underestimation of the flow stress that can be accounted for by using Eq. 5.12 to isothermally correct the flow stress. Eq. 5.12 is a rearrangement of two simultaneous equations in the form of Eq. 5.18 (see section 5.2.3.5) for the instantaneous stress at the instantaneous temperature versus the isothermal stress at the isothermal temperature.

$$\sigma_{iso} = \sigma_i + \frac{Q_{def}}{\beta R} \left(\frac{1}{T_{iso}} - \frac{1}{T_i} \right) \quad (5.12)$$

Where σ_{iso} is the isothermally corrected stress, Q_{def} is an apparent activation energy for hot deformation, R is the universal gas constant, β is a material dependent coefficient, T_{iso} is the nominal desired test temperature, and T_i is the instantaneous value of recorded temperature.

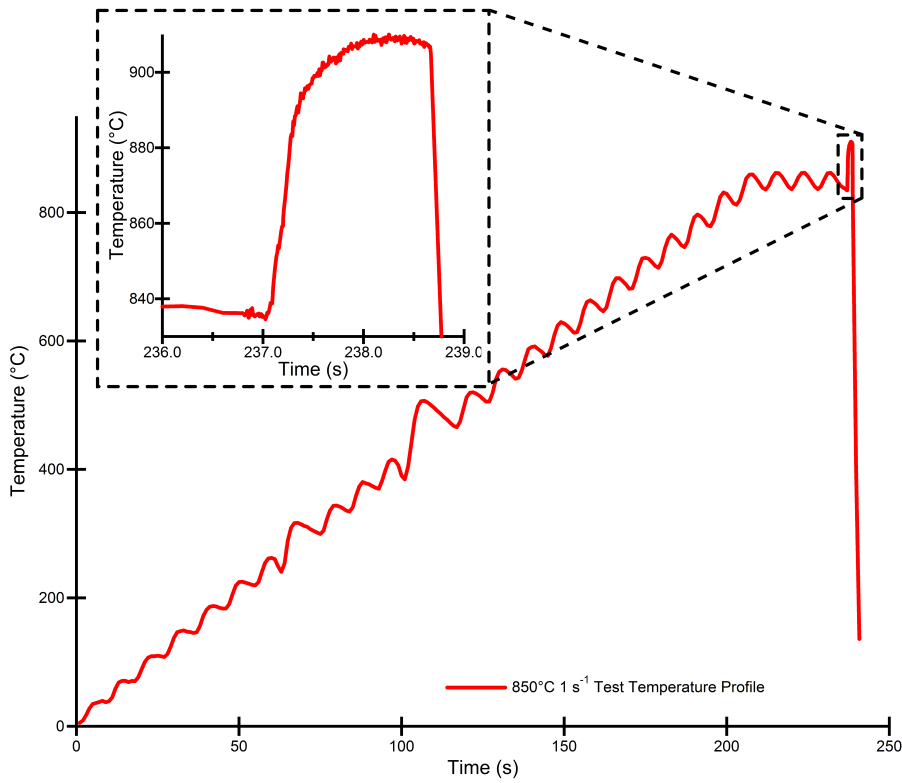


Figure 5.5 – Graph of an example temperature profile during a TMC axisymmetric compression test for induction heating, deformation (zoomed area), and quenching. (Example data is from a Ti-6Al-4V HDH test at 850°C and 1 s⁻¹)

In order to perform the isothermal correction it can be seen that a value for Q_{def} is required. This value can be found using relationships defined in the following section on constitutive equation development. First it is necessary to substitute Eq. 5.15 into Eq. 5.18, taking the natural logarithm of both sides, and rearranging, see Eq. 5.13. Then plotting $\ln(\dot{\epsilon})$ vs. $\frac{1}{T}$ and fitting a straight line to the data will give a gradient of $-\frac{Q_{def}}{R}$ and intercept of $(\beta\sigma + \ln(A_2))$, see Fig 5.6c.

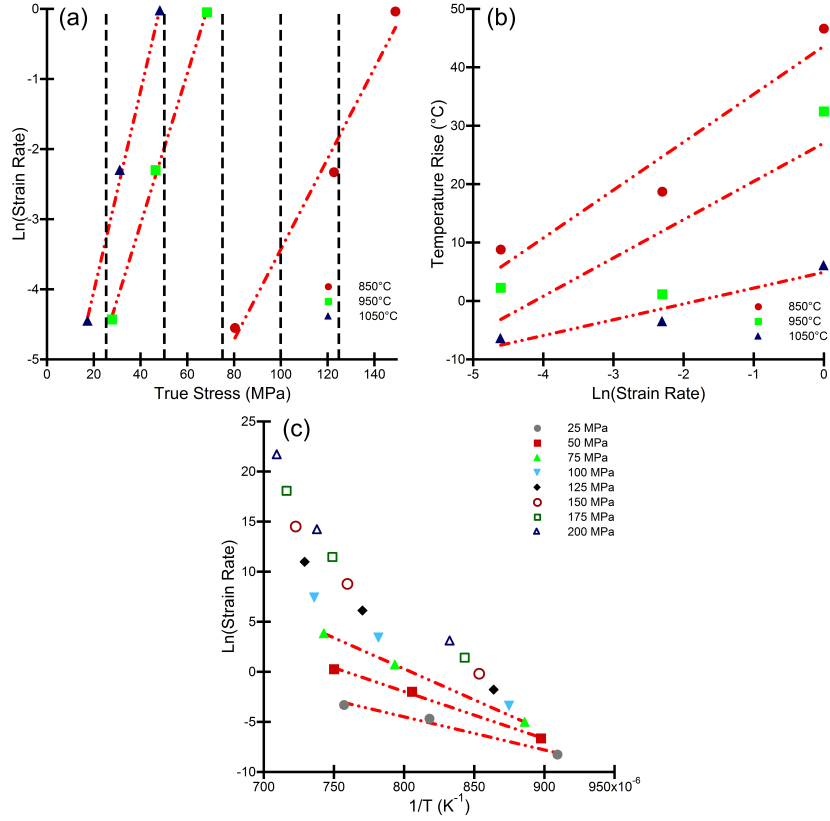


Figure 5.6 – Figure showing the graphs used to calculate a value for Q_{def} for Ti-6Al-4V HDH tested at 850°C, 950°C, and 1050°C, at strain rates of 0.01 s⁻¹, 0.1 s⁻¹, and 1 s⁻¹. These graphs are at the strain increment of 0.6; the same methodology was performed at additional strain increments but is not presented. (a) Graph showing the relationship between instantaneous values of $\ln(\dot{\epsilon})$ and σ_i allowing the calculation of $\ln(\dot{\epsilon})$ at fixed σ_i and temperature; where the vertical lines intersect the linear trendlines. (b) Graph showing the relationship between measured temperature rise and $\ln(\dot{\epsilon})$ allowing the prediction of temperature as $\dot{\epsilon}$ varies using the linear trendlines. (c) Graph of interpolated values of $\ln(\dot{\epsilon})$ vs. $\frac{1}{T}$ for fixed true stress, where the average gradient of the linear trendlines is $-\frac{Q_{def}}{R}$; constructed using the values obtained from parts (a)+(b).

$$\ln(\dot{\epsilon}) = -\frac{Q_{def}}{R} \frac{1}{T} + \left(\beta \sigma + \ln(A_2) \right) \quad (5.13)$$

For this technique, the values of $\ln(\dot{\epsilon})$ need to be known at constant values of stress for each nominal test temperature. Therefore, it is first required to calculate the relationship between $\ln(\dot{\epsilon})$ and σ_i at the testing temperatures and at increasing levels of strain, see Fig. 5.6a for a strain of 0.6; values of $\ln(\dot{\epsilon})$ to produce exact values of stress at 25 MPa intervals can be calculated from the equations of the linear regression lines fitted to the experimental data. It

is necessary to repeat this analysis at multiple discrete values of strain (0.05, 0.1, 0.15, 0.2, 0.25, 0.3, 0.4, 0.5, 0.6, 0.7, 0.8, 0.9, 1.0, 1.2, and 1.4 in this case). The data recorded by the TMC during the tests is seldom at exactly these strains and therefore the MS Excel spreadsheet automatically finds the strain value immediately below and immediately above the desired discrete value and performs a linear interpolation to give the temperature, stress, and strain rate at these exact strain values.

It is also necessary to account for the temperature rise at these values of strain rate at each testing temperature and value of strain, see Fig 5.6b for a strain of 0.6. It is then possible to plot $\ln(\dot{\epsilon})$ against $\frac{1}{T}$ at discrete stresses and discrete strains to obtain values for Q_{def} . Ideally Q_{def} should be a constant but that is not the case in this instance, however it is felt that for the purpose of this analysis it is acceptable to take an average value of the gradients across all strains.

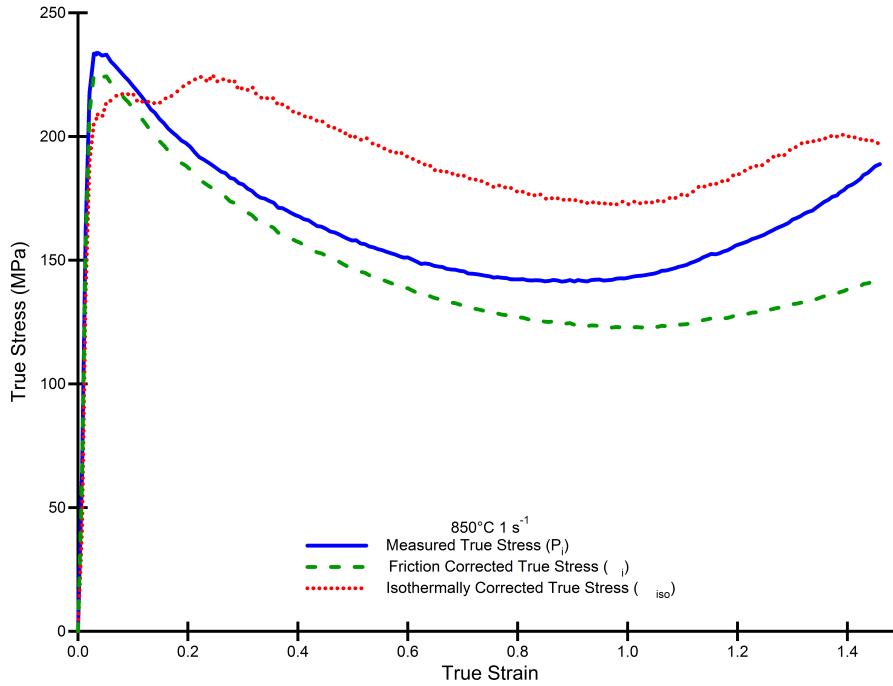


Figure 5.7 – Graph for Ti-6Al-4V HDH tested at 850°C and 1 s⁻¹ showing the measured true stress P_i vs. true strain, which has first been corrected for frictional effects σ_i , and then isothermally corrected for deformational heating effects σ_{iso} .

The values for β can be found by using Eq. 5.23; defined in the following section on constitutive equation development. Linear trendlines fitted to a plot of $\ln(Z)$ vs. $\ln(\sigma_i)$ will have a gradient equal to β , see Fig. 5.8a. The values of β are only valid at the specific value of strain they were calculated at, and typically the values of strain recorded during testing increase in much smaller increments.

Therefore a plot of the calculated β values vs. ϵ is required in order to fit a curve to their variation, see Fig. 5.9a. The equation of this curve can be used to give continuous values of β at every value of recorded ϵ .

It is now possible to isothermally correct every value of stress using Eq. 5.12 to give a fully corrected true stress vs. true strain curve for each test condition, see Fig. 5.7.

5.2.3.5 Initial Constitutive Equation Development

The first stage of developing constitutive equations is to derive a relationship between the flow stress at discrete strains, σ_ϵ , and the Zener-Holloman parameter Z , see Eq. 5.14. Z is a temperature compensated strain rate, see Eq. 5.15 [99], where Q_{def} is an apparent activation energy for deformation, $\dot{\epsilon}$ is the instantaneous strain rate defined by Eq. 5.16, R is the universal gas constant, and T is the temperature.

$$\sigma_\epsilon = B_\epsilon f(Z) \quad (5.14)$$

$$Z = \dot{\epsilon} \exp\left(\frac{Q_{def}}{RT}\right) \quad (5.15)$$

$$\dot{\epsilon} = \frac{v}{h} \quad (5.16)$$

Some typical forms of first stage constitutive equations describing the relationship of flow stress to Z are shown below. Eq. 5.17 is the power law equation, which is typically valid at lower-stresses. Eq. 5.18 is the exponential law equation, which is typically valid at higher-stresses. Eq. 5.19 is the hyperbolic sine relationship that is valid over the entire range of stresses as it reduces to Eq. 5.17 at low stresses and Eq. 5.18 at high stresses. Where A_1 , A_2 , A_3 , α , β , n , and n' are material dependant coefficients and α is calculated via Eq. 5.20.

Instantaneous values of Z can be calculated (using the value of Q_{def} calculated in the previous section) allowing the determination of the values of the coefficients in the first-stage constitutive equations. The values for A_1 and n can be found by taking the natural logarithm of both sides of Eq. 5.17 and rearranging to give Eq. 5.21 and Eq. 5.22. Fitting a linear trendline to a plot of $\ln(Z)$ vs. $\ln(\sigma)$, see Fig. 5.8a, will give a gradient equal to n and an intercept equal to $\ln(A_1)$.

$$Z = A_1 \sigma^n \quad (5.17)$$

$$Z = A_2 \exp(\beta \sigma) \quad (5.18)$$

$$Z = A_3 (\sinh(\alpha \sigma))^{n'} \quad (5.19)$$

$$\alpha = \frac{\beta}{n} \quad (5.20)$$

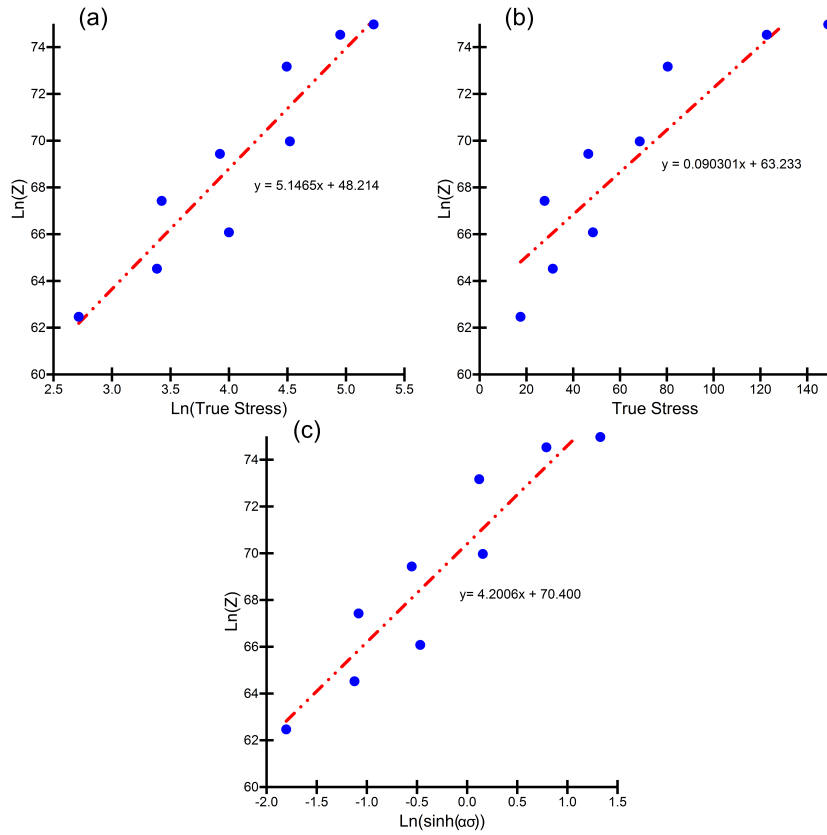


Figure 5.8 – Figure showing the graphs used to calculate the coefficients for constitutive equations. (a) $\ln(Z)$ vs. $\ln(\sigma)$ to obtain A_1 and n for Eq. 5.17, (b) $\ln(Z)$ vs. σ to obtain A_2 and β for Eq. 5.18, (c) $\ln(Z)$ vs. $\ln(\sinh(\alpha\sigma))$ to obtain A_3 and n' for Eq. 5.19

The values for A_2 and β can be found by taking the natural logarithm of both sides of Eq. 5.18 and rearranging to give Eq. 5.23 and Eq. 5.24. Fitting a linear trendline to a plot of $\ln(Z)$ vs. σ , see Fig. 5.8b (which is analogous to Fig. 5.6a), will give a gradient equal to β and an intercept equal to $\ln(A_2)$. The values for A_3 and n' can be found by taking the natural logarithm of both sides of Eq. 5.19 and rearranging to give Eq. 5.25 and Eq. 5.26. Fitting a linear trendline to a plot of $\ln(Z)$ vs. $\ln(\sinh(\alpha\sigma))$, see Fig. 5.8c will give a gradient equal to n' and

an intercept equal to $\ln(A_3)$.

$$\ln(Z) = n \ln(\sigma) + C_1 \quad (5.21)$$

$$A_1 = \exp(C_1) \quad (5.22)$$

$$\ln(Z) = \beta \sigma + C_2 \quad (5.23)$$

$$A_2 = \exp(C_2) \quad (5.24)$$

$$\ln(Z) = n' \ln(\sinh(\alpha\sigma)) + C_3 \quad (5.25)$$

$$A_3 = \exp(C_3) \quad (5.26)$$

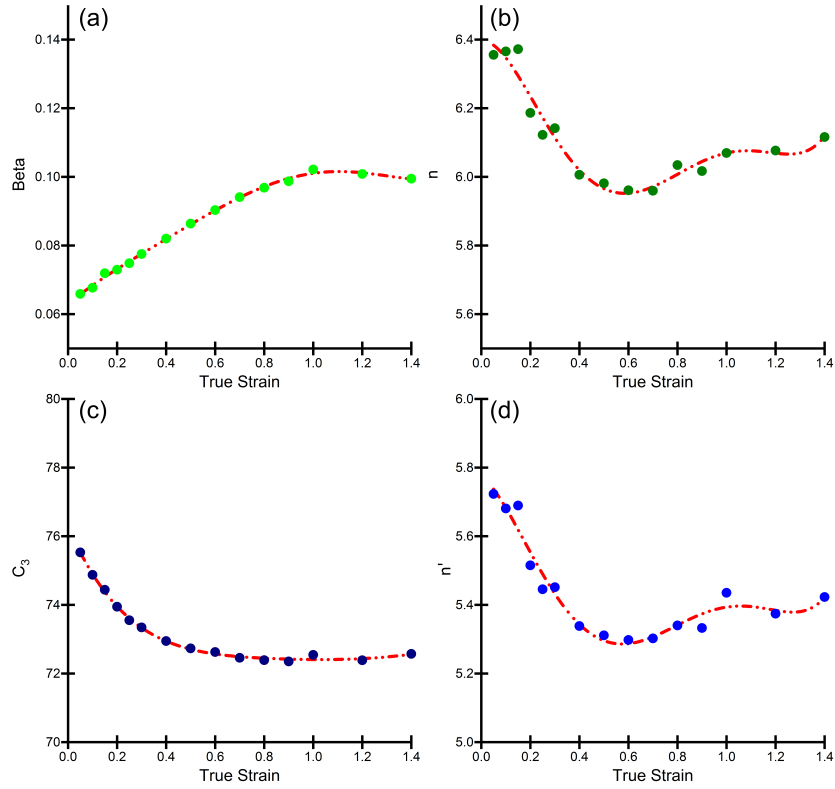


Figure 5.9 – Plots of constitutive equation coefficients as functions of strain with fitted polynomial trendlines allowing calculation for continuous values of strain.

(a) β vs. ϵ . (b) n vs. ϵ . (c) C_3 vs. ϵ . (d) n' vs. ϵ .

As described for the β coefficient the values of A_1 , A_2 , A_3 , α , n , and n' are only valid at the specific value of strain they were calculated at and therefore a plot of these coefficients vs. ϵ is required to determine their variation. A polynomial curve can be fitted to these points to provide an equation that describes them as a function of ϵ , which then allows the calculation of the coefficients for continuous values of ϵ , see Fig. 5.9.

Ultimately this allows using Eq. 5.27 to calculate a value for σ at every point.

$$\sigma = \left(\frac{1}{\alpha}\right) \sinh^{-1} \left(\frac{Z}{A_3}\right)^{n'} \quad (5.27)$$

5.2.3.6 Strain Rate Correction

The axisymmetric compression tests were performed in true strain rate control, meaning that in an ideal test the deformation should occur at the selected constant strain rate for the entire test. This requires the velocity of the tool to decrease in proportion with the specimen height. The TMC achieves this through a closed loop control system operating servo-valves attached to the main actuator, which moves the tool post. Perfect velocity control can be achieved under zero-load conditions as the force required for movement is constant. Excellent control can also be achieved during testing when there is no sudden change in the gradient of the stress-strain curve; i.e. after the initial peak load. As the strain rates used in this study were well within the capabilities of the machine it was deemed not necessary to perform any correction for strain rate variation during testing. Graphs showing examples of the typical variation in strain rates seen during the testing for this work can be seen in Fig. 5.10. It should be noted that although there appears to be fluctuations in the strain rate curves (especially at 0.01 s^{-1}) that these are actually caused by uncertainties in the displacement measurements and not actual measured variations in the strain rate. The actual strain rate will be given by averaging the noise, and thus the strain rate control can be claimed to be accurate enough for the purposes of this investigation.

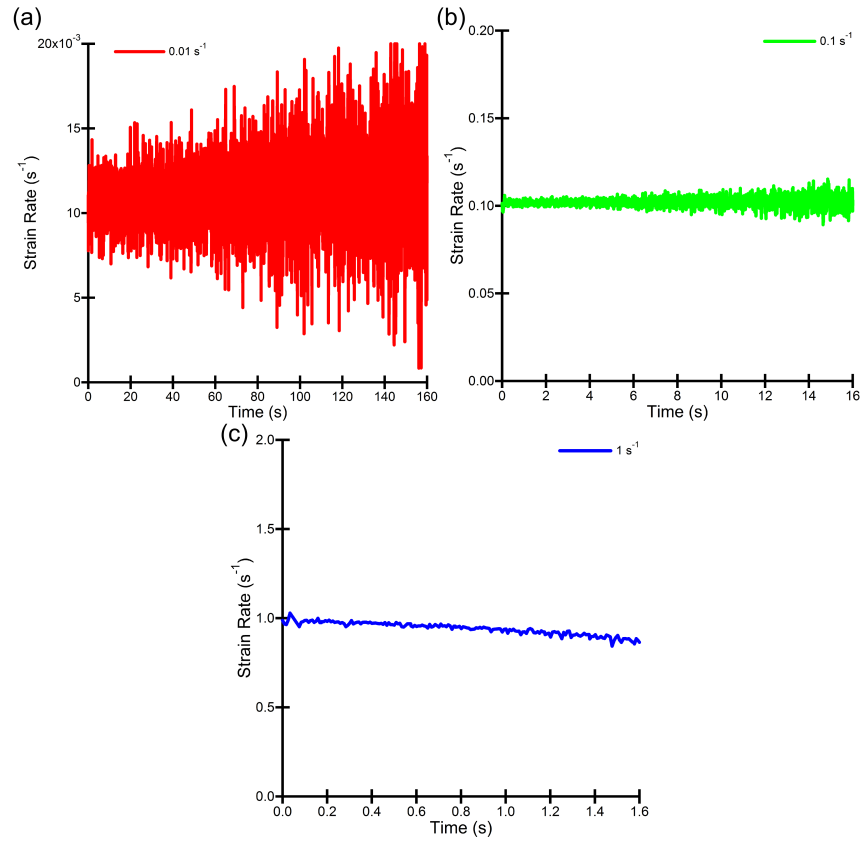


Figure 5.10 – Plots showing typical behaviour of strain rate vs. time for the three testing conditions used in this investigation (a) 0.01 s^{-1} , (b) 0.1 s^{-1} , and (c) 1 s^{-1} .

5.2.4 Finite Element Simulation of the Axisymmetric Compression

The finite element software DEFORMTM [17], see section 3.1.8, was used to simulate the axisymmetric compression tests of the cylindrical specimens. The load and displacement data produced allowed an easy way to check the validity of the model. For an accurate simulation there should be good agreement when plotting the experimentally obtained data against the simulation data. The simulations also provided information on the levels of strain across the deformed specimens.

A 2-D axisymmetric model of half the cylinder geometry was meshed with 3144 elements. Rheology data generated during the axisymmetric testing of the cylinder specimens was used in a tabular form (stress values at a range of strains for each testing condition) for the material model. A constant shear friction factor of $\bar{m} = 0.3$ was used.

5.3 Results and Discussions

5.3.1 Microstructure and Density After FAST Processing

The microstructures produced after FAST processing at 1200°C with 22 MPa pressure are shown at low and high magnification in Fig. 5.11; a dwell time of 30 minutes and heating rate of 200°Cmin⁻¹ was used for the HDH Ti-6Al-4V in parts (a)-(b), HDH CP-Ti in parts (e)-(f), and GA Ti-5553 in parts (g)-(h), and a dwell time of 10 minutes and heating rate of 25°Cmin⁻¹ for the rutile-derived alloy in parts (c)-(d). As would be expected, and as was shown in chapter 4, the microstructures are all significantly altered from the starting powders. The commercial alloys also show microstructures typical of cooling from above the β transus temperature. In each alloy there has been growth of the (prior) β grains beyond the dimensions of the largest starting powder particles. The microstructures are also comparable to those produced in chapter 4 during the dwell time and heating rate parametric study, see section 4.3.2.2. The densities achieved are >99.8 % for the commercial alloys and ~98 % for the rutile-derived alloy, which is again in line with what was seen in chapter 4 for 20 mm diameter specimens.

The HDH Ti-6Al-4V shows a classical transformed β microstructure with α colonies after slow-cooling from above the β transus temperature [100, 29], with a prior β grain size of ~200-400 μ m. This demonstrates the high density and level of particle diffusion bonding achieved as the removal of the majority of porosity has prevented the pinning of grain boundary migration and allowed the grains to grow beyond the initial particle size. There is a near continuous layer grain boundary α present that is 3-5 μ m thick, α colonies that range from 5-50 μ m thick, with α laths that are 1-3 μ m thick. The density calculated via image analysis, see section 3.1.7, is 99.91 %.

The PS rutile-derived alloy shows very similar behaviour to the HDH Ti-6Al-4V in having a transformed β microstructure with α colonies as was seen previously, due to containing small amounts of α and β stabilisers. It is more difficult to assess the prior β grain size as the boundaries are less obvious, although it appears it may be slightly less than for the Ti-6Al-4V. The α colonies and α laths are also of comparable dimensions to the Ti-6Al-4V. The density calculated via image analysis is 98.01 %. The plasma spheroidisation has removed the internal spongy porosity that was initially present but there still remains larger spherical

pores in some particles, which have not been removed during sintering.

The HDH CP-Ti also shows a transformed β structure similar to what is reported in the literature [2] but no clear prior β grains are discernible; possibly due to being larger than the field of view of the microscope. There are colonies of α laths but they are less elongated and thicker than in the $\alpha + \beta$ alloys. The microstructure is very similar to that produced by Zadra et al. [88] when using FAST to consolidate grade 3 CP-Ti at 1150°C. The density calculated via image analysis is 99.83 %.

The GA Ti-5553 exhibits β grains with diameters of $\sim 100\text{--}800\ \mu\text{m}$ with small but continuous amounts of α visible at the grain boundaries and sub-grain boundaries due to the comparatively slower cooling rate of the 80 mm FAST mould assembly. This microstructure is typical of what is reported for the β annealed condition of Ti-5553 [1, 101, 102]. The density calculated via image analysis is 99.96 %.

5.3.2 Flow Curves and Microstructures after Hot Axisymmetric Compression

Graphs of friction corrected and isothermally corrected true stress vs. true strain, and micrographs of the deformed microstructures, for each of the four alloys at the nine experimental conditions are presented in this section. These flow curves have been derived from the raw data recorded by the TMC according to the methodology described in section 5.2.3. It is apparent that, as would be expected, the maximum flow stress for all of the materials increases with increasing strain rate and decreases with increasing temperature. The shapes of a flow curve can be indicative of the type of mechanisms occurring during deformation, but microstructural examination can offer additional insight. The micrographs shown are taken from the centre of each specimen where the highest strain occurs (~ 2.1) and from the middle of the radial edge where a much lower strain occurs (~ 1.1).

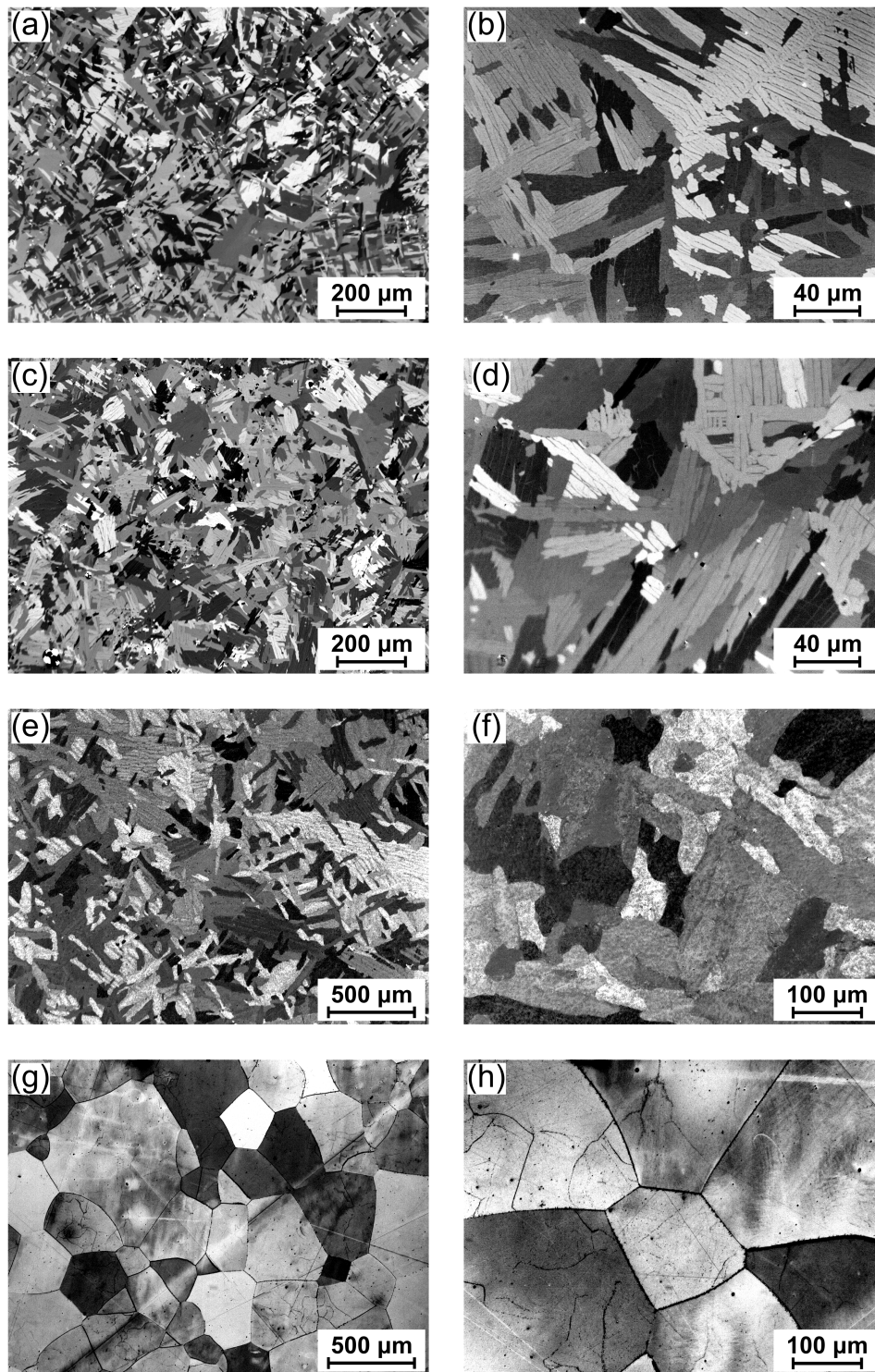


Figure 5.11 – Low and high magnification cross-polarised light micrographs (a)-(f) and bright field after etching with Kroll's reagent (g)-(h) showing the post-FAST microstructures of Ti-6Al-4V HDH (a)+(b), rutile-derived PS alloy (c)+(d), CP-Ti HDH(e)+(f), and Ti-5553 GA (g)+(h).

Values of Q_{def} and β were required for isothermal correction, and A_3 , n , and n' for constitutive equations. The average values of Q_{def} , calculated according to section 5.2.3.4, for each material are presented in Table 5.2.

It should be noted that the parameter Q_{def} , the apparent activation energy for hot deformation, used in this analysis is an empirical factor calculated from experimental data, which is used as an indicator of the degree of difficulty to deform the material under the utilised conditions. The term Q_{def} can be seen as a lumped parameter representation of the incredibly complex interaction of deformation processes that are occurring during hot working (such as recovery and recrystallisation), rather than an inherent physical property of the material being tested [103]. As such, there a vast number of factors that can influence the calculated and reported values (see Table 5.2) of Q_{def} ; alloy composition and purity, microstructure pre-deformation, and testing conditions could all have an influence [104, 105].

Table 5.2 – Calculated values of activation energy for deformation Q_{def} for the four alloys used in this study and additional example values from the literature.

Material	FAST Conditions	Q_{def} (kJmol ⁻¹)	Literature Q_{def} Values			
Ti-6Al-4V HDH	1200°C, 22 MPa, 30 min, 200°Cmin ⁻¹	733	530 [38]	619 [106]	536 [107]	720 [108]
Rutile-derived PS	1200°C, 22 MPa, 30 min, 200°Cmin ⁻¹	341				
CP-Ti HDH	1200°C, 22 MPa, 10 min, 25°Cmin ⁻¹	245	α : 200-360 [109]	β : 180-220 [109]	242 [110]	
Ti-5553 GA	1200°C, 22 MPa, 30 min, 200°Cmin ⁻¹	137	130-175 [111]	183 [101]	188 [112]	

As discussed in section 5.2.3.5 the coefficients of the constitutive equations vary with strain and need to have a curve fitted to allow calculation at all values of strain, see Fig. 5.9. It was found that a 6th-order polynomial, in the form of Eq. 5.28 where $x_1 - x_7$ are constants, provided the highest coefficient of determination and thus the best fit to the data.

$$\beta = x_1\epsilon^6 + x_2\epsilon^5 + x_3\epsilon^4 + x_4\epsilon^3 + x_5\epsilon^2 + x_6\epsilon + x_7 \quad (5.28)$$

Whilst a 6th-order polynomial provides the highest coefficient of determination, it can be seen in Fig. 5.9b and Fig. 5.9d that this introduces an inflection point to the curve (with a maximum value at a strain of ~ 1). Roebuck reports in the GPG [44] that the systematic errors found in hot axisymmetric compression tests are mostly due to the presence of frictional forces and deformational heating effects, whilst the magnitudes of the errors are governed by material properties and test conditions. The friction and testpiece geometry are the most significant source of error, followed by strain and strain rate at intermediate importance, and testpiece volume and test temperature as least important. Evans [97] states that when following the GPG procedures for axisymmetric compression testing that the combination of all the measurement errors will produce an uncertainty in measurement of the flow stress in the region of $\pm 2 - 3$ %. Therefore, the small inflections seen in the 6th-order polynomial trendlines are most likely a result of measurement uncertainty rather than representing a physically real event occurring in the material due to the hot deformation process.

The constants for each coefficient of the 6th-order polynomial trendline for Ti-6Al-4V HDH can be seen in Table 5.3, in Table 5.4 for the rutile-derived alloy, in Table 5.5 for the CP-Ti HDH, and in Table 5.6 for the Ti-5553 GA.

Table 5.3 – Values of the constants need to fit a 6th-order polynomial equation to the variation of constitutive equation coefficients with strain for the data produced by axisymmetric compression of Ti-6Al-4V HDH consolidated via FAST.

	x_1	x_2	x_3	x_4	x_5	x_6	x_7
β	0.0506	-0.1744	0.2082	-0.1135	0.0195	0.0473	0.0635
n	-5.6995	27.6821	-51.7101	45.5075	-17.7217	1.6671	6.3262
n'	-0.7478	6.2444	-16.0670	16.8960	-6.3513	-0.3499	5.7667
C_3	8.6118	-38.5381	70.4563	-70.7568	45.2043	-18.9325	76.3887

Table 5.4 – Values of the constants need to fit a 6th-order polynomial equation to the variation of constitutive equation coefficients with strain for the data produced by axisymmetric compression of rutile-derived PS consolidated via FAST.

	x_1	x_2	x_3	x_4	x_5	x_6	x_7
β	-9.1685	30.9138	-40.3305	25.4347	-7.9218	1.1445	0.0804
n	-211.9116	675.9714	-824.8696	479.1050	-134.0516	16.4607	2.4047
n'	-64.1824	232.6583	-314.5576	193.6356	-50.8424	3.0578	2.0099
C_3	77.2016	-246.3490	320.1463	-222.2773	91.0578	-22.7516	32.5115

Table 5.5 – Values of the constants need to fit a 6th-order polynomial equation to the variation of constitutive equation coefficients with strain for the data produced by axisymmetric compression of CP-Ti HDH consolidated via FAST.

	x_1	x_2	x_3	x_4	x_5	x_6	x_7
β	0.2818	-1.5287	3.3216	-3.7243	2.2853	-0.7262	0.1725
n	-4.7811	18.9981	-28.5316	21.1018	-9.5403	3.0784	2.7572
n'	-6.9043	37.8659	-78.9593	80.1335	-43.1835	12.1324	0.9445
C_3	-8.1712	47.2133	-102.0686	107.3501	-60.0429	16.4569	23.1792

Table 5.6 – Values of the constants need to fit a 6th-order polynomial equation to the variation of constitutive equation coefficients with strain for the data produced by axisymmetric compression of Ti-5553 GA consolidated via FAST.

	x_1	x_2	x_3	x_4	x_5	x_6	x_7
β	-0.4728	1.9644	-3.0646	2.1994	-0.7084	0.0867	0.0319
n	-10.7114	42.6797	-64.3944	45.9682	-16.1954	2.9372	1.0445
n'	-6.5404	26.7911	-42.0120	31.3318	-11.3383	1.9112	0.9986
C_3	20.9084	-87.8859	141.7722	-112.2369	47.3815	-11.4564	14.6309

5.3.2.1 Ti-6Al-4V

Graphs of the flow curves obtained from axisymmetric compression of HDH Ti-6Al-4V specimens produced by FAST are shown in Fig. 5.12. The drop in steady-state flow stress between 850°C and 950°C is much greater than 950°C to 1050°C. This is linked with the similar pattern of the non-linear reduction of the harder to deform α phase volume fraction as temperature increases [113].

There are two types of flow curves apparent; those exhibiting flow softening after a peak stress until a steady-state value is reached, and those showing near constant steady-state flow behaviour after an initial amount of work hardening. All the strain rates at 850°C show approximately equal amounts of flow softening behaviour after a peak stress is reached. All strain rates at 950°C appear to show flow softening when only corrected for frictional effects, but when deformational heating is corrected for it can be seen that this is no longer the case. The curves at 1050°C display almost immediate steady state behaviour.

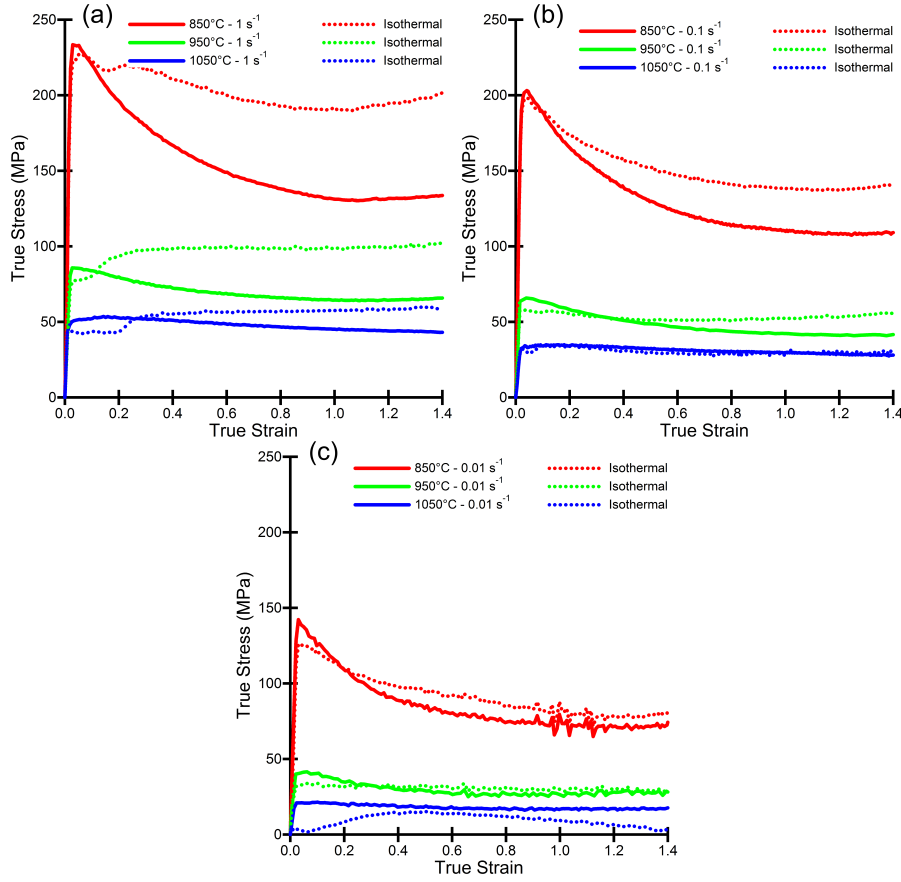


Figure 5.12 – Flow curves showing true stress vs. true strain behaviour at the labelled axisymmetric compression conditions for Ti-6Al-4V HDH powder processed via FAST.

The curves produced after isothermal correction show some features that are not typically expected. There is a clear kink in the curves, especially at strain rates of 1 s^{-1} . This is a result of the test specimen typically cooling to slightly below the nominal test temperature during transfer from the FTTU to the test furnace and then heating back above the test temperature in the furnace during deformation. This kink is not physically representative of the stress state occurring during the testing, but is the best that can be achieved within the limitations of the test data collected and the assumptions that allow the analysis.

The values for the flow curves agree with those reported in the literature for conventionally processed Ti-6Al-4V with a transformed β microstructure [40, 39, 100, 38, 114]. The transformation from flow softening behaviour when in the $\alpha + \beta$ phase region to continuous steady-state behaviour when in the single β phase region is also typical of conventionally processed $\alpha + \beta$ alloys.

There is considerable variation in the values of Q_{def} reported in the literature. Examples in the range 530-720 kJmol⁻¹ are cited in Table 5.2, but values as low as the self-diffusion in β titanium (153 kJmol⁻¹) were discovered. As discussed, the large variation can be probably be attributed to the vast range of starting microstructures, testing conditions, and calculation methods used in the different studies; the value calculated in this work was amongst the highest seen at 733 kJmol⁻¹. This may be related to the slightly elevated levels of interstitial elements compared to conventional aerospace grade Ti-6Al-4V. Alternatively, the microstructure produced after FAST processing at the conditions used in this study is not typical of conventionally processed Ti-6Al-4V that was tested in the majority of the reported research. However, the calculated value for Q_{def} is certainly within the correct order of magnitude, which indicates that Ti-6Al-4V HDH consolidated via FAST is behaving in a manner similar to conventionally processed material.

Light micrographs of the Ti-6Al-4V HDH etched with Kroll's reagent after hot compression are shown in Fig. 5.13 for high strain (~ 2.1) and Fig. 5.14 for lower strain (~ 1.1). If deformed below the β transus temperature the microstructure exhibits a bi-modal morphology, and when deformed above the β transus temperature the microstructure has very fine acicular α laths in transformed β grains, due to the water quenching. The microstructures vary depending upon the deformation temperature, strain rate, and strain.

At higher strains in the central region there is less primary α , at every strain rate, when deformation occurs at 950°C compared to 850°C. The primary α is elongated perpendicular to the compression axis and is more continuous as the strain rate increases. At 0.01 s⁻¹ and 850°C and 950°C the α become approximately equiaxed through globularisation. The amount of globularisation decreases within increasing strain rate and decreasing temperature. There is a reduction in prior β grain size as strain rate increases at 1050°C, and the grains tend to more elongated perpendicular to the compression direction. There is obviously an order of magnitude less time at each increment of strain rate, which limits the amount of grain growth possible. There are no observable wedge cracks at the grain triple points, or micro-voids, in the microstructure.

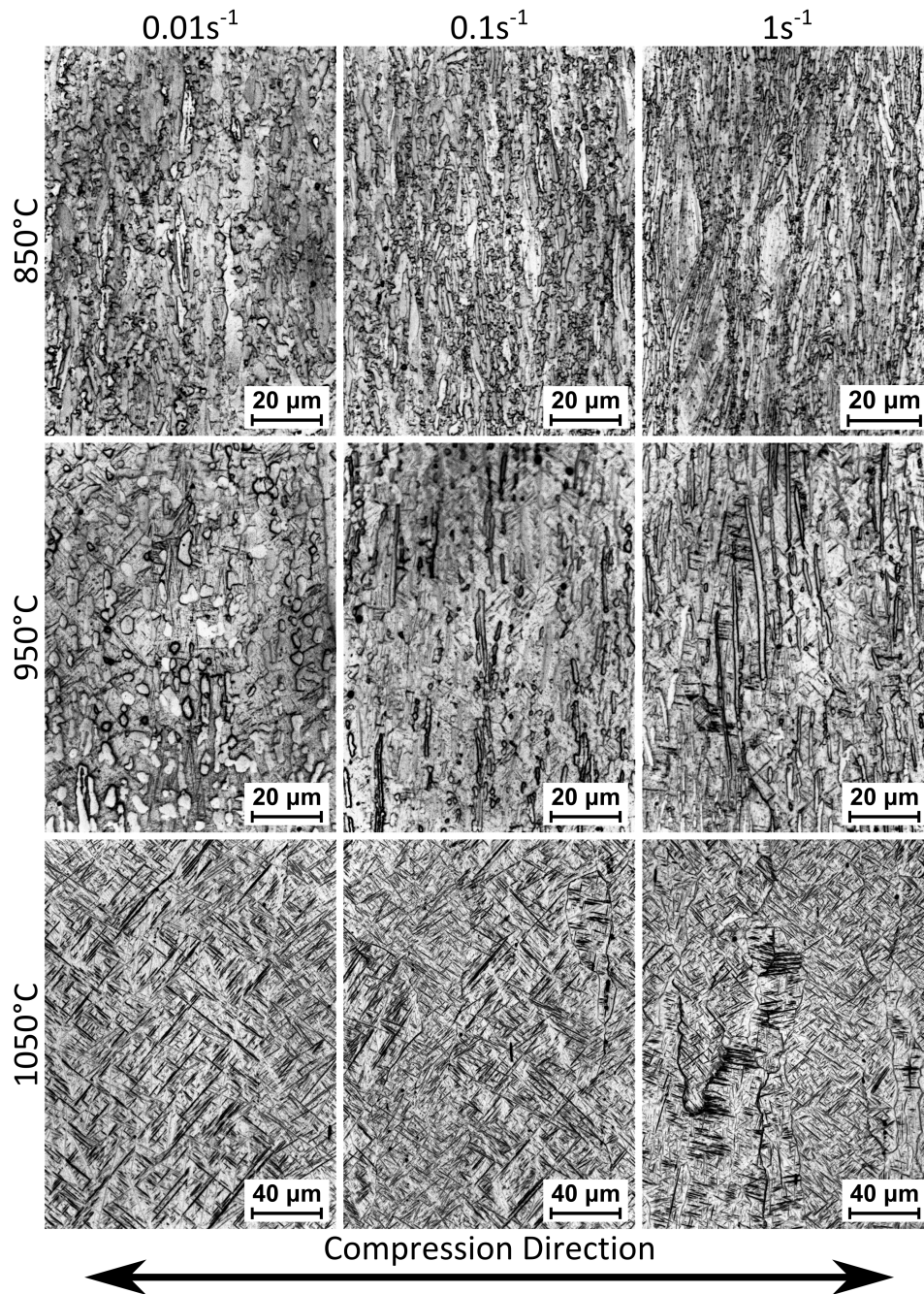


Figure 5.13 – Light micrographs of the higher strain central regions of the deformed Ti-6Al-4V HDH FAST specimens.

At lower strains in the edge region there is not a significant change in microstructure from that observed after FAST. The most noticeable change is at 1050°C where the grain boundary α is no longer present on the transformed structure is much finer. At the test temperatures below the β transus temperature there are coarser primary α laths surrounded by a finer transformed

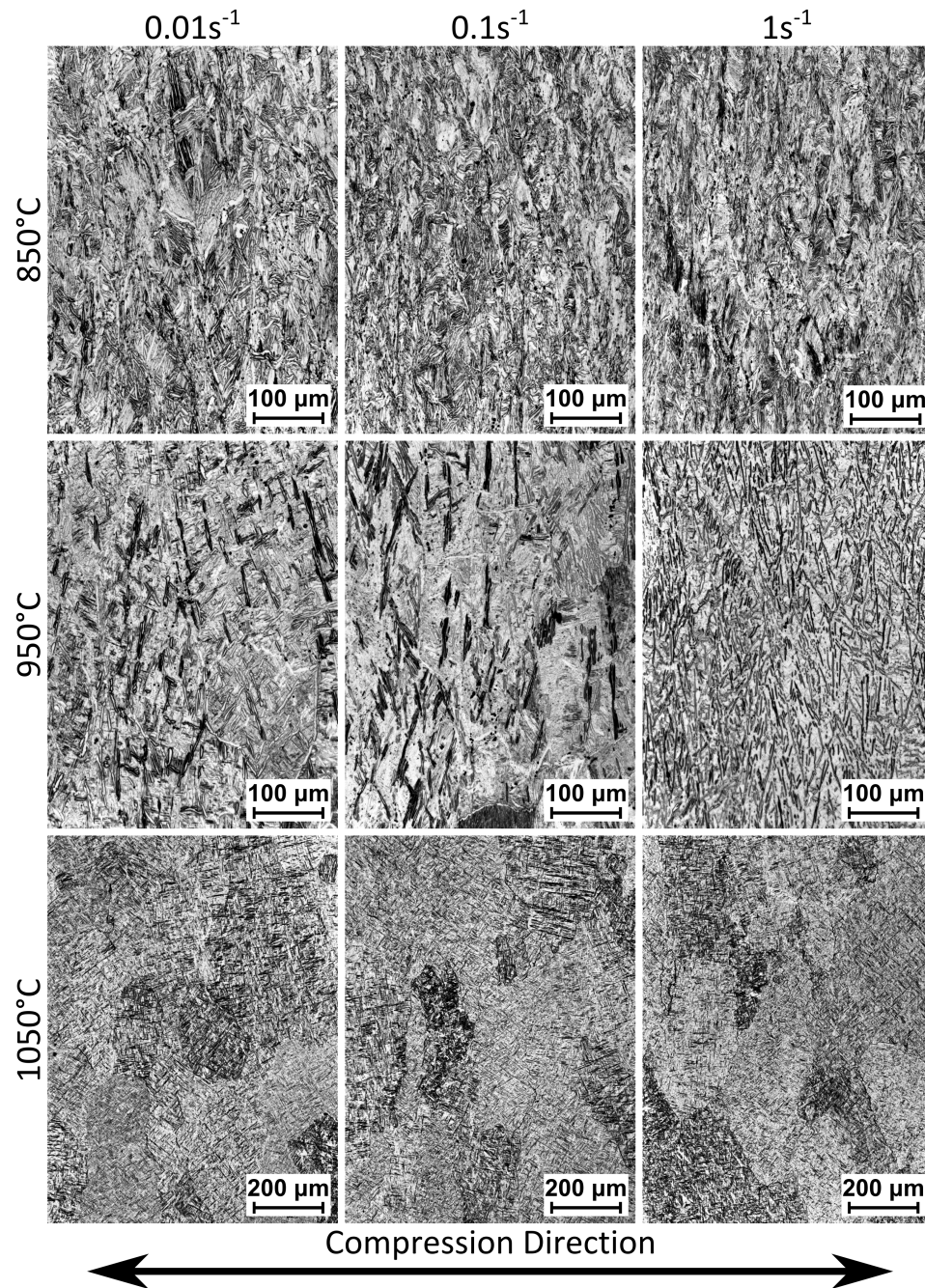


Figure 5.14 – Light micrographs of the lower strain edge regions of the deformed Ti-6Al-4V HDH FAST specimens.

structure. Unlike in the high strain regions there has not been significant rotation of the α laths perpendicular to the compression direction, although there is a slight elongation of the prior β grains. There is some kinking/buckling of the the primary α laths visible, which is the precursor to the onset of globularisation [42].

5.3.2.2 Rutile

Graphs of the flow curves obtained from axisymmetric compression of PS rutile-derived alloy specimens produced by FAST are shown in Fig. 5.15. The curves show typical behaviour associated with hot deformation of $\alpha + \beta$ alloys. Again after friction correction the majority of the curves show flow softening behaviour, especially at 850°C. This is reduced and in some cases removed after isothermal correction so that only the 850°C curves exhibit it after correction. This is analogous to the behaviour of the Ti-6Al-4V except that the level of flow softening is much lower. It is difficult to give context to the value of Q_{def} calculated for the rutile-derived alloy as it has not been reported upon previously.

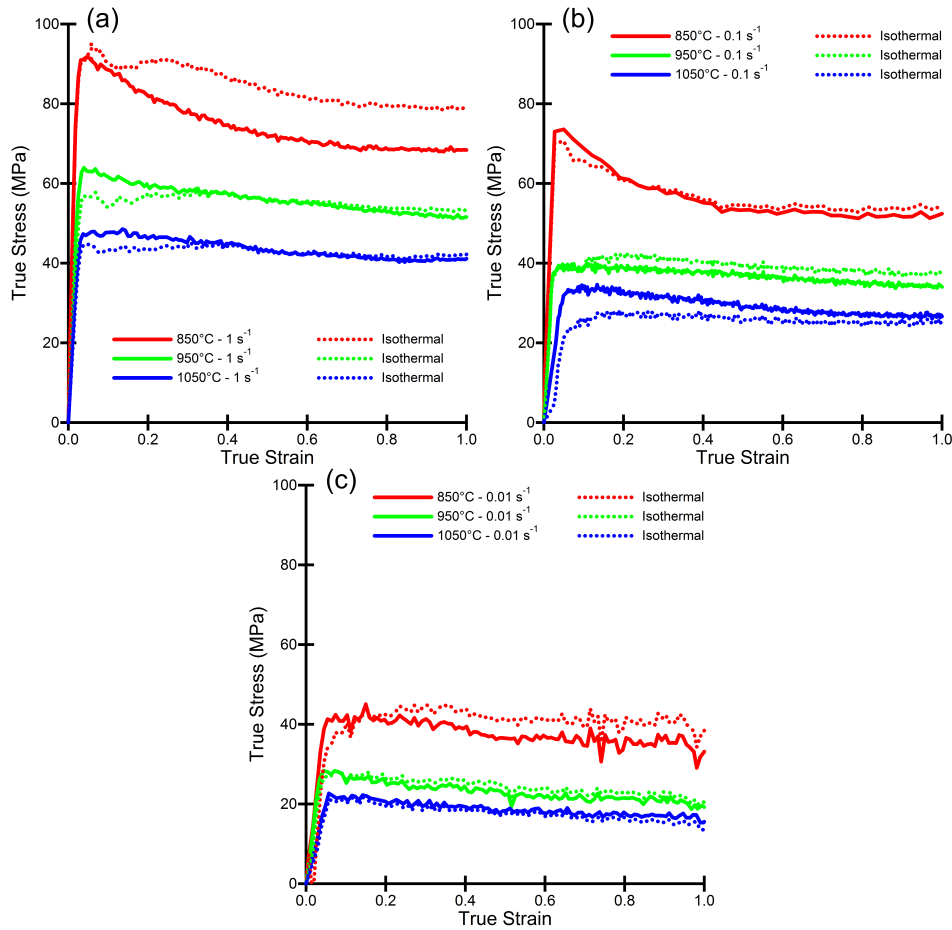


Figure 5.15 – Flow curves showing true stress vs. true strain behaviour at the labelled axisymmetric compression conditions for rutile-derived PS powder processed via FAST.

Similarly to HDH Ti-6Al-4V the drop in steady-state flow stress between 850°C and 950°C is greater than between 950°C to 1050°C, presumably due to a similar α phase volume fraction relationship. There appears to be a

relationship between temperature and strain rate such that a 100°C decrease in temperature is counteracted almost equivalently by a factor of ten decrease in strain rate; 1050°C - 1 s⁻¹, 950°C - 0.1 s⁻¹, and 850°C - 0.01 s⁻¹ have approximately equivalent steady state values of flow stress, as do 950°C - 1 s⁻¹ and 850°C - 0.1 s⁻¹, and 1050°C - 0.1 s⁻¹ and 950°C - 0.01 s⁻¹.

It initially appears as though the rutile-derived alloy is much easier to deform than Ti-6Al-4V. After the dwell temperature and pressure study, see section 4.3.1.2, it appeared as though the rutile-derived alloy had a β transus temperature above 990°C as below that point there were not signs of homogenisation or a transformed microstructure. However, it can clearly be seen from Fig. 5.16 and Fig. 5.17 that the microstructures displayed after compression at 950°C (and 1050°C) are those of an alloy that has been rapidly cooled from above its β transus temperature. There is a Widmanstätten/colony structure with finer α laths than the starting material and a removal of grain boundary α . Work undertaken since the testing presented here has shown that the β transus temperature is in the region of ~900°C [115], approximately 100°C lower than Ti-6Al-4V. This is reflected in the observed flow stresses, where the values of the curves at 850°C and 950°C for the rutile-derived alloy correspond to the Ti-6Al-4V curves at 950°C and 1050°C respectively. It is thought that the high levels of oxygen (more than treble the PS levels) in the angular-spongy rutile-derived alloy were responsible for the apparent high β transus temperature that led to the selection of the testing conditions for this study.

Cross-polarised light micrographs of the PS rutile-derived alloy after hot compression are shown in Fig. 5.16 for the highest strain and Fig. 5.17 for lower strain. When deformed at 850°C the microstructure shows classical bi-modal sub-transus $\alpha + \beta$ alloy behaviour as shown in the preceding section 5.3.2.1 for Ti-6Al-4V. As already discussed when deformed at 950°C and 1050°C the microstructure shows features of being processed above the β transus temperature.

At 850°C and higher strain there is a rotation perpendicular to the compression direction and subsequent break up of the primary α laths in the globularisation process. This becomes more pronounced with decreasing strain rate and there is also a slight coarsening of the primary α , possibly due to the additional time

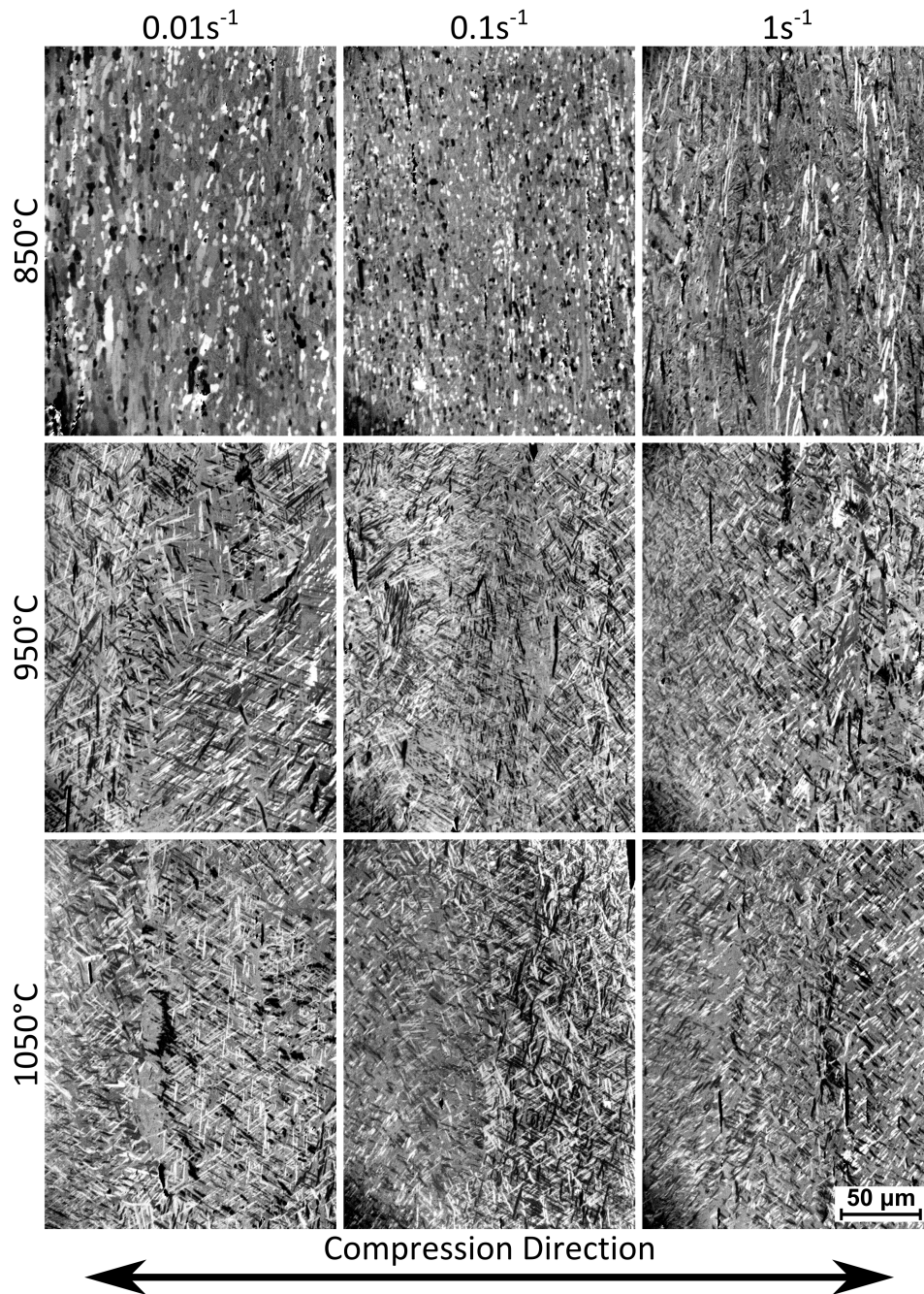


Figure 5.16 – Light micrographs of the higher strain central regions of the deformed rutile-derived PS FAST specimens.

at temperature. The behaviour at 950°C and 1050°C is very similar to that described for Ti-6Al-4V at 1050°C. There is a reduction in prior β grain size and the grains tend to more elongated perpendicular to the compression direction. There is also a refinement of the α laths in transformed β grains due to the water quenching causing a more rapid cooling rate than after FAST processing.

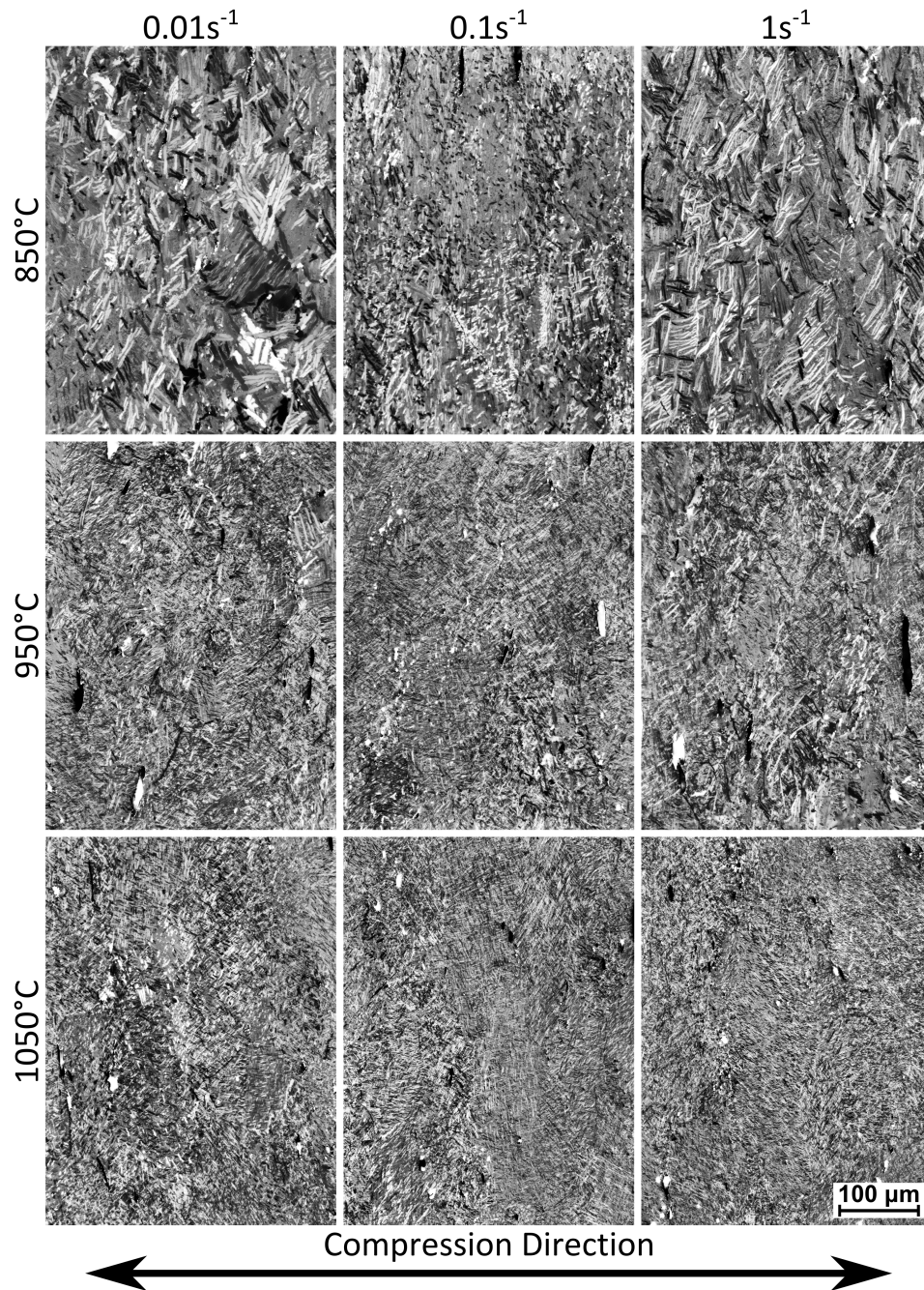


Figure 5.17 – Light micrographs of the lower strain edge regions of the deformed rutile-derived PS FAST specimens.

At lower strains in the edge region there is again not a significant change in microstructure from that observed after FAST. At 950°C and 1050°C the prior β grain size remains similar and the α laths have been refined due to increased cooling rate. At 850°C, below the β transus temperature, there are primary α laths with thickness similar to the starting structure in a finer transformed structure. There has not been significant rotation of the α laths but some

kinking/buckling is visible, and there is a slight elongation of the prior β grains.

The porosity that was seen after FAST is still present; visible as the black areas on the micrographs. In general the pores have been deformed and elongated perpendicular to the compression direction. There does not seem to have been significant removal of porosity during the compression step. If there is gas (typically argon) from the spheroidisation process trapped in the pores found within the particles then it has been shown to be extremely difficult to remove during ALM - HIP - heat treatment processing [116]. It is expected similar mechanisms will also occur in FAST with subsequent thermomechanical processing as the diffusivity of argon in titanium is extremely low [117].

5.3.2.3 CP-Ti

Graphs of the flow curves obtained from axisymmetric compression of HDH CP-Ti specimens produced by FAST are shown in Fig. 5.18. It can be seen that after isothermal correction there is an initial period of work hardening followed by a regime of near steady-state flow with little flow softening observed, which correlates with what has been previously observed. Prasad et al. deformed CP-Ti with 0.15 wt.% oxygen content at 800°C and 0.001-100 s⁻¹ [118] and their values match closely to this study. The steady-state region seen is likely due to the rate of dislocation creation equalling the annihilation through dynamic recovery processes [109].

The flow curves, microstructure, and activation energy reported for grade 2 CP-Ti by Weiss et al. [109] also correlate closely with the results seen in this study. A small amount of flow softening was also reported when deforming CP-Ti with a Widmanstätten starting microstructure compared to an equiaxed structure. This study had a Widmanstätten/colony starting microstructure and low-levels of flow softening were observed, except at 700°C - 1 s⁻¹ where it was more pronounced. The value of Q_{def} calculated is comparable with multiple literature sources, which gives confidence in the data collected.

Cross-polarised light micrographs of the CP-Ti HDH after hot compression are shown in Fig. 5.19 for the highest strain and Fig. 5.20 for lower strain.

At the higher strains as temperature increases and strain rate decreases the microstructure becomes closer to fully equiaxed. At each temperature when the strain rate is increased then there is a clear reduction in the size of the

equiaxed α grains, possibly due to spending less time at temperature. At each strain rate when the temperature is decreased the microstructure becomes less homogeneous. At 700°C there are large pancaked grains containing sub-grain structure (variation in contrast within the grain) surrounded by much finer equiaxed grains. The 700°C at 1 s⁻¹ test shows a different microstructure to the other tests. The deformational heating took this test above the β transus temperature and thus the majority of the refinement seen in the other test conditions has been lost in this case.

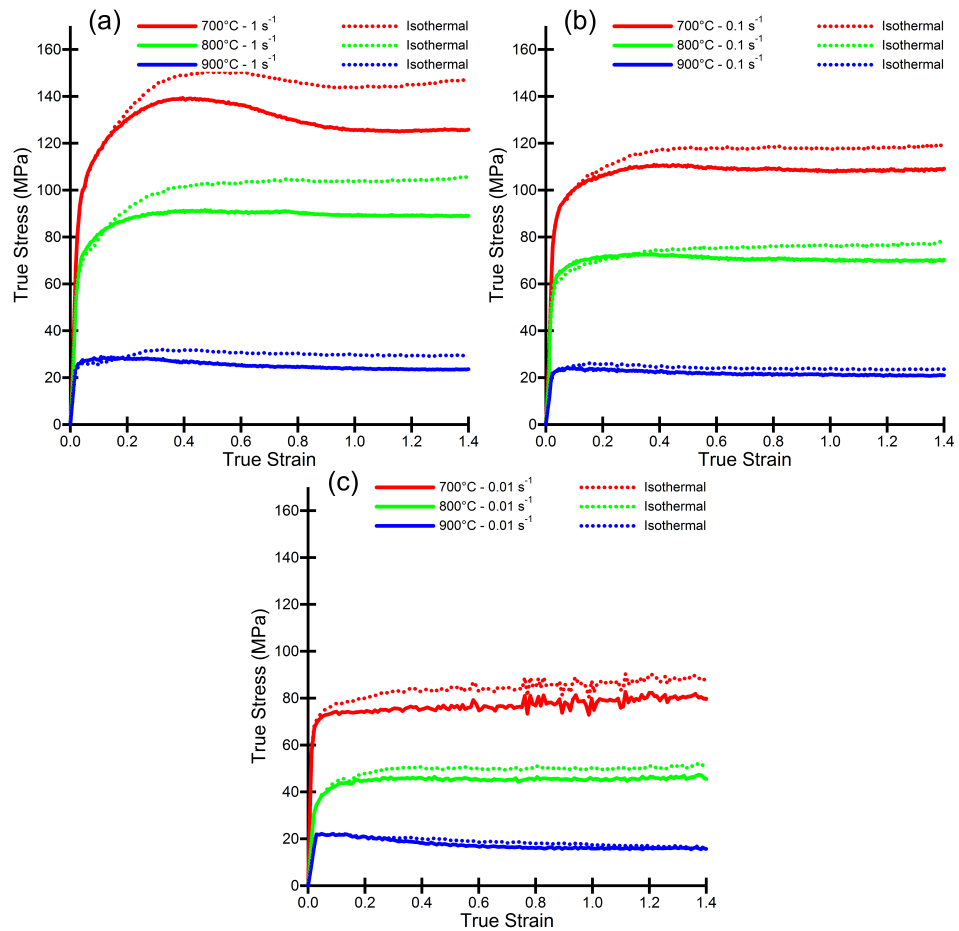


Figure 5.18 – Flow curves showing true stress vs. true strain behaviour at the labelled axisymmetric compression conditions for CP-Ti HDH powder processed via FAST.

At the edge of the specimens where there are lower strains there have been less pronounced changes from the starting microstructure. The α laths have not been completely broken up and equiaxed as at the higher strains but there has

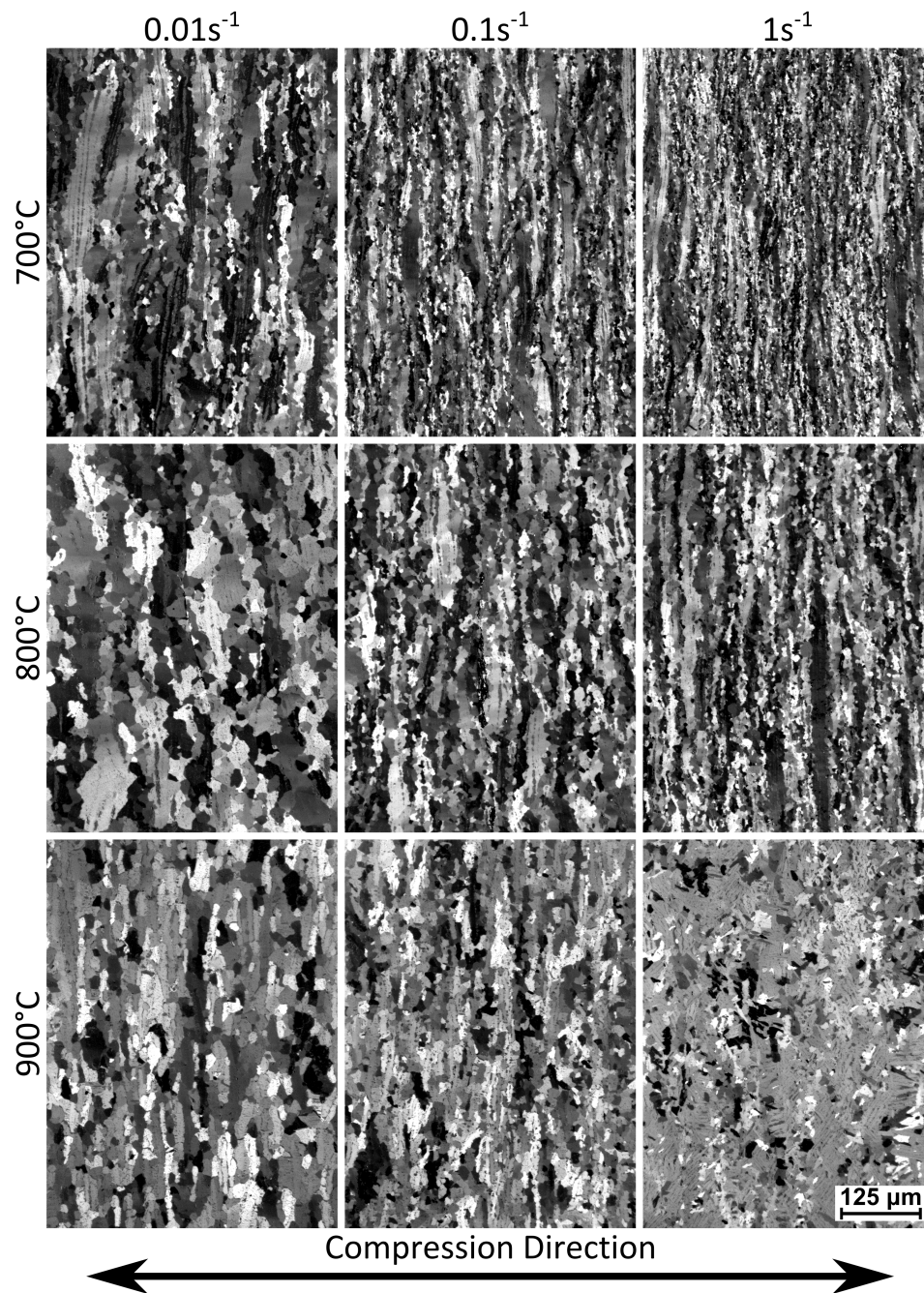


Figure 5.19 – Light micrographs of the higher strain central regions of the deformed CP-Ti HDH FAST specimens.

been significant rotation away from the compression direction with kinking and buckling also observed. The process to begin producing the equiaxed α phase has begun as there are some regions of very fine equiaxed α .

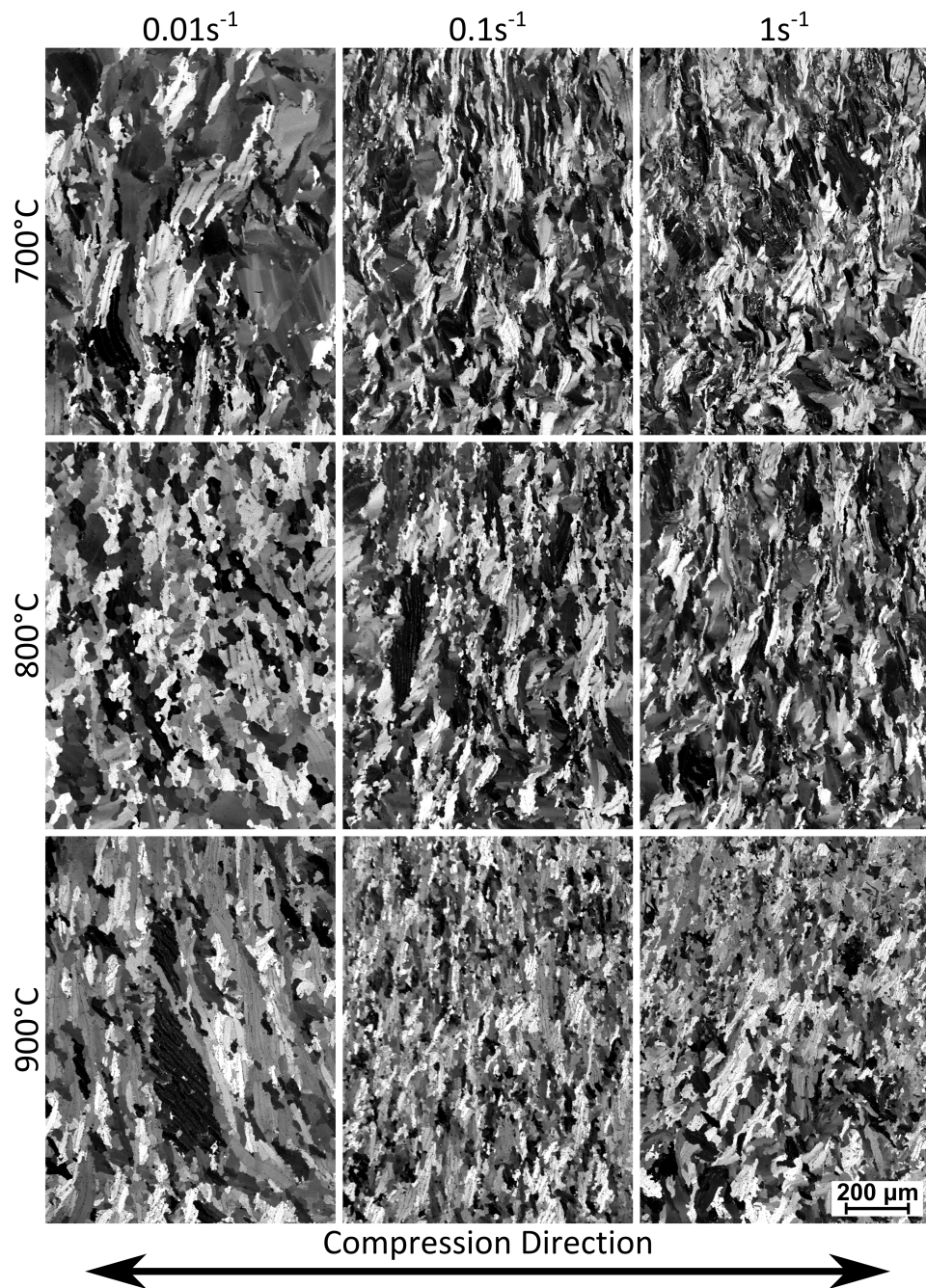


Figure 5.20 – Light micrographs of the lower strain edge regions of the deformed CP-Ti HDH FAST specimens. Post-Forge edge region

5.3.2.4 Ti-5553

Graphs of the flow curves obtained from axisymmetric compression of GA Ti-5553 specimens produced by FAST are shown in Fig. 5.21. For clarity only the isothermally corrected curves are plotted as due to the testing temperatures selected all the curves are in close proximity. All curves show a very small initial period of work hardening before flow softening to a region of approximate steady-state behaviour. The behaviour seen in the 1 s^{-1} curves is of interest as it shows the discontinuous yielding phenomenon usually only observed when deforming in the single β phase field [111]; the β transus temperature of Ti-5553 is $\sim 845^\circ\text{C}$. A period of work hardening is seen after the discontinuous yielding, before flow softening to a steady-state by a strain of 0.8.

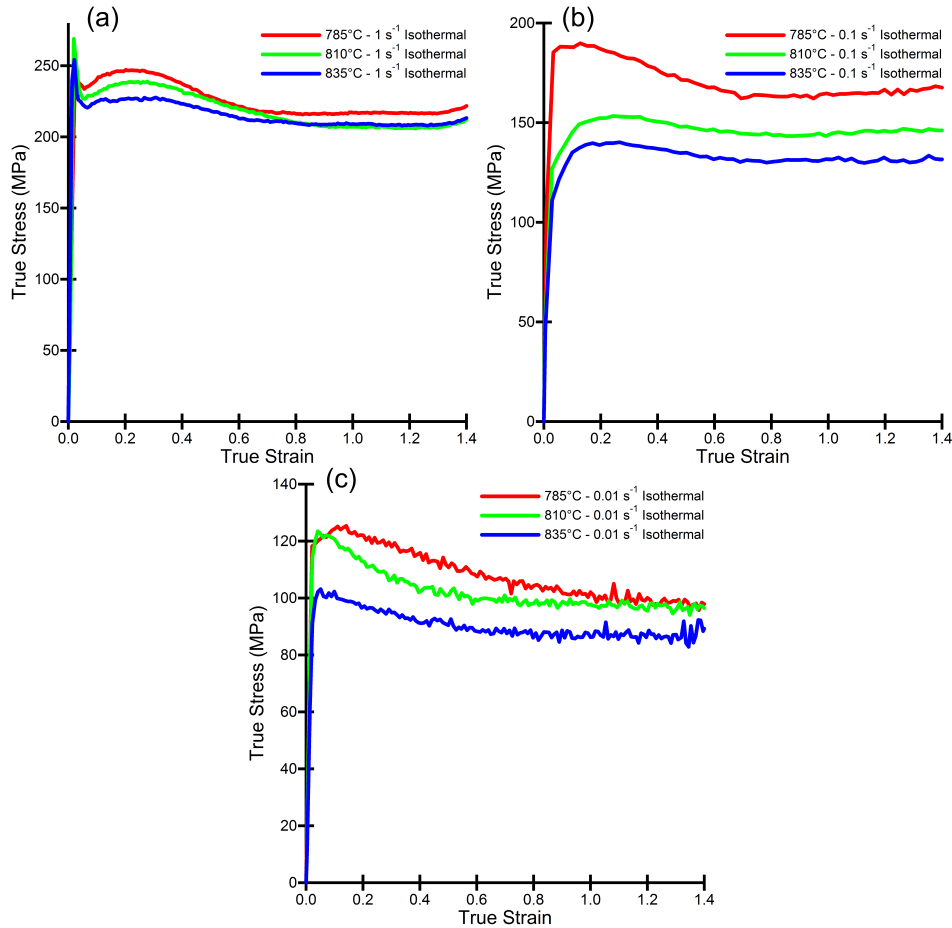


Figure 5.21 – Flow curves showing true stress vs. true strain behaviour at the labelled axisymmetric compression conditions for Ti-5553 GA powder processed via FAST.

Discontinuous yielding below the β transus temperature was also observed by Jones et al. [102]. They rapidly cooled a specimen held above the transus for 30 min to allow a fully β structure to form and deformed it below the transus where discontinuous yielding occurred. This was attributed to the slow precipitation kinetics of the α phase in Ti-5553 allowing retention of the β phase. The hold time at temperature before deformation in this work was 30 s and therefore it is possible that the almost fully β phase produced after FAST was retained; therefore allowing discontinuous yielding to be observed when deforming below the β transus temperature. Why this was only observed at a strain rate of 1 s^{-1} is not clear, although the additional time may be a factor. The small period of work hardening after discontinuous yielding has not previously been reported and is not seen on the friction corrected curves in this study. Therefore, the method of isothermal correction utilised may have introduced this period of work hardening, which is not realistic.

Light micrographs of the Ti-5553 GA etched with Kroll's reagent after hot compression are shown in Fig. 5.22 for the higher strains and Fig. 5.23 for the lower strains. The micrographs are not easy to correlate with those presented in the literature as, due to the fine nature of the α phase, scanning electron microscopy is more typically used. However, it can be observed that at the higher strains the amount of α phase appears to decrease with temperature as expected, but also with strain rate. It is not thought this is inherently due to the strain rate causing microstructural changes. It is more likely a by-product of longer time at temperature due to lower strain rates allowing increased precipitation and/or the deformational heating caused at the higher strain rates raising the temperature above the β transus.

The microstructures at a strain rate of 1 s^{-1} show little α phase presence, which supports the theory presented for the observed discontinuous yielding. At 1 s^{-1} the prior β grain boundaries also show increasing serration and at 835°C (and at $835^\circ\text{C} - 0.1 \text{ s}^{-1}$) there appear to be small recrystallised grains formed on the prior β grain boundaries, which was also reported by Weiss et al. [111].

Weiss et al. [111] also reported values of activation energy Q_{def} in the range of $130\text{--}175 \text{ kJmol}^{-1}$ and Jones et al. [101] as 183 kJmol^{-1} . This supports the value of 137 kJmol^{-1} calculated in this study. These values are very close to the activation energy of self-diffusion in β titanium of 153 kJmol^{-1} . The calculated

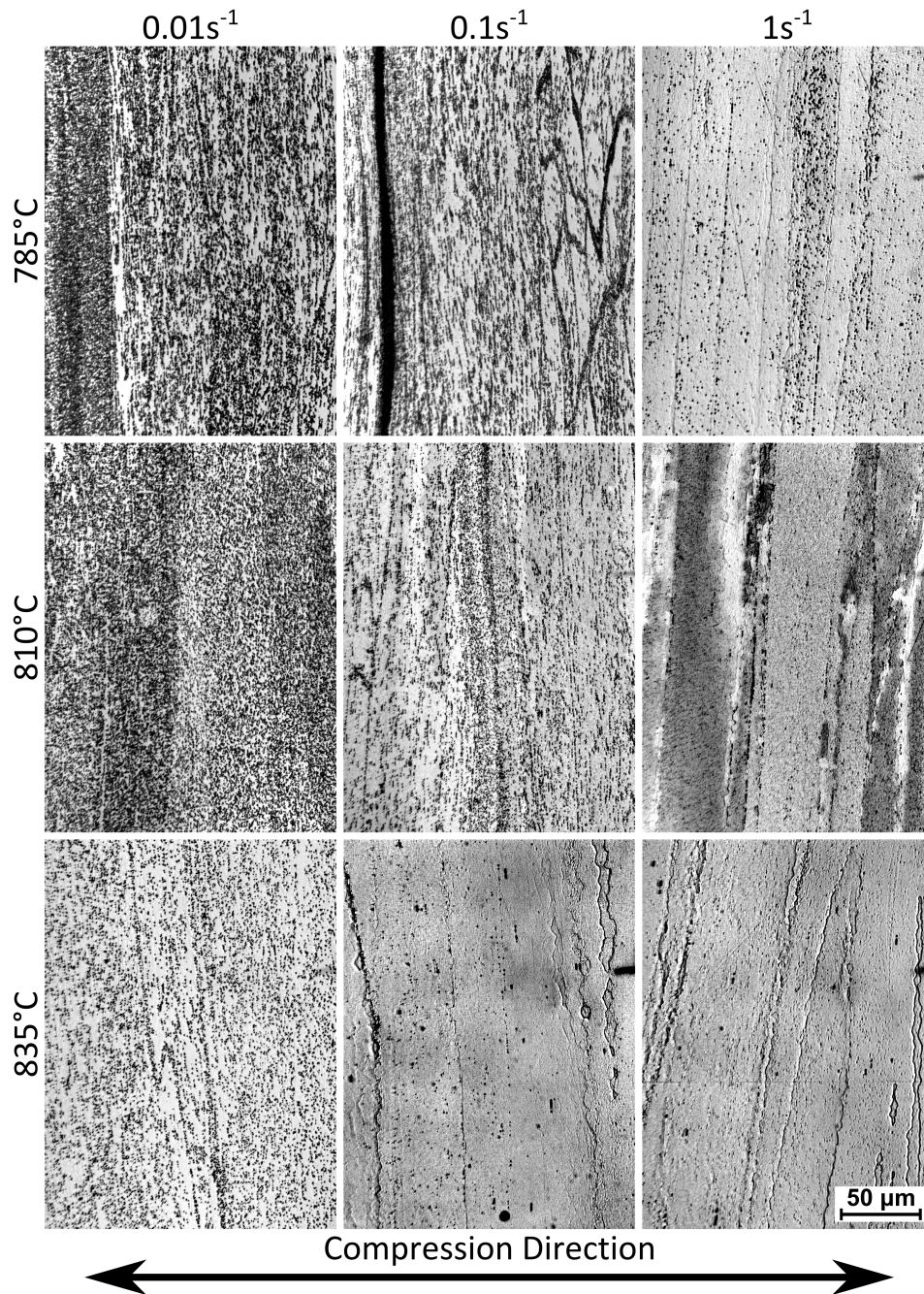


Figure 5.22 – Light micrographs of the higher strain central regions of the deformed Ti-5553 GA FAST specimens.

value of Q_{def} in conjunction with the flow curves and microstructures indicate the dominant deformation mechanism. As the microstructure is essentially small hard α particles in a β matrix it is likely the matrix accommodates the majority of deformation. This, along with the value of Q_{def} , would be consistent with the mechanism being dynamic recovery in the β phase. Dynamic recovery is

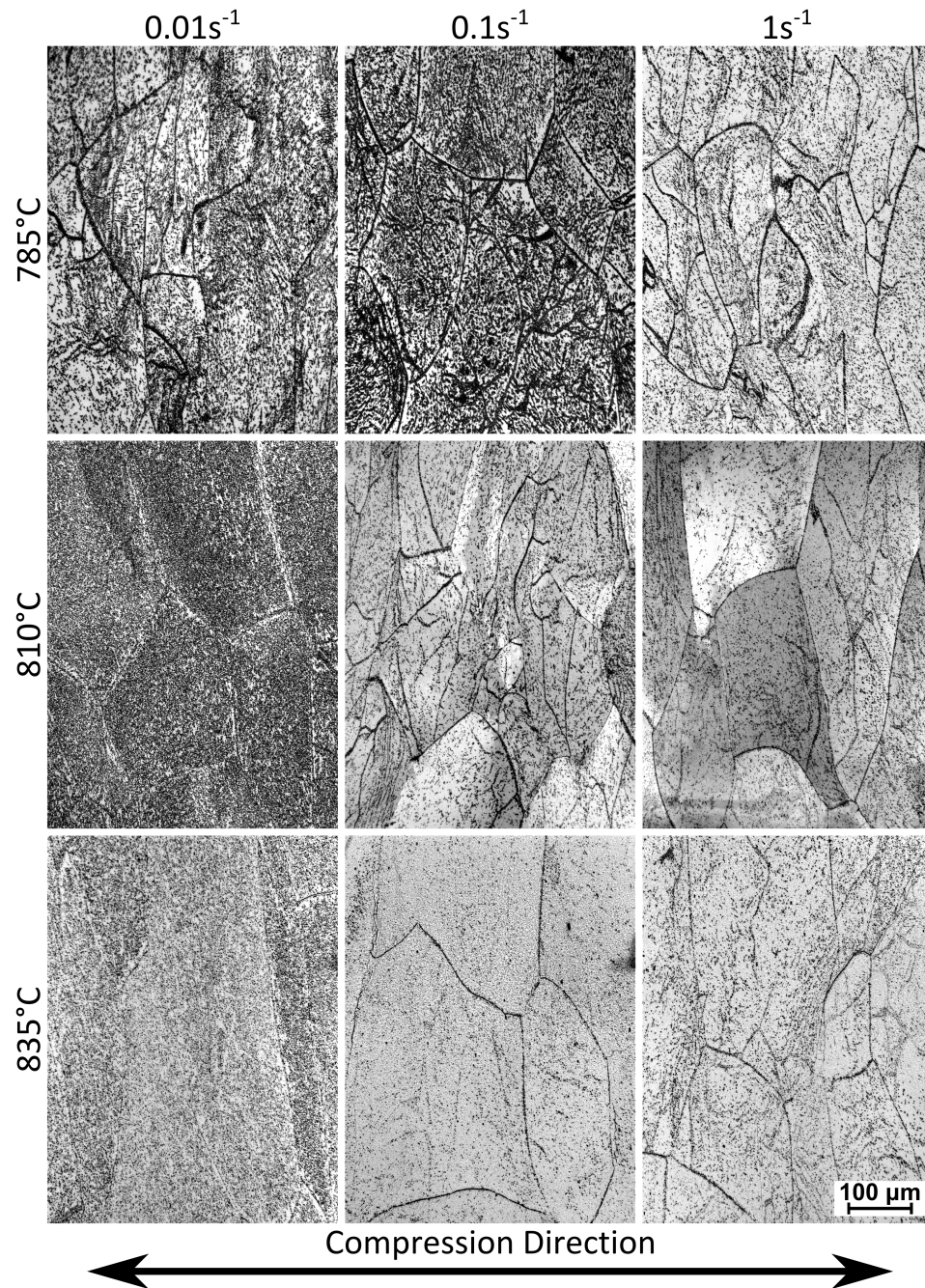


Figure 5.23 – Light micrographs of the lower strain edge regions of the deformed Ti-5553 GA FAST specimens.

facilitated by dislocation climb, which is analogous to vacancy diffusion, thus the activation energy should be similar to that for self-diffusion in β titanium [101].

5.3.3 Integrating the Generated Material Data into FE Modelling

The methodology used to develop a constitutive equation to describe the flow behaviour of the alloys did not produce satisfactory results, see an example for Ti-6Al-4V HDH in Fig. 5.24. The constitutive equation curves are significantly different to the curves produced from the experimentally measured values. It would be possible to manipulate the coefficients reported in section 5.3.2 to attain a better fit, although it was felt that this would become a “curve-fitting” exercise rather than a representation of reality. Therefore, the isothermal true stress data at a series of discrete strains were used instead as the material model for the FE simulation. The results of the modelling of the Ti-6Al-4V are shown in this section to demonstrate the validity of the approach, and that it could also be applied to the other alloys.

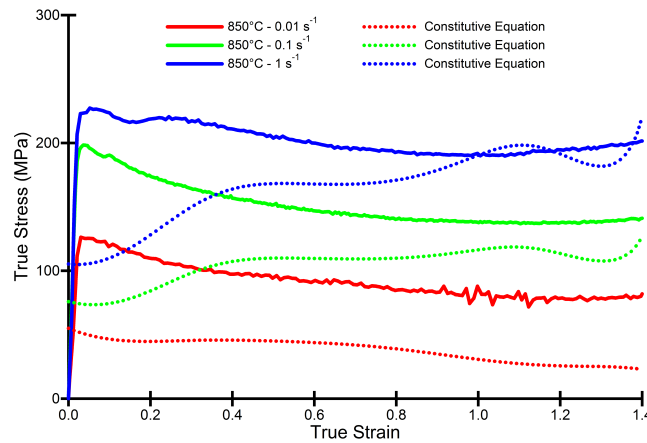


Figure 5.24 – Graph showing the disparity in values between the experimentally measured true stress values and those calculated through the developed constitutive equation for Ti-6Al-4V HDH.

Data on the load upon the upper tool with respect to its displacement (stroke) were extracted after the FE simulations at each experimental condition and are directly compared with the load and displacement data logged by the TMC in Fig. 5.25. The model shows excellent agreement with the experimental data indicating that the friction conditions used and material model have been successfully integrated. This result is largely to be expected as the tabulated data used for the material model was calculated from the experimental data. However, it is always necessary to validate that simulations are producing the expected outputs. The limitation of the tabulated data material model is that it is unlikely to work accurately outside of the conditions it contains.

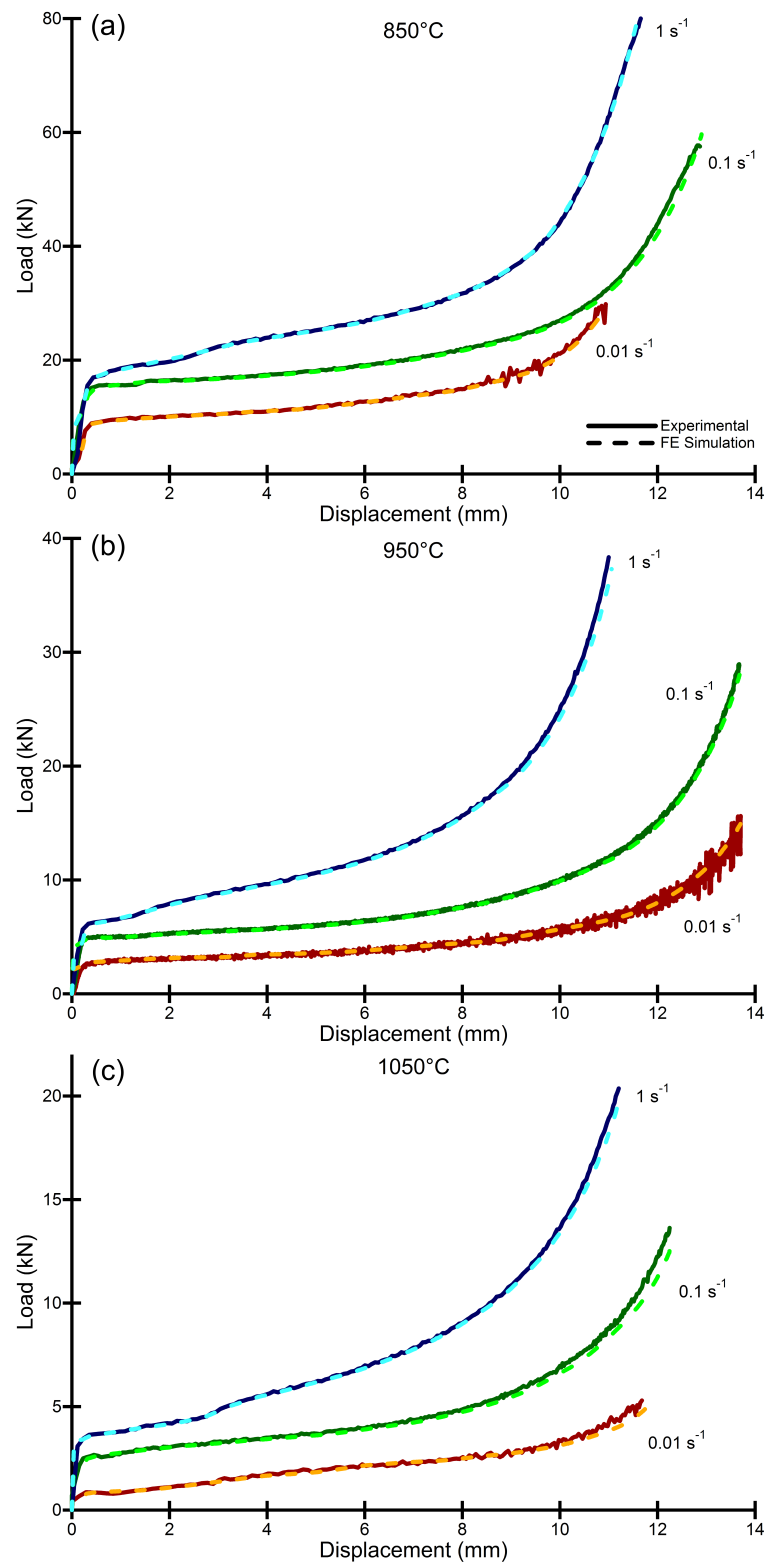


Figure 5.25 – *Ti-6Al-4V HDH Experiment vs. Simulation Load-displacement curves*

5.3.4 Vickers Microhardness Testing

Table 5.7 – Vickers microhardness values for the Ti-6Al-4V HDH powder after FAST processing and subsequent hot axisymmetric compression at the listed conditions.

Temperature	Strain Rate		
	0.01 s ⁻¹	0.1 s ⁻¹	1 s ⁻¹
FAST	318±3		
850°C	353±3	357±2	374±4
950°C	395±2	403±1	404±4
1050°C	393±5	403±3	396±4

An indication of the mechanical properties of a material can be obtained through microhardness values. The results of the Vickers microhardness indent testing are shown in Table 5.7. The compression testing at all conditions causes an increase in hardness, which would approximately correlate with an increase in tensile strength. There is a significant increase in hardness when the compression temperature is increased from 850-950°C, but there is no noticeable effect when the temperature is increased from 950-1050°C. This is possibly due to the increased amount of harder martensite, and reduced primary α phase, produced by quenching from higher in the $\alpha + \beta$ phase field, and then from the β phase field. The trend at 850°C sees the hardness increase at the highest strain rate, but at 950°C and 1050°C the hardness is largely unaffected by strain rate. It is possible that at the lower temperature and higher strain rate that the dislocations produced do not have time to recover during the deformation causing the increase in hardness.

5.4 Conclusions

Consolidation of titanium powder via FAST produces preforms that behave in a manner very similar to conventionally processed material for all four alloys tested in this study. The observed behaviour correlates both in terms of flow data and microstructural evolution. As expected the flow stress increases with increasing strain rate and decreasing temperature for each material.

The rheology data produced for Ti-6Al-4V HDH was used as a tabulated data material model for FE simulation of the axisymmetric compression testing using the software DEFORM. The simulation was able to accurately reproduce the load and displacement data seen in the experimental compression tests. This will in future allow simulation of more complex forging processes, which will help with developing a shaped FAST preform billet to allow optimisation of the forging step.

Microstructural analysis of the four alloys at the various testing conditions has also shown that significant microstructural refinement can be achieved after FAST processing. A fully globularised bi-modal microstructure was produced for the Ti-6Al-4V HDH. This microstructural refinement is also seen in the hardness data gathered for the Ti-6Al-4V, which indicates that the FAST and thermomechanically processed material should have tensile properties to compete with conventional melt-wrought product.

The work in this chapter and the previous chapter has demonstrated the fundamentals of a cost-effective processing route to consolidate titanium alloy powder to semi-finished near net shape components in two processing steps. Using FAST to produce a preform billet, followed by a one-step precision forge to achieve the desired final shape and microstructure.

Investigating the production of shaped preforms via FAST is now of great importance. Successfully producing shaped preform billets, which behave in manner similar to the material seen in this chapter, will allow future optimisation of the processing route. There may be the potential allow a “one-step” forging operation to be performed to finish shaped FAST preforms to near net shape components. This work is undertaken in the following chapter to ascertain whether a truly cost-effective processing route can be developed.

6. FAST-*forge* – a new cost-effective hybrid processing route for consolidating titanium powder into near net shape forged components

This chapter is based upon the paper published in the Journal of Materials Processing Technology by Weston et al. [67]. The final publication is available from Elsevier via: <http://dx.doi.org/10.1016/j.jmatprotec.2016.12.013>. Permission for reuse has been obtained and the agreement can be seen in Fig. B.3 in appendix B.

6.1 Introduction

The capability of FAST to successfully sinter a range of commercial and development titanium alloy powders was demonstrated in chapter 4 and also in Weston et al. [65]. It was shown that FAST is tolerant of powder morphology and chemistry, and high heating rates could be used to lower processing times with minimal effect on microstructure or density. Simple disc shapes of constant thickness achieved uniform powder packing and consolidation without density gradients, which allows microstructural homogeneity throughout specimens, even when scaling up to larger sizes (250 mm diameter and 5.5 kg). Additionally, limited interstitial pick-up from the starting powder levels was measured for carbon, oxygen, and nitrogen (between 100-250 ppm). The ability to utilise feedstocks that are larger and angular, including those from alternative extraction methods or even recycled swarf, and still achieve high density and homogeneous microstructures means that FAST has an advantage over traditional sintering operations as these feedstocks are potentially of a significantly lower-cost.

Chapter 5 investigated the response of a range of alloys to a subsequent, post-FAST, thermomechanical processing step and heat treatment in order to

demonstrate that components with complex geometries for critical applications needing wrought properties could be produced. As previously stated, it is thought that the geometries and mechanical properties required by most titanium alloy components will not generally be producible by using FAST as a consolidation process in isolation. The large-grained transformed β microstructure with continuous grain boundary α produced when sintering above the β transus temperature is not optimal for components that need a good balance of properties; a bi-modal microstructure, produced by hot-working (high) in the $\alpha + \beta$ phase region, offers advantages for most applications [37]. It was shown that powder that has undergone consolidation via FAST into preform billet material behaves in a manner largely similar to conventionally processed melt-wrought product when subjected to thermomechanical processing; both in terms of microstructural evolution and mechanical properties. Rheology data gathered from the experimental work was also successfully integrated into finite element simulations of the hot axisymmetric compression tests, which will allow simulation of more complex forging operations in the future.

In summary, so far it has been possible to produce simple disc specimens via FAST and then show excellent forgeability whilst producing a range of microstructures through subsequent thermomechanical processing. This route would allow the production of components, but multiple forging operations would be required to go from the disc/cylinder shaped FAST preforms to the final geometry. Additionally, this is not likely to be a near net shape (NNS) process so significant material wastage would occur. The reduction of thermomechanical processing to a minimum is necessary in order for any processing route to be the most efficient and cost-effective possible, see Fig. 1.1. The ultimate goal, and it is believed to be possible with sufficient process design and control, is that the post-FAST processing could be a one-step NNS forging operation. In order to achieve this it is likely that a semi-complex shaped preform will be required. It would be possible to extract such a shape from bulk FAST discs, as was done in chapter 5, to allow the reduction of thermomechanical processing costs but the additional complexity and time required to produce the preform would be likely to more than counteract this. Therefore, to demonstrate a truly cost-effective processing route, whilst achieving the desired post-forge geometry and strain levels, and thus microstructures, a preform billet with shape and definition will need to be produced directly via FAST.

Finite element (FE) modelling has become a common tool to provide load and microstructural predictions during complex forging operations, although a comprehensive data set is required to achieve this. Therefore, from a process modelling point of view, the effect of thermomechanical processing parameters on microstructural evolution needs to be understood due to their inevitable variation, even when nominally isothermal forging. Levels of strain, strain rate and temperature can significantly affect the microstructure of titanium alloys and a large test matrix would be needed to characterise this if using traditional cylindrical axisymmetric compression specimens. The novel double truncated cone testing approach developed by Jackson et al. [50] allows this microstructural characterisation in far fewer tests due to the predictable and controlled strain distribution in the forged specimen. A double cone specimen can be tested at a set temperature and strain rate to give information relating to a larger range of strains compared to a cylinder, from almost zero at the edge to high strains in the centre. Small specimen dimensions limit temperature variations so that a good approximation of isothermal forging can be realised, as well as allowing metallographic preparation and inspection of the entire specimen.

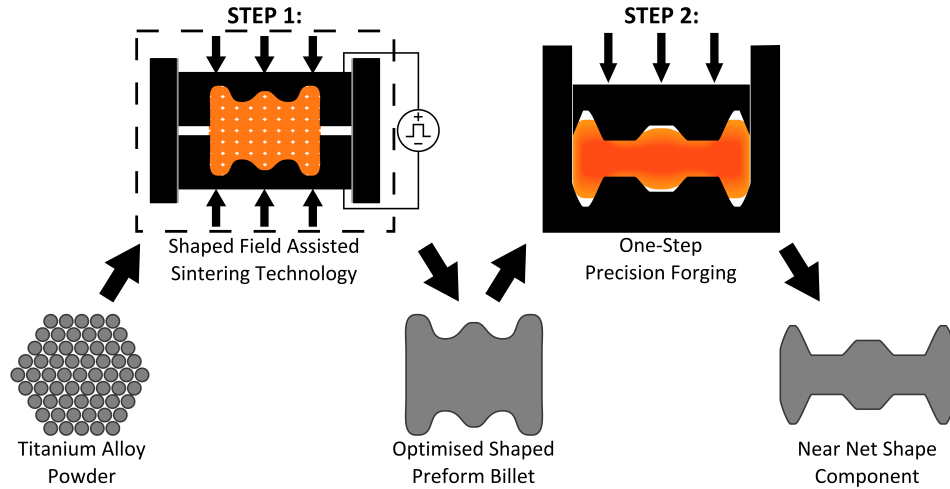


Figure 6.1 – Schematic diagram outlining the two-step hybrid “FAST-forge” process – a proposed cost-effective solid-state processing route for producing titanium alloy components from powder.

The aim of this chapter is to demonstrate, at the laboratory-scale, that it is possible to produce titanium components from powder in two steps, as shown schematically in Fig. 6.1; using Field Assisted Sintering Technology to produce a shaped preform billet, which is finished to NNS with a one-step precision forging operation. Specifically, double truncated cones will be produced that will then

be hot upset forged to further assess forgeability and microstructural evolution of shaped-FAST material. Depending upon the application it is envisaged that a subsequent heat treatment would allow tailoring of the microstructure if required and/or a minimal finish machining operation would produce an acceptable surface roughness. This novel solid-state hybrid processing route, termed by Weston and Jackson as “FAST-forge” [67], will allow production from powder of components with forged properties for dynamically loaded applications. It is believed that the mechanical properties achieved by the additional forging of FAST material will allow FAST-forge products to be used in areas and applications not conventionally considered possible for as-sintered PM components. It is also envisaged that with further development FAST-forge will become disruptive technology for a range of sectors. The combination of this cost-effective consolidation method with powder from an alternative (potentially lower-cost) extraction method will provide a step change in the economics of titanium components.

6.2 Experimental Approach

The experimental approach adopted in this chapter aimed to demonstrate four key developments. Firstly, the capability of FAST to produce simple shaped preforms to be used in the FAST-forge process. Secondly, to show the possibility of utilising alternative materials for the FAST mould assembly. Thirdly, that the FAST-forge concept was viable through a laboratory-scale demonstration, see Fig. 6.2. Fourthly, to link microstructural evolution of FAST produced preforms to thermomechanical processing parameters by utilising the double truncated cone specimen geometry as the shaped preform billet; thus gaining valuable information for future process optimisation through FE modelling.



Figure 6.2 – Photograph demonstrating the outcome at each stage of the two-step FAST-forge process; the starting Ti-6Al-4V HDH powder (left) to the intermediate shaped preform billet, a double truncated cone FAST specimen with a light surface machine (centre), and the final forged specimen (right).

An initial study was undertaken to investigate any limitations associated with producing double cone preforms via FAST. This took the form of reducing the upper and lower diameters of the truncated cone from 20 mm to 0 mm (in 5 mm increments), see Fig. 6.3, whilst utilising varying masses of powder. Technical drawings of these shaped graphite inserts can be found in appendix A, see Fig. A.3. The preforms were assessed for die filling, density, and microstructural homogeneity. Additionally during this study, the effect of changing the mould assembly material from all-graphite to all-steel was studied; and a mixture of the two materials with 5 mm diameter double cone inserts was investigated. The aim was to be able to increase the dwell pressure, currently limited due to the strength of graphite, and reduce the electric power requirements through isolating the powder and punches from the ring with an electrical-thermal barrier based on the work of Majkic and Chennoufi [119, 78].

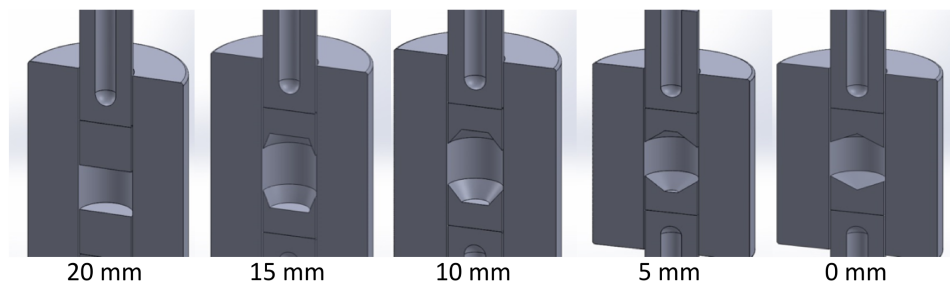


Figure 6.3 – Schematic showing the shaped graphite inserts used to assess the capabilities of FAST to produce shaped preforms; from l-r the upper and lower diameters decrease from 20 mm to 0 mm in 5 mm increments.

After the initial study into producing shaped preforms the demonstration of the FAST-forge process was undertaken. Two methods were used to create the double cone specimens, see Fig. 6.4. The first method was to electrical discharge machine (EDM) 20 mm diameter \times 15 mm thick cylinders from a 100 mm diameter \times 15 mm thick FAST disc, which were then machined to the final dimensions shown in Fig. 6.4 (known as “bulk” double cone specimens hereafter). The second method was to produce shaped preforms by placing shaped graphite inserts into a 20 mm diameter FAST mould assembly, which were also lightly machined to the same final dimensions (known as “shaped” double cone specimens hereafter). The same sintering cycle and hot compression testing conditions were applied for both methods of double cone specimen production. The aim of creating additional specimens from bulk material was to allow a comparison of behaviour with shaped preform specimens produced directly via

FAST; thus demonstrating that the shaped FAST method does not adversely affect either the powder consolidation or subsequent forging response. Finally, a small selection of the FAST-forged specimens were subjected to a simple heat treatment to assess the microstructural response, which is key to developing the final mechanical properties.

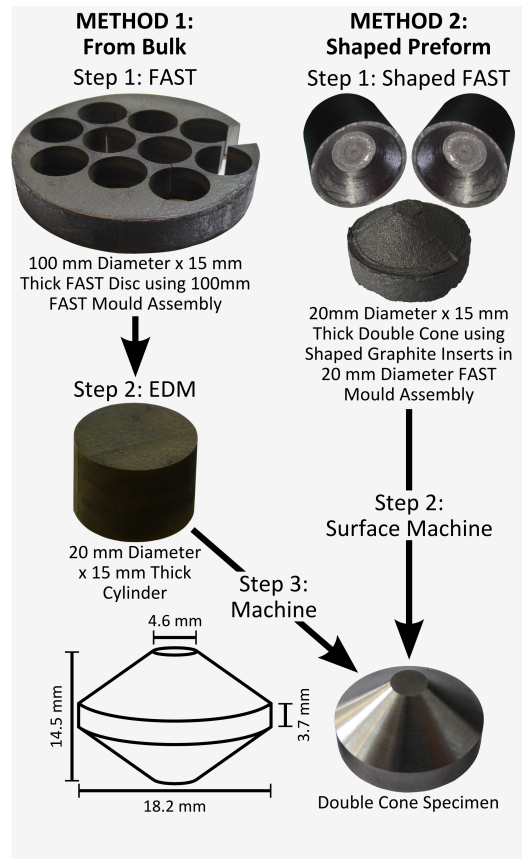


Figure 6.4 – Schematic showing the two methods used to make the double truncated cone specimens. Method 1 produced a 100 mm diameter × 15 mm thick FAST disc, which smaller cylinders were extracted from via electro-discharge machining (EDM), and then machined to the final dimensions shown (known as “bulk” double cone specimens). Method 2 used shaped graphite inserts in a 20 mm diameter FAST mould assembly to produce shaped preforms, which then had a surface machine to give the final dimensions shown (known as “shaped” double cone specimens).

6.2.1 Materials

Ti-6Al-4V HDH powder (see section 3.2 for full details) was used for these proof-of-concept demonstrations, to enable comparison with conventionally produced wrought product, as well as setting a benchmark for any future work with lower-cost powders from alternative extraction methods.

6.2.2 FAST

6.2.2.1 FAST Processing for Initial Shaped Mould and Mould Material Study

The standard procedure for producing FAST specimens outlined in section 3.1.1 was followed with the exception of (1) the material used for the mould assembly (2) the addition of a pair of shaped graphite inserts to produce the required shape and (3) adding a thermal-electrical insulation layer between the ring and pistons in place of graphite foil. The steel selected was Sandvik's 253 MA[®] (EN 1.4835) austenitic chromium-nickel stainless steel due to its high temperature strength and a maximum operating temperature of 1150°C [120]. The all-steel mould assembly consisted of the same components (ring, pistons, and supports) described in section 3.1.1, but with dimensions altered slightly to allow for the additional graphite inserts; a technical drawing is provided in appendix A, see Fig. A.4. The shaped graphite inserts have previously been described and can be seen in Fig. 6.3. They were lined with a double layer of graphite foil to increase their life and aid with specimen removal. The lining was manually cut to shape from sheets of graphite foil to fit each specific variant of insert. The material selected for the insulation was 0.5 mm thick Cogemicanite 132P purchased from Presspahn Ltd, which retains its properties up to temperatures of 1000°C and has a dielectric strength of $>20 \text{ kVmm}^{-1}$ [121].

Initial runs were undertaken using the all-steel mould assembly with the insulation layer. The first of these runs used a mass of powder that would ensure the edges of the inserts touched before high density was achieved, referred to as “underfill” runs, see Table 6.1 for details. The dwell temperature, dwell pressure, and heating rate were kept low as the suitability of the steel mould was unknown at this point of the study. The subsequent runs used enough powder to ensure that the edges would not meet during consolidation, referred to as “overfill” runs, see Table 6.1. The dwell temperatures, dwell pressure, and heating rate were increased as the steel mould had performed adequately in the first runs. The moulds were underfilled to assess the die filling and to ascertain whether preferential sintering was observed in certain areas, i.e. the homogeneity of densification behaviour. The overfilled runs again allowed an assessment of die filling and the homogeneity of densification, and additionally allowed examination of the microstructural development as higher density was achieved.

6. FAST-forge – a new cost-effective hybrid processing route for consolidating titanium powder into near net shape forged components

Table 6.1 – FAST processing conditions, type of double cone inserts, mass of powder, and mould material used for the initial study on producing shaped FAST preforms.

Run Description	Mass (g)	Dwell Temp. (°C)	Pressure (MPa)	Dwell Time (min)	Heating Rate (°C)	Mould Type
0 mm Insert - Underfill	4.51	800	15	10	25	All-Steel
5 mm Insert - Underfill	6.11	800	15	10	50	All-Steel
10 mm Insert - Underfill	8.41	800	15	10	50	All-Steel
15 mm Insert - Underfill	11.40	800	15	10	50	All-Steel
0 mm Insert - Overfill	12.00	1000	22	10	100	All-Steel
5 mm Insert - Overfill	12.00	900	22	10	200	All-Steel
10 mm Insert - Overfill	16.00	1000	22	10	200	All-Steel
5 mm Insert - Mould Test	16.00	1050	50	10	300	All-Steel
5 mm Insert - Mould Test	16.00	1050	50	10	300	All-Graph.
5 mm Insert - Mould Test	16.00	1050	50	10	300	Steel ring, steel supports, graph. pistons
5 mm Insert - Mould Test	16.00	1050	50	10	300	Steel ring, graph. supports, graph. pistons
5 mm Insert - Forging	15.00	1200	50	30	100	All-Graph.
5 mm Insert - Forging	15.00	1200	50	30	100	All-Graph.
5 mm Insert - Forging	15.00	1200	50	30	100	All-Graph.
5 mm Insert - Forging	15.00	1200	50	30	100	All-Graph.
5 mm Insert - Forging	15.00	1200	50	30	100	All-Graph.

A further set of FAST runs was undertaken to assess the improvements to power consumption and any effect on temperatures through using the steel mould vs. graphite mould assembly. Four variations of mould assembly using the two different materials were utilised with the 5 mm shaped inserts, see Table 6.1. The normal all graphite mould assembly was used, as was an all-steel assembly. Additionally a configuration with the steel ring and graphite supports and graphite pistons was used, and so was a configuration with the steel ring and steel supports with graphite pistons. All these runs used 16 g of powder, a dwell temperature of 1050°C, dwell pressure of 50 MPa, heating rate of 300°Cmin⁻¹, and a dwell time of 10 min. Additional temperature monitoring

of the assemblies was achieved through inserting thermocouples into the ring and the upper support.

6.2.2.2 FAST Processing for FAST-*forge* Study

For the FAST-*forge* study the 100 mm diameter disc was produced on the large-scale machine at Kennametal Manufacturing (UK) Ltd and the 20 mm diameter shaped preforms were sintered on the small-scale machine at The University of Sheffield. All specimens were produced using the standard processing procedure described in section 3.1.1. 520 g of powder was inserted between two flat-ended graphite pistons in an all graphite mould assembly to produce the 100 mm bulk disc specimen. 15 g of powder was placed into an all graphite mould assembly between 5 mm shaped graphite inserts to produce the five double cone specimens, see Fig. 6.4. Four of the specimens were machined into forging specimens and the fifth was sectioned for microstructural examination. A dwell temperature of 1200°C, a dwell pressure of 50 MPa, a heating rate of 100°Cmin⁻¹, and a dwell time of 30 min were used. Due to the difference in mould size and powder mass it was necessary to use two different methods to achieve the same cooling rate (and therefore microstructure) for the two methods of specimen production. For the 100 mm bulk disc the current was turned off and the specimen allowed to “free” cool. For the shaped double cone specimens, the current was used to achieve a “controlled” cooling rate to match the bulk disc cycle. The “controlled” cool is achieved by the FAST furnace software reducing the applied current to a level where the heat loss exceeds the Joule heat generated by the correct amount to attain the desired cooling rate.

6.2.3 Hot Upset Forging

The TMC machine was used to replicate the hot upset forging of the double cone specimens, see section 3.1.2.2 for an overview of the general testing procedure followed. Bulk double cone specimens were deformed at 850°C, 950°C, and 1050°C, and at strain rates of 0.01 s⁻¹, 0.1 s⁻¹ and 1 s⁻¹. The shaped double cone specimens were deformed at 950°C, at strain rates of 0.01 s⁻¹, 0.1 s⁻¹ and 1 s⁻¹.

6.2.4 Heat Treatment

Heat treatments were performed on the hot forged double cone specimens as detailed in section 3.1.3. The bulk double cones forged at 950°C were chosen for the heat treatment. After forging the specimens were sectioned centrally parallel

to the compression direction. Half the specimen was used for microstructural examination and the remaining part was sectioned in half again. These two quarters were coated in glass lubricant and heat treated in a tube furnace under flowing argon. They were placed into the furnace at 950°C for 120 min. One quarter was then water quenched (WQ) and the other quarter remained in the furnace after it was turned off and allowed to cool to room temperature, referred to as furnace cooled (FC). The heat treated specimens were then micrographically prepared and examined in areas of high and low forging strain.

6.2.5 Finite Element Simulation of the Forging

The finite element software DEFORMTM [17], see section 3.1.8, was used to simulate the compression tests of the double cone specimens to give the strain profiles across the specimens seen in Fig. 6.18-6.20. These strain profiles allow the linking of microstructural evolution to thermomechanical processing parameters (strain, strain rate, temperature). A 2-D model of half the double cone geometry meshed with 3160 elements was used. Rheology data for Ti-6Al-4V HDH, generated in chapter 5, in a tabular form (stress values at a range of strains for each testing condition) was used for the material model.

6.3 Results and Discussions

The results and discussions of the initial simple double cone shape study will be presented first, followed by those for the FAST-forge study.



Figure 6.5 – Photographs of the underfilled and overfilled 0-15 mm double cone FAST specimens.

6.3.1 Simple Shaped FAST Study

The initial “underfill” and “overfill” study demonstrated that it was possible to fully fill the double cone moulds with powder during sintering. Upon examination of the specimens after removal of the graphite foil there was no indication of any voids, see the photograph of all seven specimens in Fig. 6.5.

6.3.1.1 Micrographs of Underfilled Moulds

To assess the die filling further, and observe any possible heterogeneity in sintering behaviour, the entire central cross-section of the “underfilled” double cone specimens was examined micrographically. These images were stitched together into a montage showing the whole area, which can be seen in Fig. 6.6 for the 0 mm diameter mould, Fig. 6.7 for the 5 mm diameter mould, Fig. 6.8 for the 10 mm diameter mould, and Fig. 6.9 for the 15 mm diameter mould.

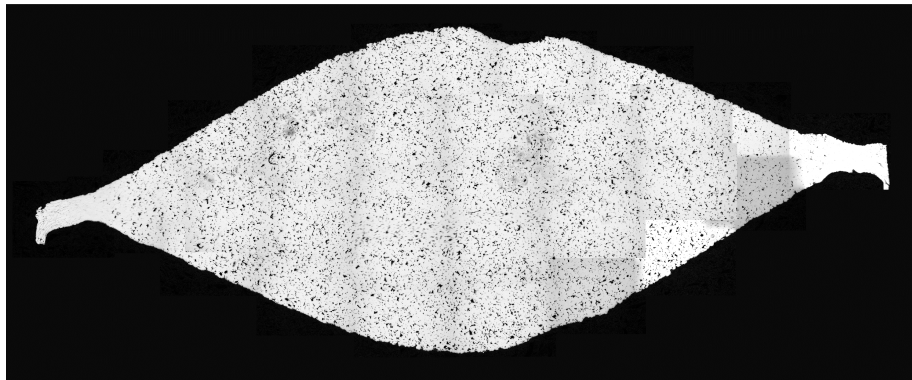


Figure 6.6 – Montage of light micrographs showing a central cross section of an underfilled 0 mm double cone demonstrating homogeneous porosity distribution.

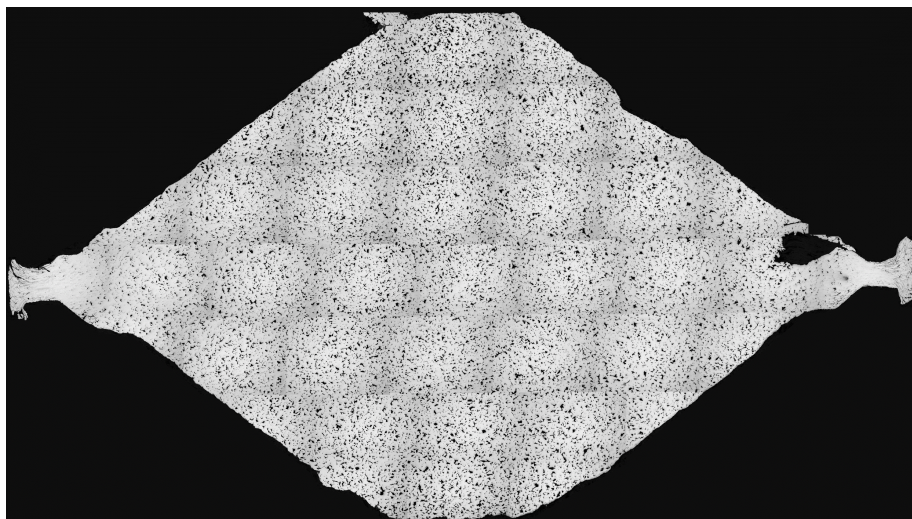


Figure 6.7 – Montage of light micrographs showing a central cross section of an underfilled 5 mm double cone demonstrating homogeneous porosity distribution.

6. FAST-forge – a new cost-effective hybrid processing route for consolidating titanium powder into near net shape forged components

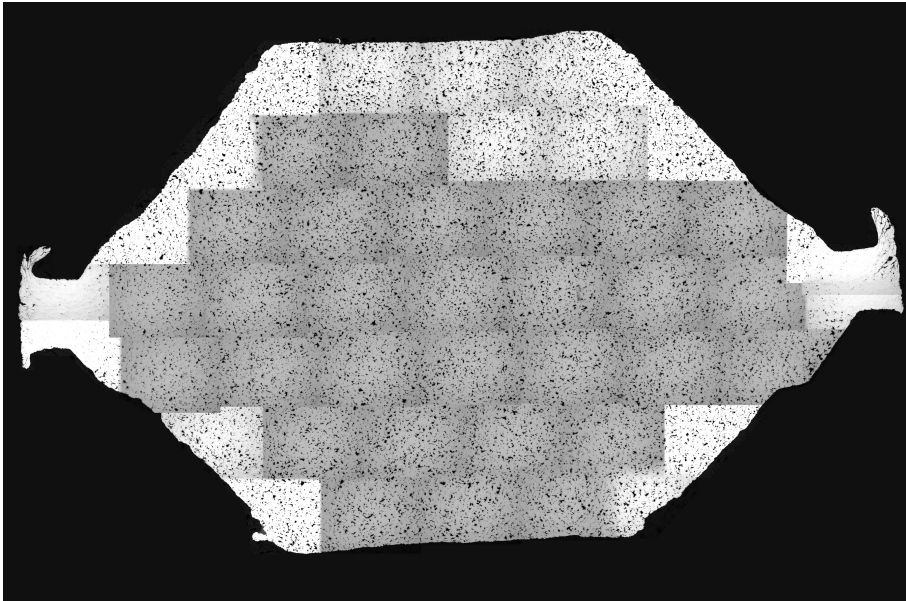


Figure 6.8 – Montage of light micrographs showing a central cross section of an underfilled 10 mm double cone demonstrating homogeneous porosity distribution.

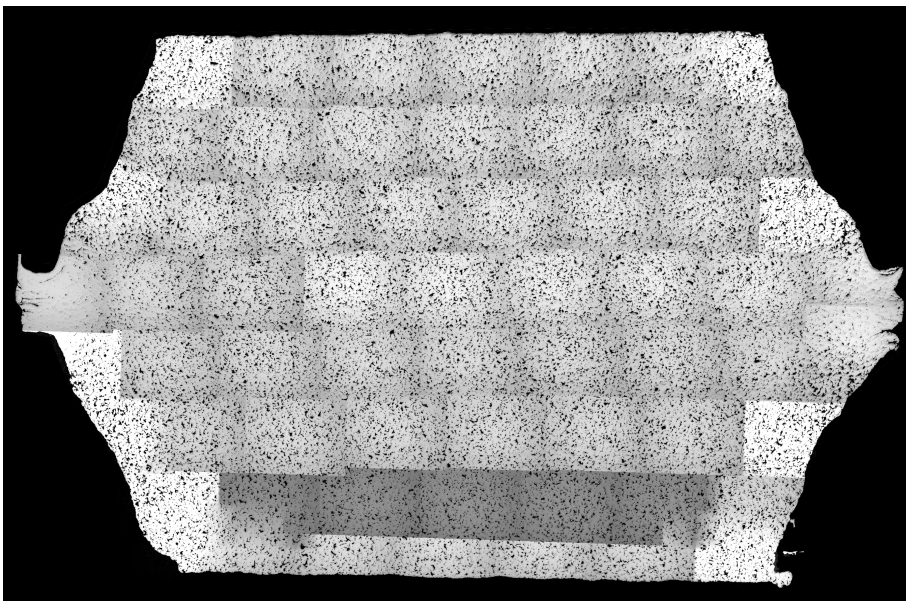


Figure 6.9 – Montage of light micrographs showing a central cross section of an underfilled 15 mm double cone demonstrating homogeneous porosity distribution.

There is clearly significant porosity remaining in all the specimens, which was the desired outcome in this study. The area of highest density is located at or near to the pinch point where the upper and lower insert came together during sintering. It was anticipated that the upper point of the mould may not be fully filled, or that it would have increased porosity compared to the rest of the

specimen, but that is not observed in any of these specimens. Due to the method of assembling the mould there is always some gap between the upper insert and the loose powder. Getting powder to flow to fill a mould has historically been considered very difficult in traditional powder metallurgy techniques. It would appear that for the titanium alloy powders used in this study, at the temperatures and pressures applied, that it is possible to fill the mould. It is postulated that the combination of high heating rate bypassing the early stages of sintering, and the high temperature and pressure used, allows the FAST processing to act similarly to a closed die hot forging operation; with material flowing to fill the die. Producing shaped preforms via FAST could therefore be considered a hybrid sinter-forge technique.

6.3.1.2 Micrographs of Overfilled Moulds

Cross-polarised light micrographs of the microstructures produced throughout the specimens when “overfilling” the shaped inserts with powder are shown in Fig. 6.10 for the 0 mm mould, Fig. 6.11 for the 5 mm mould, and Fig. 6.12 for the 10 mm mould. It should be noted that the 5 mm mould specimen was nominally processed below the β transus temperature, whereas the other two specimens were processed above it. However, the accuracy of the temperature measurement cannot be guaranteed due to the pyrometer reading being taken off the inside of the steel piston. The change of mould material from graphite to steel adds an uncertainty to the temperature profiles within the mould assembly and the powder that is not fully understood. For the purposes of this analysis it will be assumed, unless the microstructure suggests otherwise, that the specimen temperature was as close to the measured temperature as during processing with graphite moulds.

The porosities calculated through image analysis at the point (a), point-centre (b), centre (c), centre-edge (d), and edge (e) of the 0 mm “overfilled” mould are 0.2 %, 0.2 %, 0.2 %, 0.2 %, 0.3 % respectively. This demonstrates the uniform consolidation behaviour shown in section 6.3.1.1 may continue up to full consolidation. However, whilst all the micrographs show the transformed β structure that is expected when cooling from 1000°C there is some significant variation in the observed prior β grain size, see Fig. 6.10. At the point (a) and the edge (e) there has been rapid β grain growth to $>500\ \mu\text{m}$, whilst in the interior at points (b), (c), and (d) the prior β grains are still in the same order of magnitude as the prior powder particles. There could be two explanations for

this. The first is that the point and edge achieve higher densities sooner than the interior region, which will allow grain growth as porosity is no longer pinning grain boundary motion. The second is that the temperature at the point and edge is higher than the interior, which would promote more rapid grain growth. It is likely to be a combination of these two factors; the rapid grain growth is very similar to that seen in section 4.3.1.2 as temperature and density increased.

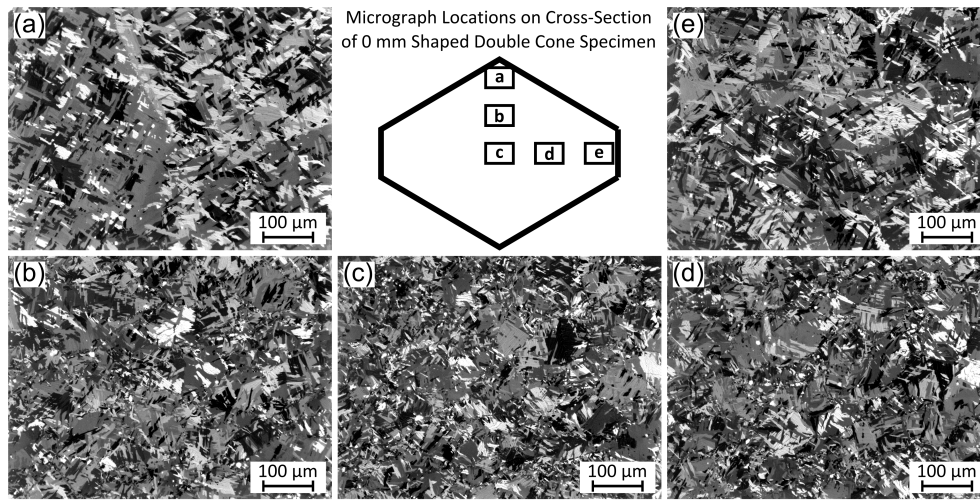


Figure 6.10 – Cross-polarised light micrographs showing the microstructure of the 0 mm double cone specimen at the locations indicated on the schematic cross-section.

The porosities calculated through image analysis at the point (a), point-centre (b), centre (c), centre-edge (d), and edge (e) of the 5 mm “overfilled” mould are 2.0 %, 1.3 %, 1.2 %, 1.4 %, 1.7 % respectively. These densities appear to show the exact opposite of what was seen with the prior β grain growth in the 0 mm mould. The interior region is $\sim 0.5\%$ denser than edge and point, which would suggest a larger grain size should have been observed there in the 0 mm mould. The microstructures in this specimen shows consistency across all locations, see Fig. 6.11, which may be due to the level of porosity measured preventing significant growth at any location. The reduced processing temperature of 900°C explains the generally increased porosity compared to the 0 mm mould at 1000°C (behaviour also seen in section 4.3.1.1) and also the lack of β grain growth. It is not clear why the porosity/microstructure trend seen in this specimen is reversed for the 0 mm mould, although non-uniform temperature profiles and being in proximity to the β transus temperature are thought to be involved.

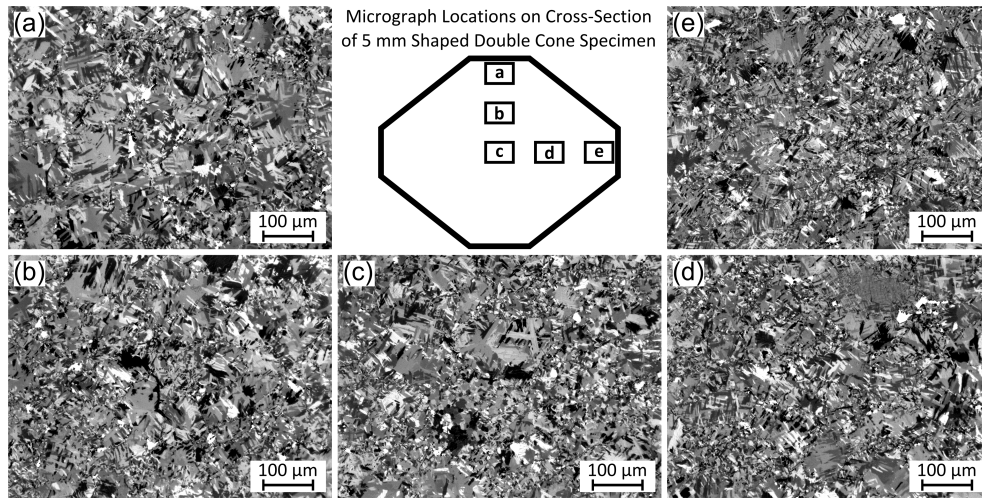


Figure 6.11 – Cross-polarised light micrographs showing the microstructure of the 5 mm double cone specimen at the locations indicated on the schematic cross-section.

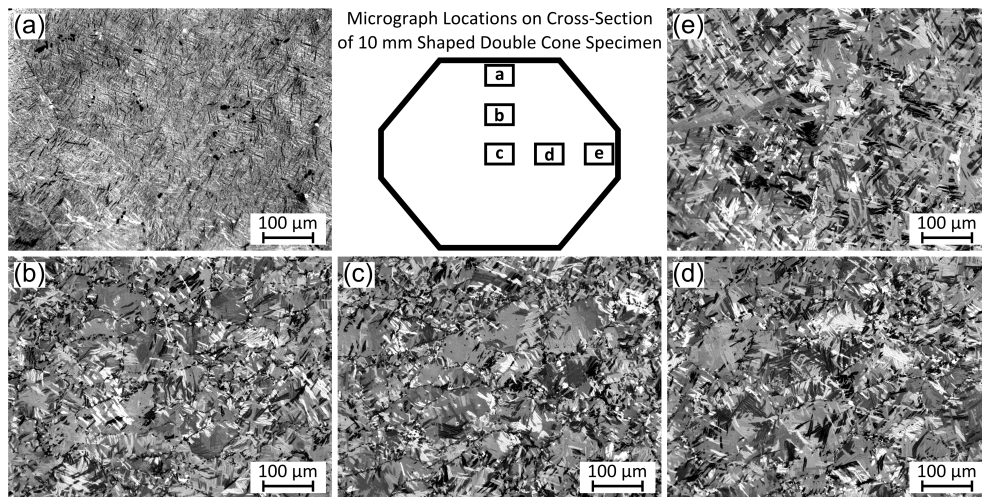


Figure 6.12 – Cross-polarised light micrographs showing the microstructure of the 10 mm double cone specimen at the locations indicated on the schematic cross-section.

The porosities calculated through image analysis at the point (a), point-centre (b), centre (c), centre-edge (d), and edge (e) of the 10 mm “overfilled” mould are 0.1 %, 0.2 %, 0.3 %, 0.3 %, 0.2 % respectively. These density levels and the microstructures, see Fig. 6.12, correlate very well with those seen for the 0 mm mould that was also processed at 1000°C. The edge and the point areas again show a much larger prior β grain size compared to the interior locations. There is one noticeable difference in the point location for this 10 mm mould specimen. The transformed β structure is considerably finer than seen at the edge in this

specimen and the edge/point in the 0 mm mould specimen. This would suggest a much more rapid cooling rate from above the β transus temperature (as was also seen in Fig. 6.15). The reason for this increased cooling rate in this specimen cannot be explained at this time.

These results are encouraging with regard to shaped mould die filling and homogeneous consolidation behaviour. However, the lack of understanding and control of temperature profiles and thus microstructures when using the all-steel mould assembly means it was decided to revert to the all-graphite assembly to produce the double cone specimens for the FAST-*forg*e study.

6.3.1.3 Power and Temperature Profiles of Steel and Graphite Mould Assemblies

The power and current needed to produce the heating rate and dwell temperature when FAST processing with a combination of the steel and graphite mould components are shown in Fig. 6.13a and Fig. 6.13b. The corresponding temperature profiles and cooling rates measured by the axial pyrometer are shown in Fig. 6.13c, and measured in the ring and upper support by thermocouple in Fig. 6.13d.

The all-graphite (AG) assembly and graphite pistons/supports (GP-GS) with steel ring showed very similar behaviour in all aspects of power, current, and temperatures. This indicates that the thermal-electrical insulation layer was performing as expected; preventing excess current flowing through the ring no matter what material it was made from. The all-steel (AS) assembly initially needed the most power to achieve the heating rate and dwell temperature, but midway through the dwell period the levels fell below the AG and GP-GS levels. There was also a significant increase in current flow through the specimen. If the effects of current are what allows FAST consolidation to improve upon traditional PM techniques then this further increased current level when using an AS mould could enhance sintering further. No evidence for this has been found in the current study but it is an interesting point to note. The clear downside of using steel in part/all of the mould assembly is the large decrease in cooling rate; the pyrometer reading took over 10 min longer to drop to 400°C and the ring also takes significantly longer to cool. This additional processing time is not desirable when designing a cost-effective processing route.

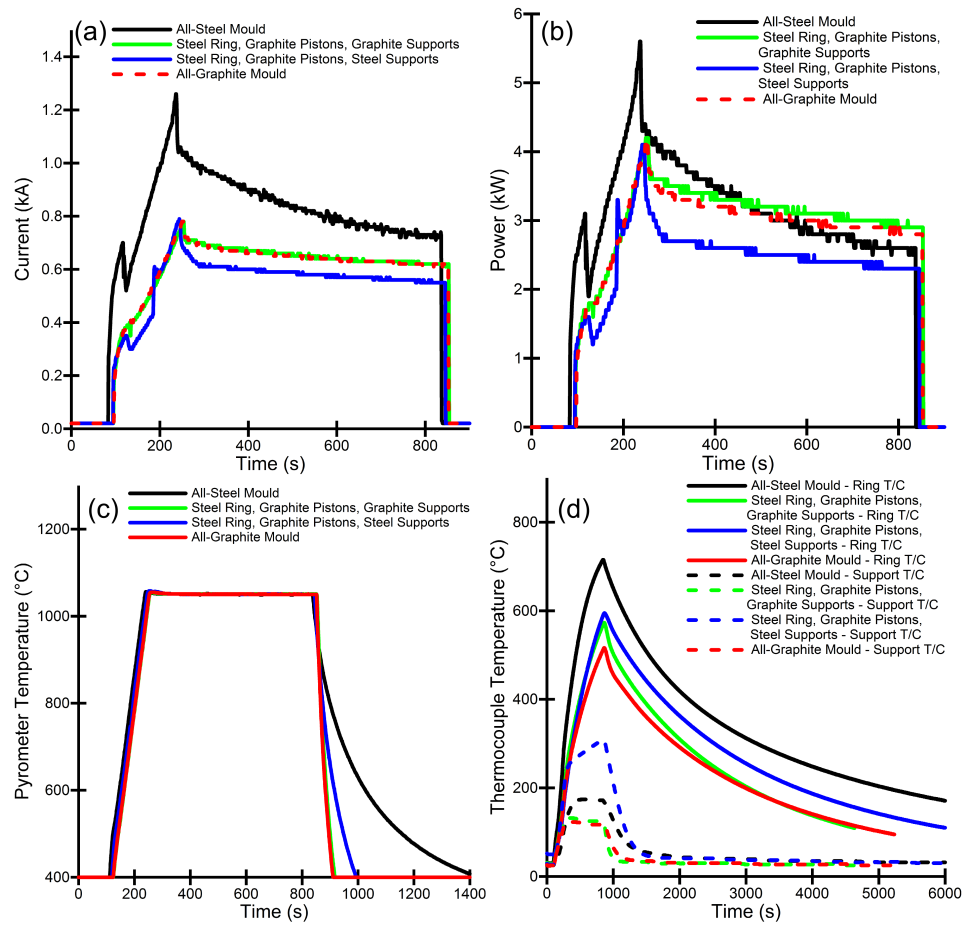


Figure 6.13 – Graphs showing various machine recorded data during FAST processing of Ti-6Al-4V HDH FAST specimens when using all-steel mould assemblies, all-graphite mould assemblies, and combinations of the two materials; (a) current, (b) power, (c) top pyrometer temperature, (d) temperature measured by thermocouple in the ring mould, and the upper support.

6.3.2 FAST-forge Study

6.3.2.1 Power and Current Requirements

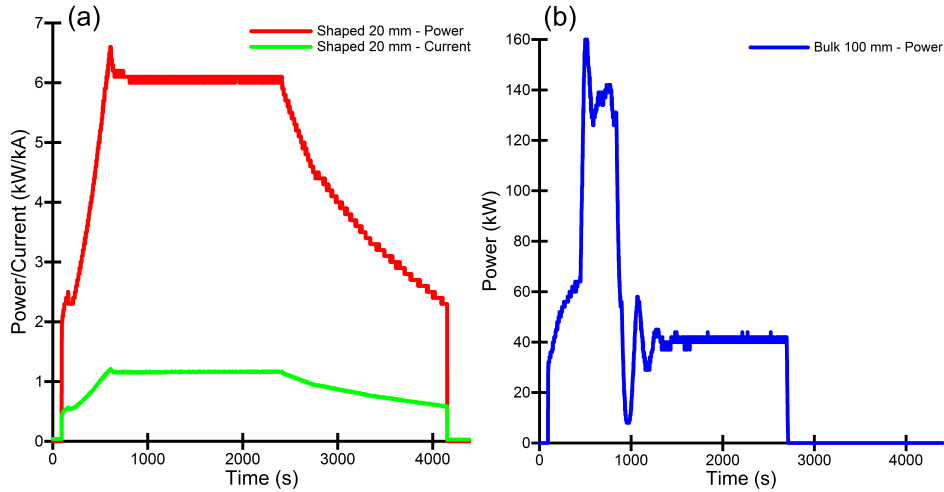


Figure 6.14 – Graph showing the current (a) and power (b) requirements during FAST processing for a 100 mm bulk disc and 20 mm mould with shaped inserts.

The values of current and power required for both methods of specimen production are shown in Fig. 6.14, although a sensor fault prevented recording of current data for the 100 mm bulk disc. For the shaped 20 mm mould the current rose steadily from an initial value of 0.45 kA to a peak of 1.2 kA and settled to between 1.12 - 1.18 kA during the dwell period. The power similarly increased from 2.0 kW to a peak of 6.6 kW and settled to between 5.9 - 6.3 kW during the dwell period. The value of power for the 100 mm disc rose steadily to 65 kW from 30 kW initially before increasing rapidly to a peak of 163 kW during heating, followed by a period of oscillation and eventually settling to 37 - 42 kW during the dwell period.

The power required to process the 10 mm disc is obviously significantly increased from the 20 mm shaped specimen and this should be a consideration when aiming to process larger scale specimens. The power appears to scale almost linearly with powder mass; the 520 g used for the 100 mm disc is 35 times greater than the 15 g for the shaped double cone, and the 100 mm steady-state power of ~40 kW is 33 times greater than the 1.2 kW needed at 20 mm.

6.3.2.2 Microstructures after FAST

Preliminary experiments demonstrated that the initial cooling rate after the current is turned off was significantly higher for the 20 mm diameter mould

assembly at $\sim 20^{\circ}\text{Cmin}^{-1}$ than for the 100 mm diameter mould at $\sim 0.33^{\circ}\text{Cmin}^{-1}$, see Fig. 6.15a. There is greater thermal mass for the larger mould assembly due to the increased amount of graphite required and it therefore takes longer to cool. This study sought to emulate the bulk material as closely as possible to allow direct comparison and therefore a “controlled” cooling rate to match the “free” cooling rate of the bulk disc was utilised for the shaped double cone specimen; it was felt that any effect of applying the current for a longer period would be negligible compared to the effect of cooling rate on microstructure. The difference in microstructure produced by the “free” and “controlled” cooling rates can be seen in Figs. 6.15b and 6.15c; as expected the quicker “free” cooling rate produced much finer α laths, where the slower “controlled” cooling rate coarsened them to a size similar to the bulk specimen (directly compared in Fig. 6.16).

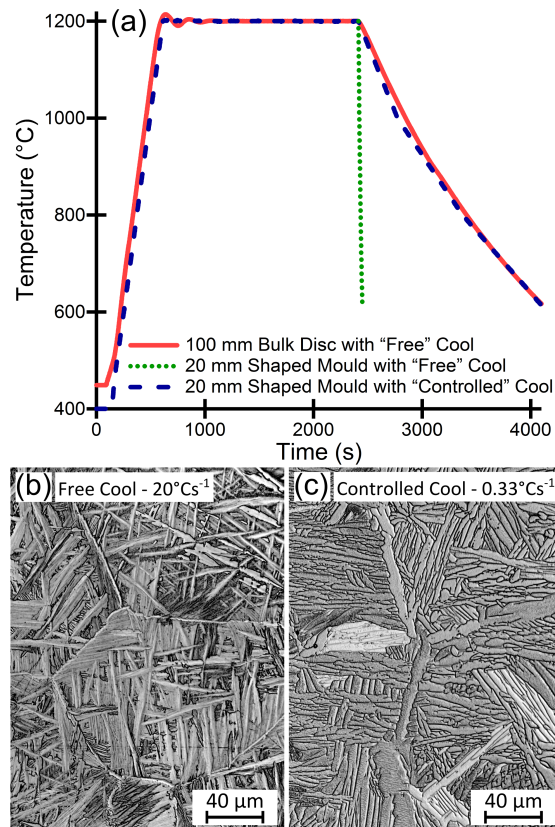


Figure 6.15 – Graph showing the temperature profiles during FAST processing of three types of Ti-6Al-4V specimen (a). A 100 mm diameter disc used for bulk double cone specimens; allowed to “free” cool after current switch-off (solid line). A 20 mm shaped mould when allowed to “free” cool after current switch-off (dotted line) with associated microstructure (b). A 20 mm shaped mould with “controlled” cool (dashed line) and associated microstructure (c).

The microstructures produced in this work when consolidating the Ti-6Al-4V HDH powder using FAST at a heating rate of $100^{\circ}\text{Cmin}^{-1}$ with dwell conditions of 1200°C and 50 MPa held for 30 min are shown in Fig. 6.16. A typical microstructure of the 100 mm diameter disc used to produce the bulk double cone specimens is shown, as are micrographs from selected locations throughout the micrographically prepared shaped double cone specimen. Both specimen types show the previously demonstrated and expected transformed β microstructure that is characteristically found when slow cooling from above the β transus temperature; prior β grains containing α laths in a Widmanstätten or colony structure with some amount of α phase present on the grain boundaries [29]. The prior β grain size ranges from approximately 200-600 μm with an α lath width in the region of 3-10 μm . The high temperature and level of consolidation during the dwell period allowed β grain growth beyond the dimensions of the initial powder particles for both bulk and shaped specimens. This β grain growth demonstrates the high density achieved as at lower levels of consolidation the remaining porosity acts to pin grain boundaries and prevent growth.

Image analysis, using the software ImageJ [94], of multiple bright field micrographs across each specimen allowed the calculation of density as 99.9% for the shaped double cone specimens and as 99.9% for the bulk double cone specimens. These values are slightly greater than the 99.01% stated by Xu [122] and similar to the 99.9% reported by Kim [123] for HIP of Ti-6Al-4V powders, which claimed to have tensile strength and elongation comparable to wrought material. The porosity will also be healed further during the forging process, which will further increase tensile properties and more importantly fatigue strength.

It can also be seen in Fig. 6.16 that microstructural homogeneity was achieved in the shaped double cone specimen, with comparable micrographs from top to bottom and from centre to edge. Graphite has a higher electrical resistivity than Ti-6Al-4V and consequently acts as the main heating element in the mould assembly. Thus, it was hypothesised that a shaped mould with non-uniform graphite thickness in the axial direction would produce uneven heating, as well as a more complex pressure distribution, which would lead to microstructural variations; although this is not observed in the shaped double cones at this scale. If temperature variations were present, they were small enough not to have had a significant effect at the processing conditions used for these experiments.

Although this may not be the case if a lower processing temperature is required, especially as the β transus temperature is approached, where there will be a reduction in the diffusional rates with increasing α content. It should be noted that the shape used here is still a relatively simple axisymmetric profile and that further experimentation will be needed, with the aid of FE modelling, to fully understand the difficulties involved in producing semi-complex shaped preform billets as part of the FAST-*forge* processing route.

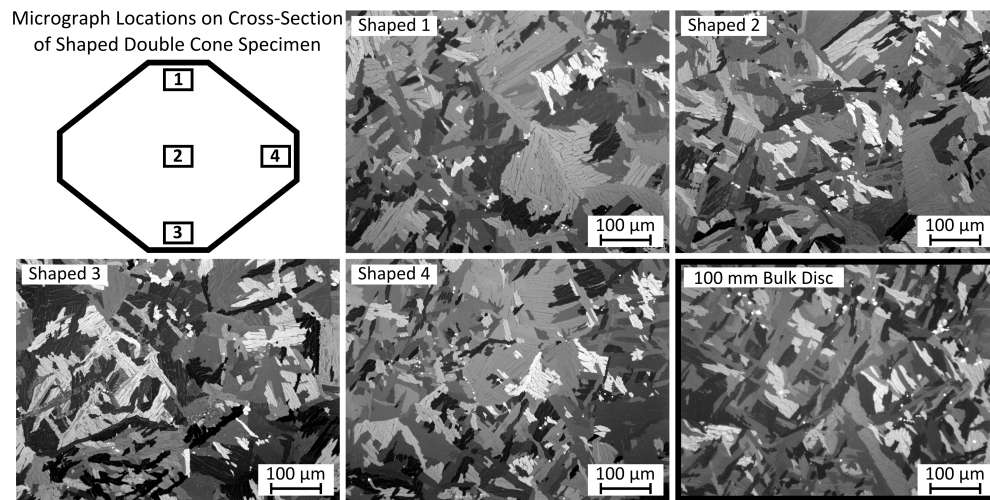


Figure 6.16 – Cross-polarised light micrographs of Ti-6Al-4V double truncated cone specimens produced via FAST at a dwell temperature of 1200°C. Showing microstructures from a shaped specimen (Shaped 1-4) at the locations outlined in the top left diagram; and a characteristic microstructure of the homogeneous bulk specimen (bottom right).

6.3.2.3 Experimental Load-Displacement Curves

Due to the non-uniform cross-sectional area of the double cone specimens it is not possible to produce meaningful plots of stress versus strain during the thermomechanical compression. Consequently, the data is presented as plots of load versus displacement, which can be seen in Fig. 6.17 for deformations at 950°C and a range of strain rates. The raw load and displacement data from the TMC machine was corrected via the method described in section 5.2.3.1.

The effect of strain rate is clearly demonstrated; as the rate of deformation increases so does the force required to achieve equivalent displacement. The influence of temperature can be seen in the load-displacement curves at 850°C, 950°C, and 1050°C, see Fig. 6.24. There is a marked reduction in the load required for equivalent displacement as temperature increases due to an increase in the more easily deformed β phase, and more active dynamic recovery

and recrystallisation processes. There are some small variations between the load-displacement behaviour of shaped double cone and bulk double cone specimens; at 1 s^{-1} the bulk specimen required a slightly higher load, at 0.1 s^{-1} the bulk specimen required a slightly lower load, and at 0.01 s^{-1} the bulk specimen required a higher load initially before finishing requiring a lower load. The level of variation seen is minimal and would be expected even when testing duplicate samples from the same parent material due to attempting to control the large number of variables seen during hot working of metals. Frictional variations were limited by using similar quantities of lubricant for each test and cleaning the tool posts between tests, but small differences would still occur. The strain rate was closely controlled by the testing software and whilst small oscillations around the set value occurred these were the same for every test and it is thought not large enough to cause the variations in load seen. There was some variation in the initial temperature between samples due to PID control issues with the FTTU causing small oscillations around the target test temperature, typically $\pm 10^\circ\text{C}$, which would also have a small effect on the loads required.

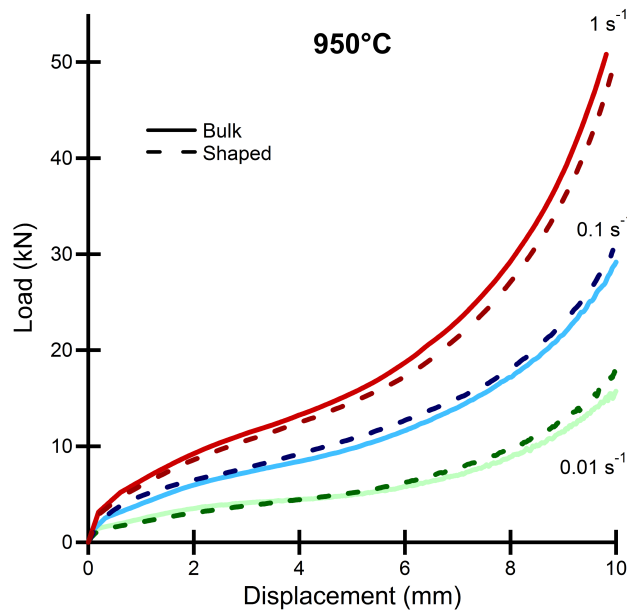


Figure 6.17 – Graphs of load displacement curves during hot upset forging of Ti-6Al-4V double truncated cone specimens at 950°C and strain rates of 0.01 s^{-1} , 0.1 s^{-1} , and 1 s^{-1} . Bulk (solid lines) and shaped (dashed lines).

6.3.2.4 Microstructure Evolution Post One-Step Forging

The microstructural evolution for both bulk and shaped double cone specimens under hot uniaxial compression at 950°C, for strain rate regimes of 0.01 s⁻¹, 0.1 s⁻¹, and 1 s⁻¹ is shown in Figs. 6.18, 6.19, and 6.20 respectively. The location of the light micrograph images, 3 mm apart along the specimen centreline, is also marked on the strain profile generated by FE simulation. The microstructural evolution of the bulk double cone specimens at 850°C and 1050°C displayed behaviour very similar to that demonstrated for cylindrical specimens, see section 5.3.2.1, and is therefore omitted from this section.

At low strains, 12 mm from the centre, there is slight coarsening of the primary α and the transformed β grains manifest a finer secondary α lath structure than post-FAST due to the water quench and higher cooling rate. As strain increases, moving towards the specimen centre, it can be seen across both bulk and shaped double cone specimens at all strain rates that primary α platelets rotate and tend to align perpendicular to the forging axis; all primary α appears to be fully aligned 6 mm from the centre (a strain of ~ 1.1). At higher strains break up of the α platelets into approximately 1-5 μm spheroidal α particles is observed. As strain rate increases the time for diffusion dominated globularisation of primary α platelets decreases and it can be seen the amount of spheroidal α particles decreases from Fig. 6.18-6.20.

6. FAST-forge – a new cost-effective hybrid processing route for consolidating titanium powder into near net shape forged components

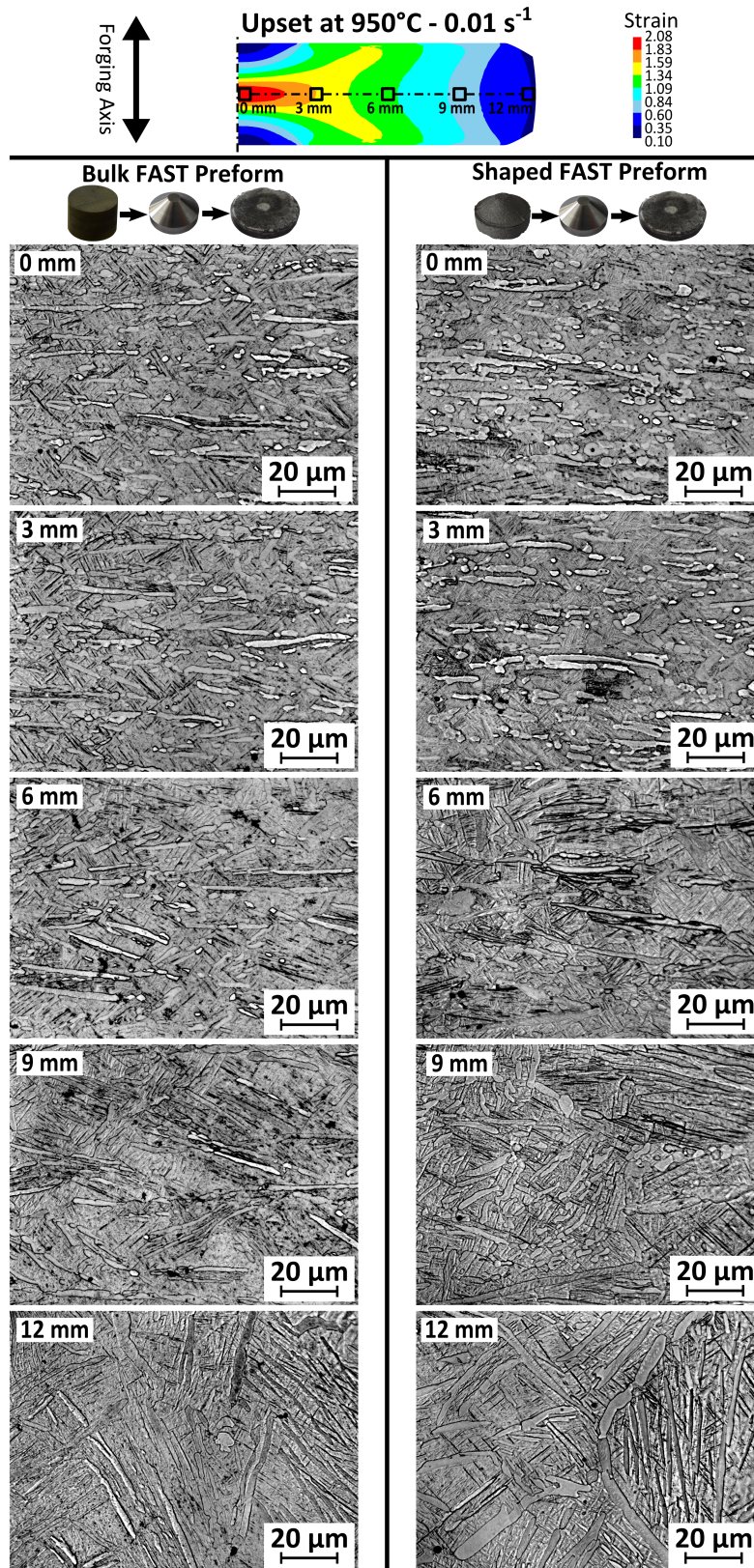


Figure 6.18 – Bright-field light micrographs after etching with Kroll's reagent of the microstructural evolution with increasing strain from edge to centre of the double truncated cone specimens after forging at 950°C and 0.01 s⁻¹; produced from bulk (left) and via shaped FAST (right).

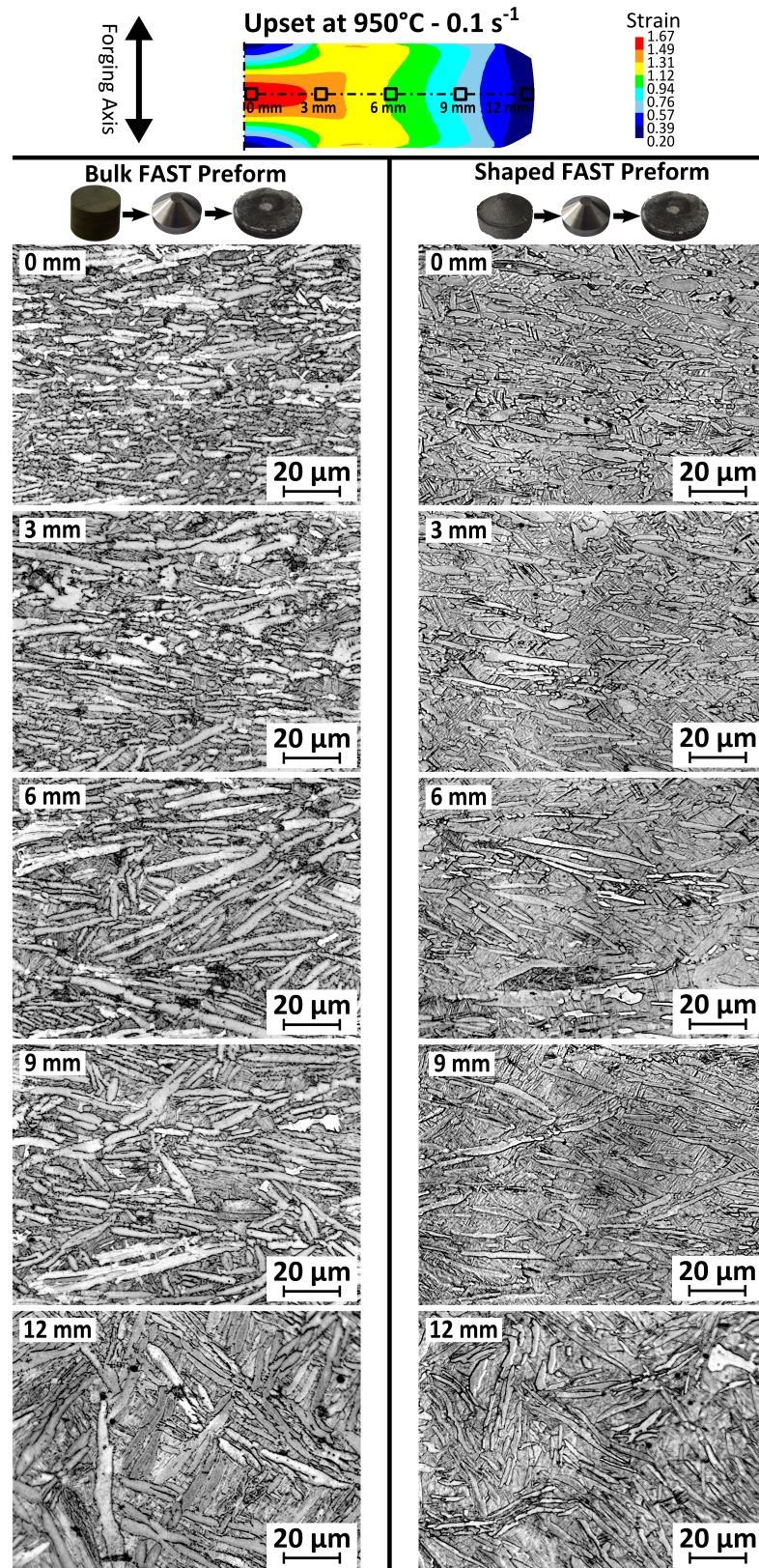


Figure 6.19 – Bright-field light micrographs after etching with Kroll's reagent of the microstructural evolution with increasing strain from edge to centre of the double truncated cone specimens after forging at 950°C and 0.1 s^{-1} ; produced from bulk (left) and via shaped FAST (right).

6. FAST-forge – a new cost-effective hybrid processing route for consolidating titanium powder into near net shape forged components

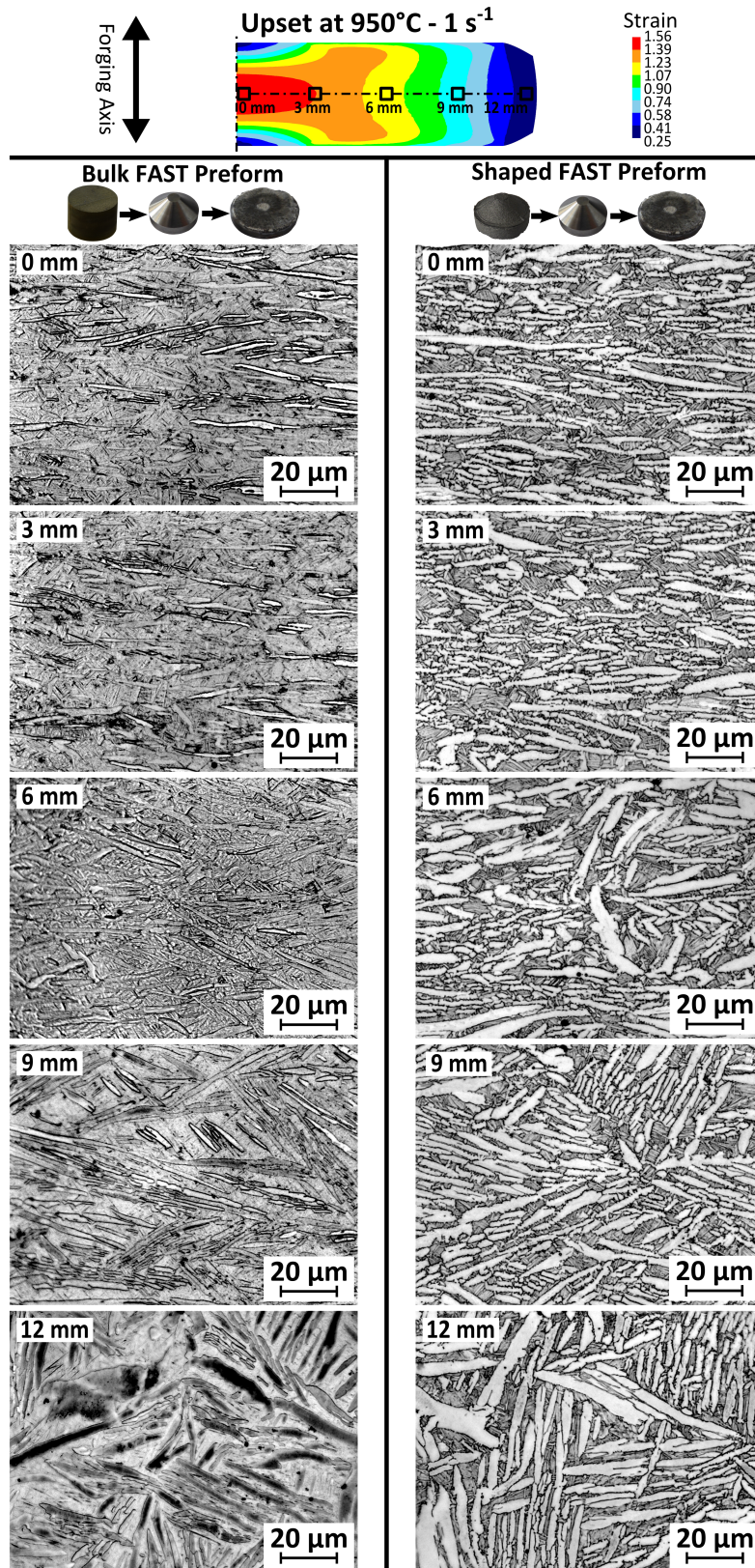


Figure 6.20 – Bright-field light micrographs after etching with Kroll's reagent of the microstructural evolution with increasing strain from edge to centre of the double truncated cone specimens after forging at 950°C and 1 s⁻¹; produced from bulk (left) and via shaped FAST (right).

The microstructural evolution of shaped double cone specimens compared to double cone specimens machined from bulk is similar for all strain rates and strains. There has been a significant coarsening of the primary α in both the bulk double cone specimen at 0.1 s^{-1} and the shaped double cone specimen at 1 s^{-1} . This is due to these specimens failing to remain in the robot gripper arms upon retrieval from the test furnace so that the quenching did not occur automatically and a slower initial cool was experienced; the specimens were manually quenched to room temperature approximately 60-120 s after forging. This slower cooling rate somewhat hinders a direct comparison between the two specimen types; however, the same microstructural trends are observed. The observed microstructural evolution is comparable to that reported during the hot working of conventionally produced Ti-6Al-4V with a colony α microstructure, as reported by Semiatin [40].

6.3.2.5 Microstructure Post Heat Treatment

Bulk FAST double cone specimen microstructures after heat treatment at 950°C for 120 min are shown in Fig. 6.21 for the specimen forged at 950°C and 0.01 s^{-1} , Fig. 6.22 at 950°C and 0.1 s^{-1} , and Fig. 6.23 at 950°C and 1 s^{-1} . The heat treatment produced a similar response in all 3 specimens regardless of the forging strain rate; with little qualitative difference in the microstructure.

In the low strain areas at the edges of the specimen there is still a transformed β structure with α colonies. The α colony size has increased and the α lath thickness has coarsened. The slower furnace cooled specimens show increased coarsening compared to the water quenched specimens.

In the high strain areas there has also been microstructural coarsening of the primary α grains, which is again more pronounced in the furnace cooled specimens. The water quenched specimens show almost equiaxed primary α grains $5\text{-}10 \text{ }\mu\text{m}$ in diameter contained in a very fine transformed beta matrix. The furnace cooled specimens have, on average, slightly larger equiaxed primary α grains contained in a very coarse transformed beta matrix. The change of shape of the primary α grains from elongated with a large aspect-ratio post-forging to equiaxed post-heat treatment indicates that recrystallisation and some subsequent grain growth is occurring. The microstructures produced correspond very well to those reported by Semiatin et al. [124] for a similar heat treatment regime.

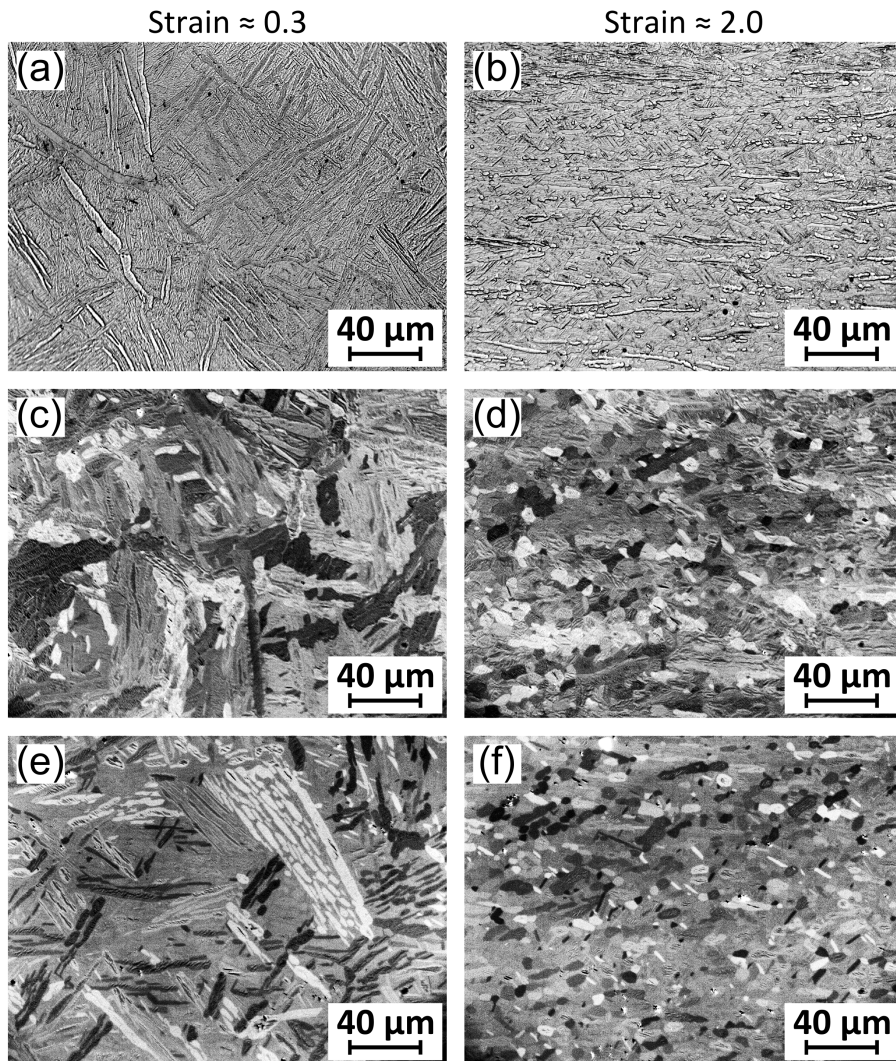


Figure 6.21 – Light micrographs showing microstructures of the bulk double cone specimen produced with FAST conditions of 1200°C , 50 MPa, $100^\circ\text{Cmin}^{-1}$, and 30 min dwell time. Forged at 950°C and a strain rate of 0.01 s^{-1} after etching with Kroll's reagent — low strain area (a) and high strain area (b). Under cross-polarised light after a subsequent heat treatment at 950°C for 120 min with either a furnace cool (low strain area (c) and high strain area (d)) or a water quench (low strain area (e) and high strain area (f)).

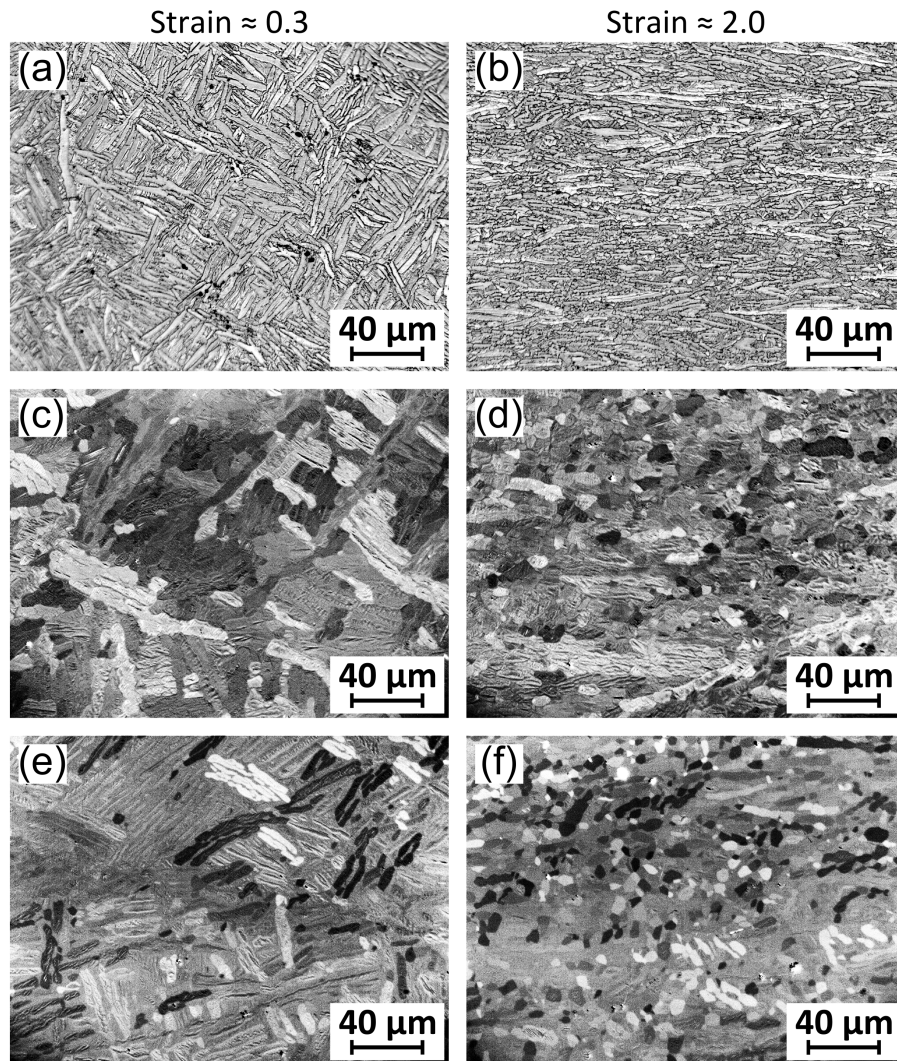


Figure 6.22 – Light micrographs showing microstructures of the bulk double cone specimen produced with FAST conditions of 1200°C , 50 MPa , $100^{\circ}\text{Cmin}^{-1}$, and 30 min dwell time. Forged at 950°C and a strain rate of 0.1 s^{-1} after etching with Kroll's reagent — low strain area (a) and high strain area (b). Under cross-polarised light after a subsequent heat treatment at 950°C for 120 min with either a furnace cool (low strain area (c) and high strain area (d)) or a water quench (low strain area (e) and high strain area (f)).

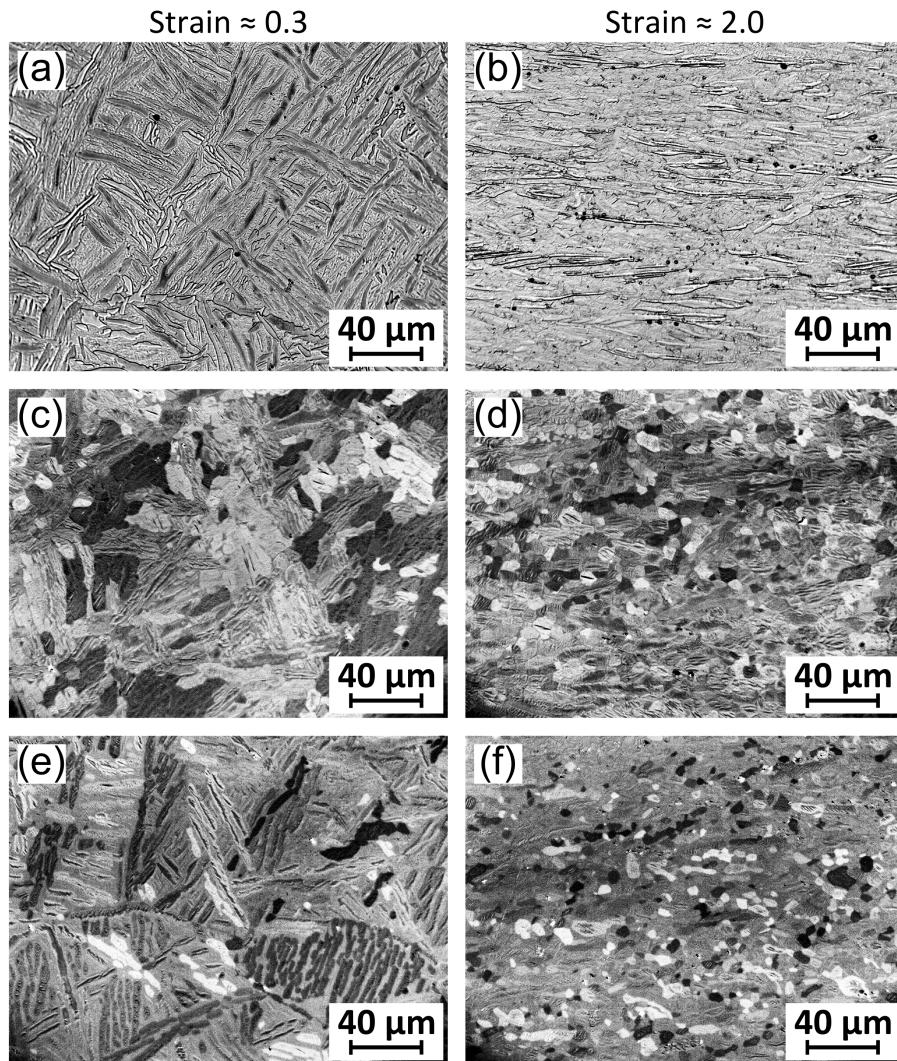


Figure 6.23 – Light micrographs showing microstructures of the bulk double cone specimen produced with FAST conditions of 1200°C, 50 MPa, 100°Cmin⁻¹, and 30 min dwell time. Forged at 950°C and a strain rate of 1 s⁻¹ after etching with Kroll's reagent — low strain area (a) and high strain area (b). Under cross-polarised light after a subsequent heat treatment at 950°C for 120 min with either a furnace cool (low strain area (c) and high strain area (d)) or a water quench (low strain area (e) and high strain area (f)).

6.3.2.6 Finite Element Simulation

The load upon the upper tool with respect to its stroke (displacement) was extracted from the data produced by running FE simulations of each experimental point in the test matrix. This data is plotted against the experimentally recorded values of load and displacement for the bulk double cone specimens in Fig. 6.24. Only data for the bulk double cone specimens is shown to allow clearer comparison, as it has been shown that the shaped double cone specimens produced very similar load data.

Overall there is good visual agreement between experimental and predicted values, which gives confidence that the predicted strain profiles are accurate. However, there is slight under prediction at 850°C and 950°C, but slight over prediction at 1050°C. The simulation was set up to mirror the recorded temperature profiles of the experiment, which due to adiabatic heating were not fully isothermal, therefore load changes due to temperature variability should be accounted for. However, the material model used was discrete tabulated data with linear interpolation between conditions, which may not be realistic. A constant shear friction factor (\bar{m}) of 0.3 was used and appears to give good visual agreement with experimental conditions, using boron nitride as a release agent, as the end shape of the simulated curves largely matches the experimental even if the absolute values differ. Friction only has a large effect at higher displacements where the contact area has increased; it can be seen in the 850°C at 0.01 s⁻¹ curve that a good match is achieved early in the test but the curves diverge at the end, which suggests that this test occurred under increased friction conditions. The material used to produce the data for the FE model was Ti-6Al-4V HDH powder processed in an 80 mm mould with a similar FAST cycle to this work, except a lower pressure of 21 MPa and allowed to free cool; the cooling rate was intermediate to those demonstrated in Fig. 6.15 and produced a transformed β microstructure with α laths of intermediate thickness to those shown here. This difference in starting microstructure may also explain some of the disparities between simulation and experiment [100]. It should be noted that as tabulated data has been used the FE model can only be employed with confidence within the processing window defined by the extremes of the experimental conditions.

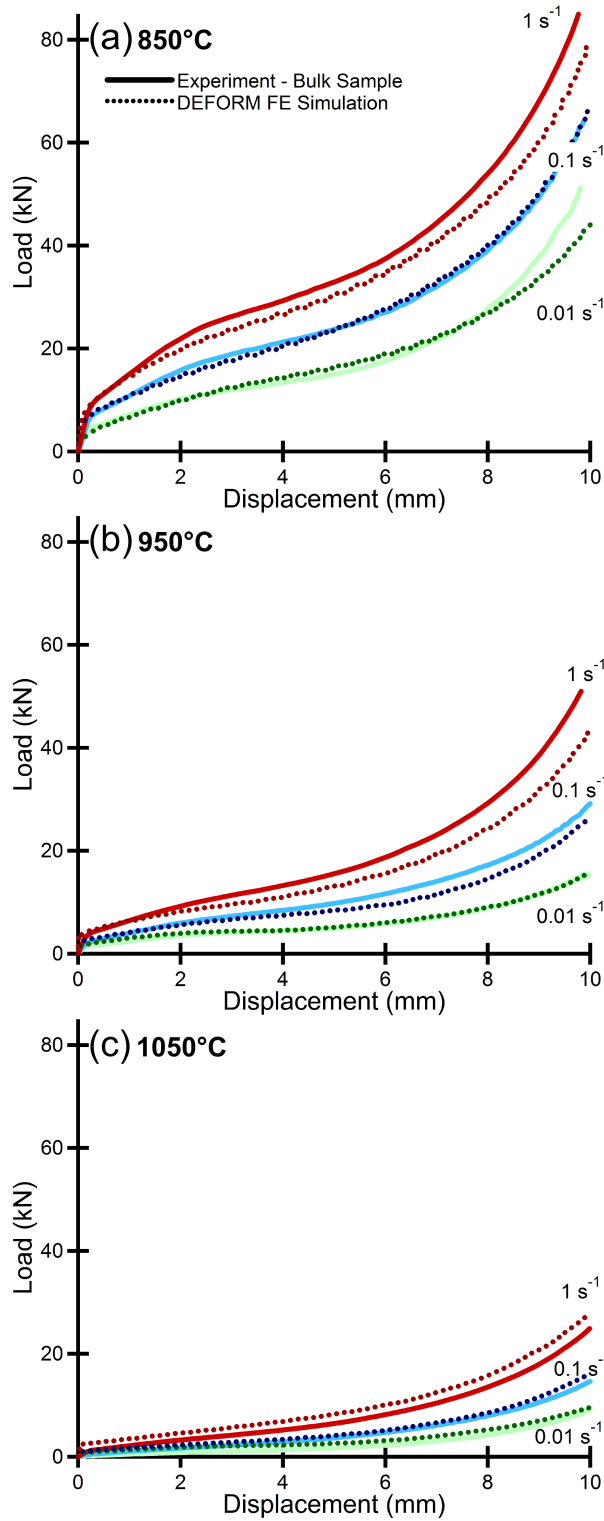


Figure 6.24 – Graphs comparing the load displacement curves during the upset forging of double truncated cone specimens at 850°C (a), 950°C (b) and 1050°C (c) at strain rates of 0.01 s^{-1} , 0.1 s^{-1} and 1 s^{-1} (as labelled); from bulk FAST material (solid lines) against those obtained from DEFORMTM FE simulation (dotted lines).

6.4 Conclusions

It is possible to fully fill a double truncated cone shaped FAST mould of varying dimensions. Full density and microstructural homogeneity can be achieved when using an all graphite mould assembly. The homogeneous nature of the consolidation indicates that there must be material flow to fill the mould; analogous to a closed die forging. This leads to a belief that the latter stages of FAST processing involves some degree of forging behaviour in addition to simple sintering; FAST could therefore be considered as a hybrid process.

The use of steel in the FAST mould assembly did not appear to offer the benefits that were hoped for. The maximum dwell temperature had to be reduced due to poorer high temperature strength and the power required for processing was slightly increased rather than reduced. Observed microstructural heterogeneity also indicated that there were more complex temperature profiles within the mould and specimen than with an all graphite assembly. A significantly slower cooling rate also greatly increased the processing cycle time.

This chapter has demonstrated at the laboratory-scale that it is possible to produce a fully dense and microstructurally refined forged titanium alloy specimen in only two steps from powder. The production of complex near net shape geometries directly via FAST may be possible in the future with further investigation, although the microstructure would in all likelihood still need refining, depending upon the application.

Directly producing shaped FAST double cone specimens did not negatively affect microstructural or deformational behaviour when compared to double cone specimens machined from homogeneous bulk material. There is very good visual correlation between the two types of specimens. This establishes that using FAST to produce shaped preforms has the potential to be an effective intermediate step in the FAST-*forge* process. Further work is required to explore the possibilities and limitations of the technology prior to scale-up, but in future it should be possible to accurately produce semi-complex shaped FAST preforms tailored for a variety of final component geometries.

The response of Ti-6Al-4V FAST material under forging conditions is very similar to that seen when thermomechanically working conventional Ti-6Al-4V billet material; post-sintering FAST preforms have characteristics similar to

conventional melt, multi-step forged product.

The agreement between experimental load displacement data and FE simulation data gives confidence that the simple tabulated data material model utilised can be used to model the forging of more complex geometries as the FAST-forge process develops (within the processing window defined by the experimental conditions). Further development of a more complex constitutive model would allow increased confidence when expanding the FE simulation requirements.

Initial examination of the microstructural evolution indicates the level of strain, temperature and strain rate required to break up the post FAST microstructure and achieve a bimodal $\alpha + \beta$ microstructure, but further analysis is needed to tie key microstructural features to thermomechanical processing parameters for use in a simple microstructural prediction model.

7. Summary, Conclusions, and Future Work

This chapter will first summarise the work that was done to achieve the aims and objectives of this project, followed by an overview of the conclusions that can be drawn from the presented results. Finally, recommendations will be given for further work that should be performed to answer outstanding questions and in new areas of interest that have become apparent as a consequence of this work.

7.1 Summary

The aim of this project was to demonstrate the possibility to produce cost-effective titanium components with wrought properties by consolidating titanium alloy powders in the fewest steps possible. The route chosen for this was a novel solid-state downstream processing route termed FAST-*forge* [67], which produces a shaped preform billet via field assisted sintering technology (FAST) that is finished to near net shape with a precision one-step forging operation. The potential to apply this cost-effective processing route in combination with a potentially lower-cost powder from an alternative extraction route was also assessed, as this will provide a true step-change in the economics of titanium.

The first two objectives were to assess whether FAST was suitable and effective at consolidating a range of titanium alloy powders and to investigate how the processing parameters and feedstock characteristics effect density and microstructure of FAST preforms. These were investigated in chapter 4 by performing parametric studies with the four main FAST processing parameters (dwell temperature, dwell pressure, dwell time, and heating rate) as inputs and measuring density and microstructural evolution as outputs. Using a range of powder morphologies and alloy chemistries also allowed insight into their effect when FAST parameters were kept constant. Finally, a range of FAST mould sizes were used to check the scalability of the process.

The third objective was to examine the response of FAST preform billet material to thermomechanical processing conditions. This was conducted in chapter 5

by performing thermomechanical processing in the form of hot axisymmetric compression testing on cylindrical specimens taken from FAST billets. In order for the forgeability and microstructural evolution of FAST preforms to be assessed this testing replicated the expected conditions (strain, strain rate, and temperature) that would be found when forging them to near net shape. Again, a range of alloy chemistries and powder morphologies was used to check their influence on post-FAST forging performance. The axisymmetric compression tests allowed generation of rheology data in the form of flow curves and viewing microstructural changes through subsequent microscopy, which allowed direct comparison of performance with conventionally processed alloys.

The final objective was to combine the FAST and forging knowledge gained from the previous three objectives to demonstrate a laboratory-scale cost-effective processing route. This initially necessitated the investigation of the ability of FAST to produce simple shaped preforms (double truncated cone geometries) and whether an alternative mould material (253 MA[®] steel) and assembly (thermal/electrical insulation of powder from the ring mould) would provide cost savings. Double truncated cones were then produced via machining from bulk and also directly by using shaped FAST moulds. These double cones were also thermomechanically processed via hot axisymmetric compression to allow comparison of the shaped and bulk material. The microstructural evolution from very low to high strain was also studied via examination of the deformed specimens.

7.2 Conclusions

Chapters 4, 5, and 6 all demonstrated that consolidation of titanium alloy feedstocks utilising FAST processing is viable. FAST is tolerant of input material chemistry and morphology, and with tailoring of processing conditions it is possible to achieve high levels of density and homogeneous microstructures. This still held true at the maximum 5.5 kg and 250 mm diameter disc produced in this study, showing the scalability of the FAST process and technology. It is encouraging that it is already possible to produce preform billets at the scale of real world components. The size of FAST furnaces commercially available is also further increasing.

7.2.1 Consolidation of Titanium Alloy Powders via FAST

Chapter 4 showed that dwell temperature and dwell pressure are the most influential FAST processing parameters on specimen density. In general it appears the highest possible dwell pressure should be used, with the strength of the graphite ring mould/punches the limiting factor found in this work. Higher densities were achieved using higher dwell temperatures when other parameters were kept constant. A dwell temperature that is high enough to sufficiently lower the powder's flow strength (allowing easier plastic deformation) and enhance diffusional sintering mechanisms is required, but this needs to be balanced against possible interstitial element contamination and excessive microstructural coarsening. For titanium alloys this manifested as improvements in density when using dwell temperatures above the β transus temperature but at the expense of rapid β grain growth. A compromise is likely to be needed that will vary depending upon each unique alloy and the subsequent processing route.

Chapter 4 also indicated when using a dwell temperature and dwell pressure that achieve high densities that the dwell time and heating rate have negligible effect upon density and only a slight effect on microstructure. The main benefit of utilising a higher heating rate is the corresponding reduction in process cycle time. The dwell period only needs to be long enough to complete consolidation, if it hasn't already occurred during heat up. However, a longer dwell time may ensure that prior particles have formed a full diffusion bond rather than merely plastically deformed around each other. This will not be immediately obvious from the FAST machine data, but will be visible upon microstructural examination of the prior β grain size.

Chapter 4 demonstrated that a smaller feedstock size allowed easier consolidation; most likely due to increased packing densities and diffusional processes acting across smaller length-scales. Particle morphology had little effect on final density, although it appeared angular particles allowed retention of a slightly smaller grain size. The most problematic morphology to produce high density with was the spongy Metalysis powders containing internal porosity. The reason that these internal pores were not as easy to remove as inter-particle voids has not been identified but may be a powder cleanliness issue. It is clear that it was not related to alloy chemistry as, when the spongy particles were spheroidised, it was possible to achieve full density. Additionally, low levels of interstitial pick-up were measured and the thin layer of stabilised α observed due

to carbon ingress is not overly problematic; it could easily be removed through a light finish machining operation, which is usually necessary after final forging anyway.

It became apparent that the FAST processing parameters used to ensure high density, and the intrinsic cooling rates of the equipment, mean the microstructures produced across the different alloy powders are not those typically required for titanium alloy components. Equally, the simple uniform thickness disc specimens are not the logical starting shape for further processing steps to produce components.

7.2.2 Thermomechanical Processing of Titanium Alloys Consolidated via FAST

Chapter 5 showed that preform billet material consolidated via FAST behaves in a manner very similar to conventionally processed material for all four titanium alloys tested in this study. The observed behaviour correlates well both in terms of flow data and microstructural evolution. None of the alloy test specimens exhibited edge cracking or non-uniform deformation characteristics. Microstructural analysis of the four alloys after deformation at a range of temperatures and strain rates found that significant microstructural refinement can be achieved by forging after FAST processing; fully globularised bi-modal microstructures were obtained with specimens produced from Ti-6Al-4V HDH powder. The level of microstructural refinement is further demonstrated in the hardness data gathered for the Ti-6Al-4V specimens, which indicates that the FAST preform billets that undergo subsequent thermomechanical processing should have tensile properties to compete with conventionally processed melt-wrought products.

Chapter 5 also successfully integrated rheology data produced from the Ti-6Al-4V HDH powder specimens into the finite element software DEFORMTM. The simulations of the axisymmetric compression tests showed excellent agreement with the experimental data. This shows if further work with alternative lower-cost alloys is performed it will be possible to quickly obtain the necessary material data via small-scale FAST processing and TMC testing to allow accurate simulation of any large-scale component forging operations required.

The highlight of chapter 5 is that the performance of preform billet material

produced from titanium alloy powders in one processing step via FAST behaves equivalently to material that has undergone the conventional processing route of Kroll extraction, VAR, and ~20-30 forging stages. This implies, through massive reduction of thermomechanical processing steps, that there are potentially huge cost savings to be made by using FAST as a powder consolidation method.

7.2.3 FAST-*forge*

Chapter 6 showed that it is possible to fully fill double truncated cone shaped FAST mould inserts in a variety of mould assemblies. Full density and microstructural homogeneity can be achieved when using shaped inserts in an all graphite mould assembly. The homogeneous nature of the consolidation indicates that there must be material flow to fill the mould; in a similar manner to a closed die forging. The belief is that the latter stages of FAST incorporates some degree of forging behaviour in addition to simple sintering and therefore can be considered a hybrid process. The direct production of double cones did not change their behaviour under subsequent thermomechanical processing. This establishes that using FAST to produce shaped preforms has the potential to be an effective initial step in the FAST-*forge* process.

The shaped preform FAST billets manufactured from Ti-6Al-4V HDH powder demonstrated very similar behaviour during thermomechanical processing to the uniform discs in chapter 5 and, as reported, this also correlates closely with conventional melt, multi-step forged products. Examination of the microstructural evolution indicates the level of strain, temperature and strain rate required to refine the post-FAST microstructure into a bimodal $\alpha + \beta$ structure.

The use of steel in the FAST mould assembly did not appear to offer significant benefits. The maximum dwell temperature had to be reduced due to poorer high temperature strength and the power required for processing was increased. More complex temperature profiles within the specimen were also observed through microstructural heterogeneity.

The key finding of chapter 6 is that it is possible, at the laboratory-scale, to produce a fully dense, and microstructurally refined, forged titanium alloy specimen in only two steps starting from a powder feedstock. Thus, it has acted as a proof-of-concept for the FAST-*forge* process.

7.2.4 Concluding Remarks

Whilst heating rates of $200^{\circ}\text{Cmin}^{-1}$ were attained when using ~ 300 g of powder on the Type HP D 25 FAST furnace, it was only possible to heat at $25^{\circ}\text{Cmin}^{-1}$ when processing 5.5 kg of powder in a 250 mm diameter mould on the Type H-HP D 250 FAST furnace due to limited available power. If very high heating rates prove to be desirable the power requirements to produce industrially sized components should be a design consideration for the next generation of FAST furnaces.

Investigating the opportunities and limitations in producing shaped preforms via FAST is now of great importance. The idea of performing a one-step forging operation to finish shaped FAST preforms to near net shape components is predicated on the ability to produce a suitably shaped preform billet. The scalability of shaped preform production will also need to be studied; although there are favourable indications with simple discs that this will not be an issue. It is hoped that the production of semi-complex near net shape geometries directly via FAST may be possible in the future with sufficient further studies. Therefore it is possible, depending upon the application and if increased microstructural control can be achieved, that a subsequent forging step may not be needed.

At the current level of FAST technology commercially available the cost-effectiveness achieved by the FAST-*forge* processing route will vary from component to component; an economic assessment on a case-by-case basis would be required. The initial set-up costs may negate benefits for small batch production. Speed of processing limitations may exclude products requiring continuous or very large and/or quick batch production. However, with expensive feedstocks such as titanium alloys there may still be cost reductions to be found via FAST-*forge*. The tooling costs for FAST compare favourably against HIP, where the steel can bonds to the titanium and needs to be machined away, as the majority of the graphite mould assembly is reusable. The longevity and cost-effectiveness of the mould assembly in terms of both material and geometry needs to be investigated further to give an understanding of tooling costs as the technology progresses in size and part complexity.

It is further anticipated that if the required mechanical properties of a component are identified then a microstructure necessary to meet these can be predicted. Using FE simulation, linked to a microstructural model, the shape of the preform

could be iteratively optimised so that the one step precision forging operation can produce the correct levels of strain at the forging conditions to yield the appropriate microstructure to meet the property requirements.

In the long-term it is believed that FAST-*forge* combined with potentially lower-cost powder from an alternative extraction method will be disruptive technology that will enable a step change in the economics of titanium alloys.

7.3 Future Work

Whilst a reasonable number of powder feedstock chemistries and morphologies have been successfully consolidated it would be useful to assess further powders. The larger the variety of feedstocks that are available to the FAST-*forge* process the wider the possible applications. This should include higher quality powders from the Metalysis process rather than the developmental powders used in this work. If powders from other lower-cost extraction methods could be obtained then it would also allow an interesting comparative study to be undertaken. Another possibility for a lower-cost feedstock is sponge fines from the Kroll process. As FAST proved tolerant to larger particle morphologies there is also the opportunity to use machining swarf instead of powder. The current titanium buy-to-fly ratio for the F-22 fighter jet is 12.2:1 meaning that for every 50 tonnes purchased 45.8 tonnes ends up as scrap; mostly in the form of machining swarf. It is therefore clear the titanium industry creates a huge amount of swarf, most of which is sold cheaply to the ferrotitanium industry to be used in purifying steel. If titanium machining swarf can be used as a feedstock, and thus recycled via the FAST-*forge* process, then it may produce incredibly cost-effective components.

The thermomechanical processing performed so far has been limited to axisymmetric compression testing that replicated open die forging. It would be of interest to assess the suitability of further thermomechanical processing techniques as the subsequent deformation step after FAST. Rotary forging or flow forming of rings produced by FAST may provide an area for further investigation. Equally hot rolling of FAST billets down to sheet could provide benefits and merits examination.

The FAST processing conditions used to produce the preforms in chapters 5 and 6 were utilised as they gave very high density but little consideration for the microstructure was given (all dwell temperatures were above the β

transus temperature); the dwell temperature, dwell pressure, and dwell time were probably higher than required. Further work is needed to establish the lower-bound of FAST parameters to achieve acceptable density. Reducing temperature, pressure, and time will help to reduce processing costs through requiring less time and energy. Additionally it will improve the lifespan of the moulds, reduce the level of carbon contamination seen, and produce a microstructure with a finer grain size. There is also scope to further examine the microstructures that can be produced by FAST processing. A study that uses dwell temperatures below the β transus temperature for $\alpha + \beta$ and β alloys has the potential to produce bimodal microstructures that may be beneficial; although not at the expense of high density. It would probably be useful to focus on a specific alloy, possibly to meet the requirements of a specific component, to fully optimise the processing route by developing a deeper understanding of the relationship between microstructure and FAST, forging, and heat treatment conditions.

This work only focused on FAST consolidation of individual titanium alloys. An interesting development would be to produce preforms with more than one titanium alloy system present. Initial studies have demonstrated that FAST produces very good diffusional bonds between two different alloys (e.g. Ti-6Al-4V and Ti-5553) with a gradual transition from one composition to the other; this could also be used to produce functionally graded materials (FGM) where multiple alloys are utilised. FAST-*forg*e has been identified as a cost-effective route for titanium alloys due to their high cost and it is unlikely to offer similar benefits for commodity metals such as steel and aluminium. However, the scope to process more exotic materials offers an exciting avenue for further work. The production of metal matrix composites, cermets, and MAX phases could all be pursued.

Some components require drastically different mechanical properties at different locations within their geometry. This is not usually accounted for in current design methodologies where the component is treated as a whole. Using FAST it may be possible to produce a preform with tailored properties in specific areas. This could be achieved by the use of different alloy chemistries or through microstructural control; by intentionally developing temperature profiles and varying dwell times, or through utilising different particle sizes and/or morphologies. The response of such preforms under thermomechanical

processing would also need to be fully understood.

Finite element simulation will be an essential tool to develop the FAST-*forge* process. The rheology data generated in this work was successfully integrated into FE simulation of the axisymmetric deformations, in a simple tabulated data material model form, with good agreement between experimental and simulation (within the processing window defined by the experimental conditions). This should allow modelling the forging of more complex geometries as the FAST-*forge* process develops, although the development of a more complex constitutive material model would allow increased confidence when expanding the FE simulation requirements. A modelling methodology would need to be developed to allow the optimisation of the geometry of the shaped preform billet so that an effective one-step forging operation can be achieved. Modelling of the FAST process will also be needed. A successfully developed and validated FAST model will aid with mould assembly/shaped die design, and also with pressure, temperature, and density profiles which could be linked to microstructure prediction.

As mentioned investigating the opportunities available and any limitations in producing shaped preforms via FAST is now very important. So far only relatively simple axisymmetric shapes have been produced. Moving towards semi-complex, non-axisymmetric shapes is desirable, whilst also assessing the limits on fillet radii and draft angles. A large portion of this work will be in appropriately designing moulds, which could also facilitate studying alternative mould materials. Graphite appears to work very well but has limitations with regards to mould life, mechanical strength, and specimen contamination.

Finally FAST-*forge* has been demonstrated at the laboratory-scale with a simple specimen geometry. Performing a case study on an actual small component is needed to truly demonstrate the proposed processing route works. This may initially mean that an optimised preform shape is designed and then machined from bulk FAST material, as done in chapter 6, to show that a one-step forging operation can be achieved. If successful, the shaped preform could then be produced directly via FAST. No mechanical property testing (tensile or fatigue) has so far been undertaken due to the small size of specimens produced, but this obviously needs to be addressed to ensure conventional wrought properties are being matched/exceeded.

Bibliography

- [1] G. Lutjering and J.C. Williams. *Titanium*. Ed. by B. Derby. 2nd. New York: Springer, 2007. ISBN: 978-3-540-71397-5.
- [2] M J Donachie. *Titanium: A Technical Guide, 2nd Edition*. ASM International, 2000. ISBN: 9781615030620.
- [3] H. Sibus. “Titanium and Titanium Alloys - From Raw Material to Semi-finished Products”. In: *Titanium and Titanium Alloys: Fundamentals and Applications*. Ed. by C Leyens and M Peters. Wiley, 2006. Chap. 7, pp. 231–244. ISBN: 3-527-30534-3.
- [4] R. R. Boyer. “Attributes, characteristics, and applications of titanium and its alloys”. In: *JOM* 62.5 (May 2010), pp. 21–24. ISSN: 1047-4838. DOI: [10.1007/s11837-010-0071-1](https://doi.org/10.1007/s11837-010-0071-1).
- [5] E. H. Kraft. *Summary of emerging titanium cost reduction technologies*. Tech. rep. Vancouver WA: EHKTechnologies, 2004.
- [6] Z. Zak Fang and Pei Sun. “Pathways to Optimize Performance/Cost Ratio of Powder Metallurgy Titanium – A Perspective”. In: *Key Engineering Materials* 520 (2012), pp. 15–23. ISSN: 1662-9795. DOI: [10.4028/www.scientific.net/KEM.520.15](https://doi.org/10.4028/www.scientific.net/KEM.520.15).
- [7] D.J. Fray. “Novel methods for the production of titanium”. In: *International Materials Reviews* 53.6 (2008), pp. 317–325. ISSN: 09506608. DOI: [10.1179/174328008X324594](https://doi.org/10.1179/174328008X324594).
- [8] M. Jackson and K. Dring. “A review of advances in processing and metallurgy of titanium alloys”. In: *Materials Science and Technology* 22.8 (2006), pp. 881–887. ISSN: 02670836. DOI: [10.1179/174328406X111147](https://doi.org/10.1179/174328406X111147).
- [9] T.E. Norgate and G. Wellwood. “The potential applications for titanium metal powder and their life cycle impacts”. In: *JOM* 58.9 (2006), pp. 58–63. ISSN: 1047-4838. DOI: [10.1007/s11837-006-0084-y](https://doi.org/10.1007/s11837-006-0084-y).

- [10] V.A. Duz et al. “Blending an elemental approach to volume titanium manufacture”. In: *Metal Powder Report* November (2006), pp. 16–21.
- [11] F.H. Froes et al. “The technologies of titanium powder metallurgy”. In: *JOM* 56.November (2004), pp. 46–48.
- [12] Anil K. Sachdev et al. “Titanium for Automotive Applications: Challenges and Opportunities in Materials and Processing”. In: *Jom* 64.5 (2012), pp. 553–565. ISSN: 1047-4838. DOI: [10.1007/s11837-012-0310-8](https://doi.org/10.1007/s11837-012-0310-8).
- [13] R. Orrù et al. “Consolidation/synthesis of materials by electric current activated/assisted sintering”. In: *Materials Science and Engineering R* 63.4-6 (2009), pp. 127–287. ISSN: 0927796X. DOI: [10.1016/j.mser.2008.09.003](https://doi.org/10.1016/j.mser.2008.09.003).
- [14] Salvatore Grasso, Yoshio Sakka, and Giovanni Maizza. “Electric current activated/assisted sintering (ECAS): a review of patents 1906–2008”. In: *Science and Technology of Advanced Materials* 10.5 (2009), p. 053001. ISSN: 1468-6996. DOI: [10.1088/1468-6996/10/5/053001](https://doi.org/10.1088/1468-6996/10/5/053001).
- [15] Z.A. Munir, U. Anselmi-Tamburini, and M. Ohyanagi. “The effect of electric field and pressure on the synthesis and consolidation of materials: A review of the spark plasma sintering method”. In: *Journal of Materials Science* 41.3 (2006), pp. 763–777. DOI: [10.1007/s10853-006-6555-2](https://doi.org/10.1007/s10853-006-6555-2).
- [16] Z.A. Munir, D. V. Quach, and M. Ohyanagi. “Electric current activation of sintering: A review of the pulsed electric current sintering process”. In: *Journal of the American Ceramic Society* 94.1 (2011), pp. 1–19. ISSN: 00027820. DOI: [10.1111/j.1551-2916.2010.04210.x](https://doi.org/10.1111/j.1551-2916.2010.04210.x).
- [17] Scientific Forming Technologies Corporation. *DEFORM (v.11.0.1)*. SFTC, Columbus, Ohio, 2016.
- [18] A. Russell. “The Rev. William Gregor (1761-1817), discoverer of titanium.” In: *Journal of the Mineralogical Society* 30.229 (1955), pp. 617–624. ISSN: 0026-461X. DOI: [10.1180/minmag.1955.030.229.01](https://doi.org/10.1180/minmag.1955.030.229.01).

- [19] W.J. Kroll. “How commercial titanium and zirconium were born”. In: *Journal Of The Franklin Institute* 260.3 (Sept. 1955), pp. 169–192. ISSN: 00160032. DOI: [10.1016/0016-0032\(55\)90727-4](https://doi.org/10.1016/0016-0032(55)90727-4).
- [20] M A Hunter. “METALLIC TITANIUM.” In: *Journal of the American Chemical Society* 32.3 (1910), pp. 330–336. DOI: [10.1021/ja01921a006](https://doi.org/10.1021/ja01921a006).
- [21] W.J. Kroll. “The Production of Ductile Titanium”. In: *Transactions of The Electrochemical Society* 78.1 (1940), p. 35. ISSN: 00964743. DOI: [10.1149/1.3071290](https://doi.org/10.1149/1.3071290).
- [22] E L Anderson et al. *Production of ductile titanium at Boulder City, Nev.* [Washington, D.C.], 1949.
- [23] M A Cook and F S Wartman. *Removal of magnesium and magnesium chloride from titanium sponge by vacuum distillation.* [Washington, D.C.], 1952.
- [24] F H Froes. *Titanium: Physical Metallurgy, Processing, and Applications*: EngineeringPro collection. A S M International, 2015. ISBN: 9781627080804.
- [25] U.S. Geological Survey. “Titanium and titanium dioxide”. In: *Mineral Commodity Summaries* 1.703 (2012), pp. 172–173.
- [26] I J Polmear. *Light Alloys: From Traditional Alloys to Nanocrystals.* Elsevier/Butterworth-Heinemann, 2006. ISBN: 9780750663717.
- [27] W D Callister and W D C William D. *Materials Science and Engineering: An Introduction, 7th Edition Wiley Plus Set.* John Wiley & Sons, Limited, 2007. ISBN: 9780470120323.
- [28] H M Flower. “Microstructural development in relation to hot working of titanium alloys”. In: *Materials Science and Technology* 6.11 (1990), pp. 1082–1092. ISSN: 02670836. DOI: [10.1179/026708390790189984](https://doi.org/10.1179/026708390790189984).
- [29] V. A. Joshi. *Titanium Alloys: An Atlas of Structures and Fracture Features.* 1st. CRC Press Taylor and Francis Group, LLC, 2006. ISBN: 9780849350108.
- [30] *Kobe Steel Data Book: Titanium.*

- [31] T. Nishimura. *Forming technology of titanium (in Japanese)*. Nikkan Kogyo Shimbun, 1992, p. 3.
- [32] M.J. Gázquez et al. “A Review of the Production Cycle of Titanium Dioxide Pigment”. In: *Materials Sciences and Applications* 05.07 (2014), pp. 441–458. ISSN: 2153-117X. DOI: [10.4236/msa.2014.57048](https://doi.org/10.4236/msa.2014.57048).
- [33] U.S. Geological Survey. “Titanium mineral concentrates”. In: *Mineral Commodity Summaries* 1.703 (2012), pp. 172–173.
- [34] Wensheng Zhang, Zhaowu Zhu, and Chu Yong Cheng. “A literature review of titanium metallurgical processes”. In: *Hydrometallurgy* 108.3-4 (2011), pp. 177–188. ISSN: 0304386X. DOI: [10.1016/j.hydromet.2011.04.005](https://doi.org/10.1016/j.hydromet.2011.04.005).
- [35] R G Becher et al. “A new process for upgrading ilmenitic mineral sands”. In: *Australasian Inst Mining Met Proc.* 214. 1965, pp. 21–44.
- [36] G E Dieter, H A Kuhn, and S.L. Semiatin. *Handbook of Workability and Process Design*. A S M International, 2003. ISBN: 9781615032280.
- [37] G. Lütjering. “Influence of processing on microstructure and mechanical properties of (alpha+beta) titanium alloys”. In: *Materials Science and Engineering: A* 243.1 (1998), pp. 32–45. ISSN: 09215093. DOI: [10.1016/S0921-5093\(97\)00778-8](https://doi.org/10.1016/S0921-5093(97)00778-8).
- [38] a. Momeni and S. M. Abbasi. “Effect of hot working on flow behavior of Ti-6Al-4V alloy in single phase and two phase regions”. In: *Materials and Design* 31.8 (2010), pp. 3599–3604. ISSN: 02641275. DOI: [10.1016/j.matdes.2010.01.060](https://doi.org/10.1016/j.matdes.2010.01.060).
- [39] E. B. Shell and S.L. Semiatin. “Effect of initial microstructure on plastic flow and dynamic globularization during hot working of Ti-6Al-4V”. In: *Metallurgical and Materials Transactions A* 30.December (1999), pp. 3219–3229. ISSN: 1073-5623. DOI: [10.1007/s11661-999-0232-4](https://doi.org/10.1007/s11661-999-0232-4).
- [40] S.L. Semiatin, V Seetharaman, and I Weiss. “Flow behavior and globularization kinetics during hot working of Ti-6Al-4V with a colony alpha microstructure”. In: *Materials Science and*

- Engineering: A* 263.2 (1999), pp. 257–271. ISSN: 09215093. DOI: [10.1016/S0921-5093\(98\)01156-3](https://doi.org/10.1016/S0921-5093(98)01156-3).
- [41] T. Seshacharyulu et al. “Microstructural mechanisms during hot working of commercial grade Ti-6Al-4V with lamellar starting structure”. In: *Materials Science and Engineering A* 325.1-2 (2002), pp. 112–125. ISSN: 09215093. DOI: [10.1016/S0921-5093\(01\)01448-4](https://doi.org/10.1016/S0921-5093(01)01448-4).
- [42] S. Zharebtsov et al. “Spheroidization of the lamellar microstructure in Ti-6Al-4V alloy during warm deformation and annealing”. In: *Acta Materialia* 59.10 (June 2011), pp. 4138–4150. ISSN: 13596454. DOI: [10.1016/j.actamat.2011.03.037](https://doi.org/10.1016/j.actamat.2011.03.037).
- [43] S.L. Semiatin, V. Seetharaman, and I. Weiss. “The thermomechanical processing of alpha/beta titanium alloys”. In: *Jom* 49.6 (1997), pp. 33–39. ISSN: 1047-4838. DOI: [10.1007/BF02914711](https://doi.org/10.1007/BF02914711).
- [44] B Roebuck, J D Lord, and M Brooks. “Measurement Good Practice Guide No 3 - Measuring Flow Stress in Hot Axisymmetric Compression Tests”. In: 3 (2002).
- [45] G E Dieter and D Bacon. *Mechanical Metallurgy*. Materials Science and Engineering Series. McGraw-Hill, 1988. ISBN: 9780070841871.
- [46] T Altan, S I Oh, and H L Gegel. *Metal forming: fundamentals and applications*. ASM series in metal processing. American Society for Metals, 1983. ISBN: 9780871701671.
- [47] A.T. Male and M.G. Cockcroft. “A method for the determination of the coefficient of friction of metals under condition of bulk plastic deformation.” In: *Journal of the Institute of Metals* (1965), pp. 38–46.
- [48] P. Davies. “An Investigation of Microstructure and Texture Evolution in the Near- α Titanium Alloy Timetal 834”. PhD. The University of Sheffield, 2009.
- [49] M.J. Thomas. “The Effect of Thermomechanical Process Parameters on the Microstructure and Crystallographic Texture Evolution of Near- α Aerospace Alloy Timetal 834.” PhD. The University of Sheffield, 2007.

- [50] M. Jackson et al. “Application of novel technique to examine thermomechanical processing of near beta alloy Ti-10V-2Fe-3Al”. In: *Materials Science and Technology* 16.11-12 (2000), pp. 1437–1444. ISSN: 02670836. DOI: [10.1179/026708300101507433](https://doi.org/10.1179/026708300101507433).
- [51] W.J. Kroll. “The Present State of Titanium Extractive Metallurgy”. In: *Trans. AIME* 215.4 (1959), pp. 545–553.
- [52] C.M. Hall. *Process of reducing aluminium from its fluoride salts by electrolysis*. 1889.
- [53] I. Mellor et al. “Titanium Powder Production via the Metalysis Process”. In: *Titanium Powder Metallurgy: Science, Technology and Applications*. Ed. by M. Qian and F. H. Froes. 1st. Oxford, UK: Butterworth-Heinemann Ltd, 2015. Chap. 4, pp. 51–67. ISBN: 978-0-12-800054-0. DOI: [10.1016/B978-0-12-800054-0.00004-6](https://doi.org/10.1016/B978-0-12-800054-0.00004-6).
- [54] L. L. Benson, I. Mellor, and M. Jackson. “Direct reduction of synthetic rutile using the FFC process to produce low-cost novel titanium alloys”. In: *Journal of Materials Science* 51.9 (2016), pp. 1–12. ISSN: 15734803. DOI: [10.1007/s10853-015-9718-1](https://doi.org/10.1007/s10853-015-9718-1).
- [55] V.A. Duz et al. “Industrial application of titanium hydride powder”. In: *Metal Powder Report* (2016). ISSN: 00260657. DOI: [10.1016/j.mprp.2016.02.051](https://doi.org/10.1016/j.mprp.2016.02.051).
- [56] D. R. Armstrong, S. S. Borys, and R. P. Anderson. *Method of making metals and other elements from the halid vapor of the metal*. 1999.
- [57] J.C. Withers. “Production of Titanium Powder by an Electrolytic Method and Compaction of the Powder”. In: *Titanium Powder Metallurgy: Science, Technology and Applications*. Ed. by M Qian and F.H. Froes. 1st. Oxford, UK: Butterworth-Heinemann Ltd, 2015. Chap. 3, pp. 33–50. ISBN: 978-0-12-800054-0. DOI: [10.1016/B978-0-12-800054-0.00003-4](https://doi.org/10.1016/B978-0-12-800054-0.00003-4).
- [58] D. S. Van Vuuren, S. J. Oosthuizen, and M. D. Heydenrych. “Titanium production via metallothermic reduction of TiCl₄ in molten salt: Problems and products”. In: *Journal of the Southern African Institute of Mining and Metallurgy* 111.3 (2011), pp. 141–148. ISSN: 22256253.

- [59] C. Doblin, A. Chryss, and A. Monch. “Titanium powder from the TiRO process”. In: *Key Engineering Materials* 520 (2012), pp. 95–100. DOI: [10.4028/www.scientific.net/KEM.520.95](https://doi.org/10.4028/www.scientific.net/KEM.520.95).
- [60] G. Z. Chen, D. J. Fray, and T. W. Farthing. “Direct electrochemical reduction of titanium dioxide to titanium in molten calcium chloride”. In: *Nature* 407.6802 (Sept. 2000), pp. 361–364. ISSN: 1476-4687. DOI: [10.1038/35030069](https://doi.org/10.1038/35030069).
- [61] D. J. Fray and G. Z. Chen. “Reduction of titanium and other metal oxides using electrodeoxidation”. In: *Materials Science and Technology* 20.3 (Mar. 2004), pp. 295–300. ISSN: 02670836. DOI: [10.1179/026708304225012242](https://doi.org/10.1179/026708304225012242).
- [62] K. Dring et al. “Direct electrochemical production of Ti-10W alloys from mixed oxide preform precursors”. In: *Journal of Alloys and Compounds* 419.1-2 (2006), pp. 103–109. ISSN: 09258388. DOI: [10.1016/j.jallcom.2005.10.029](https://doi.org/10.1016/j.jallcom.2005.10.029).
- [63] Randall M. German. *Sintering: From Empirical Observations to Scientific Principles*. 2014, pp. 1–535. ISBN: 978-0-12-401682-8. DOI: [10.1016/B978-0-12-401682-8.00011-2](https://doi.org/10.1016/B978-0-12-401682-8.00011-2).
- [64] M Qian and F H Froes. *Titanium Powder Metallurgy: Science, Technology and Applications*. Elsevier Science, 2015. ISBN: 9780128009109.
- [65] N.S. Weston et al. “Spark plasma sintering of commercial and development titanium alloy powders”. In: *Journal of Materials Science* 50.14 (July 2015), pp. 4860–4878. ISSN: 0022-2461. DOI: [10.1007/s10853-015-9029-6](https://doi.org/10.1007/s10853-015-9029-6).
- [66] N.S. Weston, Fatos Derguti, and Martin Jackson. “Exploitation of Spark Plasma Sintering and One-Step Forging for Cost-Effective Processing of Titanium Alloy Powders”. In: *Proceedings of the 13th World Conference on Titanium* (2016). Ed. by V. Venkatesh et al., pp. 123–128. DOI: [10.1002/9781119296126.ch18](https://doi.org/10.1002/9781119296126.ch18).
- [67] N.S. Weston and M. Jackson. “FAST-forge - a new cost-effective hybrid processing route for consolidating titanium powder into near net shape forged components”. In: *Journal of Materials Processing Technology* 243 (2017), pp. 335–346. ISSN: 09240136. DOI: [10.1016/j.jmatprotec.2016.12.013](https://doi.org/10.1016/j.jmatprotec.2016.12.013).

- [68] M. Eriksson, M. Radwan, and Z. Shen. “Spark plasma sintering of WC, cemented carbide and functional graded materials”. In: *International Journal of Refractory Metals and Hard Materials* 36 (Jan. 2013), pp. 31–37. ISSN: 02634368. DOI: [10.1016/j.ijrmhm.2012.03.007](https://doi.org/10.1016/j.ijrmhm.2012.03.007).
- [69] D. M. Hulbert et al. “The absence of plasma in spark plasma sintering”. In: *Journal of Applied Physics* 104.3 (2008), p. 033305. ISSN: 00218979. DOI: [10.1063/1.2963701](https://doi.org/10.1063/1.2963701).
- [70] J.E. Garay, U. Anselmi-Tamburini, and Z.A. Munir. “Enhanced growth of intermetallic phases in the Ni–Ti system by current effects”. In: *Acta Materialia* 51.15 (Sept. 2003), pp. 4487–4495. ISSN: 13596454. DOI: [10.1016/S1359-6454\(03\)00284-2](https://doi.org/10.1016/S1359-6454(03)00284-2).
- [71] JR J.R. Friedman et al. “Modified interfacial reactions in Ag–Zn multilayers under the influence of high DC currents”. In: *Intermetallics* 12.6 (June 2004), pp. 589–597. ISSN: 09669795. DOI: [10.1016/j.intermet.2004.02.005](https://doi.org/10.1016/j.intermet.2004.02.005).
- [72] N Bertolino, J Garay, and Z.A. Munir. “Electromigration effects in Al–Au multilayers”. In: *Scripta Materialia* 44 (2001), pp. 737–742.
- [73] W. Chen et al. “Fundamental investigations on the spark plasma sintering/synthesis process I. Effect of dc pulsing on reactivity”. In: *Materials Science and Engineering: A* 394.1-2 (Mar. 2005), pp. 132–138. ISSN: 09215093. DOI: [10.1016/j.msea.2004.11.020](https://doi.org/10.1016/j.msea.2004.11.020).
- [74] Naoki Toyofuku et al. “Effect of pulsed DC current on neck growth between tungsten wires and tungsten plates during the initial stage of sintering by the spark plasma sintering method”. In: *Journal of Materials Science* 47.5 (Oct. 2011), pp. 2201–2205. ISSN: 0022-2461. DOI: [10.1007/s10853-011-6026-2](https://doi.org/10.1007/s10853-011-6026-2).
- [75] J. M. Frei, U. Anselmi-Tamburini, and Z.A. Munir. “Current effects on neck growth in the sintering of copper spheres to copper plates by the pulsed electric current method”. In: *Journal of Applied Physics* 101.11 (2007), pp. 114914–1 – 114914–8. ISSN: 00218979. DOI: [10.1063/1.2743885](https://doi.org/10.1063/1.2743885).
- [76] Guoqiang Xie et al. “Frequency effect on pulse electric current sintering process of pure aluminum powder”. In: *Materials Science*

- and Engineering: A* 359.1-2 (Oct. 2003), pp. 384–390. ISSN: 09215093. DOI: [10.1016/S0921-5093\(03\)00393-9](https://doi.org/10.1016/S0921-5093(03)00393-9).
- [77] C. Musa et al. “Energy efficiency during conventional and novel sintering processes: the case of Ti–Al₂O₃–TiC composites”. In: *Journal of Cleaner Production* 17.9 (June 2009), pp. 877–882. ISSN: 09596526. DOI: [10.1016/j.jclepro.2009.01.012](https://doi.org/10.1016/j.jclepro.2009.01.012).
- [78] N. Chennoufi et al. “Temperature, Current, and Heat Loss Distributions in Reduced Electrothermal Loss Spark Plasma Sintering”. In: *Metallurgical and Materials Transactions A* 40A.10 (Aug. 2009), pp. 2401–2409. ISSN: 1073-5623. DOI: [10.1007/s11661-009-9934-x](https://doi.org/10.1007/s11661-009-9934-x).
- [79] D. Handtrack et al. “Fabrication of ultra-fine grained and dispersion-strengthened titanium materials by spark plasma sintering”. In: *Materials Science and Engineering A* 437.2 (Nov. 2006), pp. 423–429. ISSN: 09215093. DOI: [10.1016/j.msea.2006.07.143](https://doi.org/10.1016/j.msea.2006.07.143).
- [80] Masaki Sumida and Katsuyoshi Kondoh. “In-Situ Synthesis of Ti Matrix Composite Reinforced with Dispersed Ti₅Si₃ Particles via Spark Plasma Sintering”. In: *Materials Transactions* 46.10 (2005), pp. 2135–2141.
- [81] R. Nicula et al. “Spark plasma sintering synthesis of porous nanocrystalline titanium alloys for biomedical applications.” In: *Biomolecular Engineering* 24.5 (Nov. 2007), pp. 564–7. ISSN: 1389-0344. DOI: [10.1016/j.bioeng.2007.08.008](https://doi.org/10.1016/j.bioeng.2007.08.008).
- [82] Yuki Sakamoto et al. “Mechanical Property of Porous Titanium Produced by Spark Plasma Sintering”. In: *Key Engineering Materials* 385-387 (2008), pp. 637–640. ISSN: 1662-9795. DOI: [10.4028/www.scientific.net/KEM.385-387.637](https://doi.org/10.4028/www.scientific.net/KEM.385-387.637).
- [83] D. He et al. “Temperature-gradient joining of Ti–6Al–4V alloys by pulsed electric current sintering”. In: *Materials Science and Engineering A* 535 (Feb. 2012), pp. 182–188. ISSN: 09215093. DOI: [10.1016/j.msea.2011.12.061](https://doi.org/10.1016/j.msea.2011.12.061).
- [84] A. Miriyev et al. “Titanium to steel joining by spark plasma sintering (SPS) technology”. In: *Journal of Materials Processing Technology* 213 (2013), pp. 161–166.

- [85] Rajesh Chaudhari and Ranjit Bauri. “Microstructure and mechanical properties of titanium processed by spark plasma sintering (SPS)”. In: *Metallography, Microstructure, and Analysis* 3.1 (Feb. 2014), pp. 30–35. ISSN: 2192-9262. DOI: [10.1007/s13632-013-0112-6](https://doi.org/10.1007/s13632-013-0112-6).
- [86] C. Menapace, N. Vicente, and A. Molinari. “Hot forging of Ti-6Al-4V alloy preforms produced by spark plasma sintering of powders”. In: *Powder Metallurgy* 56.2 (Apr. 2013), pp. 102–110. ISSN: 00325899. DOI: [10.1179/1743290112Y.0000000003](https://doi.org/10.1179/1743290112Y.0000000003).
- [87] M. Eriksson, Z. Shen, and M. Nygren. “Fast densification and deformation of titanium powder”. In: *Powder Metallurgy* 48.3 (Sept. 2005), pp. 231–236. ISSN: 0032-5899. DOI: [10.1179/174329005X71939](https://doi.org/10.1179/174329005X71939).
- [88] M. Zadra et al. “Microstructure and mechanical properties of cp-titanium produced by spark plasma sintering”. In: *Powder Metallurgy* 51.1 (Mar. 2008), pp. 59–65. ISSN: 0032-5899. DOI: [10.1179/174329008X277000](https://doi.org/10.1179/174329008X277000).
- [89] S. Muñoz and U. Anselmi-Tamburini. “Temperature and stress fields evolution during spark plasma sintering processes”. In: *Journal of Materials Science* 45.23 (July 2010), pp. 6528–6539. ISSN: 0022-2461. DOI: [10.1007/s10853-010-4742-7](https://doi.org/10.1007/s10853-010-4742-7).
- [90] U. Anselmi-Tamburini et al. “Fundamental investigations on the spark plasma sintering/synthesis process II. Modeling of current and temperature distributions”. In: *Materials Science and Engineering A* 394.1-2 (Mar. 2005), pp. 139–148. ISSN: 09215093. DOI: [10.1016/j.msea.2004.11.019](https://doi.org/10.1016/j.msea.2004.11.019).
- [91] Gustav Mie. “Beiträge zur Optik trüber Medien, speziell kolloidaler Metallösungen”. In: *Annalen der Physik* 330.3 (1908), pp. 377–445. ISSN: 00033804. DOI: [10.1002/andp.19083300302](https://doi.org/10.1002/andp.19083300302).
- [92] ASTM International. *ASTM E384: Standard Test Method for Knoop and Vickers Hardness of Materials*. West Conshohocken, PA: ASTM International, 2012, pp. 1–43. ISBN: 5935522004. DOI: [10.1520/E0384-11E01](https://doi.org/10.1520/E0384-11E01).

- [93] ASTM International. *ASTM C194-09: Standard Test Method for Bulk Density and Volume of Solid Refractories by Wax Immersion*. West Conshohocken, PA: ASTM International, 2015, pp. 1–3. DOI: [10.1520/C0914-09R15](https://doi.org/10.1520/C0914-09R15).
- [94] W. S. Rasband. *ImageJ*. <http://imagej.nih.gov/ij/>: U.S National Institutes of Health, Bethesda, Maryland, USA, 1997.
- [95] S B Davenport et al. “Development of Constitutive Equations for Modelling of Hot Rolling”. In: *Materials Science and Technology* 16.May (2000), pp. 539–546. ISSN: 0267-0836. DOI: [10 . 1179 / 026708300101508045](https://doi.org/10.1179/026708300101508045).
- [96] MS Loveday et al. “Measurement of flow stress in hot plane strain compression tests”. In: *Materials at High Temperatures* 23.2 (Jan. 2006), pp. 85–118. ISSN: 0960-3409. DOI: [10.1179/mht.2006.006](https://doi.org/10.1179/mht.2006.006).
- [97] RW Evans. “Axisymmetric compression test and hot working properties of alloys”. In: *Materials science and technology* 17.August (2001), pp. 995–1004.
- [98] K H Grote and E K Antonsson. *Springer Handbook of Mechanical Engineering*. Springer Handbook of Mechanical Engineering v. 10. Springer, 2009. ISBN: 9783540491316.
- [99] C. Zener and J. H. Hollomon. “Effect of strain rate upon plastic flow of steel”. In: *Journal of Applied Physics* 15.1 (1944), pp. 22–32. ISSN: 00218979. DOI: [10.1063/1.1707363](https://doi.org/10.1063/1.1707363).
- [100] S.L. Semiatin and T.R R. Bieler. “The effect of alpha platelet thickness on plastic flow during hot working of Ti-6Al-4V with a transformed microstructure”. In: *Acta Materialia* 49.17 (Oct. 2001), pp. 3565–3573. ISSN: 13596454. DOI: [10 . 1016 / S1359 - 6454 \(01 \) 00236 - 1](https://doi.org/10.1016/S1359-6454(01)00236-1).
- [101] N.G. Jones et al. “Thermomechanical processing of Ti-5Al-5Mo-5V-3Cr”. In: *Materials Science and Engineering: A* 490.1-2 (Aug. 2008), pp. 369–377. ISSN: 09215093. DOI: [10.1016/j.msea.2008.01.055](https://doi.org/10.1016/j.msea.2008.01.055).
- [102] N.G. Jones and M. Jackson. “On mechanism of flow softening in Ti-5Al-5Mo-5V-3Cr”. In: *Materials Science and Technology* 27.6

- (June 2011), pp. 1025–1032. ISSN: 02670836. DOI: [10 . 1179 / 026708310X12668415533720](https://doi.org/10.1179/026708310X12668415533720).
- [103] J. J. Jonas, C. M. Sellars, and W. J. McG. Tegart. “Strength and structure under hot-working conditions”. In: *International Materials Reviews* 14.July (1969), pp. 1–24. ISSN: 09506608. DOI: [10.1179/095066069790138056](https://doi.org/10.1179/095066069790138056).
- [104] Cangji Shi, Weimin Mao, and X. Grant Chen. “Evolution of activation energy during hot deformation of AA7150 aluminum alloy”. In: *Materials Science and Engineering A* 571 (2013), pp. 83–91. ISSN: 09215093. DOI: [10.1016/j.msea.2013.01.080](https://doi.org/10.1016/j.msea.2013.01.080).
- [105] Amir Momeni. “The physical interpretation of the activation energy for hot deformation of Ni and Ni–30Cu alloys”. In: *Journal of Materials Research* 31.08 (2016), pp. 1077–1084. ISSN: 0884-2914. DOI: [10.1557/jmr.2016.81](https://doi.org/10.1557/jmr.2016.81).
- [106] Nho Kwang Park, Jong Taek Yeom, and Young Sang Na. “Characterization of deformation stability in hot forging of conventional Ti-6Al-4V using processing maps”. In: *Journal of Materials Processing Technology* 130-131 (2002), pp. 540–545. ISSN: 09240136. DOI: [10.1016/S0924-0136\(02\)00801-4](https://doi.org/10.1016/S0924-0136(02)00801-4).
- [107] Jun Cai et al. “Constitutive equations for elevated temperature flow stress of Ti–6Al–4V alloy considering the effect of strain”. In: *Materials & Design* 32.3 (2011), pp. 1144–1151. ISSN: 02613069. DOI: [10.1016/j.matdes.2010.11.004](https://doi.org/10.1016/j.matdes.2010.11.004).
- [108] W A Bryant. “Correlation of data on the hot deformation of Ti - 6Al-4V”. In: *Journal of Materials Science* 10.10 (1975), pp. 1793–1797. ISSN: 0022-2461. DOI: [10.1007/BF00554942](https://doi.org/10.1007/BF00554942).
- [109] I. Weiss and S.L. Semiatin. “Thermomechanical processing of alpha titanium alloys - an overview”. In: *Materials Science and Engineering: A* 263.1-2 (Mar. 1999), pp. 243–256. ISSN: 09215093. DOI: [10.1016/S0921-5093\(98\)01155-1](https://doi.org/10.1016/S0921-5093(98)01155-1).
- [110] H J Frost and M F Ashby. *Deformation-mechanism maps: the plasticity and creep of metals and ceramics*. Pergamon Press, 1982. ISBN: 9780080293370.

- [111] I. Weiss and S.L. Semiatin. “Thermomechanical processing of beta titanium alloys—an overview”. In: *Materials Science and Engineering: A* 243.1-2 (Mar. 1998), pp. 46–65. ISSN: 09215093. DOI: [10.1016/S0921-5093\(97\)00783-1](https://doi.org/10.1016/S0921-5093(97)00783-1).
- [112] Hiroaki Matsumoto et al. “Hot forging characteristic of Ti-5Al-5V-5Mo-3Cr alloy with single metastable beta microstructure”. In: *Materials Science and Engineering A* 611 (2014), pp. 337–344. ISSN: 09215093. DOI: [10.1016/j.msea.2014.06.006](https://doi.org/10.1016/j.msea.2014.06.006).
- [113] Jeoung Han Kim et al. “Microstructure prediction of two-phase titanium alloy during hot forging using artificial neural networks and fe simulation”. In: *Metals and Materials International* 15.3 (2009), pp. 427–437. ISSN: 15989623. DOI: [10.1007/s12540-009-0427-7](https://doi.org/10.1007/s12540-009-0427-7).
- [114] Ren Guo Guan et al. “Effect of microstructure on deformation behavior of Ti-6Al-4V alloy during compressing process”. In: *Materials & Design* 36 (Apr. 2012), pp. 796–803. ISSN: 02613069. DOI: [10.1016/j.matdes.2011.11.057](https://doi.org/10.1016/j.matdes.2011.11.057).
- [115] L. L. Benson. *Private Communication*. 2016.
- [116] S. Tamas-Williams et al. “Porosity regrowth during heat treatment of hot isostatically pressed additively manufactured titanium components”. In: *Scripta Materialia* 122 (2016), pp. 72–76. ISSN: 13596462. DOI: [10.1016/j.scriptamat.2016.05.002](https://doi.org/10.1016/j.scriptamat.2016.05.002).
- [117] S. Shao et al. “Solubility of argon in laser additive manufactured α -titanium under hot isostatic pressing condition”. In: *Computational Materials Science* 131 (2017), pp. 209–219. ISSN: 09270256. DOI: [10.1016/j.commatsci.2017.01.040](https://doi.org/10.1016/j.commatsci.2017.01.040).
- [118] Y.V.R.K. Prasad and T Seshacharyulu. “Processing maps for hot working of titanium alloys”. In: *Materials Science and Engineering: A* 243 (1998), pp. 82–88. ISSN: 09215093. DOI: [10.1016/S0921-5093\(97\)00782-X](https://doi.org/10.1016/S0921-5093(97)00782-X).
- [119] G. Majkic et al. “Synthesis of NiTi by low electrothermal loss spark plasma sintering”. In: *Metallurgical and Materials Transactions A: Physical Metallurgy and Materials Science* 38.10 (2007), pp. 2523–2530. ISSN: 10735623. DOI: [10.1007/s11661-007-9307-2](https://doi.org/10.1007/s11661-007-9307-2).

- [120] Sandvik. *SANDVIK 253 MA*.
- [121] Presspahn Ltd. *Flexible Cogemicanite 132*.
- [122] Lei Xu et al. “Effect of Hot Isostatic Pressing Conditions and Cooling Rate on Microstructure and Properties of Ti-6Al-4V Alloy from Atomized Powder”. In: *Journal of Materials Science and Technology* 30.12 (2014), pp. 1289–1295. ISSN: 10050302. DOI: [10.1016/j.jmst.2014.04.011](https://doi.org/10.1016/j.jmst.2014.04.011).
- [123] Youngmoo Kim et al. “Microstructure and mechanical properties of hot isostatically pressed Ti–6Al–4V alloy”. In: *Journal of Alloys and Compounds* 603 (2014), pp. 207–212. ISSN: 09258388. DOI: [10.1016/j.jallcom.2014.03.022](https://doi.org/10.1016/j.jallcom.2014.03.022).
- [124] S.L. Semiatin et al. “Microstructure evolution during alpha-beta heat treatment of Ti-6Al-4V”. In: *Metallurgical and Materials Transactions A* 34.October (2003), pp. 2377–2386. ISSN: 1073-5623. DOI: [10.1007/s11661-003-0300-0](https://doi.org/10.1007/s11661-003-0300-0).

A. Technical Drawings of FAST Mould Assemblies and Components

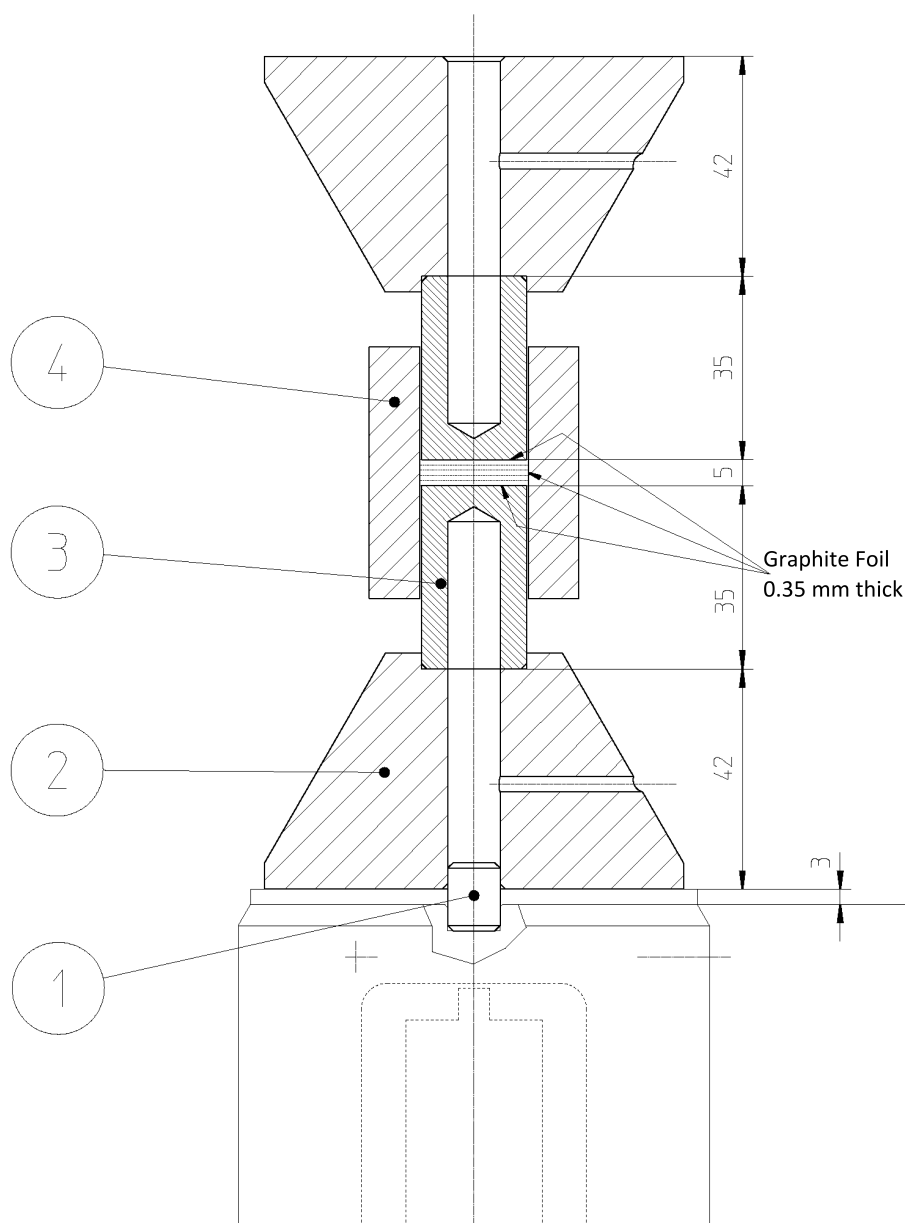


Figure A.1 – Technical drawing showing the dimensions of the components of the 20 mm diameter all-graphite FAST mould assembly.

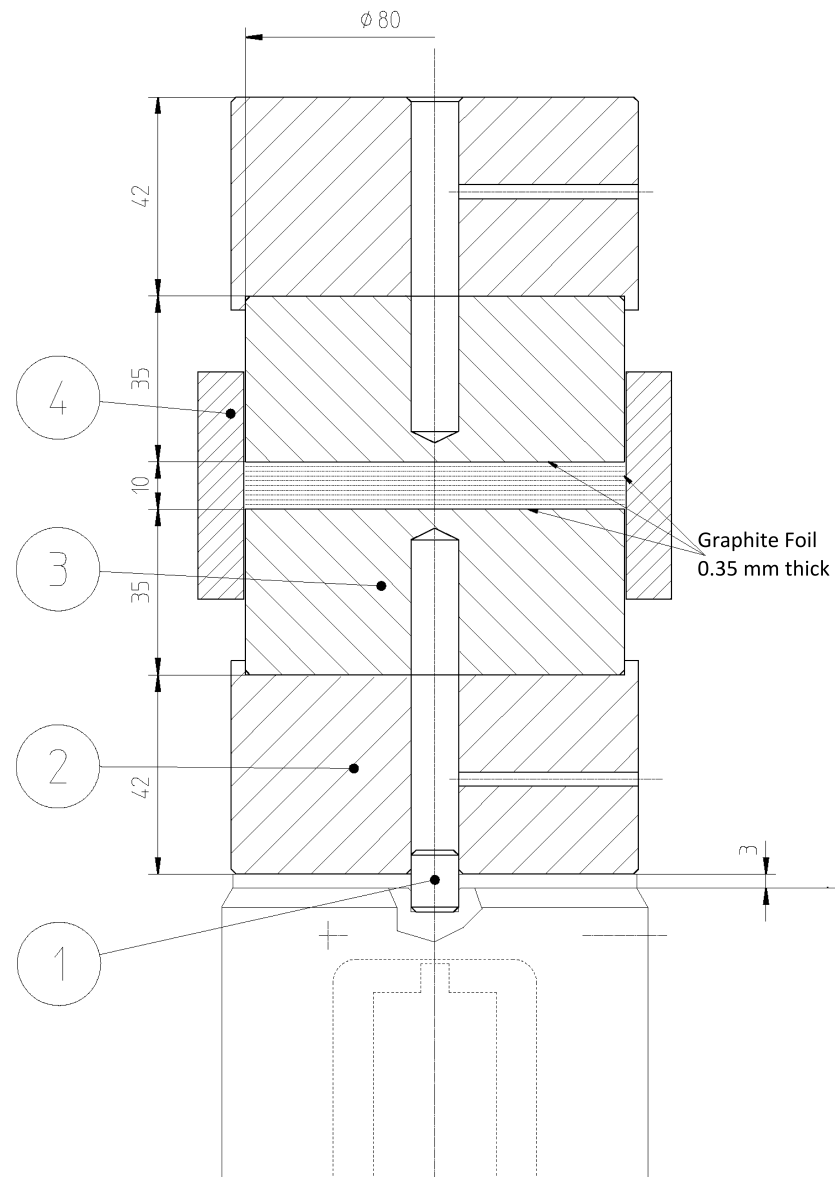


Figure A.2 – Technical drawing showing the dimensions of the components of the 80 mm diameter all-graphite FAST mould assembly.

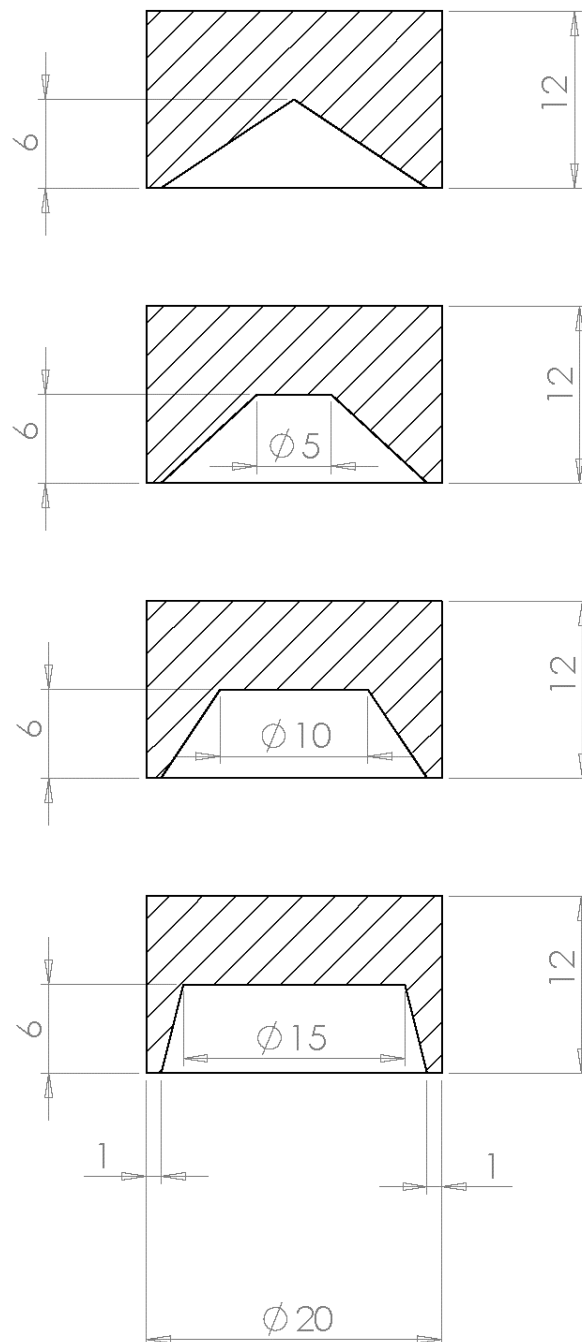


Figure A.3 – Technical drawing showing the dimensions of the 20 mm diameter shaped graphite inserts for the 20 mm FAST mould assemblies.

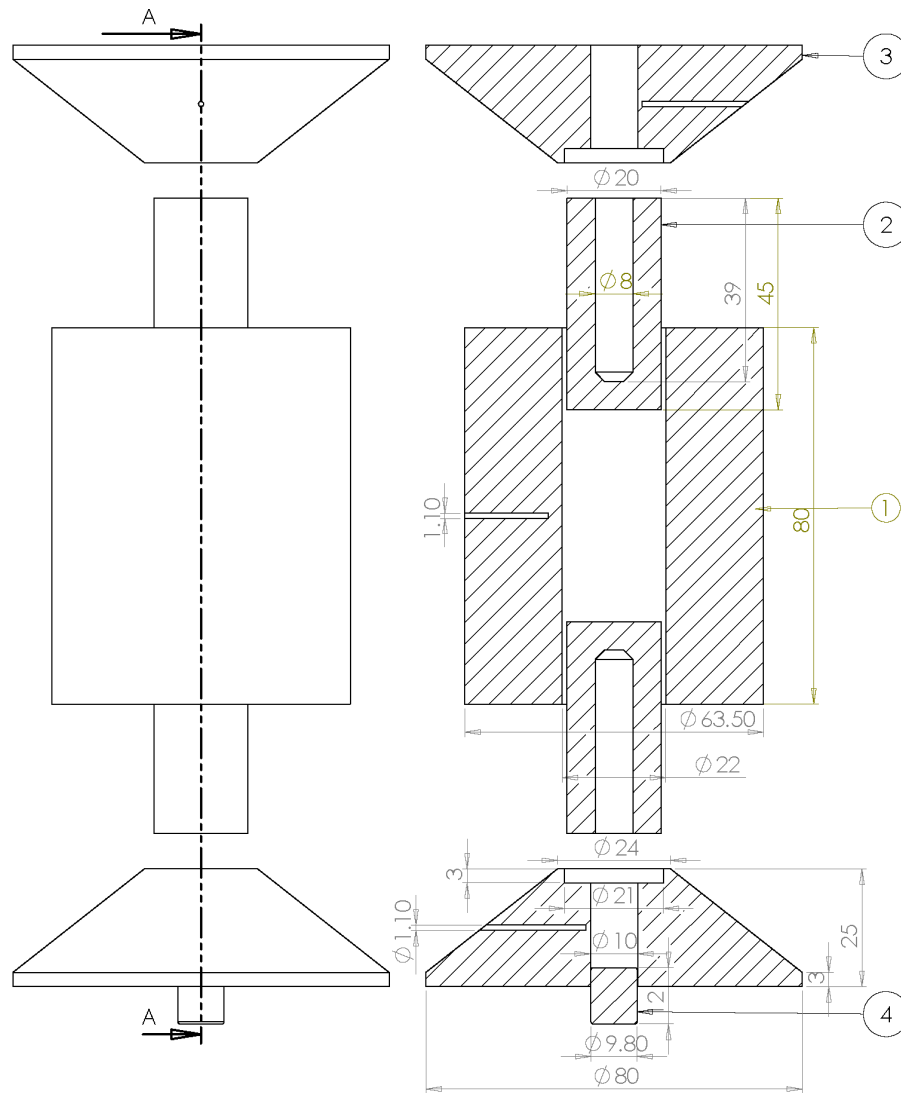


Figure A.4 – Technical drawing showing the dimensions of the components of the 20 mm diameter all-steel FAST mould assembly used in chapter 6.

B. Published Work Reuse Permissions

SPRINGER LICENSE TERMS AND CONDITIONS	
Jan 16, 2017	
<hr/>	
This Agreement between Nick S Weston ("You") and Springer ("Springer") consists of your license details and the terms and conditions provided by Springer and Copyright Clearance Center.	
License Number	4030990662178
License date	Jan 16, 2017
Licensed Content Publisher	Springer
Licensed Content Publication	Journal of Materials Science (full set)
Licensed Content Title	Spark plasma sintering of commercial and development titanium alloy powders
Licensed Content Author	N. S. Weston
Licensed Content Date	Jan 1, 2015
Licensed Content Volume Number	50
Licensed Content Issue Number	14
Type of Use	Thesis/Dissertation
Portion	Full text
Number of copies	3
Author of this Springer article	Yes and you are the sole author of the new work
Order reference number	
Title of your thesis / dissertation	A novel solid-state processing route to generate cost-effective titanium alloy components
Expected completion date	Mar 2017
Estimated size(pages)	180
Requestor Location	Nick S Weston University of Sheffield Sir Robert Hadfield Building Mappin Street Sheffield, South Yorkshire S1 3JD United Kingdom Attn: Nick S Weston
Billing Type	Invoice
Billing Address	Nick S Weston University of Sheffield Sir Robert Hadfield Building Mappin Street Sheffield, United Kingdom S1 3JD Attn: Nick S Weston
Total	0.00 USD

Figure B.1 – License giving permission to reproduce the paper published in the *Journal of Materials Science* by Weston et al. [65].

**JOHN WILEY AND SONS LICENSE
TERMS AND CONDITIONS**

Jan 16, 2017

This Agreement between Nick S Weston ("You") and John Wiley and Sons ("John Wiley and Sons") consists of your license details and the terms and conditions provided by John Wiley and Sons and Copyright Clearance Center.

License Number	4030980888828
License date	Jan 16, 2017
Licensed Content Publisher	John Wiley and Sons
Licensed Content Publication	Wiley eBooks
Licensed Content Title	Exploitation of Spark Plasma Sintering and One-Step Forging for Cost-Effective Processing of Titanium Alloy Powders
Licensed Content Author	Nicholas Weston,Fatos Derguti,Martin Jackson
Licensed Content Date	May 6, 2016
Licensed Content Pages	6
Type of use	Dissertation/Thesis
Requestor type	Author of this Wiley chapter
Format	Print and electronic
Portion	Full chapter
Will you be translating?	No
Title of your thesis / dissertation	A novel solid-state processing route to generate cost-effective titanium alloy components
Expected completion date	Mar 2017
Expected size (number of pages)	180
Requestor Location	Nick S Weston University of Sheffield Sir Robert Hadfield Building Mappin Street Sheffield, South Yorkshire S1 3JD United Kingdom Attn: Nick S Weston
Publisher Tax ID	EU826007151
Billing Type	Invoice
Billing Address	Nick S Weston University of Sheffield Sir Robert Hadfield Building Mappin Street Sheffield, United Kingdom S1 3JD Attn: Nick S Weston
Total	0.00 GBP

Figure B.2 – License giving permission to reproduce the paper published in the *Proceedings of the 13th World Conference on Titanium* by Weston et al. [66].

**ELSEVIER LICENSE
TERMS AND CONDITIONS**

Mar 25, 2017

This Agreement between Nick S Weston ("You") and Elsevier ("Elsevier") consists of your license details and the terms and conditions provided by Elsevier and Copyright Clearance Center.

License Number	4075880341747
License date	Mar 25, 2017
Licensed Content Publisher	Elsevier
Licensed Content Publication	Journal of Materials Processing Technology
Licensed Content Title	FAST-forged – A new cost-effective hybrid processing route for consolidating titanium powder into near net shape forged components
Licensed Content Author	N.S. Weston, M. Jackson
Licensed Content Date	May 2017
Licensed Content Volume	243
Licensed Content Issue	n/a
Licensed Content Pages	12
Start Page	335
End Page	346
Type of Use	reuse in a thesis/dissertation
Portion	full article
Format	both print and electronic
Are you the author of this Elsevier article?	Yes
Will you be translating?	No
Order reference number	
Title of your thesis/dissertation	A novel solid-state processing route to generate cost-effective titanium alloy components
Expected completion date	Mar 2017
Estimated size (number of pages)	180
Elsevier VAT number	GB 494 6272 12
Requestor Location	Nick S Weston University of Sheffield Sir Robert Hadfield Building Mappin Street Sheffield, South Yorkshire S1 3JD United Kingdom Attn: Nick S Weston
Publisher Tax ID	GB 494 6272 12
Total	0.00 GBP

Figure B.3 – License giving permission to reproduce the paper published in the *Journal of Materials Processing Technology* by Weston et al. [67].